Planck: maps, likelihoods, cosmology

Matthieu Tristram

HABILITATION À DIRIGER DES RECHERCHES

Spécialité : Physique (Cosmologie)

Matthieu TRISTRAM

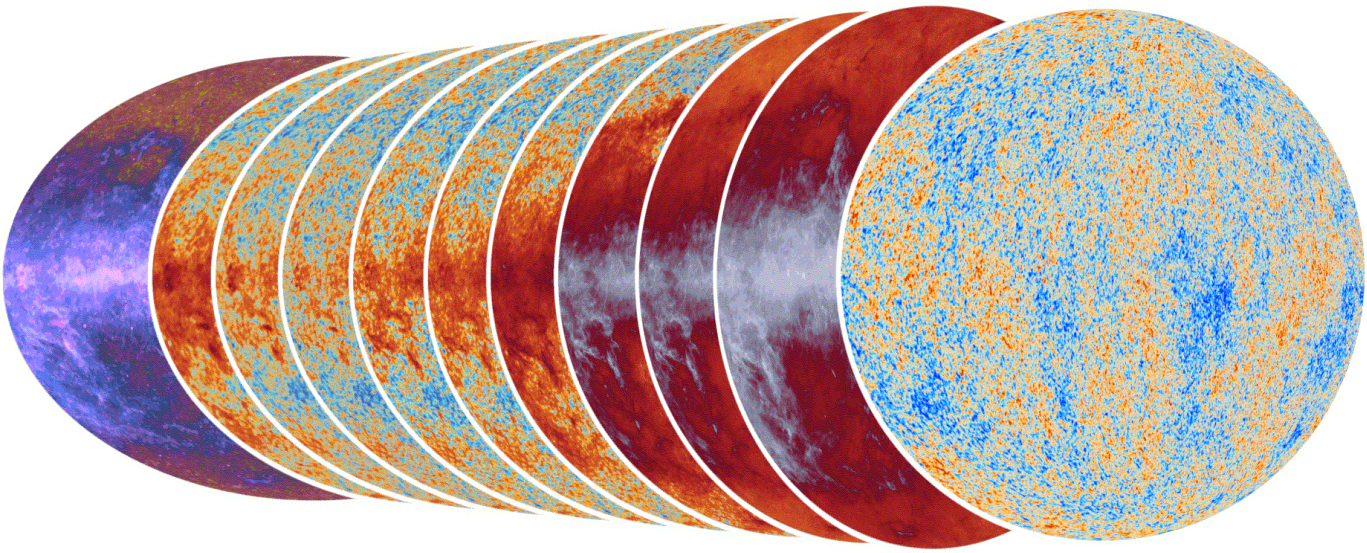

PLANCK

maps, likelihoods, cosmology

Soutenance le 22 janvier 2018 devant le jury d'examen suivant :

Nabila	AGHANIM	*(IAS, Orsay)*	Rapportrice
George	EFSTATHIOU	*(Kavli Institute, Cambridge)*	Rapporteur
Eiichiro	KOMATSU	*(MPI, Garching)*	Rapporteur
Etienne	POINTECOUTEAU	*(IRAP, Toulouse)*	
Achille	STOCCHI	*(LAL, Orsay)*	Président
Radoslaw	STOMPOR	*(APC, Paris)*	

n° LAL 18-002

Contents

Introduction

In this document, we describe how we derive constraints on cosmological models using CMB anisotropies measurements focusing on the work I have participated in during the last 10 years working on the *Planck* mission. As cosmologist, we want to compare the measurements to the theoretical predictions for a given choice of pre-supposed models (which are described in this section). This comparison is done through the use of a combined-likelihood which is made of the various likelihoods discussed in Part II. We can also make use of additional constraints from other observations such as CMB lensing, Baryon acoustic oscillations, measurements of the Hubble constant, and Type Ia supernovae.
The CMB likelihoods make use of observational data which take the form of CMB temperature and polarisation maps. These are obtained through measurement of the sky at sub-millimeter wavelength. In this document, we are using the measurements from the *Planck* satellite mission. The process of map reconstruction for the *Planck* data is described in details in Part I.
The *Planck* measurements are well described by a spatially-flat ΛCDM cosmology with a power-law spectrum of adiabatic scalar perturbations (see Part III). This standard model includes only six free parameters describing the physical densities of baryons ($\Omega_b h^2$) and cold dark matter ($\Omega_c h^2$) today, the angular size of the sound horizon at recombination ($\theta_\star$), the amplitude (A_s) and the spectral index (n_s) of the primordial scalar power-spectrum and the reionization optical depth (τ). These define the initial conditions and the ionization history. The other parameters can be derived from them or are fixed as described in the following and resumed in Table 1. Extensions are then studied to test the robustness of the ΛCDM. As an exemple, we have worked on $N_{\rm eff}$ interpreted as a gravitational waves (Ω_{gw}) in Henrot-Versillé et al. (2015), $A_{\rm lens}$ in Couchot et al. (2017b) or the sum of neutrino masses in Couchot et al. (2017a).

Theoretical model

We follow the cosmological description published in *Planck* papers and in particular in Planck Collaboration XVI (2014). We treat the Cosmological Microwave Background anisotropies as small fluctuations in the Friedmann-Robertson-Walker metric whose evolution is described by General Relativity. Within this framework, the evolution of the perturbations can be computed accurately using a CMB Boltzmann code once the initial conditions, ionization history and constituents of the Universe are specified.
We usually make use of the `class` Boltzmann code (Lesgourgues 2011a) but our conventions are consistent with those of the `camb` code (Lewis et al. 2000). Numerical stability and accuracy of the calculation at the sensitivity of *Planck* has been explored in detail (Hamann et al. 2009; Lesgourgues 2011b; Howlett et al. 2012), demonstrating that the raw numerical precision is sufficient for numerical errors on parameter constraints from *Planck* to be less than 10% of the statistical error around the assumed cosmological model.

Matter and radiation content. We assume that the cold dark matter is pressureless, stable and non-interacting, with a physical density $\omega_c \equiv \Omega_c h^2$. The baryons, with density $\omega_b \equiv \Omega_b h^2$, are assumed to consist almost entirely of hydrogen and helium. The mass fraction in helium is parameterized by Y_P.
The relation between Y_P, the baryon density and the effective number of relativistic species $N_{\rm eff}$ is modelled for standard big-bang nucleosynthesis (BBN) using the PArthENoPE algorithm (Pisanti et al. 2008; Hamann et al. 2008) (neglecting the impact of chemical potential of electron neutrinos). For the *Planck* best-fitting base model (assuming no additional relativistic components and negligible neutrino degeneracy), we found Y_P=0.2477 (Planck Collaboration XVI 2014).
We use the photon temperature T_0=2.7255±0.0006K as measured in Fixsen (2009).
Our model is made of three neutrinos under a minimal-mass normal hierarchy with $\sum m_\nu$=0.06eV (corresponding to $\Omega_\nu h^2 \approx \sum m_\nu / 93.04{\rm eV} \approx 0.0006$) inferred from global fits to recent oscillation and other data (Forero et al. 2012). This is usually approximated for current cosmological data as a single massive eigenstate (see Couchot et al. 2017a, for the impact of this approximation). Full thermal equilibrium is assumed prior to neutrino decoupling. The decoupling of the neutrinos is nearly, but not entirely, completed by the time of electron-positron annihilation. This leads to a slight

Parameter	Baseline	Definition
$\omega_{\rm b}\equiv\Omega_{\rm b}h^2$	...	Baryon density today
$\omega_{\rm c}\equiv\Omega_{\rm c}h^2$	...	Cold dark matter density today
$100\theta_{\rm D}$	...	100× angular extent of photon diffusion at last scattering (see text)
τ	...	Thomson scattering optical depth due to reionization
$\ln(10^{10}A_{\rm s})$	...	Log power of the primordial curvature perturbations (k_0=0.05Mpc^{-1})
$n_{\rm s}$	...	Scalar spectrum power-law index (k_0=0.05Mpc^{-1})
Ω_K	0	Curvature parameter today with $\Omega_{\rm tot}$=1−Ω_K
$\sum m_\nu$	0.06	The sum of neutrino masses in eV
w_0	−1	Dark energy equation of state, $w(a)$=w_0+(1−a)w_a
w_a	0	As above (perturbations modelled using PPF)
$N_{\rm eff}$	3.046	Effective number of neutrino-like relativistic degrees of freedom (see text)
$Y_{\rm P}$	BBN	Fraction of baryonic mass in helium
$A_{\rm L}$	1	Amplitude of the lensing power relative to the physical value
$n_{\rm t}$	$n_{\rm t}$=−$r_{0.05}$/8	Tensor spectrum power-law index (k_0=0.05Mpc^{-1})
$dn_{\rm s}/d\ln k$	0	Running of the spectral index
$r_{0.05}$	0	Ratio of tensor primordial power to curvature power at k_0=0.05Mpc^{-1}
Ω_Λ	derived	Dark energy density divided by the critical density today
$\Omega_{\rm m}$	derived	Matter density (inc. massive neutrinos) today divided by the critical density
t_0	derived	Age of the Universe today (in Gyr)
σ_8	derived	RMS matter fluctuations today in linear theory
$z_{\rm re}$	derived	Redshift at which Universe is half reionized
H_0=100h	derived	Current expansion rate in kms^{-1}Mpc^{-1}
$r_{0.002}$	derived	Ratio of tensor primordial power to curvature power at k_0=0.002Mpc^{-1}
z_*	derived	Redshift for which the optical depth equals unity (see text)
r_*=$r_{\rm s}(z_*)$	derived	Comoving size of the sound horizon at z=z_*
$100\theta_*$	derived	100× angular size of sound horizon at z=z_* ($r_*/D_{\rm A}$)
$z_{\rm drag}$	derived	Redshift at which baryon-drag optical depth equals unity (see text)
$r_{\rm drag}$=$r_{\rm s}(z_{\rm drag})$	derived	Comoving size of the sound horizon at z=$z_{\rm drag}$
$k_{\rm D}$	derived	Characteristic damping comoving wavenumber (Mpc^{-1})
$100\theta_{\rm MC}$	derived	100× approximation to $r_*/D_{\rm A}$ (CosmoMC)
$z_{\rm eq}$	derived	Redshift of matter-radiation equality (massless neutrinos)
$100\theta_{\rm eq}$	derived	100× angular size of the comoving horizon at matter-radiation equality
$r_{\rm drag}/D_{\rm V}(0.57)$	derived	BAO distance ratio at z=0.57

Table 1: Cosmological parameters for ΛCDM models. The top block contains the 6 parameters which define the baseline model. Typical extension parameters are list in the second black. The lower block define various derived parameters.

heating of the neutrinos in addition to that expected for the photons and hence to a small departure from the thermal equilibrium prediction T_γ=$(11/4)^{1/3}T_\nu$ between the photon temperature T_γ and the neutrino temperature T_ν. We account for the additional energy density in neutrinos by assuming that they have a thermal distribution with an effective energy density

$$\rho_\nu = N_{\rm eff}\frac{7}{8}\left(\frac{4}{11}\right)^{4/3}\rho_\gamma, \tag{1}$$

with $N_{\rm eff}$=3.046 in the baseline model (Mangano et al. 2005). This density is divided equally between three neutrino species while they remain relativistic. In Couchot et al. (2017a), we give realistic constraints on the sum of neutrino masses and discuss the actual limit on the neutrino hierarchy.
In Henrot-Versillé et al. (2015), we consider the possibility of extra radiation, beyond that included in the Standard Model. We present the option that all this radiation is due to primordial gravitational waves and discuss the impact on cosmic string models.

Initial conditions. The ΛCDM baseline model assumes scalar perturbations purely adiabatic, with a curvature power spectrum parameterized by

$$\mathcal{P}_\zeta(k) = A_{\rm s}\left(\frac{k}{k_0}\right)^{n_{\rm s}(k)-1}. \tag{2}$$

At first order, $n_{\rm s}$ dependency on k is usually written as $n_{\rm s}(k)$=$n_{\rm s}$+$\frac{1}{2}\frac{dn_{\rm s}}{d\ln k}\ln(\frac{k}{k_0})$. *Planck* results are fully consistent with this hypothesis (Planck Collaboration XIII 2016; Planck Collaboration XX 2016) and show no deviation from a power-law spectrum with constant spectral index i.e. no "running" ($dn_{\rm s}/d\ln k$=0). The value for $A_{\rm s}$ depends on the choice of the pivot scale k_0. In *Planck* papers, we choose k_0=0.05Mpc^{-1}, roughly in the middle of the logarithmic range of scales probed by the instrument, thus limiting the degeneracy between $n_{\rm s}$ and $A_{\rm s}$. *Planck* provides an accurate measurement of the amplitude of the small-scale linear CMB power spectrum, which is proportional to $A_{\rm s}e^{-2\tau}$. The degeneracy between τ and $\ln A_{\rm s}$ can be broken measuring the relative amplitude of polarisation and temperature at large angular scales or introducing CMB lensing.

Tensor modes are introduced using the most general linearized perturbations of the Friedmann-Lemaître-Robertson-Walker metric

$$ds^2=a^2[d\eta^2-(\delta_{ij}+2H_{ij})dx^i dx^j] \tag{3}$$

where H_{ij} is a transverse-traceless spatial tensor and its power spectrum reads $\mathcal{P}_{\rm t}(k)=\partial_{\ln k}\langle 2H_{ij}2H^{ij}\rangle$. The tensor mode power spectrum is parameterized as a power-law with

$$\mathcal{P}_{\rm t}(k)=A_{\rm t}\left(\frac{k}{k_0}\right)^{n_{\rm t}}. \tag{4}$$

We define $r_{k_0}\equiv A_{\rm t}/A_{\rm s}$, the primordial tensor-to-scalar ratio at $k=k_0$. Our constraints are only weakly sensitive to the tensor spectral index, $n_{\rm t}$ (which is assumed to be close to zero), and we adopt the single-field inflation consistency relation $n_{\rm t}=-r/8$. Most previous CMB experiments have reported constraints on $r_{0.002}$ i.e. using $k=0.002{\rm Mpc}^{-1}$, which is closer to the scale at which there is some sensitivity to tensor modes in the large-scale power spectra. Given the definition in Eq. 2 and Eq. 4, the relation scales like $(0.05/0.002)^{-r/8}$ which gives $r_{0.002}$ lower by 4% at $r\sim0.1$ wrt $r_{0.05}$ (and consequently less than 0.4% for $r<0.01$).

Dark energy. The ΛCDM model assumes that the dark energy is a cosmological constant with current density parameter Ω_Λ and that the dark energy does not interact with other constituents other than through gravity. Beyond ΛCDM, when considering a dynamical dark energy component, we parameterize the equation of state as

$$w(z)\equiv\frac{p}{\rho}=w_0+(1-a)w_a=w_0+w_a\frac{z}{1+z} \tag{5}$$

which is well behaved to high redshift and serves as an excellent approximation to slow roll scalar field models of dark energy (Linder 2003).

Ionization history. To make accurate predictions for the CMB power spectra, the background ionization history (through the determination of the ionization fraction $\boldsymbol{x}_{\rm e}$) has to be calculated at the sub-percent level.
At recombination, the Universe undertakes a transition from a state of fully ionized hydrogen and helium in the early Universe, up to a very low residual electron fraction ($x_{\rm e}\sim10^{-4}$) at the end of recombination. The CMB power spectra are sensitive to the details of $x_{\rm e}$ through changes of the sound horizon at recombination and the detailed shape of the recombination transition, which affects the thickness of the last-scattering surface and hence the amount of small-scale diffusion (Silk) damping, polarization, and line-of-sight averaging of the perturbations. The physical processes involved during recombination can be modelled numerically using multi-level atom codes such as `HyRec` (Switzer & Hirata 2008; Hirata 2008), and `CosmoRec` (Chluba & Thomas 2011). In *Planck*, we are using a simpler model developed by Seager et al. (2000) and implemented in the `recfast` code with appropriately chosen small correction functions calibrated to the full numerical results (Rubino-Martin et al. 2009; Shaw & Chluba 2011).
At late time, the Universe reionized via ultra-violet photons from stars and/or active galactic nuclei (Planck Collaboration Int. XLVII 2016) and Chapter 9. In standard cosmological model, we approximate the reionization as being relatively sharp ($\Delta z=0.5$) and parametrized by a mean redshift $z_{\rm re}$ where $x_{\rm e}=0.5$. We assume the first reionization of helium happened at the same time as the hydrogen reionization. The value of the reionization redshift directly affects the CMB power spectra at low-multipoles but the latter are marginally sensitive to the details of the shape of the transition.

Lensing. Information from CMB lensing enters in two ways in the cosmological constraints. Firstly, the photons from the last scattering surface are affected by the gravitational potential along their path. This effect dominates at early times, $z\lesssim10$, where the large scale structures have formed. In practice, the CMB power spectra computed at the time of recombination are then modelled using the lensing potential, resulting in a smoothing effect of the acoustic peaks by approximately 5%.
Secondly, we can reconstruct the lensing potential power spectrum (averaged over the line-of-sight) using the three-point correlation function of the CMB anisotropy maps (Planck Collaboration XV 2016). From this power spectrum, we have built a *Planck* lensing likelihood which directly compares the measured lensing power spectrum to theoretical expectations.
The theoretical predictions for the lensing potential power spectrum include corrections for the non-linear matter power spectrum. If the corrections on the temperature power spectrum can be neglected for the basic ΛCDM model, the impact is important on some particular extensions (such that the sum of the neutrino masses $\sum m_\nu$) and for the reconstruction of the lensing potential. We commonly use the model `halofit` (Smith et al. 2003) as updated by Takahashi et al. (2012) to model the impact of non-linear growth on the theoretical prediction for the lensing potential power.

Likelihood

Given that the distribution of the CMB anisotropies is compatible with a Gaussian distribution (as measured by *Planck* in Planck Collaboration XVII 2016), all the relevant statistical information is encoded in the two points correlation function

of the CMB temperature and polarization anisotropies or, equivalently, its projection in harmonic space: the angular power spectrum of the CMB temperature and polarization fields. This is defined as $\hat{C}_\ell=\langle a_{\ell m}a^*_{\ell' m'}\rangle\delta_{\ell\ell'}$, where $a_{\ell m}$ are the coefficients of the spherical harmonic decomposition. The connection between the measured CMB data and the theory is done through the CMB likelihood function $\mathcal{L}=P(\mathbf{d}|C_\ell(\alpha))$ that quantifies the match between the CMB data $\mathbf{d}$ and a given theoretical model parametrized e.g. by a theoretical power spectrum $C_\ell(\alpha)$ defined in terms of a set of cosmological parameters α.
For full-sky coverage maps with a huge number of pixels (more than 50 millions) such as *Planck* maps, we decided to split the likelihood information between the low and the high multipoles, taking advantage of the best likelihood approximations for both range of multipoles.

high multipoles likelihood. On the full-sky, the distribution of auto-spectra is a scaled-χ^2 with $2\ell+1$ degrees of freedom. The distribution of the cross-spectra is slightly different (see Appendix A in Mangilli et al. 2015), however, above $\ell\gtrsim20$, the number of modes is large enough so that we can safely assume that the C_ℓ are Gaussian distributed. When considering only a part of the sky, the C_ℓs get correlated so that for high multipoles, the resulting distribution can be approximated by a multi-variate Gaussian taking into account ℓ-by-ℓ correlations:

$$-2\ln\mathcal{L}=\boldsymbol{R}^\dagger\boldsymbol{\Sigma}^{-1}\boldsymbol{R}+\ln|\boldsymbol{\Sigma}| \tag{6}$$

where $\boldsymbol{R}_\ell=\hat{\boldsymbol{C}}_\ell-\boldsymbol{C}_\ell$ denotes the difference between the estimated cross-power spectrum $\hat{\boldsymbol{C}}_\ell$ and the model $\boldsymbol{C}_\ell$, the latter of which includes the CMB signal and the potential foregrounds residuals for each polarisation mode considered (TT,EE,TE). The matrix $\boldsymbol{\Sigma}=\left\langle\boldsymbol{R}\boldsymbol{R}^T\right\rangle$ is the full covariance matrix which includes the instrumental variance from the data as well as the cosmic variance from the model. The latter is directly proportional to the model so that the matrix $\boldsymbol{\Sigma}$ does, in principle, depend on the model (although, in practice, the current knowledge of the cosmological model allows to recover low-bias estimates with an accurate estimation of the error bars using a fiducial model).
For *Planck*, three implementations of high-ℓ likelihoods have been compared (see Planck Collaboration XI 2016). Chapter 6 describes our implementation named HiLLiPOP.

low multipoles likelihood. So far the analysis of the CMB anisotropies at large angular scales has mostly been based on methods that rely on low resolution maps in order to compute the exact CMB likelihood function in pixel space, $\mathcal{L}=P(\mathbf{d}|C_\ell(\alpha))$, with $\mathbf{d}\equiv M(\mathbf{p})=\sum_{\ell m}a_{\ell m}Y_{\ell m}(\mathbf{p})$. This approach is based on the fact that, given that the CMB anisotropies are compatible with a gaussian distribution with random phases, the $a_{\ell m}$ follow a multi-variate Gaussian distribution. The likelihood function, written in pixel space or, equivalently, in terms of the $a_{\ell m}$ coefficients, is gaussian and therefore can be computed exactly (Gorski et al. 1994; Slosar et al. 2004; Page et al. 2007; Bennett 2013).
Alternatively, the likelihood function could be defined in the harmonic space as done e.g. in the small scales analysis where the data compression from CMB maps to angular power spectra is necessary for computational and numerical reasons. However, the complication of working in harmonic space at large angular scales (low-ℓ multipoles) is related to the fact that the distribution of the $\hat{C}_\ell$ estimators at low-ℓ is non-Gaussian. In harmonic space the $\hat{C}_\ell$ consist in the sum of the square of the harmonic coefficients $a_{\ell m}$ and they have a reduced-χ^2 distribution. Therefore the likelihood of a theoretical power spectrum as a function of the measured $\hat{C}_\ell$ is non-Gaussian. Contrary to the small-scales analysis, the CMB low-ℓ analysis is particularly concerned by this issue given that the central limit theorem cannot be invoked. Previous studies (Percival & Brown 2006; Hamimeche & Lewis 2008) developed a CMB analysis on large angular scales based on the likelihood definition in harmonic space in terms of auto-spectra, that is to say CMB angular power spectra obtained from a given single frequency/dataset CMB map. This approach however shared problems similar to the pixel based likelihood approach, in particular in terms of the dependency to the noise and of the accurate characterization of the systematics effects at the auto-spectra levels.
For *Planck*, at low multipoles ($2\leq\ell\leq49$), the temperature likelihood was based on a Blackwell-Rao estimator applied to Gibbs samples computed by the `Commander` algorithm (Eriksen et al. 2008) from *Planck* maps in the frequency range 30–353 GHz over 91% of the sky. The likelihood at low multipoles therefore accounts for errors in foreground cleaning. For polarization, Chapter 5 describes our implementation of a likelihood based on the extension of the Hamimeche & Lewis (2008) approximation to the cross-spectra, which have been used to derive the constraints from low-ℓ polarisation maps in 2015 (Planck Collaboration Int. XLVII 2016).

Sampling and confidence intervals

Parameter estimation in cosmology is predominantly performed using Bayesian inference, particularly following the introduction of Markov chain Monte Carlo (MCMC) techniques (Christensen et al. 2001). Many scientists in the field use the sophisticated `CosmoMC`[1] software (Lewis & Bridle 2002) to study cosmological parameters, and several experiments provide ready-to-use plugins for it. The analysis of the *Planck* cosmological parameters (Planck Collaboration XVI 2014; Planck Collaboration XIII 2016) is based on Bayesian inference using dedicated versions of `CosmoMC`. In this methodology, the likelihood leads to the posterior distribution of the parameters once it has been multiplied by some prior distribution that encompasses an a-priori degree of belief before the measurement is performed. For *Planck*, wide

[1] Available from http://cosmologist.info/cosmomc/readme_planck.html

bounds on uniform distributions have typically been used. However the choice of a particular set of parameters for MCMC sampling, such as the efficient "physical basis" used in `CosmoMC`, may also be viewed as an implicit prior choice.

In the frequentist framework, one instead builds *profile likelihoods* (Wilks 1938) for individual parameters and, by construction, the individual parameter estimates are derived from the maximum likelihood estimate (MLE) values. Frequentist methods do not need priors, other than some limits on the explored domain that are used in practice and can be seen as the bounds of some "uniform priors". The MLE does not depend on the choice of the set of parameters, since it possesses the property of *invariance*: if $\hat{\theta}$ represents the MLE of the parameter θ, then the MLE of any function $\tau(\theta)$ is $\hat{\tau}=\tau(\hat{\theta})$. This means that one can compute the MLE with any set of parameters. This property is also used to obtain asymmetric confidence intervals.

MCMC sampling is sometimes used to perform a "poor-man's" determination of the maximum likelihood (e.g., Reid et al. 2010): one bins a given parameter and reports the sample of maximum likelihood in other dimensions. As pointed out in Hamann (2012), in many dimensions it is most likely that the real maximum was never reached in any reasonably-sized chain. The authors suggest changing the temperature of the chain, but this still requires running lengthy evaluations of the likelihood and is less straightforward than directly using a multi-dimensional minimization algorithm.

In the MCMC procedure, once the chains have converged, individual parameter contours are obtained through *marginalization*, which is performed by a simple projection of the samples onto one or sometimes two axes integrating over the other dimensions of the parameter space. This may however lead to so-called "volume effects", where the mean of the projected distribution can become incompatible with the multi-dimensional MLE (Hamann et al. 2007).

Given the sensitivity of the *Planck* data, statistical methodologies may matter. This is the reason why we built the CAMEL software[2]. In this software, we combine the Bayesian and Frequentist methodology with an adaptative MCMC algorithm and a powerful minimizer based on the mature and widely-used `Minuit` software (James & Roos 1975). We interfaced it to the modular `class` Boltzmann solver (Blas et al. 2011) which, from a set of input cosmological parameters, computes the corresponding temperature and polarization power spectra that are tested against the CMB likelihoods. The high sensitivity of data from *Planck* and from the ground-based high resolution experiments (such as the South Pole Telescope SPT and Atacama Cosmology Telescope ACT projects) requires the simultaneous fit of a larger number of parameters, up to about 40, with some nuisance ones being poorly constrained. We therefore need to tune the `class` precision parameters to a level where the numerical noise can be handled by our high-quality minimizer (see Planck Collaboration Int. XVI 2014).

In Planck Collaboration Int. XVI (2014), we investigated whether the use of priors or marginalization can affect the determination of the cosmological parameters by comparing the published Bayesian results to a frequentist method. For the base ΛCDM model, it happens that the cosmological parameter posteriors are essentially Gaussian, so it is expected that frequentist and Bayesian methods will lead to similar results. In extensions to the standard ΛCDM model this is however not true for some parameters (e.g., the sum of neutrino masses), and priors have been shown to play some role in parameter determination (Hamann et al. 2007; Gonzalez-Morales et al. 2011; Hamann 2012; Couchot et al. 2017a).

[2] `camel.in2p3.fr`

Bibliography

Bennett, C. L. e. 2013, ApJS, 208, 20
Blas, D., Lesgourgues, J., & Tram, T. 2011, J. Cosmology Astropart. Phys., 7, 034
Chluba, J. & Thomas, R. M. 2011, MNRAS, 412, 748
Christensen, N., Meyer, R., Knox, L., & Luey, B. 2001, Classical and Quantum Gravity, 18, 2677
Couchot, F., Henrot-Versillé, S., Perdereau, O., et al. 2017a, ArXiv e-prints [arXiv:1703.10829]
Couchot, F., Henrot-Versillé, S., Perdereau, O., et al. 2017b, A&A, 597, A126
Eriksen, H. K., Jewell, J. B., Dickinson, C., et al. 2008, ApJ, 676, 10
Fixsen, D. J. 2009, ApJ, 707, 916
Forero, D., Tortola, M., & Valle, J. 2012 [arXiv:1205.4018]
Gonzalez-Morales, A. X., Poltis, R., Sherwin, B. D., & Verde, L. 2011, ArXiv e-prints [arXiv:1106.5052]
Gorski, K. M., Hinshaw, G., Banday, A. J., et al. 1994, ApJ, 430, L89
Hamann, J. 2012, Journal of Cosmology and Astroparticle Physics, 2012, 021
Hamann, J., Balbi, A., Lesgourgues, J., & Quercellini, C. 2009, JCAP, 0904, 011
Hamann, J., Hannestad, S., Raffelt, G. G., & Wong, Y. Y. Y. 2007, J. Cosmology Astropart. Phys., 8, 021
Hamann, J., Lesgourgues, J., & Mangano, G. 2008, J. Cosmology Astropart. Phys., 3, 004
Hamimeche, S. & Lewis, A. 2008, Phys.Rev., D77, 103013
Henrot-Versillé, S., Robinet, F., Leroy, N., et al. 2015, Classical and Quantum Gravity, 32, 045003
Hirata, C. M. 2008, Phys.Rev., D78, 023001
Howlett, C., Lewis, A., Hall, A., & Challinor, A. 2012, JCAP, 1204, 027
James, F. & Roos, M. 1975, Computer Physics Communications, 10, 343
Lesgourgues, J. 2011a, ArXiv e-prints [arXiv:1104.2932]
Lesgourgues, J. 2011b, ArXiv e-prints [arXiv:1104.2934]
Lewis, A. & Bridle, S. 2002, Phys. Rev. D, 66, 103511
Lewis, A., Challinor, A., & Lasenby, A. 2000, ApJ, 538, 473
Linder, E. V. 2003, ArXiv Astrophysics e-prints [astro-ph/0311403]
Mangano, G., Miele, G., Pastor, S., et al. 2005, Nucl.Phys., B729, 221
Mangilli, A., Plaszczynski, S., & Tristram, M. 2015, MNRAS, 453, 3174
Page, L. et al. 2007, Astrophys.J.Suppl., 170, 335
Percival, W. J. & Brown, M. L. 2006, Mon.Not.Roy.Astron.Soc., 372, 1104
Pisanti, O., Cirillo, A., Esposito, S., et al. 2008, Computer Physics Communications, 178, 956
Planck Collaboration XVI. 2014, A&A, 571, A16
Planck Collaboration XI. 2016, A&A, 594, A11
Planck Collaboration XIII. 2016, A&A, 594, A13
Planck Collaboration XV. 2016, A&A, 594, A15
Planck Collaboration XVII. 2016, A&A, 594, A17
Planck Collaboration XX. 2016, A&A, 594, A20
Planck Collaboration Int. XVI. 2014, A&A, 566, A54
Planck Collaboration Int. XLVII. 2016, A&A, 596, A108
Reid, B. A., Verde, L., Jimenez, R., & Mena, O. 2010, J. Cosmology Astropart. Phys., 1, 003
Rubino-Martin, J. A., Chluba, J., Fendt, W. A., & Wandelt, B. D. 2009 [arXiv:0910.4383]
Seager, S., Sasselov, D. D., & Scott, D. 2000, Astrophys. J. Suppl., 128, 407
Shaw, J. R. & Chluba, J. 2011, MNRAS, 415, 1343
Slosar, A., Seljak, U., & Makarov, A. 2004, Phys.Rev., D69, 123003
Smith, R. E. et al. 2003, Mon. Not. Roy. Astron. Soc., 341, 1311
Switzer, E. R. & Hirata, C. M. 2008, Phys. Rev., D77, 083006
Takahashi, R., Sato, M., Nishimichi, T., Taruya, A., & Oguri, M. 2012, ApJ, 761, 152
Wilks, S. S. 1938, Ann. Math. Statist., 9, 60

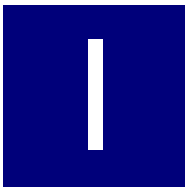

Map Making & Calibration

Chapter 1

pre-flight Planck Map-Making

extracted from Tristram et al. (2011)

"Iterative destriping and photometric calibration for Planck-HFI, polarized, multi-detector map-making"

The LAL group has been in charge of the map-making since early times in Planck. Among several map-making solutions that have been studied for a long time, the destriping algorithm was the most suitable choice for the Planck characteristics. Indeed, the low knee-frequency of the 1/f noise expected for the Planck detectors combined to the scanning strategy of observations allows to fulfill the destriping hypothesis.
When I arrived at LAL in 2005, we started to implement an algorithm that could treat polarisation based on the first implementation in Temperature already done by the LAL team (`Mokapix`*). The resulting code, developed with Olivier Perdereau, François Touze and in collaboration with Radek Stompor (from APC), called* `Polkapix` *allowed for reconstruction of the polarisation signal while estimating a constant offset per stable-pointing period (so-called "ring"). With our PhD student Clément Filliard, we further implemented and studied the absolute photometric calibration based on the orbital dipole signal and the relation with the destriping algorithm.*

1.1 Introduction

Once the data has been "cleaned", the time-ordered samples must be projected onto a pixelized map of the sky using the associated pointing information. To each measurement in time is associated a pixel in its pointing direction. The most common pixelization scheme used in CMB data analysis today is the Hierarchical Equal Area isoLatitude Pixelization, or HEALPix[1] (Górski et al. 2005), in which each pixel is exactly equal-area, and in which pixels lay on sets of rings at constant latitude. This allows one to take advantage of fast Fourier transforms in the analysis, when decomposing the map data into spherical harmonics (Muciaccia et al. 1997). For polarization, given the orientations of the detectors on the sky as a function of time, maps of the Q and U stokes parameters are also reconstructed from the signal.
We have developed an iterative scheme designed to recover calibrated I, Q, and U maps from *Planck*-HFI data using the orbital dipole due to the satellite motion with respect to the Solar System frame. It combines a map reconstruction, based on a destriping technique, juxtaposed with an absolute calibration algorithm. We evaluate systematic and statistical uncertainties incurred during both these steps with the help of realistic, Planck-like simulations containing CMB, foreground components and instrumental noise, and assess the accuracy of the sky map reconstruction by considering the maps of the residuals and their spectra. In particular, we discuss destriping residuals for polarization sensitive detectors similar to those of *Planck*-HFI under different noise hypotheses and show that these residuals are negligible (for intensity maps) or smaller than the white noise level (for Q and U Stokes maps), for ℓ>50. We also demonstrate that the combined level of residuals of this scheme remains comparable to those of the destriping-only case except at very low ℓ where residuals from the calibration appear. For all the considered noise hypotheses, the relative calibration precision is on the order of a few 10^{-4}, with a systematic bias of the same order of magnitude.

[1] http://healpix.jpl.nasa.gov

The *Planck* mission[2], launched on May 14 2009, is a third-generation satellite dedicated to observations of cosmic microwave background (CMB) anisotropies after COBE[3] and WMAP[4]. Its primary objectives are to measure the full-sky CMB anisotropies down to the cosmic variance limit reaching beyond ℓ~2000 in temperature and ℓ~1500 in E-mode polarization. Other scientific goals include in-depth studies of the Galactic emissions, extraction of catalogs of galaxy clusters and extragalactic sources and searches for non-Gaussianity.
Planck observes the sky in nine frequency bands using two instruments: *LFI* with three channels centered at 30, 44, and 70 GHz and *HFI* with six channels at 100, 143, 217, 353, 545, and 857 GHz with an angular resolution in the HFI CMB-dominated bands, 217 and 143 GHz, of from 5 to 10 arcmin. A map-making procedure designed to recover the sky maps from the noisy time-ordered measurements is a necessary step down the data analysis pipeline of the Planck data needed to ensure a delivery of high quality sky images in the observed bands.
Map-making algorithms have been extensively tested and compared with each other within the Planck framework (see e.g. Ashdown et al. 2007b,a) assuming some standardized, and unavoidably, idealized circumstances. This study complements these earlier works describing an iterative procedure to combine map-making and CMB orbital-dipole-based calibration procedures and investigating in detail its precision and its dependence on low-frequency correlated noise due to drifts and artifacts present in *HFI*-like timelines. The map-making technique used in this paper is destriping (e.g., Burigana et al. 1999; Delabrouille 1998; Maino et al. 1999; Revenu et al. 2000; Maino et al. 2002; Keihänen et al. 2004), which is designed to mitigate the long-term correlation of the *HFI* bolometers and approach the white noise limit in the map domain. The algorithm first projects the time-ordered data (TOD) for each stable pointing period of the Planck satellite separately onto the sky resulting in a set of overlapping *ring*-like maps. The relative offsets of these (one per ring), i.e. ones that lead to a coherent full-sky map, are then derived using a maximum-likelihood method that marginalizes over the sky signal. The sky maps are produced by projecting the offset-corrected TOD onto the sky. Calibration is done iteratively using offsets determined from a previous step to constrain the next approximation of the calibration coefficients using the maximum likelihood algorithm. We also address the validity of the destriping hypothesis for different models of Fourier noise spectrum and estimate the effect of iteration on the calibration for the high-precision polarized map-making of Planck.
This chapter is organized as follows. We first describe the algorithm for destriping and calibration in Sects. 1.2 and 1.3. Section 1.4 is devoted to Polkapix, the implementation of those algorithms (ring-making, offset determination, calibration and projection) within the Planck-*HFI* Data Processing Center infrastructure. Simulations are detailed in Sect. 1.5. The results of destriping and calibration are described in Sects. 1.6 and 1.7, respectively. Finally, the results of the combined method solving for offsets and gain by iteration are discussed in Sect. 1.8.

1.2 Map-making

1.2.1 The map-making problem

Planck-HFI bolometers measure the brightness of the sky in a given direction convolved with an instrumental beam. The time-ordered data vector, $\mathbf{d}$, may therefore be modeled as the sum of the signal from the convolved sky $\mathbf{T}$ and the noise $\mathbf{n}$

$$\mathbf{d}=\mathbf{A}\cdot\mathbf{T}+\mathbf{n}. \tag{1.1}$$

The pointing matrix $\mathbf{A}$, of size $N_s \times N_p$, relates each time sample of a detector, s, to the corresponding pixel p in the sky. It can typically be represented as very sparse. For an axisymmetric beam response, the “smearing" and “pointing" operations commute, and one can solve directly for the beam-convolved map, assuming that the matrix $\mathbf{A}$ contains only one (three for polarization-sensitive detectors) non-null values in each row, as each sample is sensitive to only one pixel of the convolved sky. The data model, Eq. 1.1 can then be written as

$$d_t=I_p+\varepsilon_t Q_p cos(2\psi_t)+\varepsilon_t U_p sin(2\psi_t)+n_t, \tag{1.2}$$

where (I_p,Q_p,U_p) are beam-smoothed Stokes parameters in pixel p. The polarization efficiency ε (equal to zero for the total power experiments) can be written in terms of the cross-polarization η: $\varepsilon=(1+\eta)/(1-\eta)$. For Planck, ε only depend on the detector, not on time. Finally, ψ_t is the angle of the detector's polarization direction, with respect to the polarization basis in the pixel p, at the time t. For Planck, it can be written $\psi_t=\phi_t^{FP}+\alpha$, as the sum of the focal plane orientation (ϕ^{FP}) and the orientation of the detector on the focal plane α.
For arbitrary beam patterns, one may either need to deal with non-trivial, position-dependent smoothing in the final maps, while retaining the simplicity of the matrix $\mathbf{A}$, or to try to mitigate these effects with the help of one of the proposed beam-deconvolution techniques (e.g. Arnau & Sáez 2000; Burigana & Sáez 2003; Armitage & Wandelt 2004), which typically require more complex pointing matrices.
After pre-processing of the TOD, noise can typically be considered as Gaussian and piece-wise stationary so that all the statistical information of the noise is contained in its covariance matrix $\mathbf{N}=\left\langle \mathbf{n}\mathbf{n}^T \right\rangle$ for which each stationary block is a symmetric Toeplitz matrix (Golub & Van Loan 1996). Nevertheless, the instrumental noise is usually not white and

[2]http://www.rssd.esa.int/planck
[3]http://lambda.gsfc.nasa.gov/product/cobe
[4]http://wmap.gsfc.nasa.gov

contains some low frequency components that, if not accounted for properly, are projected to the sky as large stripes following the scan pattern.
The Map-Making problem consist in finding the best estimation of $\mathbf{T}$ given the data $\mathbf{d}$. The general solution of this problem is to minimize the norm $\|\mathbf{d}-\mathbf{AT}\|_M$. The solution for the estimator $\hat{\mathbf{T}}$ and its covariance is then:

$$\hat{\mathbf{T}} = \left(\mathbf{A}^T\mathbf{M}\mathbf{A}\right)^{-1}\cdot\mathbf{A}^T\mathbf{M}\,\mathbf{d} \tag{1.3}$$

$$\hat{N}_p = \left(\mathbf{A}^T\mathbf{M}\mathbf{A}\right)^{-1}\left(\mathbf{A}^T\mathbf{M}\mathbf{N_t}\mathbf{M}\mathbf{A}\right)\left(\mathbf{A}^T\mathbf{M}\mathbf{A}\right)^{-1} \tag{1.4}$$

where $\mathbf{N_t}$ is the noise covariance matrix in time domain, i.e. $\mathbf{N_t}=\left\langle \mathbf{n}\mathbf{n}^T\right\rangle$ and $\mathbf{M}$ is an arbitrary positive definite matrix associated to the norm.
Substituting Eq. 1.1 in Eq. 1.3, we obtain

$$\begin{aligned}\hat{\mathbf{T}} &= \left(\mathbf{A}^T\mathbf{M}\mathbf{A}\right)^{-1}\cdot\mathbf{A}^T\mathbf{M}\cdot(\mathbf{A}\mathbf{T}+\mathbf{n})\\ &= \left(\mathbf{A}^T\mathbf{M}\mathbf{A}\right)^{-1}\cdot\left(\mathbf{A}^T\mathbf{M}\mathbf{A}\right)\mathbf{T}+\left(\mathbf{A}^T\mathbf{M}\mathbf{A}\right)^{-1}\cdot\mathbf{A}^T\mathbf{M}\,\mathbf{n}\\ &= \mathbf{T}+\left(\mathbf{A}^T\mathbf{M}\mathbf{A}\right)^{-1}\cdot\mathbf{A}^T\mathbf{M}\,\mathbf{n}\end{aligned} \tag{1.5}$$

We can see that the estimator is unbiased in mean for any matrix $\mathbf{M}$ as $<\mathbf{n}> = 0$. However, the covariance directly depends on the choice of the matrix $\mathbf{M}$.

1.2.2 Maximum likelihood (ML) methods

The most general solution to the map-making problem is obtained by maximizing the likelihood of the data given a noise model (Wright 1996; Tegmark 1997; Stompor et al. 2002):

$$P(\mathbf{T}|\mathbf{d})\propto\frac{1}{\left|(2\pi)^{N_t}\mathbf{N_t}\right|^{1/2}}\exp\left\{-\frac{1}{2}(\mathbf{d}-\mathbf{AT})^T\mathbf{N_t}^{-1}(\mathbf{d}-\mathbf{AT})\right\} \tag{1.6}$$

where we assume Gaussian noise and a uniform prior on the sky temperature.
The solution, resulting in a minimum variance map, is given by the well-known generalized least squares (GLS) equations, which provide an estimate of the sky signal and its covariance

$$\hat{\mathbf{T}} = \left(\mathbf{A}^T\mathbf{N}^{-1}\mathbf{A}\right)^{-1}\cdot\mathbf{A}^T\mathbf{N}^{-1}\mathbf{d} \tag{1.7}$$

$$\mathcal{N} = \left(\mathbf{A}^T\cdot\mathbf{N}^{-1}\cdot\mathbf{A}\right)^{-1}. \tag{1.8}$$

Note that it is strictly equivalent to the solution Eq. 1.3 for $\mathbf{M}=\mathbf{N_t}^{-1}$. This procedure is called "optimal" or "Maximal Likelihood" map-making as $\hat{\mathbf{T}}$ is also the minimum variance estimate of the map for gaussian noise. If the noise is not Gaussian, the GLS estimator still has the minimum variance among all linear estimators.
In practice, the inversion or even the calculation of the $N_p\times N_p$ matrix $\mathbf{A}^T\mathbf{N}^{-1}\mathbf{A}$ is impossible for large datasets such as Planck, where the number of sky pixels, N_p, can be as large as many millions. Thus, Eq. 1.7 is usually solved using iterative methods such as the preconditioned conjugate gradient (PCG) (Golub & Van Loan 1996) and capitalizes on fast Fourier transforms (FFT) to perform the Toeplitz matrix-vector products (Doré et al. 2001; de Gasperis et al. 2005; Cantalupo et al. 2010).

1.2.3 Destriping methods

So-called "destripers" attempt to simplify the general map-making problem described above for Planck-like scanning strategy when the solution would require too many resources. The destriping technique for the CMB map-making has been investigated in minute detail for the Planck satellite (Burigana et al. 1999; Delabrouille 1998; Maino et al. 1999; Revenu et al. 2000; Maino et al. 2002; Keihänen et al. 2004; Stompor & White 2004). This technique takes advantage of the detectors observing large circles on the sky when the Planck telescope is spinning. Each circle is observed several times (of order 50) consecutively. Averaging over these circles enables us to compile datasets of higher signal-to-noise ratio. It has been shown by Janssen et al. (1996) that the low frequency noise can be represented by a uniform offset on a given baseline, corresponding in the case of Planck to a stable pointing period called a ring. However, it can also be adapted to ground-based or balloon-borne experiments (Sutton et al. 2010).
In the destriping approach, the noise is approximated as a low-frequency component represented by the offsets $\mathbf{x}$ unfolded to time-ordered data by the offset 'pointing' matrix $\mathbf{\Gamma}$ and remaining Gaussian noise $\mathbf{n}$ characterized by a correlation matrix, $\mathbf{N}$

$$\mathbf{d}=\mathbf{A}\cdot\mathbf{T}+\mathbf{\Gamma}\cdot\mathbf{x}+\mathbf{n}. \tag{1.9}$$

The matrix $\mathbf{\Gamma}$ assigns to every consecutive piece of the time stream data the respective offset amplitude and its elements are therefore either 1 or 0. The maximum-likelihood estimates of the offset amplitudes, $\mathbf{x}$, can be found from the time-ordered data, $\mathbf{d}$, by solving

$$\left(\mathbf{\Gamma}^T\mathbf{N}^{-1}\mathbf{Z}\mathbf{\Gamma}\right)\cdot\mathbf{x}=\mathbf{\Gamma}^T\mathbf{N}^{-1}\mathbf{Z}\cdot\mathbf{d}, \tag{1.10}$$

where

$$\mathbf{Z}=\mathbf{I}-\mathbf{A}\left(\mathbf{A}^T\mathbf{N}^{-1}\mathbf{A}\right)^{-1}\cdot\mathbf{A}^T\mathbf{N}^{-1} \tag{1.11}$$

and the covariance matrix for offsets reads

$$C_{\mathbf{x}}=\left(\mathbf{\Gamma}^T\mathbf{N}^{-1}\mathbf{Z}\mathbf{\Gamma}\right)^{-1}. \tag{1.12}$$

We note that, unlike Eq. 1.10, which provides an unbiased, though potentially non-optimal, estimate of the offset amplitudes even if the assumed and actual properties of the instrumental noise differ, this last equation holds only if our data model given by Eq. 1.9 and the assumed noise correlation, $\mathbf{N}$, are both correct. This is worth emphasizing as in the destriper applications one usually assumes that the remaining noise, $\mathbf{n}$, is uncorrelated and typically piece-wise white, and thus the matrix $\mathbf{N}$ is diagonal. This is indeed a key assumption from which the performance advantage of the destriper technique stems (Ashdown et al. 2009). Once the offsets, $\mathbf{x}$, are estimated, we can calculate the sky map, by coadding samples into pixels after first subtracting the estimated offsets from the TODs, i.e.,

$$\mathbf{m}=\left(\mathbf{A}^t\mathbf{N}^{-1}\mathbf{A}\right)^{-1}\mathbf{A}^t\mathbf{N}^{-1}(\mathbf{d}-\mathbf{\Gamma}\mathbf{x}). \tag{1.13}$$

Again such an estimate of the sky signal will be unbiased even if the simplifying assumptions about the noise, $\mathbf{n}$, are adopted. If these are correct, or sufficiently accurate, then the error covariance matrix of the destriper map can be calculated as

$$C_{\mathbf{m}}=\left(\mathbf{A}^t\mathbf{N}^{-1}\mathbf{A}\right)^{-1}+\left(\mathbf{A}^t\mathbf{N}^{-1}\mathbf{A}\right)^{-1}\mathbf{A}^t\mathbf{N}^{-1}\mathbf{\Gamma}\left(\mathbf{\Gamma}^T\mathbf{N}^{-1}\mathbf{Z}\mathbf{\Gamma}\right)^{-1}\mathbf{\Gamma}^t\mathbf{N}^{-1}\mathbf{A}\left(\mathbf{A}^t\mathbf{N}^{-1}\mathbf{A}\right)^{-1}. \tag{1.14}$$

Equations 1.12 & 1.14 can clearly provide at least some insights into the error correlation structure of the recovered maps and even be suitable for at least some of their statistical analyses, even if the reminder noise, $\mathbf{n}$, is not strictly speaking uncorrelated and for this reason their calculation is included in the software described here and discussed later on.
As shown in Poutanen et al. (2006) and Ashdown et al. (2007a), the baseline length used to define the offsets need not be tied to the length of a Planck ring. Including priors on the low frequency noise, the destriping algorithm is equivalent to the GLS algorithm in the short baseline limit. In the Planck case, the duration of the stable pointing period is not constant over the time so that the baseline lengths vary slightly from 40 to 65 min. However, as we show later, this generalization of the Janssen et al. (1996) prescription does not affect the destriper performances.

1.3 Photometric calibration

The bolometer signal measured through I-biasing is proportional to the small variation in the incoming power from the sky. To express the measurement in sky temperature units, one has to determine a gain per detector based on a known source in the sky. For low frequency channels (roughly between 20 and 300 GHz) for which the CMB signal is sufficiently high, the CMB dipole is usually used as a primary calibrator for experiments with large sky coverage. This is because it is only marginally affected by pointing errors and beam uncertainties, is a stronger signal than CMB anisotropies (by a factor 100) but not bright enough to cause non-linearities in the detectors, and has the same electromagnetic spectrum. At higher frequency (typically above 300 GHz), calibration of data on Galactic signal, based on ancillary data (e.g. FIRAS maps Finkbeiner et al. 1999), is preferred. For smaller sky coverage, calibration is usually derived from point source objects of known flux.
The CMB dipole is induced by the Doppler effect of the relative motion of the satellite with respect to the last scattering surface. The solar system motion with respect to the last scattering surface (referred to as the *solar dipole*) is the dominant component of the satellite velocity. A residual contribution (called hereafter the *orbital dipole*) is induced by the motion of the satellite with respect to the solar system. The solar dipole can be considered as sky stationary during the observations and is thus projected onto the sky as an ℓ=1 component with an amplitude measured by WMAP of 3.355±0.008 mK (Hinshaw et al. 2009). Relativistic corrections to the solar dipole produce second order anisotropies at higher multipoles with amplitudes proportional to β^ℓ and more importantly couple both the dipole components as we discuss later on. Though the orbital dipole flux is typically one order of magnitude lower than the solar dipole, it is time dependent, and its time-variability is precisely determined by the satellite velocity.
The orbital dipole signal is modulated on a one year period. As it is not projected onto the sky, the ring-ordered data, $\mathbf{d}$, for each sample s is modeled as

$$\mathbf{d}=\mathbf{A}\cdot\mathbf{T}+g\times\mathbf{t}_{orbital}+\mathbf{n}, \tag{1.15}$$

where $\mathbf{A}$ is the pointing matrix relating ring pixels to those of the sky, and $\mathbf{t}_{orbital}$ is the time-dependent orbital dipole signal. The unknown are the sky temperature $\mathbf{T}$ (including the solar dipole) and the gain g.
As $\mathbf{t}_{orbital}$ is known, the calibration problem is linear and can be solved directly in the same way as the destriping problem. For instance, the maximum-likelihood estimate of the coefficient g can be obtained by marginalizing for $\mathbf{T}$ over the sky solving the equation

$$\left(\mathbf{t}^T_{orbital}\mathbf{N}^{-1}\mathbf{Z}\mathbf{t}_{orbital}\right)\times g=\mathbf{t}^T_{orbital}\mathbf{N}^{-1}\mathbf{Z}\cdot\mathbf{d}, \tag{1.16}$$

where

$$\mathbf{Z}=\mathbf{I}-\mathbf{A}\left(\mathbf{A}^T\mathbf{N}^{-1}\mathbf{A}\right)^{-1}\cdot\mathbf{A}^T\mathbf{N}^{-1}, \tag{1.17}$$

and subsequently used to estimate the sky map.
For Planck, using polarization-sensitive detectors to solve such a calibration problem for a single detector at a time turns out to be insufficient, as the map-making problem is either degenerate if polarization is explicitly modeled, or the answer biased, if polarization is neglected (see Sect. 1.7.1). However including multiple detectors in the calibration problem in Eq. 1.16 leads to a set of non-linear equations. To avoid this problem, our algorithm performs only a single detector gain estimation at any given time, although it does this for a few detectors in parallel, the calibrated data of which are then used to determine offset estimates. The latter are subsequently used for the calibration estimates resulting in an iterative procedure.

1.4 Implementation

In the context of Planck data analysis, several destriper codes have been developed, such as MADAM (Keihänen et al. 2005, 2010) and Springtide (Ashdown et al. 2007b). In this paper, we present a modular code called Polkapix based on four separate steps: the ring-making, the offset determination, the photometric calibration, and the projection of the rings onto a map. The offset determination and the calibration are solved iteratively. We note that explicit ring-making is not necessary in destriper codes, although we use it not only as a convenient means of compressing the data but also as intermediate stage products that are useful for monitoring the systematics. In addition, and for the same reason, our implementation allows for internal, thus potentially different, sky resolutions for the offset and calibration determination independently of the one used for the final map projection.

1.4.1 Ring-making

Rings are partial sky maps produced via a projection onto the sky of each single pointing period separately. These rings therefore provide a compressed and higher signal-to-noise ratio rendition of the original TODs. The length of each stable pointing period varies between 40 and 65 min (with a mean of 45 min) in the Planck scanning strategy. During each period, noise is assumed to be white, with the low frequency part folded in as an overall ring offset, and consequently the rings are computed using a simple noise-weighted projection procedure. The resulting noise in the ring domain is thus (nearly) white, modulo the offset, and mostly uncorrelated from one ring to another.
For calibration purposes, as in Eq. 1.16, the orbital dipole has to be averaged in the same way for each pixel of the ring. This is done using the pointing direction and the satellite velocity calculated at each sample. As the dispersion of the observed direction falling into each ring pixel is very low (below 10^{-3}), the averaging effects of pixelization are found to be negligible and no loss of accuracy is incurred as a result.
To avoid introducing any additional binning of the data, we choose a sky pixelization as a basis for this ring making (HEALPix, Górski et al. 2005). Our ring structure is therefore called HPR for HEALPix Rings in the following. As the ring are produced via simple projection assuming white noise only, samples that are flagged as bad, are simply not included in the ring making procedure, without any need for additional processing, such as gap-filling (e.g., Stompor et al. 2002).

1.4.2 Offsets determination

The destriping algorithm solves Eq. 1.10 for the offsets x (one offset per ring) taking as an input a set of HPR, $\mathbf{d}$, computed at the ring-making stage. We also impose the external constraint $\sum\mathbf{x}$=const to break the degeneracy in the offset determination and set the arbitrary constant to 0 [5] using a Lagrange multiplier.
We thus minimize the likelihood

$$-2\ln\mathcal{L}=(\mathbf{d}-\mathbf{A}\cdot\mathbf{T}-\mathbf{\Gamma}\cdot\mathbf{x})^T\mathbf{N}^{-1}(\mathbf{d}-\mathbf{A}\cdot\mathbf{T}-\mathbf{\Gamma}\cdot\mathbf{x})+\mu\ \mathcal{L}(\mathbf{x}) \tag{1.18}$$

with $\mathcal{L}(\mathbf{x})=\mathbf{1}^T\cdot\mathbf{x}=\sum_{\text{ring }r}x_r=0$
After derivation with respect to $\mathbf{T}$, the offsets $\mathbf{o}$ and the Lagrange parameter μ, we substitute the solution for $\mathbf{T}$ and Eq. 1.10 now becomes

$$\begin{pmatrix}\mathbf{\Gamma}^T\mathbf{N}^{-1}\mathbf{Z}\mathbf{\Gamma} & \mathbf{1}\\ \mathbf{1}^T & 0\end{pmatrix}\cdot\begin{pmatrix}\mathbf{x}\\ \mu\end{pmatrix}=\begin{pmatrix}\mathbf{\Gamma}^T\mathbf{N}^{-1}\mathbf{Z}\cdot\mathbf{d}\\ 0\end{pmatrix} \tag{1.19}$$

Though we typically use the same underlying pixelization, HEALPix (Górski et al. 2005), for the ring and sky signals, these may have different resolutions for the intensity and polarization parts. The resolution should be high enough for the sky signal to be considered constant across the pixel, thus typically lower than the characteristic instrumental beam scale. However, a trade-off should be made between the offsets uncertainty related to the level of noise in each pixel (which decreases for larger pixels) and the correlation between offsets (demanding smaller pixels). Moreover, to satisfy the first criterion above it is typically necessary to mask the inner part of the Galaxy, while estimating the offsets, as the galactic

[5] so that the mean value of the TODs (unphysical in any case) is conserved

gradients are often too strong, leading to a poor estimate of the sky signal. These questions are discussed in more detail in Sect. 1.6.
Two solvers of Eq. 1.10 have been implemented here: the full inversion approach, allowing for, and requiring, the estimation of the offset covariance matrix C and a (much faster) iterative method through conjugate gradient.

The code has been implemented within the HFI Data Processing Center infrastructure, and is fully parallelized as far as both the workload and memory consumption are concerned. It is able to deal simultaneously with data from several detectors at the same frequency, as needed, for instance, to reconstruct polarization sky. As an example, the destriping is performed in a few minutes for 4 detectors on 32 processors using the full simulation described in Sect. 1.5.
The reconstruction of the polarization for each pixel requires the inversion of each three-by-three elements of the $(\mathbf{A}^T\mathbf{N}^{-1}\mathbf{A})$ matrix, some of which may be ill-conditioned for pixels with a insufficient number of bolometer orientations (see Ashdown et al. 2007b). We considered only pixels for which the condition number for this three-by-three matrix is lower than 10^3.
The code described in this work was used to produce the Planck Early Release (Planck HFI Core Team et al. 2011) and is one of the workhorses of the Planck-HFI Data Processing Centers. The implemented algorithm is overall very close to that of Springtide as discussed in detail in Ashdown et al. (2007b). We checked that indeed both these implementations produce the same offsets on a simple simulation of 4 HFI detectors at 143 GHz and including only the CMB signal (see Sect. 1.5 for details on simulations). The residual maps, i.e., a difference between noiseless input and output maps, give very similar r.m.s. with relative differences being: $\sim 10^{-6}$ for I and $\sim 5\cdot 10^{-5}$ for Q and U. The r.m.s. offsets differences agree within a relative error of $\sim 5\cdot 10^{-8}$. For a detailed comparison of map-making methods, we refer the reader to the papers of the Planck-CTP Working Group (Ashdown et al. 2007b,a, 2009).

1.4.3 Dipole calibration

The calibration module solves Eq. 1.16 for gain g for each of the included bolometers individually. As an input, it takes pre-computed rings corrected for the offset estimates, x, as derived earlier. The code is parallelized so that the gain estimation is achieved in fewer then two minutes on 16 processors. We use an underlying sky pixelization for intensity based on HEALPix and set its resolution as discussed in Sect 1.7. The calibration error in the fitted gain is then estimated as

$$\sigma_g^2 = \mathcal{F}_{cal}^{-1} = \mathbf{t}_{orbital}^T \mathbf{N}^{-1} \mathbf{Z} \mathbf{t}_{orbital}. \tag{1.20}$$

We note that this equation is an approximation neglecting the errors due to an offset determination. However, as we use multiple detectors for the latter, the approximation is expected to be very good.
The calibration algorithm takes advantage of the orbital dipole not being fixed on the sky, unlike the solar dipole. In practice, relativistic corrections couple solar and orbital dipoles creating a additional non-stationary signal. Though the latter is three orders of magnitude (β=10^{-3}) below the orbital dipole signal, we have to include the relativistic correction in the calibrator. We measure a relative bias of 6×10^{-6} to the recovered gain when using the orbital dipole, instead of the non-stationary signal (with coupling corrections). Given the statistical error ($\sim 5\times 10^{-5}$, see Sect. 1.7.2), we conclude that the orbital dipole can be safely used as a calibrator for Planck-HFI data even if, for the rest of the study, we use the exact non-stationary calibrator constructed as the difference between the CMB dipole (including solar, orbital, and relativistic corrections) and the solar dipole.
The procedure may be susceptible to pixelization effects caused by signals with large intra-pixel variations such as those found in the Galactic plane or for point sources. We evaluate the impact of this effect using a Galactic mask in Sect. 1.7.1.
The calibration code can also provide a constraint on the gain due to the data corresponding to each sky pixel separately, as well as an estimate of its uncertainty. The overall calibration constraint is then a weighted average of the these pixel-specific values, with the weight being its estimated uncertainty. Thanks to this facility, we can identify the sky areas that contribute most significantly to the final result of the calibration procedure.

1.4.4 Rings projection

Once the offsets have been estimated, they are subtracted from each ring, which removes the low frequency noise component from the data. A “corrected" map is then obtained by simply coadding ring-pixel amplitudes corresponding to the same sky pixels and weighted by the estimated ring-pixel white noise estimate. We note that though the resolution of the final map does not have to be the same as that of the rings it should be typically no higher than that. In this paper, we always project the final full-sky maps on high resolution (nside = 1024), whereas we study the impact of degrading the resolution on the underlying maps in both destriping and calibration.

In practice, from Eq. 1.2, we now write:

$$d_t = I_p + \rho_t Q_p \cos 2\psi_t + \rho_t U_p \sin 2\psi_t + n_t = \begin{pmatrix} 1 & \rho_t \cos 2\psi_t & \rho_t \sin 2\psi_t \end{pmatrix} \cdot \begin{pmatrix} I_p \\ Q_p \\ U_p \end{pmatrix} + n_t \tag{1.21}$$

where the pixel p is the pixel seen at time t.

The elements of the matrix **A** thus read:

$$A_{tq}=\delta_{p_t q}\begin{pmatrix} 1 & \rho_t\cos 2\psi_t & \rho_t\sin 2\psi_t \end{pmatrix} \tag{1.22}$$

As a consequence, in the case of white noise (i.e. **N** diagonal), the elements of the pixel-pixel matrix $\mathbf{A}^T\mathbf{N}^{-1}\mathbf{A}$ simply become

$$\begin{aligned}\left(A^T N^{-1} A\right)_{pp'} &= \sum_{i,j} A^T_{pi} N^{-1}_{ij} A_{jp'} \\ &= \sum_{i,j} \delta_{p_i p}\delta_{p_j p'} w_i \delta_{ij} \begin{pmatrix} 1 \\ \rho_i\cos 2\psi_i \\ \rho_i\sin 2\psi_i \end{pmatrix}\cdot\begin{pmatrix} 1 & \rho_j\cos 2\psi_j & \rho_j\sin 2\psi_j \end{pmatrix} \\ &= \begin{pmatrix} \sum_{i\in p} w_i & \sum_{i\in p} w_i\rho_i\cos 2\psi_i & \sum_{i\in p} w_i\rho_i\sin 2\psi_i \\ \sum_{i\in p} w_i\rho\cos 2\psi_i & \sum_{i\in p} w_i\rho_i^2\cos^2 2\psi_i & \sum_{i\in p} w_i\rho_i^2\cos 2\psi_i\sin 2\psi_i \\ \sum_{i\in p} w_i\rho\sin 2\psi_i & \sum_{i\in p} w_i\rho_i^2\cos 2\psi_i\sin 2\psi_i & \sum_{i\in p} w_i\rho_i^2\sin^2 2\psi_i \end{pmatrix}\delta_{pp'}\end{aligned}$$

and vector at the right-hand side of Eq. 1.7

$$\left(A^T N^{-1} m\right)_p = \sum_{i,j}\delta_{p_i p}\begin{pmatrix} 1 \\ \rho_i\cos 2\psi_i \\ \rho_i\sin 2\psi_i \end{pmatrix} w_i\delta_{ij}m_j = \begin{pmatrix} \sum_{i\in p} w_i m_i \\ \sum_{i\in p} w_i m_i\rho_i\cos 2\psi_i \\ \sum_{i\in p} w_i m_i\rho_i\sin 2\psi_i \end{pmatrix}$$

In these formula, the sum are on all samples that falls into pixel p and the inverse-noise weighting is defined as $w_i = (N^{-1})_{ii} = 1/\sigma_i^2$. For white noise, the pixels are uncorrelated which means that we can solve the 3×3 system for each pixel independently. Note that for a small number of different angles ψ, the system is ill-conditioned and cannot be inverted. In practice, we apply a threshold on the condition number of the matrix $(A^T N^{-1} A)_{pp}$ to avoid the pixels where the Q and U information is not measured.

Additional note on correction for the polarisation angle ψ inside a pixel.
When averaging the angles from the samples falling into a given pixel, one has to take into account the rotation of coordinates. For each sample, the polarisation coordinates are given with the y-axis towards the north galactic pole. Before summing angles, one needs to rotate the polarization as for the origin of the pixel (the center of the pixel "pc" of coordinates $\theta_{\rm pc}$, $\phi_{\rm pc}$):

$$\psi_i \leftarrow \psi_i + (\phi_i - \phi_{\rm pc})\cos\theta_{\rm pc}$$

This correction can be non-negligible for large pixel size and also at the pole where the ϕ angle strongly varies within a pixel.

1.5 Simulations

Time-ordered data (TOD) were simulated for 380 days of observations corresponding to slightly more than two sky surveys. The sampling frequency for HFI was set to 180 Hz, so that the total number of samples is about 5.6×10^9 per bolometer. For 12 detectors and the addition of the pointing information, the total volume of the data amounts to 700 Gb per simulation. We restrict our discussion to four bolometers only per channel, which allows for a polarization reconstruction while limiting the overall data size to one more readily manageable. Nevertheless, we rescale the noise level so that noise in the final map is comparable to that expected for a complete Planck-like channel map. We focus on two CMB channels centered at 143 and 217 GHz. Simulations were done using the Level-S simulation codes (Reinecke et al. 2006) ported into the DPC-HFI infrastructure, and in particular the Planck I/O library. Beam effects were simulated assuming Gaussian circular beams.

1.5.1 Scanning strategy

We used a Planck-like cycloidal scanning strategy. The satellite was assumed to be spin-stabilized and rotates on its axis once per minute. The spin axis follows a cycloidal path on the sky by step-wise displacements of approximately 2 arcmin every 48 min. The stable pointing period between two repointings is not constant in order to take into account the spin axis not remaining in the Ecliptic plane but following a cycloid path (Fig. 1.1). Between the repointings, the spin axis nutates with a mean amplitude of 2 arcsec. Detectors scan the sky following almost great circles as they point at 83.8°away from the spin axis (Fig. 1.2). We also include small variations in the spin rate (rms 2.16arcsec/s).
For the polarization studies, we simulated four bolometers at 143 GHz coming from two horns of the Planck-HFI focal plane (143-1 and 143-3). Each horn groups two detectors (labeled *a* and *b*) sharing the same pointing with a polarized grid orientation rotated by 90°. The two horns follow the same path on the sky but are 2° apart from each other. Their relative orientation of the polarized grids in each horn differ by 45°. During the 12.5 months of the mission, the four detectors observe each pixel on the sky with multiple polarization orientation in a 3.44 arcmin resolution map (HEALPix nside=1024). Therefore we are able to determine the three Stokes components in each pixel. In addition, we simulated one total power, 217 GHz bolometer.

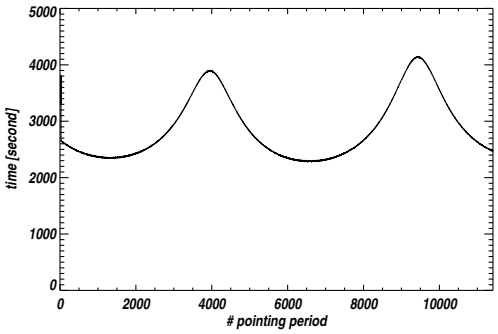

Figure 1.1: Dwelling time of the simulated stable pointing periods for the 12.5 month-long observation. The variation in the period length reflects that the spin axis does not remain in the Ecliptic plane but follows a cycloid path.

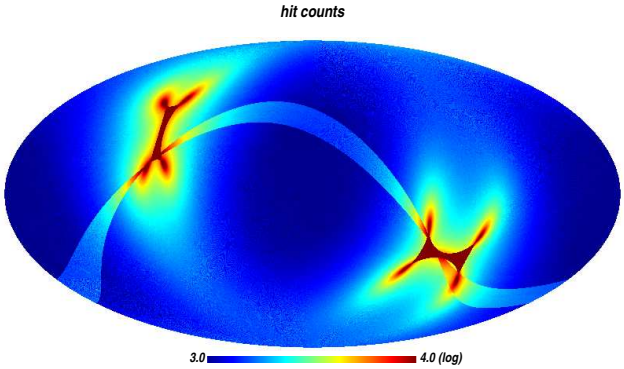

Figure 1.2: A map of hit counts per 3.4 arcmin pixels (Nside =1024) in Galactic coordinates corresponding to 12.5 months of observation for four detectors. The sky is covered at least twice. Redundancy of the revisits is maximal around the Ecliptic poles. The conspicuous s-shaped band with a higher hit count corresponds to the beginning of the third survey.

1.5.2 Sky signals

The simulated signal combines the CMB and diffuse Galactic foregrounds from the Planck Sky Model[6] at a resolution of 1.7 arcmin (HEALPix nside = 2048). The CMB anisotropies are generated using CMBFAST (Seljak & Zaldarriaga 1996) with the WMAP five-year best-fit model without lensing (Ω_m=0.257,Ω_b=0.044,Ω_Λ=0.743,h=0.719,τ=0.1,n_s=0.963,r= 0.02). Both solar and orbital dipoles are included. The Galactic foreground signals include thermal and spinning dust, synchrotron radiation, and free-free scattering in intensity. Polarized signals for thermal dust and synchrotron are also added. More details about the sky model used for this work can be found in (Leach et al. 2008) and (Betoule et al. 2009). The maps were smoothed using a symmetric Gaussian beam with FWHM of 7.05 and 4.72 arcmin at 143 and 217 GHz, respectively. TODs were then generated using Level-S codes (Reinecke et al. 2006) extracting the signal from the input sky maps according to the scan strategy. No bolometer time constant was included.

1.5.3 Noise properties

Streams of $1/f^\alpha$-noise were generated at the TOD level using the algorithm described in Plaszczynski (2007). We selected one of two values of the slope (α=1 and 2) and two knee frequencies (f_{knee}=0.1 and 0.01 Hz), with a cutoff frequency $f_{\rm min}$=10^{-5}Hz below which noise becomes white. In this approach, a white Gaussian noise realization is generated and the long range correlations are obtained through a linear digital filter. For a given *seed* of the generator, one can directly study the effect of the pure $1/f^\alpha$-noise component using the difference of reconstructed maps with and without the correlation turned on. For Monte Carlo simulations, we need a significant number of noise realizations, which renders impractical the writing of the TOD to disk. We therefore directly project the noise at HPR level using a pre-computed HPR pointing matrix.

The thermal fluctuation expected for Planck-HFI detectors are usually modeled by a $1/f^2$ Fourier spectrum with a low knee frequency. The noise power spectra of HFI bolometers are more accurately described by a $1/f$ spectrum (α=1) with $f_{knee}\simeq$0.1 Hz plus white noise (Planck HFI Core Team et al. 2011). We set the TOD white noise level in order to match the expected noise level of the foreseen *Planck*-HFI, 143 GHz frequency map. Thus, the noise r.m.s. per sample was set to 589 μK in thermodynamic CMB scale (Collaboration 2005). The noise covariance matrix in the map domain is given by Eq. 1.8. If correlated errors are small, the covariance matrix for (I, Q, U) at pixel p reads

$$\mathbf{M}_p=\frac{1}{\sigma^2}\begin{pmatrix} \sum 1 & \varepsilon\sum\cos(2\alpha_i) & \varepsilon\sum\sin(2\alpha_i) \\ \varepsilon\sum\cos(2\alpha_i) & \varepsilon^2\sum\cos^2(2\alpha_i) & \varepsilon^2\sum\cos(2\alpha_i)\sin(2\alpha_i) \\ \varepsilon\sum\sin(2\alpha_i) & \varepsilon^2\sum\cos(2\alpha_i)\sin(2\alpha_i) & \varepsilon^2\sum\sin^2(2\alpha_i) \end{pmatrix}^{-1} = \sigma^2\begin{pmatrix} \frac{1}{n_p} & 0 & 0 \\ 0 & \frac{2}{\varepsilon^2 n_p} & 0 \\ 0 & 0 & \frac{2}{\varepsilon^2 n_p} \end{pmatrix} \tag{1.23}$$

where the sums extend over all samples of all considered detectors falling into the pixel p, and we have assumed that the polarization efficiency, Eq. 1.2, is the same for all detectors. The second step results from the cancellation of the off-diagonal contributions coming from two detectors of each horn, which thus have their polarizers rotated by 90 degrees with respect to each other. As the polarization efficiencies are not all the same and the polarizers are not rotated by exactly 90 degrees, the second step is only an approximation with the off-diagonal elements being on the order of $O(\Delta\epsilon)$ and $O(\Delta\alpha)$, where $\Delta\epsilon$ denotes a difference between the polarization efficiencies of two detectors of the same horn and $\Delta\alpha$ the deviation from orthogonality. The off-diagonal terms are further suppressed for sky pixels, which are observed by the same horn multiple times with different attack angles (the correlation is lower than 5% for our scanning strategy).

[6]See http://www.planck.fr/heading79.html

Consequently, the matrices $\mathbf{M}_p$ are usually diagonally dominated for sufficiently well-observed pixels, with the diagonal elements being approximately given by Eq. 1.23. Given the hit counts per pixel n_p (Fig. 1.2) and the characteristics of the HFI detectors that we used (ε=0.83, 0.85, 0.84, 0.90), the averaged white noise per pixel we expect in our simulations is therefore 15.4 μK_{CMB} for I and 25.6 μK_{CMB} for Q and U maps at 143 GHz. In the following, we compare the level of residuals with those values.

1.6 Destriping parameters and performances

1.6.1 Systematic studies

We now investigate the various systematic effects possibly affecting the offset determination. We use a simulated sky with CMB and Galactic signal at 143 GHz for four bolometers, allowing for intensity and polarization reconstruction. For each bolometer, we generate 100 pure white noise realizations. HPR are constructed at high resolution (nside = 2048) and the final full-sky map is projected at nside = 1024. We first built the signal map using coaddition in each pixel. We also compiled the white noise map for each realization without destriping. For each noise realization, we constructed the residual map subtracting the signal+white noise map from the destriped map. We then computed full-sky angular power spectra for each residual map using the *Xpol* code (an extension of (Tristram et al. 2005) for polarisation), based on the S^{2}HAT library[7] (Hupca et al. 2010; Szydlarski et al. 2011) and averaged them over the simulated realizations.

First we investigate the effect of large signal variations within the pixels on the offset determination. These pixels can be found mostly in the Galactic plane so we remove the pixels with the highest Galactic signal using a mask (based on FIRAS intensity maps) in the offset determination. We gradually increase the masked-out sky fraction from 0% to 25%. We use the destriping module to estimate the offsets using an internal sky resolution of 6.9 arcmin (HEALPix nside = 512). The results are shown in Fig. 1.3. We can see that only temperature residuals are sensitive to the masking and that a 5% mask is sufficient to suppress pixel effects due to strong sub-pixel signal gradients caused by the Galactic signals. Consequently for the following, we use an internal 5% Galactic mask at 143 GHz for offset determination.

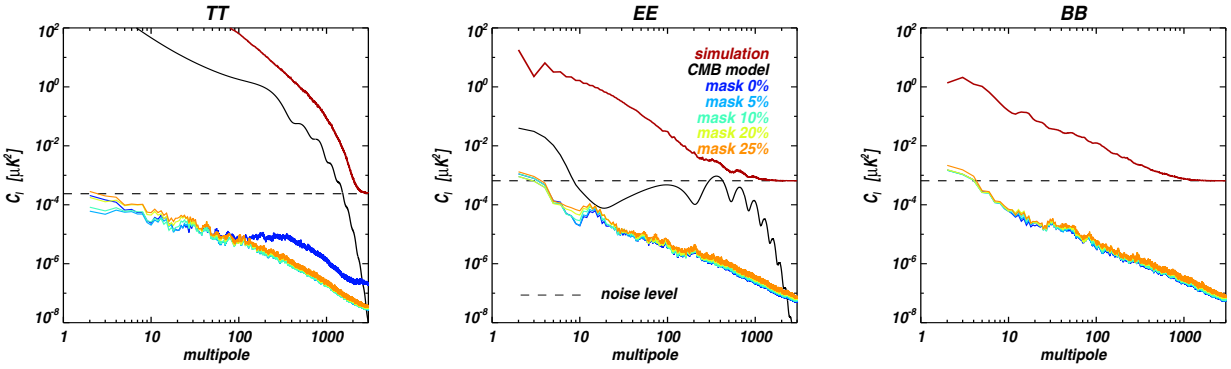

Figure 1.3: Noise residual full-sky power spectra with various internal Galactic mask applied to the offset determination. Residual maps are at nside = 1024. Spectra are smoothed over five multipoles. Signal spectra are plotted in *red*. As a reference, we also plot the CMB WMAP five-year fiducial model (*black*) and a total power of the simulated sky signal, CMB+Galaxy+noise, (*red curve*). *From left to right:* temperature, E-mode, and B-mode.

Subsequently, we assess the impact of the assumed sky resolution on the offset determination procedure. We do this in two steps. First, we neglect the polarization signal while determining the offsets, and consider several internal resolutions from nside = 64 to 2048 in the offset determination. Figure 1.4 shows the power spectra of the destriping residuals for a pure white noise. In terms of temperature, at low internal resolutions (nside lower than 256), residuals due to the pixelization effect dominate at low multipoles over the instrumental noise level. Residual power spectra in polarization are unaffected by changes in the internal resolution for the temperature and are consistently higher at low-ℓs than the noise level. We attribute this last observation to no polarization being included during the offset computation step.

Finally, we compare the destriping performances when the polarization is included (for various internal sky resolutions) in the offset determination. For this comparison, the internal resolution for intensity is fixed at 3.4 arcmin (HEALPix nside = 1024). As shown in Fig. 1.5, including the polarization reduces the level of the residuals of the E and B mode polarized spectra. For polarization, at high resolution (nside greater than 512), we found residuals no larger than the white noise level over the entire ℓ range, including the low multipole range (ℓ<20). At higher multipoles, a higher resolution seems to produce a slight increase in the residuals but we understand this is negligible given the white noise level. As far as the intensity is concerned, a low resolution for polarization induces strong residuals in the intensity map for multipoles lower than ℓ=100.

[7] http://www.apc.univ-paris7.fr/~radek/S2HAT.html

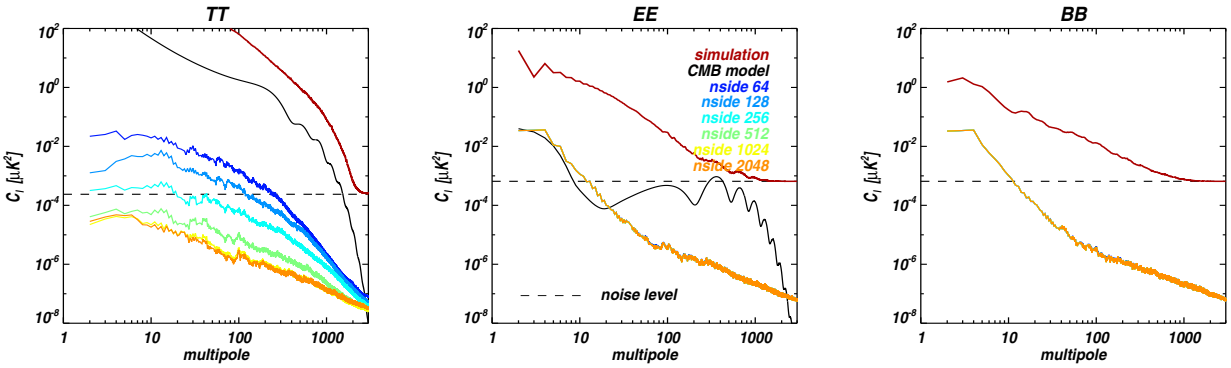

Figure 1.4: Noise residual full-sky power spectra with various internal resolutions (nside = 64, 128, 256, 512, 1024) and neglecting polarization in the offset determination. Residual maps are at nside = 1024. Spectra are smoothed over five multipoles. Signal spectra are plotted in *red*. As a reference, we also plot the CMB WMAP-5yr fiducial model (*black*). The horizontal, dashed lines show the predicted noise level. *From left to right:* temperature, E-mode, and B-mode.

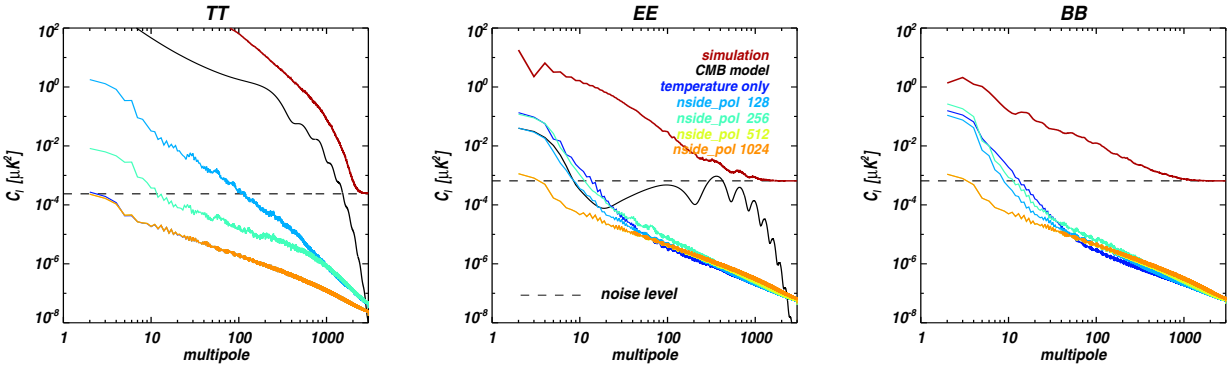

Figure 1.5: Noise residual full-sky power spectra when using different internal sky resolution for polarization in the offset determination. Internal resolution for intensity is fixed to nside = 1024. Residual maps are at nside = 1024. Spectra are smoothed over five multipoles. Signal spectra are plotted in *red*. As a reference, we also plot the CMB WMAP five-year fiducial model (*black*). *From left to right:* temperature, E-mode, and B-mode.

From these studies, we conclude that polarization must be taken into account during the destriping, even if this requires more data (for Planck at least four bolometers) leading to an increase in the CPU time as well as the introduction of possible systematics due to detector mismatches (not discussed here). Moreover, we have demonstrated that a resolution of 6.9 arcmin (HEALPix nside = 512) for both intensity and polarization ensures that the residuals remain negligible relative to white noise level.

1.6.2 Statistical uncertainties and offset covariance matrix

The statistical uncertainties in the offset determination are quantified by the offset-covariance matrix, $C_{\mathbf{x}}$, which in general depends not only on the scanning strategy but also instrumental characteristics, both of which enter via the pointing matrices $\mathbf{A}$ and $\mathbf{\Gamma}$, Eq. 1.12, as well as noise properties of the detectors encoded in the matrix $\mathbf{N}$. However, this is typically the scan pattern, which plays a dominant role in determining the overall structure of the noise covariance (e.g. Stompor & White 2004; Efstathiou 2007), and conversely most of the major features of the covariance can be traced back to the details of the scanning. Below we discuss the results of the numerical computations of $C_{\mathbf{x}}$, examples of which are displayed in Figs. 1.6, 1.7, 1.8, and 1.9, emphasizing this connection. To this end, we first rewrite Eq. 1.12 more explicitly as

$$C_{\mathbf{x}}=\left(\mathbf{\Gamma}^t\mathbf{N}^{-1}\mathbf{\Gamma}\right)^{-1}+\left(\mathbf{\Gamma}^t\mathbf{N}^{-1}\mathbf{\Gamma}\right)^{-1}\left(\mathbf{\Gamma}^t\mathbf{N}^{-1}\mathbf{A}\right)C_{\mathbf{m}}\left(\mathbf{A}^t\mathbf{N}^{-1}\mathbf{\Gamma}\right)\left(\mathbf{\Gamma}^t\mathbf{N}^{-1}\mathbf{\Gamma}\right)^{-1}, \tag{1.24}$$

where, $C_{\mathbf{m}}$ is the sky error covariance, given in general by Eq. 1.14, and which for our purpose in this section will be approximated as either diagonal or block-diagonal for the unpolarized and polarized detectors respectively as given by the first term on the right-hand side (*rhs*) of Eq. 1.14.

The first term on the rhs of Eq. 1.24 describes the offset variance derived assuming that the sky signal is known. The effect of the marginalization over the unknown sky performed in the presence of the crossings between the rings is then quantified by the second term. We emphasize that no correction is explicitly applied in the above equation to account for the singularity of the problem (see Sect. 1.4.2). Though this is sufficient for the qualitative discussion presented here, it

does have to be treated in the actual numerical work. In the following, we discuss separately two specific cases of interest: one assuming unpolarized total power detectors and the other polarization-sensitive ones. For simplicity, we assume the noise variance per sample, σ_t^2, to be time-independent and the same for all considered detectors.

Total power detectors

For total power detectors, the entries of the sky pointing matrix, $\mathbf{A}$, are either 0 or 1, with the indices of the non-zero elements, (t, p), defining which pixel p has been observed at the time, t. The matrix, $\mathbf{C}_m$ is approximately diagonal with the elements equal to the estimated noise level for each pixel. Elements of the matrix, $\mathbf{\Gamma}^t\mathbf{N}^{-1}\mathbf{A}$ are then given by a number of times each pixel was observed within each offset baseline, i.e., a ring, weighted by the sample noise. In this special case, we can therefore rewrite Eq. 1.24 as

$$[C_{\mathbf{x}}]_{(d,r)(d',r')} \simeq \frac{\sigma_t^2}{n_{obs}(r,d)}\left(\delta^K_{rr'}\delta^K_{dd'} + \frac{1}{n_{obs}(r',d')}\sum_{p\in r\cap r'}\frac{n_{obs}(p,r,d)n_{obs}(p,r',d')}{n_{obs}(p)}\right). \tag{1.25}$$

Hereafter we use n_t, n_r to denote the total number of samples and rings per detector; n_p the total number of pixels observed by all detectors; $n_{obs}(p,r,d)$ the number of observations of a pixel p within a pointing period (ring), r, for a detector, d, where $n_{obs}(p) \equiv \sum_{r,d} n_{obs}(p,r,d)$ is the total number of its observations; and $n_{obs}(r,d)$ the number of samples in a pointing period r. Moreover, r and r' denote two rings corresponding to the pointing periods of two detectors, d and d', respectively, and a symbol $p\in r\cap r'$ refers to the pixels observed during both pointing periods, r and r'. We note that the second term on the *rhs* is always non-negative and vanishes if $r\cap r'=\emptyset$. It therefore increases the offset determination uncertainty and leads to a correlation, rather than an anti-correlation, of the offsets. This reflects that the offset determination precision is always slightly lower whenever the sky signal has to be estimated simultaneously. This has an easy intuitive explanation: if one of two offsets corresponding to two rings, which cross on the sky, turns out to be overestimated, the sky signal in pixels common to both rings will be on average underestimated, and the offset of the second ring will tend to compensate for this and therefore be overestimated as well. Nevertheless, the anti-correlations are unavoidably present in the offset correlation matrices. This can be seen in Figs. 1.7 and 1.8 and arises because of the condition we impose on the sum of all offsets in order to break the problem singularity. This effectively requires that the sum of all the elements in each matrix column or row vanishes, hence that at least some, or more typically many, elements of the correlation matrix are indeed negative.

We first consider the case with $r=r'$ and $d=d'$. Equation 1.25 then reads

$$[C_{\mathbf{x}}]_{(d,r)(d,r)} \simeq \frac{\sigma_t^2}{n_{obs}(r,d)}\left(1 + \frac{1}{n_{obs}(r,d)}\sum_{p\in r}\frac{n_{obs}^2(p,r,d)}{n_{obs}(p)}\right). \tag{1.26}$$

Given that typically $n_{obs}(r,d)\sim n_t/n_r \gg 1$, the second term in the parenthesis is strongly suppressed. However, the magnitude of the sum over the pixels observed in the period, r, can be large enough to compensate for this, rendering this term important. To illustrate this, we first observe that

$$\sum_{p\in r} n_{obs}(p,r,d) = n_{obs}(r,d) \sim \frac{n_t}{n_r}, \tag{1.27}$$

and consequently that the sum in Eq. 1.26 is larger, whenever $n_{obs}^2(p,r,d)$ varies more rapidly from a pixel to a pixel along the ring, or, in other words, whenever the distribution of the observation within the pointing period, r, is more inhomogeneous. In contrast, whenever both $n_{obs}(p,r,d)$ and $n_{obs}(p)$ are homogeneous, thus pixel-independent, the second term is given as

$$\frac{1}{n_{obs}(r,d)}\sum_{p\in r}\frac{n_{obs}^2(p,r,d)}{n_{obs}(p)} \sim \frac{n_p}{n_r n_p^2(r,d)} \lesssim \frac{1}{n_p(r,d)} \ll 1, \tag{1.28}$$

where $n_p(r,d)$ is the number of pixels observed in the period, r. The offset covariance is then close to its minimum, where it is dominated by the first term, with the second term contribution nearly negligible thanks to an implicitly implied perfectly linked network of rings on the sky.

At the other extreme, all samples of the ring r are located in a single pixel, p. The second term is then roughly given by

$$\frac{1}{n_{obs}(r,d)}\sum_{p\in r}\frac{n_{obs}^2(p,r,d)}{n_{obs}(p)} \sim \frac{n_t}{n_r n_{obs}(p)} \lesssim 1, \tag{1.29}$$

as $n_{obs}(p)\geq n_{obs}(p,r,d)=n_t/n_r$ and the equality is realized whenever p is observed only within the considered pointing period. We thus conclude that the second term, though typically smaller, may be comparable in magnitude to the first one. The important consequence of these considerations is that whenever the inhomogeneity of pixel observations for some pointing period increases the diagonal elements of the offset-offset covariance matrix tend to increase. This explains the results displayed in Fig. 1.6, which display a noticeable increase in the offset variances as a result of a decrease in pixel size, which in turn enhances the observation inhomogeneity. This has important practical implications when selecting an

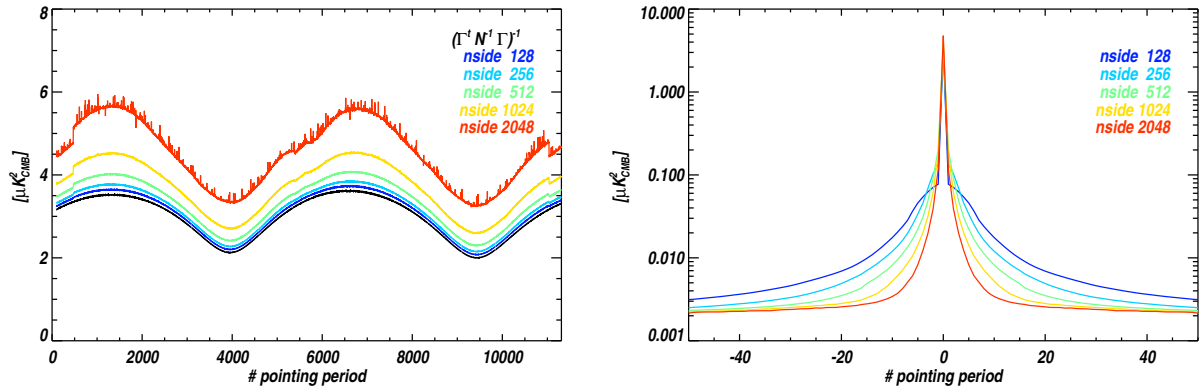

Figure 1.6: *Left:* Diagonal of the offset covariance matrix for various internal sky resolutions used for the offset recovery. Black line shows the first term of Eq. 1.25. *Right:* Offset covariance matrix profiles centered on the diagonal showing the ring-to-ring covariance for various internal sky resolution.

appropriate pixel size during the offset determination step (see Sect. 1.6.1). We note that for large pixels the second term is unimportant to the observation distribution among the pixels reaching the limit as discussed earlier in the context of Eq. 1.28.

For two different rings, i.e., $r \neq r'$ or $d \neq d'$, the first term in the expression for the covariance is absent and therefore the latter is determined by the second term. Its magnitude is now driven by two effects, the first one – as in the previous case – related to the observations inhomogeneity, which in general tends to increase the strength of the correlations, and the second one related to the number of pixels in common between the two rings. The latter effect is however the one that drives the large-scale appearance of the offset correlation matrix, Fig. 1.7. Consequently, the matrix is diagonal dominated with the correlations decaying away from the diagonal as the number of crossing pixels between the two rings decreases. The decay rate as well as the auto-correlation change with the ring number as does the Planck scan pattern, during which the satellite spin axis follows a cycloid in the Ecliptic coordinates. Consequently, the width of the diagonal band is found to vary along the diagonal. As Planck observes a full sky in six months of observations, with the end of the six month corresponding roughly to ring 5000, the overlaps between the rings separated by ∼5000 are again enhanced leading to a significant level of the corresponding correlations. This again happens for the ring separation of on the order of 10000, when the third full-sky survey starts. We note that the pattern of sky scanning changes between the first and second survey, owing to the different satellite tilt at which it is preformed, and consequently the offset correlations at this lag are somewhat more smeared out than those around the main diagonal. As the third scan follows the first nearly exactly, the correlations at the lag of ∼10000 are expected to resemble those at the diagonal very closely as indeed already seen to some extent in the figure.

Owing to the two competing effects mentioned above, the impact of the pixel size on the off-diagonal correlations is more complex than on the offset auto-correlations as they tend to change the correlation amplitude in an opposite way. Hence, though the correlation length will decrease when any pixel is shared on average by fewer rings, the changes in the correlation amplitude will depend on the fine details of the scanning strategy and in general will be neither simple nor easy to predict. This is indeed confirmed by the tests presented in the right panel of Fig. 1.6.

The contribution of the second term in Eq. 1.25 is sensitive to the pixels that are retained for the offset determination. This is true in particular when only a few pixels are shared between two rings, or whenever well-observed pixels are removed. In this context, the pixel selection is vitally important to practical applications as discussed in more detail in Sect. 1.6.1. Here we only illustrate it in Fig. 1.7 by contrasting two covariance matrices, obtained with all sky pixels included (left panel) or with those corresponding to the discarded Galactic plane (middle).

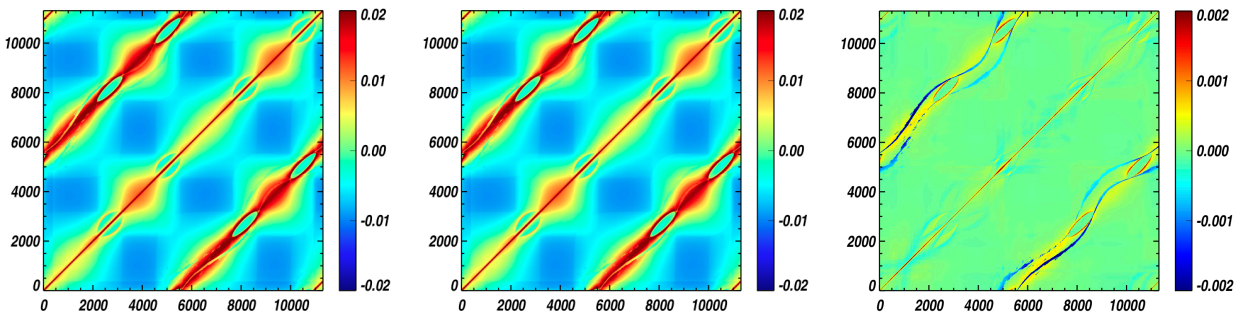

Figure 1.7: Offset covariance matrix without (*left*), with a Galactic mask (*middle*) and the difference (*right*).

For two rings that are different on the sky, whether they correspond to pointing periods of a single or two different detectors is completely irrelevant. This is because of our assumptions about lack of time-domain noise correlations and the same value of the noise variance. This, together with all the detectors being assumed to scan the sky in the same way, explains the periodic structure of the four detector offset covariance shown in Fig. 1.9. We indeed see that all the off-diagonal blocks are essentially identical, while the only difference between any of the diagonal and any of the off-diagonal blocks is caused by their diagonal values and is a result of the non-vanishing contribution to the first term in the case of the diagonal blocks. Our assumptions about the scanning imply that $n_{obs}(p,r,d)$ is independent of the detector number, rendering the off-diagonal blocks symmetric with respect to their diagonal.
We also checked our calculation of the offset covariance matrix from Polkapix using 10000 Monte-Carlo simulations of pure white noise. We simulated a simplified sky with CMB and Galactic emissions for a single *Planck*-HFI detector at 217 GHz. We then generated 10000 white noise realizations. For each simulation, we estimated the offsets using a 5% Galactic mask. We found a very good agreement between the MC standard deviation and the covariance matrix as shown in Fig. 1.8.

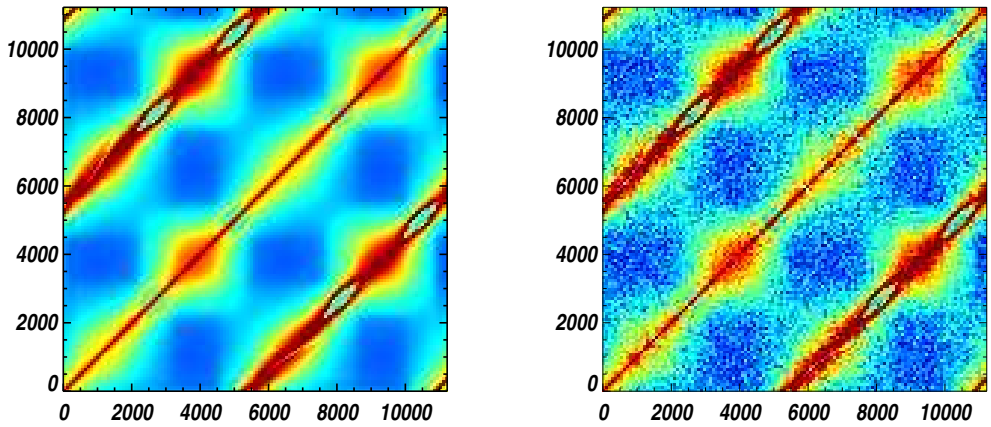

Figure 1.8: Binned offset covariance matrices. *left:* Polkapix estimate, *right:* covariance for 10000 MC. The bin width is 100 rings.

Polarization-sensitive detectors

For polarization-sensitive detectors, the pointing matrix, $\mathcal{A}$, is more complex, Eq. 1.2, with elements, that can be both positive and negative. The sky covariance can be approximated, as before, by the first term of Eq. 1.14. This would in general render a block-diagonal structure with each block of a size 3×3 characterizing single-pixel correlations of three Stokes parameters. However, in our case (see Sect. 1.5 and in particular Eq. 1.23) where the data of four detectors are analyzed simultaneously, it can again be treated as diagonal with the diagonal elements corresponding to Q and U parameters always being a factor $2/\varepsilon^2$ different than those for the total intensity, I. Hereafter, for brevity we omit the polarization efficiency ε. Assuming as before that the white noise is stationary over the course of the entire set of observations for which an rms value, σ_t^2, is identical for all detectors, we can now specialize Eq. 1.24 to the case at hand obtaining

$$[C_{\mathbf{x}}]_{(d,r)(d',r')} \simeq \frac{\sigma_t^2}{n_{obs}(r,d)} \left\{ \delta^K_{rr'}\delta^K_{dd'} + \frac{1}{n_{obs}(r',d')} \sum_{p\in r\cap r'} \frac{n_{obs}(p,r,d)n_{obs}(p,r',d')}{n_{obs}(p)} \right. \\ \left. \left[1+2\Big(\langle\cos2\psi\rangle_{(p,r,d)}\langle\cos2\psi\rangle_{(p,r',d')}+\langle\sin2\psi\rangle_{(p,r,d)}\langle\sin2\psi\rangle_{(p,r',d')}\Big)\right]\right\}. \tag{1.30}$$

Here,

$$\langle\cos2\psi\rangle_{(p,r,d)} \equiv \frac{1}{n_{obs}(p,r,d)} \sum_{t\in p\cap r} \cos2\psi_t^d. \tag{1.31}$$

We note that for each ring, r, and each detector, d, the averages above are done separately and therefore the arguments used in simplifying Eq. 1.23 do not apply here and the terms with cosines and sines do not vanish trivially in the Planck case. In contrast, they have an important and easily discernibly impact on the offset covariance matrix as shown in Fig. 1.9. For Planck scans, the angle between the polarizer orientation and the celestial coordinate system for a given pixel p and during a ring r does not change significantly from one to another pixel crossing as they are fixed with respect to the scanning direction. The averages of the trigonometric functions are therefore well approximated by the cosines and sines

of this specific angle. Equation 1.30 can then be simplified yielding

$$[C_{\mathbf{x}}]_{(d,r)(d',r')} \simeq \frac{\sigma_t^2}{n_{obs}(r,d)} \left\{ \delta^K_{rr'}\delta^K_{dd'} + \frac{1}{n_{obs}(r',d')} \sum_{p\in r\cap r'} \frac{n_{obs}(p,r,d)n_{obs}(p,r',d')}{n_{obs}(p)} \left[1+2\cos\Big(2(\psi(p,r,d)-\psi(p,r',d'))\Big)\right] \right\}. \quad (1.32)$$

Consequently, for any single ring, i.e., $r{=}r'$ and $d{=}d'$, the extra terms due to polarization are always positive, and, twice as large as the third, angle-independent term on the rhs. For the two corresponding rings belonging to two detectors in the same horn, e..g, with the relative polarizer orientation at 90 degrees, the third term is equal to -2 forcing the corresponding element of the offset covariance to be negative. If the two detectors above are chosen from two different horns, i.e., their polarizers are either at 45 or 135 degrees with respect to each other, the corresponding rings of the detectors are again positively correlated. Moreover, in the latter case and for two different rings, r and r' the cosine function in Eq. 1.32 turns into a sine and the contribution is asymmetric with respect to an exchange of $r\leftrightarrow r'$ giving rise to an asymmetry of the corresponding off-diagonal blocks. This is not so for the same horn detector blocks as the correlations are given by a cosine function, symmetric with respect to ring exchanges. All these observations and in particular a dichotomy between identical and different horn detectors are indeed confirmed by our numerical calculations, Fig. 1.9.
As in the unpolarized case discussed earlier, we can track the pattern of each block to the specific, single-detector scan features, such as the beginning of the second ($r{\sim}5{,}000$) and the third ($r{\sim}10{,}000$) full sky survey, leading to an overlap between their respective rings with those of the previous surveys and thus to an enhancement in the strength of the correlations.

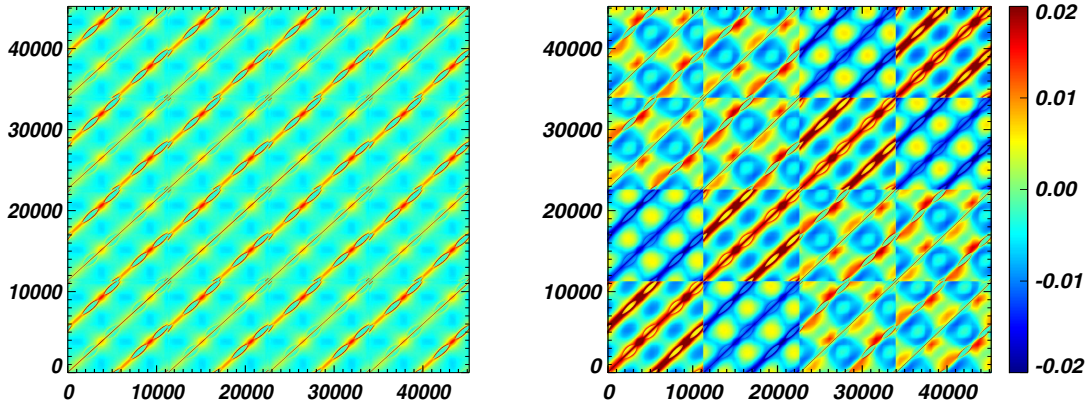

Figure 1.9: Offset correlation matrix for four polarization-sensitive bolometers at 143GHz without (*left*) and with (*right*) polarization reconstruction in the destriping.

Offset covariance – a recap

We briefly summarize all salient points of the discussion presented above. We have found that in the Planck case the offset covariance matrix is in general non-diagonal and has a rather complex structure, major features of which are due to the pattern of the Planck scan. The computation of this matrix requires rather lengthy and involved numerical calculations, although quick intuitive insights can be obtained in a semi-analytic way (see also, e.g., Stompor & White 2004; Efstathiou 2007). Those can be not only useful in devising new, efficient scanning strategies but also provide a useful cross-check of the numerical results. We have also tested the latter by means of extensive Monte Carlo simulations and found good agreement.
We have demonstrated that the offset variance and their correlations depend on the observation inhomogeneity and thus on the assumed pixel size and the number of crossing points between the rings, i.e., sky areas covered by the experiment within a single pointing period. We have also found that the overall structure of the covariance depends on whether the detectors are polarization-sensitive, an effect that, for a Planck-like scanning, has to be accounted for if a high-precision offset determination is desired. This last conclusion seconds one of the conclusions obtained in Sect. 1.6.1.

1.6.3 Residuals from low frequency noise

In the previous sections, we have described the systematic effects related to the destriping algorithm presented in Sect. 1.4. In particular, we have shown that the pixelization effects linked to the strong variation in the sky signal within a pixel are negligible for the offset estimation. However, we have found that a significant level of residuals arise whenever the polarization signal is neglected or the resolution adopted for the estimation of the underlying sky signal is reduced. In this section, we study the residuals for various levels of correlated noise. For each bolometer, we add to the simulated signal

(containing CMB and Galactic emissions) 100 noise realizations for three cases: pure white noise, correlated noise with α=2 for two knee frequencies (f_{knee}=0.1 and 0.01 Hz), and α=1 for a knee frequency of 0.1 Hz. We reduce the systematic bias using a 5% internal Galactic mask and an internal sky resolution of 6.9 arcmin (HEALPix nside = 512), as shown in Sect. 1.6.1.
Figure 1.10 shows the power spectra of the residuals computed for the three selected cases in both temperature and polarization. The level of the residuals is determined by the level of low-frequency noise introduced into the TOD. Thus, residuals increase with both the knee frequency f_{knee} and the slope α. We show that low-frequency noise residuals are negligible for $f_{knee}\leq$0.01 Hz when α=2. For a higher f_{knee}, a residual at low frequency biased the spectrum from a pure white-noise power spectrum at low multipoles (ℓ<50). In the case of α=1, the residuals are lower by one order of magnitude.

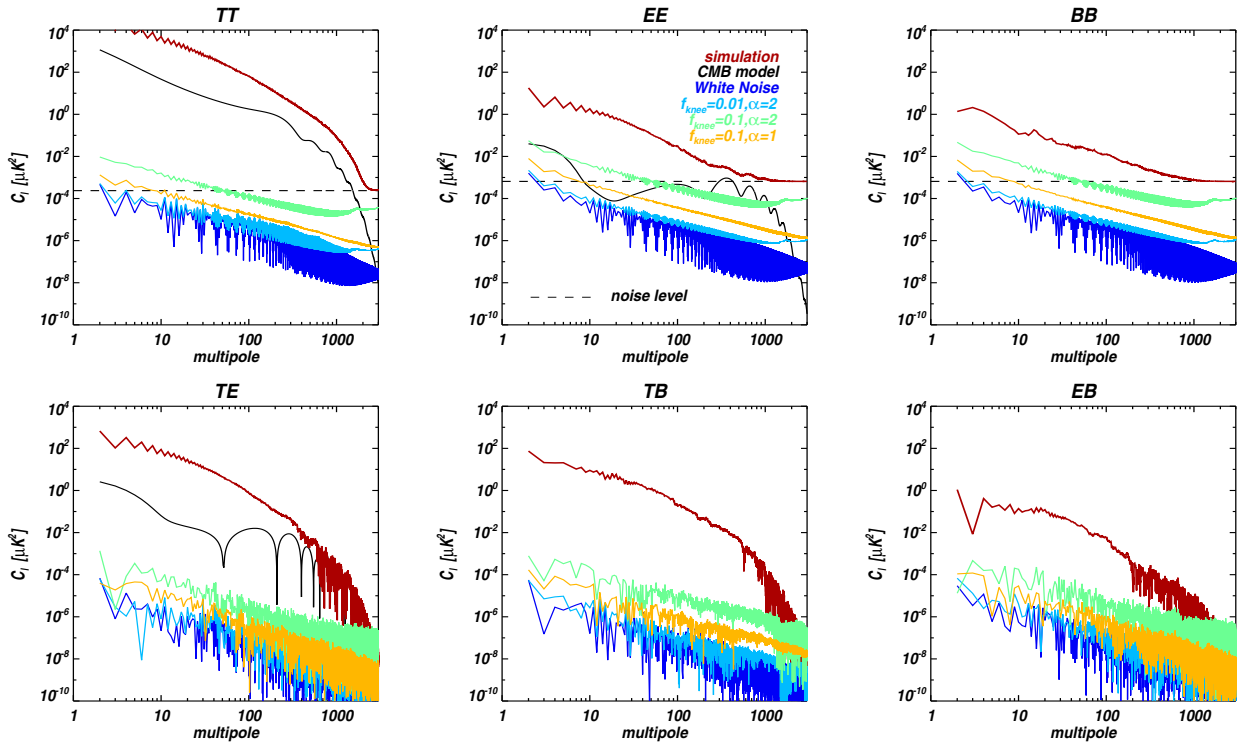

Figure 1.10: Residuals spectra after destriping the signal plus noise in the three cases of (1) pure white noise (*blue*), low frequency noise plus white noise with (α=2,f_{knee}=0.1 Hz), (2) (α=2,f_{knee}=0.01 Hz) and (α=1,f_{knee}=0.1 Hz) compared to the simulation power spectra (*red*), and (3) CMB WMAP five-year fiducial model (*black*) on 100 simulations. *Upper line, from left to right:* temperature, E-mode, and B-mode. *Bottom line, from left to right:* cross-correlation TE, TB, and EB.

Apart from the small deviations coming from the realistic scanning strategy used in this study, we found results that are fully compatible with the analytical predictions of Efstathiou (2007). In particular, we found that the power spectra of the residuals scale like σ^2 (where σ is the white noise level in map domain) in a similar way to the noise power spectra itself. This implies that the results discussed in this section do not depend on the value of the white noise level but only on the characteristics of the correlated noise (through the f_{knee} and α parameters of the noise Fourier spectrum).

1.7 Calibration results

1.7.1 Systematics

The calibration method is based on the assumption that when observing the same pixel of the sky at different times, the only variation in signal is due to the orbital dipole (assuming that the low-frequency noise is perfectly handled previously by the destriping). Any other effect leading to a difference between two different measurements of the sky power in one pixel, e.g. due to polarization because of a change in the bolometer orientation or a large signal variation inside the pixel) will result in a bias in the gain reconstruction. We performed a simulation including only CMB and Galactic emission intensities and estimate the gain for several internal resolutions and various internal mask sizes. The masks are based on the gradient of the Galactic emission, which is the component inducing the strongest intra-pixel variations. We have found a bias smaller than 10^{-5} for all considered internal resolutions as soon as the 1% most variable Galactic plane areas were masked. As shown in Fig. 1.11, the gain is biased only for the lowest resolution when the Galaxy is not masked at

all ($g \leq 6 \cdot 10^{-5}$). We conclude that in the calibration case, intra-pixel variations induce very small systematics. To match the destriping settings, we fix hereafter the internal resolution to nside = 512.

We also evaluate the bias in the gain reconstruction caused by the polarized sky signals from the Galaxy and CMB. We study three cases: CMB including intensity and polarization, Galactic emission with only polarized signal, and CMB + Galaxy (intensity and polarization). We reconstruct the gain applying several internal masks based on the intensity of polarization of the Galactic component. Figure 1.12 shows the bias of the reconstructed gain for the three simulations using each mask. We first note that the CMB polarization induces a bias (typically $\sim 5 \cdot 10^{-5}$) that is constant with respect to the percentage of sky masked but depends on the CMB realization and the bolometer characteristics. For a polarized Galactic signal, we find a stronger bias of up to $4 \cdot 10^{-4}$, which decreases with the mask size, reaching zero for a 20% masked fraction. The statistical error bar increases with the size of the mask because of the smaller sky coverage.

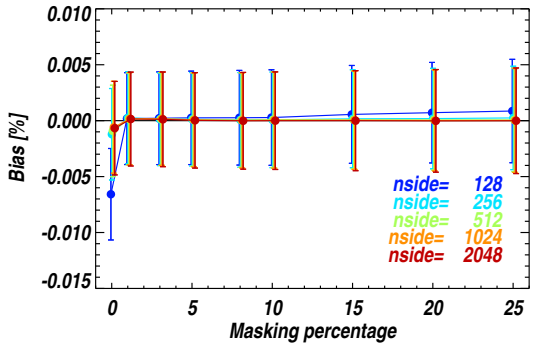

Figure 1.11: Evolution of the calibration bias due to the sky resolution with the masked fraction. Error bars are statistical estimates from POLKAPIX.

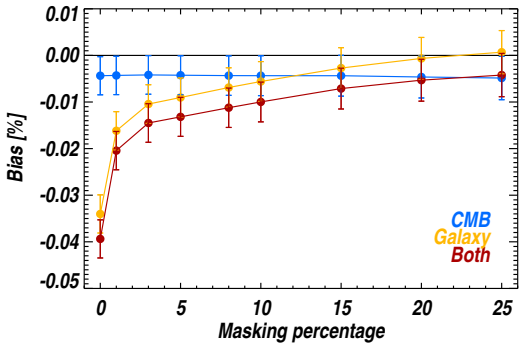

Figure 1.12: Evolution of the calibration bias due to the polarized signal and the masked fraction (*blue:* simulation of CMB; *orange:* simulation of Galactic emissions; *red:* simulation of CMB + Galaxy). Error bars are statistical estimates from POLKAPIX.

Bias in the gain reconstruction leads to a mis-estimation of the amplitude of the recovered intensity map. Its effects are however more dramatic for the polarization. If the bias affects all the detectors at the selected frequency in the same way, in the case of Planck-HFI, this would not result in a leakage of the total intensity into the polarization. However, in our case, the bias depends on the detector and it will cause a leakage of the temperature signal (dominated by the solar dipole) into Q and U Stokes parameters. Figure 1.13 illustrates the effect of this leakage on residual Q and U maps for a gain error of 5×10^{-5}.

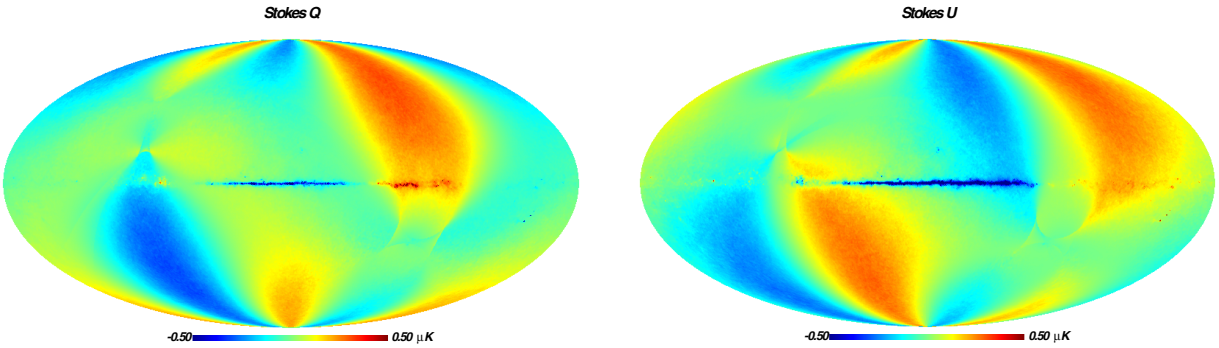

Figure 1.13: Residual maps of the Q and U Stokes parameters for a calibration uncertainty of 5×10^{-5}. The main features on large scales are related to the CMB dipole leaking into the polarization.

1.7.2 Gain statistical error

The uncertainty in the gain reconstruction is estimated from Eq. 1.20. We have verified this estimation using 1000 Monte Carlo simulations including only the CMB dipoles together with pure white noise for one bolometer at 143 GHz. We apply the 20% Galactic mask used in the previous section. Figure 1.14 shows the distribution of the gain bias (the relative difference between the reconstructed and simulated gains) for the 1000 simulations compared to a Gaussian with FWHM derived from Eq. 1.20. The standard deviation of the MC is fully compatible with the analytical error bar given by the number of simulations. The statistical error does not depend on the input signal or noise characteristics but only on the white noise level and the orbital dipole signal. For the four bolometers at 143 GHz, statistical errors are $\sim 4.5 \times 10^{-5}$.

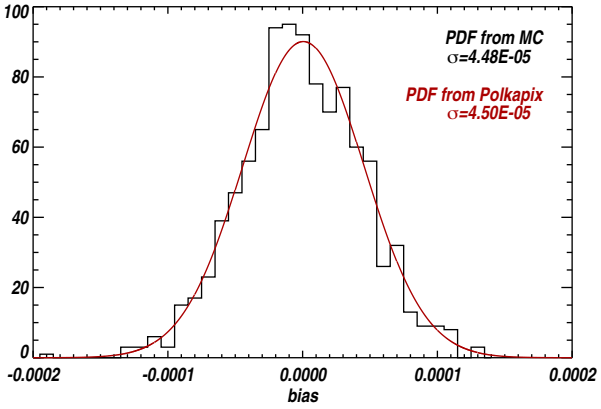

Figure 1.14: Gain bias distribution for 1000 simulations including CMB dipoles and pure white noise relative to Polkapix posterior PDF. A mask covering 20% of the sky is applied prior to calibration.

1.8 Solving for offsets and gain by iteration

Precise knowledge of the gains is required for destriping in order to precisely estimate the sky (I,Q,U) and the offsets, and remove the non-stationary component (the orbital dipole). In contrast, calibration cannot be performed before the removal of the low-frequency noise, i.e. the subtraction of the offsets from the data. This leads to the following iterative pipeline scheme. At each iteration step, we calibrate the detectors independently and then estimate offsets on a multi-detector basis. We repeat these operations until the relative difference between two consecutive gain estimations for each detector is smaller than 10^{-7}.

1.8.1 Characterization of the convergence

To check the convergence of the iterations for both gain and offset reconstruction, we present in Fig. 1.15 an example of the decrease in the gain bias with respect to the number of iterations for one of our simulations of signal (CMB and Galactic emissions) plus pure white noise. The initial condition corresponds to random gain factors generated with 5% r.m.s. of the simulated value. We reach the convergence level in about five iterations. Figure 1.16 shows, for the same simulation, the r.m.s of the offset residuals with respect to the iteration number.

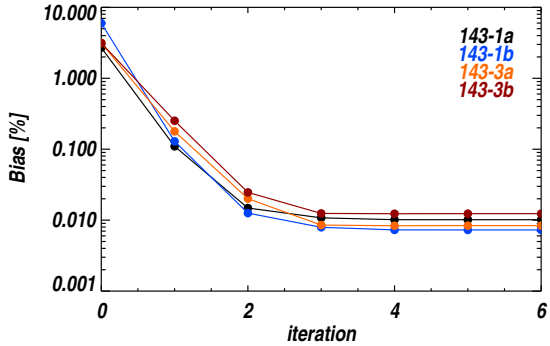

Figure 1.15: Bias of the reconstructed gains versus an iteration number in percent for a simulation with CMB, Galactic emission and pure white noise. The iterations are stopped when the relative differences between consecutive gains reaches 10^{-7}.

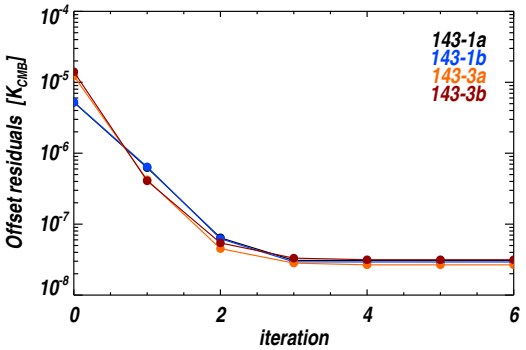

Figure 1.16: R.m.s. of the offset residuals with respect to iteration number in $K_{\rm CMB}$ for a simulation with CMB, Galactic emission, and pure white noise.

1.8.2 Gain and sky map accuracy

We now present results from the analysis of simulations including four bolometers at 143 GHz (see Sect. 1.5 for details). The sky signal is the combination of CMB (including the dipoles) and Galactic emissions to which we have added different noise TOD of pure white noise, or correlated noise with either (α=2,f_{knee} = 0.01 or 0.1 Hz) or (α=1,f_{knee}=0.1 Hz). One hundred noise realizations were generated in each case. Table 1.1 describes the results of the gain reconstruction for one bolometer (143-1a). As for the destriping (see Sect. 1.6.3), the calibration precision is significantly worse in this case (α=2,f_{knee}=0.1 Hz). However, even in this case, the relative precision is on the order of a few 10^{-4}.

Simulation	White Noise	f_{knee}=0.01 α=2	f_{knee}=0.1 α=2	f_{knee}=0.1 α=1
gain bias	8.6×10^{-5}	8.4×10^{-5}	6.8×10^{-5}	8.5×10^{-5}
statistical error	4.5×10^{-5}	4.5×10^{-5}	4.5×10^{-5}	4.5×10^{-5}
polar systematic	5.3×10^{-5}	5.3×10^{-5}	5.3×10^{-5}	5.3×10^{-5}
$1/f^{\alpha}$ systematic	0.1×10^{-5}	1.1×10^{-5}	25.0×10^{-5}	6.9×10^{-5}

Table 1.1: Gain biases and errors for bolometer 143-1a, for the four simulated noises: pure white noise, correlated noise with (α=2,f_{knee} = 0.01 or 0.1 Hz), and (α=1,f_{knee}=0.1 Hz). Statistical error is constant (see Sect. 1.7.2). Polarized signals introduce a systematic bias which we reduce to 5.3×10^{-5} by removing 20% of the brightest Galactic regions (see Sect. 1.7.1).

Figure 1.17 summarizes the calibration reconstruction accuracy for the four bolometers at 143 GHz. The gain biases are all consistent with zero given the statistical and systematic errors. The first set corresponds to gains reconstructed without destriping, for the pure white noise simulations. The following points represent the results of the pipeline for each dataset. The averaged gain for each bolometer is stable when changing the noise properties. The systematic bias, on the order of 5×10^{-5}, results from the anisotropies of the CMB polarization, as explained in section 1.7.1.

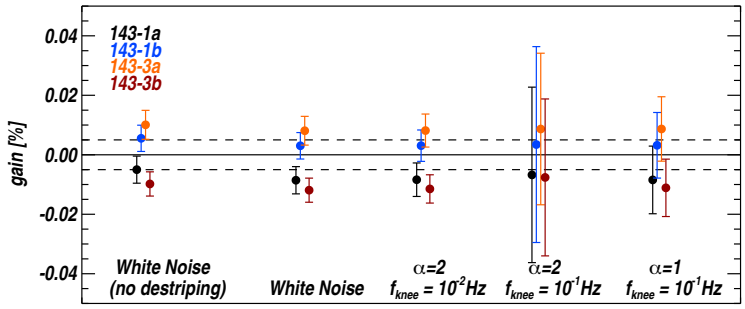

Figure 1.17: Gain biases for the four bolometers averaged over the Monte Carlo simulations, considering each dataset (*from left to right:* pure white noise without destriping, pure white noise after iterations, and low frequency noise with (α=2,f_{knee}=0.01), (α=2,f_{knee}=0.1), and (α=1,f_{knee}=0.1)). Error bars are derived from Monte Carlo simulations. *dash line:* systematics estimated in Sect. 1.7.1.

To evaluate the quality of the sky map reconstruction from our pipeline, we used a similar procedure to that adopted for the destriping analysis presented in Sect. 1.6. Figure 1.18 presents a compilation of averaged power spectra from residual maps for each datasets. The residual spectra have an additional excess power at low ℓ (below ~20) compared to those shown in Fig. 1.10. We attribute this excess to the calibration uncertainty that induces a leakage, of roughly 1 μK, of the orbital dipole signal into polarization. We computed the power spectra of the difference in the pure signal I, Q, U maps built with the recovered gains and the input maps (Fig. 1.13). As shown in Fig. 1.18, it matches the increase in power in the residual power spectra.
Figure 1.19 shows an example of the residual maps after iterations for one of the MC simulation. We clearly see the large-scale structures correlated with the orbital dipole residuals together with the stripes produced by the destriping errors.

1.9 Conclusion

We have presented an iterative scheme for map-making, by means of the destriping and photometric calibration of *Planck*-HFI data. This method has been fully implemented and tested within the HFI Data Processing Center. We have used simulated datasets for 143 and 217 GHz HFI detectors, under various noise hypotheses to evaluate the performances and derive the impact of systematics.
We have first set the parameters of the destriping to minimize the systematic effects that could bias the offset determination (foregrounds signal, sky pixelization). We have shown that for correlated noise with a knee frequency up to 0.1 Hz, destriping residuals are below the white noise level except for ℓ<50 for temperature and polarization. We found a significant bias for polarization at a knee frequency above 0.01 Hz. For a Planck-like Fourier spectrum presented by Planck HFI Core Team et al. (2011), we found residuals below the white noise level above ℓ=5.
We have then studied the performances of a gain reconstruction scheme based on the orbital dipole signal. We have demonstrated that in the same noise hypothesis as previously, we are able to reconstruct the photometric calibration with a statistical error of 5×10^{-5}. For pure white noise, we have also evaluated the systematic uncertainty to be 5×10^{-5}, which is dominated by CMB polarization anisotropies that are not modeled in our single-bolometer calibration scheme.
Finally, we presented the results when solving for offsets and gain by iteration. With low frequency noise, the gain bias stays constant but the uncertainties increase up to a few 10^{-4} for correlated noise with (α=2,f_{knee}=0.1 Hz). The calibration

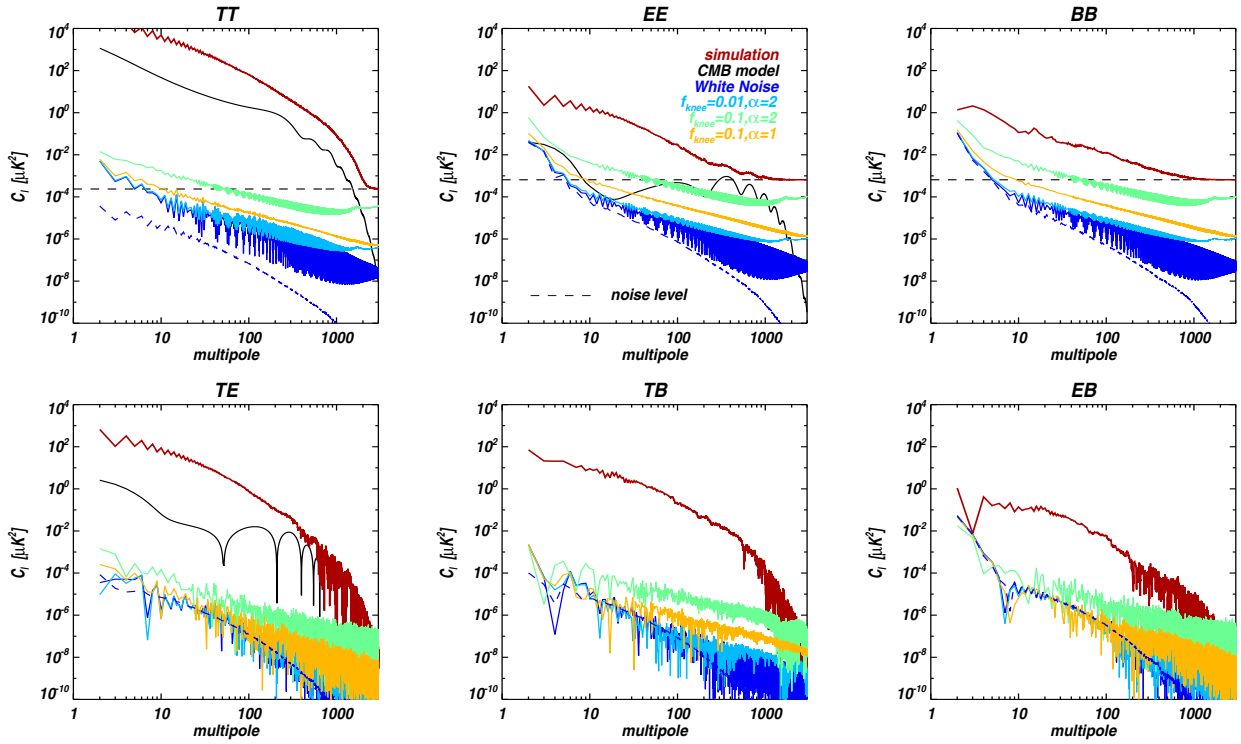

Figure 1.18: Average full-sky spectra of noise residual maps after the destriping and calibration pipeline for the datasets: pure white noise, and low frequency noise plus white noise with f_{knee}=0.1 Hz and 0.01 Hz. The effect of the calibration uncertainty is represented by the spectra of the residual map constructed using estimated gains (*blue dashed line*). The simulation power spectra and CMB WMAP-5yr fiducial model are also plotted for comparison. *Upper line, from left to right:* temperature, E-mode, B-mode. *Bottom line, from left to right:* cross-correlation TE, TB, and EB.

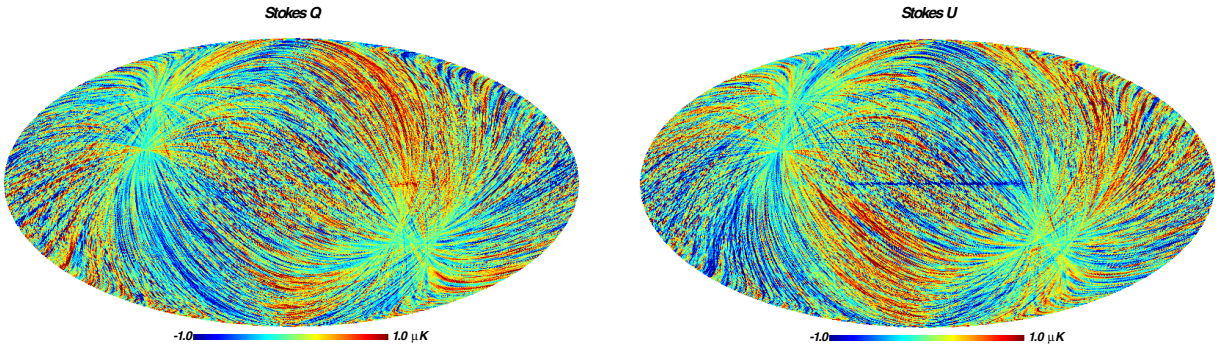

Figure 1.19: Residual maps of the Q and U Stokes parameters after iteration on a simulation of signal (CMB+Galactic emissions) plus low frequency noise (α=1,f_{knee}=0.1). Maps are degraded at 27.5 arcmin (HEALPix nside = 128). Large-scale residuals are compatible with the orbital dipole leakage as shown in Fig. 1.13. Stripes are destriping residuals.

uncertainty induces a further worsening of the destriping residuals concentrated at very low multipoles (ℓ<20). Altogether, this scheme could be fruitfully applied to the *Planck*-HFI flight data, provided they satisfy our very basic noise hypotheses.

We acknowledge the use of the Planck Sky Model, developed by the Component Separation Working Group (WG2) of the Planck Collaboration. We thank also the CTP working group for fruitful discussions on map-making algorithms. We acknowledge use of CC-IN2P3 facilities. The authors would like to thank F. Couchot and S. Plaszczynski for a detailed review of our manuscript.

Bibliography

Armitage, C. & Wandelt, B. D. 2004, Phys. Rev. D, 70, 123007
Arnau, J. V. & Sáez, D. 2000, New Astron., 5, 121
Ashdown, M. A. J., Baccigalupi, C., Balbi, A., et al. 2007a, A&A, 471, 361
Ashdown, M. A. J., Baccigalupi, C., Balbi, A., et al. 2007b, A&A, 467, 761
Ashdown, M. A. J., Baccigalupi, C., Bartlett, J. G., et al. 2009, A&A, 493, 753
Betoule, M., Pierpaoli, E., Delabrouille, J., Le Jeune, M., & Cardoso, J.-F. 2009, A&A, 503, 691
Burigana, C., Malaspina, M., Mandolesi, N., et al. 1999, ArXiv Astrophysics e-prints [astro-ph/9906360], internal Report at ITeSRE
Burigana, C. & Sáez, D. 2003, A&A, 409, 423
Cantalupo, C. M., Borrill, J. D., Jaffe, A. H., Kisner, T. S., & Stompor, R. 2010, ApJS, 187, 212
Collaboration, P. 2005, ESA publication, ESA-SCI(2005)/01
de Gasperis, G., Balbi, A., Cabella, P., Natoli, P., & Vittorio, N. 2005, A&A, 436, 1159
Delabrouille, J. 1998, A&AS, 127, 555
Doré, O., Teyssier, R., Bouchet, F. R., Vibert, D., & Prunet, S. 2001, A&A, 374, 358
Efstathiou, G. 2007, MNRAS, 380, 1621
Finkbeiner, D. P., Davis, M., & Schlegel, D. J. 1999, ApJ, 524, 867
Golub, G. H. & Van Loan, C. F. 1996, Matrix Computations (3rd Ed.) (Baltimore, MD, USA: Johns Hopkins University Press)
Górski, K. M., Hivon, E., Banday, A. J., et al. 2005, ApJ, 622, 759
Hinshaw, G., Weiland, J. L., Hill, R. S., et al. 2009, ApJS, 180, 225
Hupca, I. O., Falcou, J., Grigori, L., & Stompor, R. 2010, ArXiv [1010.1260]
Janssen, M. A., Scott, D., White, M., et al. 1996, ArXiv Astrophysics e-prints [astro-ph/9602009]
Keihänen, E., Keskitalo, R., Kurki-Suonio, H., Poutanen, T., & Sirviö, A.-S. 2010, A&A, 510, A57
Keihänen, E., Kurki-Suonio, H., & Poutanen, T. 2005, MNRAS, 360, 390
Keihänen, E., Kurki-Suonio, H., Poutanen, T., Maino, D., & Burigana, C. 2004, A&A, 428, 287
Leach, S. M., Cardoso, J.-F., Baccigalupi, C., et al. 2008, A&A, 491, 597
Maino, D., Burigana, C., Górski, K. M., Mandolesi, N., & Bersanelli, M. 2002, A&A, 387, 356
Maino, D., Burigana, C., Maltoni, M., et al. 1999, A&AS, 140, 383
Muciaccia, P. F., Natoli, P., & Vittorio, N. 1997, ApJ, 488, L63
Planck HFI Core Team, Ade, P. A. R., Aghanim, N., et al. 2011, A&A, 536, A4
Plaszczynski, S. 2007, Fluctuation and Noise Letters, 7, R1, last version (corrected web site)
Poutanen, T., de Gasperis, G., Hivon, E., et al. 2006, A&A, 449, 1311
Reinecke, M., Dolag, K., Hell, R., Bartelmann, M., & Enßlin, T. A. 2006, A&A, 445, 373
Revenu, B., Kim, A., Ansari, R., et al. 2000, A&AS, 142, 499
Seljak, U. & Zaldarriaga, M. 1996, ApJ, 469, 437
Stompor, R., Balbi, A., Borrill, J. D., et al. 2002, Phys. Rev. D, 65, 022003
Stompor, R. & White, M. 2004, A&A, 419, 783
Sutton, D., Zuntz, J. A., Ferreira, P. G., et al. 2010, MNRAS, 407, 1387
Szydlarski, M., Esterie, P., Falcou, J., Grigori, L., & Stompor, R. 2011, ArXiv [1106.0159]
Tegmark, M. 1997, Phys. Rev. D, 55, 5895
Tristram, M., Filliard, C., Perdereau, O., et al. 2011, A&A, 534, A88
Tristram, M., Macías-Pérez, J. F., Renault, C., & Santos, D. 2005, MNRAS, 358, 833
Wright, E. L. 1996, ArXiv [astro-ph/9612006]

Chapter 2

Map-making for the 2013 release

extracted from Planck Collaboration VIII (2014)

"Planck 2013 results. VIII. HFI photometric calibration and mapmaking"

For the 2013 release, I was co-leading the responsibility of the map production for Planck-HFI with Olivier Perdereau. From the cleaned TOD and the corresponding data flags, we produced the maps at the six HFI frequencies (100, 143, 217, 353, 545 and 857 GHz). Temperature sky maps were provided for the nominal Planck mission and also, separately, for the first two single surveys, the third one being covered only for a small part during the nominal mission. As a secondary product, maps with estimates of the Zodiacal light and Far-Side-Lobes contribution removed were also provided. Were also produced maps covering the nominal survey but using only half of the available data. These are: the "half-ring" maps, which are built using the first and second half of the stable pointing part in each pointing period; and the "detsets" maps, which are produced from a subset of detectors in a frequency channel (although they were not part of the first Planck data release). All these maps have been extensively compared and characterized to give a good description of their noise properties and potential systematic residuals. In particular, the map-making algorithm had to be adapted to account for ADC non-linearities resulting, at first order, in apparent gain variations along the mission.
This work for the Planck collaboration was published as one of the Planck 2013 release papers Planck Collaboration VIII (2014).

2.1 Introduction

This work describes the processing applied to *Planck* High Frequency Instrument (HFI) cleaned time-ordered information (TOI) to produce photometrically-calibrated sky maps.
CMB experiments can be calibrated using the dipole anisotropy induced by the motion of the instrument relative to the cosmological frame. This anisotropy is naturally separated into two components: we refer to the component generated by the motion of Planck around the sun as the *orbital dipole*, and that generated by the sun's motion relative to the CMB as the *solar dipole*.
In principle, the orbital dipole is the most precise calibrator, as it depends on the very well known orbital parameters and the temperature of the CMB, measured precisely by the *COBE*-FIRAS experiment (Mather et al. 1999). However, calibration using the orbital dipole involves comparison of data taken at large time separation (typically 6 months), and the precision one can achieve using this calibrator is thus directly linked to that of the time stability of the data, and to the precision reached in addressing any time variable systematics. We have identified one such systematic, induced by non-linearities in the analogue-to-digital converters of the bolometers' read-out electronic chain, and for the present release have chosen to use the solar dipole, based on the measurement of the solar dipole parameters from *WMAP* (Hinshaw et al. 2009), as the main calibrator for the 100 to 353 GHz channels. These parameters are summarized in Table 2.1.
At high frequency ($\nu \geq 500$ GHz), the dipole becomes too faint with respect to the Galactic foregrounds to give an accurate calibration. Although we used the Galactic emission as measured by FIRAS for the calibration of the *Planck* early papers (Planck HFI Core Team 2011a), we have now obtained a better accuracy using planet measurements. Thus, the absolute calibration of the two high-frequency channels is done using Uranus and Neptune.

At all frequencies, the zero levels of the maps are obtained by assuming no Galactic emission at zero gas column density, and adding the Cosmic Infrared Background (CIB) mean level.
The chapter is organized as follows. We first summarize the mapmaking procedure (Sect. 2.2). We outline the calibration method used for the CMB-dominated channels (100 to 353 GHz) in Sect. 2.3. We discuss in this section unexpected response variations with time, and present an effective correction. The calibration for the 545 and 857 GHz channels and how the zero level of the maps are fixed is not describe in this document (see Planck Collaboration VIII 2014). We finally quantify the accuracy of the photometric calibration, and give basic characteristics of the delivered maps in Sect. 2.4. Conclusion are given in Sect. 2.5.

Amplitude [mK_{CMB}]	3.355 ± 0.008
Galactic longitude [°]	263.99 ± 0.14
Galactic latitude [°]	41.74 ± 0.03

Table 2.1: Parameters of the solar dipole, as measured by *WMAP* (Hinshaw et al. 2009)

2.2 Pipeline for map production

The products of the HFI mapmaking pipeline are maps of I, Q and U, together with their covariances, pixelized according to the HEALPix scheme (Górski et al. 2005) with a resolution parameter $N_{\rm side}$=2048. For a given channel, data sample i may be described as

$$d_i = G\left(I_p + \frac{1-\eta}{1+\eta}\left(Q_p \cos 2\psi_i + U_p \sin 2\psi_i\right)\right) + n_i, \tag{2.1}$$

where p denotes the sky pixel with Stokes parameters I_p, Q_p and U_p, n_i is the noise realization, η is the cross-polarization parameter (equal to 1 for an ideal spider-web bolometer and 0 for an ideal polarization sensitive bolometer), ψ_i is the detector orientation on the sky, at sample i, and G is the detector's gain. Given *Planck*'s scanning strategy, reconstructing I, Q and U requires combining measurements from several detectors for most pixels. According to bolometer models, and given the stability of the HFI operational conditions during the mission, G is not expected to vary significantly.
In order to deal efficiently with the large HFI data set and the large number of maps to be produced, we use a two-step scheme to make maps from the HFI TOIs. The first step takes advantage of the redundancy of the observations on the sky. For each detector, we average the measurements in each HEALPix pixel visited during a stable pointing period (hereafter called *ring*), into an intermediate product, called an HPR for HEALPix Pixels Ring. Subsequent calibration and mapmaking operations use the HPR as input. As we produce HEALPix maps with the resolution parameter $N_{\rm side}$ set to 2048 we use the same internal resolution for building the HPR.
The in-flight noise of the HFI detectors, after TOI processing, is mostly white at high frequency, with a "$1/f$" increase at low frequency (Planck HFI Core Team 2011a). In such a case, a destriping approach is well suited for the mapmaking (Ashdown et al. 2009). In this approach, the noise in a ring r is represented by an offset, denoted by $\mathbf{o}_r$, and a white noise part $\mathbf{n}$, which is uncorrelated with the low-frequency noise. We may then reformulate Eq. 2.1 as

$$\mathbf{d}_i = G \times \mathsf{A}_{ip} \cdot \mathsf{T}_p + \mathsf{\Gamma}_{ir} \cdot \mathbf{o}_r + \mathbf{n}_i, \tag{2.2}$$

where T represents the sky (which may be a 3-vector if polarization is accounted for) in pixel p, A is the pointing matrix (which makes the link between data samples and their positions on the sky) and $\mathsf{\Gamma}$ is the matrix folding the ring onto samples. From the above equation, $\mathbf{o}_r$ are derived through maximum likelihood. As there is a degeneracy between the average of the offsets and the zero level of the maps, we impose the constraint $\langle \mathbf{o} \rangle = 0$. Tristram et al. (2011) have shown that with scanning and noise like those of HFI, an accurate reconstruction of the offsets $\mathbf{o}_r$ requires a precise measurement of G for each channel.
In addition, some signal components vary with time, adding more complexity to Eq. 2.2. Such components include the zodiacal light emission, the CMB dipole anisotropy component induced by the motion of the satellite with respect to the Solar System, and the far sidelobe (FSL) pick-up signal. Time variability of the former comes from the variation of the observation angle of the Solar System region emitting this radiation, due to the ellipticity and cycloid modulation of the satellite's orbit. The FSL are discussed in Planck Collaboration VII (2014) and Planck Collaboration XIV (2014). Accounting for these components in the mapmaking process requires an accurate calibration. Moreover, we need to take into account the low-frequency noise in the calibration process, so both operations (mapmaking and calibration) are interleaved.
For the production of the maps of the 2013 HFI data release, we followed a four-step process.

1. We first build the HPR for all detectors, for three data sets: all the data for each ring, and (for null tests) the data from just the first or just the second half of each ring.
2. We then apply the following calibration operations to the HPR:
   - solar dipole calibration, which sets the overall calibration factors for the 100–353 GHz detectors,

- planet calibration (Uranus and Neptune), which is used to get the calibration factors for the 545–857 GHz detectors,
- determine the relative gain variations over time of the 100–217 GHz detectors, using the `bogopix` tool (see Sect. 2.3.3).

3. For each data set we then do the destriping and projections, using the `polkapix` tool that was thoroughly validated in Tristram et al. (2011). We compute one set of offsets using the full mission (29 months) data set, and then use these offsets to compute the maps for the full mission, as well as for restricted time intervals (corresponding to each individual survey, and to the 15-months nominal mission). Maps are built by simple co-addition in each pixel of the destriped, calibrated, and time varying component-subtracted signal. We subtract the *WMAP* measured CMB dipole from all our maps, using the non-relativistic approximation.
4. The zero-levels for the maps are set a posteriori.

We have produced single-detector temperature maps, as well as temperature and polarization maps using all the detectors of a single frequency and some detector subsets. We have also produced hit-count maps and variance maps for the I, Q and U values computed in each pixel. Overall, a total of about 6500 sky maps have been produced. We used this data set to evaluate the performance of the photometric calibration. Note that the HFI pipeline we have described is quite similar to that used for the Low Frequency Instrument (LFI) (Planck Collaboration II 2014).

In order to take into account the Galactic signal integrated in the FSL and zodiacal light (hereafter called `zodi`) components, which vary in time, we have constructed templates for the combination of both components at frequencies where Galactic emission in the FSL matters, i.e., 545 and 857 GHz, and of `zodi` only at lower frequencies, as described in Planck Collaboration XIV (2014). These templates are used to build HPRs. We provide two sets of maps. The first set is built without removing these spurious components, while the second set is the differences between maps from the previous set and maps from which the `zodi` and FSL have been removed. The difference maps can be used to correct the HFI maps for specific applications.

In the following sections we will describe the calibration procedures and then assess their performance, and present some characteristics of the resulting maps.

2.3 Photometric calibration of the low-frequency channels: dipole-based calibration

2.3.1 ADC non-linearities and calibration

With a larger data set than that analyzed in Planck HFI Core Team (2011b), we could ideally use an orbital-dipole-based calibration, as described in Tristram et al. (2011). However, the additional redundancies revealed new systematic effects, ADC non-linearities and very long time constants (of the order of a few seconds) with very low energy content in the system's response. The former induce apparent gain variations with time. The latter shifts the CMB dipole a few arcmin in the scan direction, and hence creates leaks from the Solar dipole into the orbital dipole signal. These systematic effects prevented us from using the orbital dipole calibration. The very long time constants were identified after correcting for the ADC non-linearities, and have not yet been fully characterized yet. Both corrections will be implemented in the Planck 2014 data release.

Effects of such ADC-induced gain variations are clearly visible when comparing Survey 3 with Survey 1 or Survey 2 with Survey 4. As an example, in Fig. 2.1 we show survey difference maps for one 143 GHz detector, built using the calibration and mapmaking scheme presented in Planck HFI Core Team (2011b). Large-scale dipolar features, aligned with the solar dipole, are prominent in these maps. This shows that the constant gain assumption used to build these maps is incorrect.

Intrinsic bolometer sensitivity variations cannot explain such gain variations. The HFI bolometers have been precisely characterized in flight using a dedicated sequence of $V(I)$ measurements, during the post-launch verification phase and end-of-life periods. The static bolometer models predict that changes of their background during the observations could not explain response variations larger than 0.1 %. In addition, such variations are corrected for within the HFI DPC pipeline. In our present understanding, these apparent response variations are the result of imperfections in the linearity of the analogue-to-digital converters (ADC) used in the bolometer read-out units. The variation of the bolometer background with time and the unevenness in the ADC quantization steps leads, at first order, to an apparent gain variation in the electronic chain. These non-linearities may also affect signals differently depending on their amplitude, for example the solar and orbital dipoles.

Figure 2.2 shows the errors on the transition code positions measured on a spare ADC chip around the mid-scale, which is the most populated area. These "integrated non-linearities" (INL) present a prominent feature in all channels: the central step is always too narrow. In addition to this, the 64-code, nearly periodic patterns contribute to the apparent gain variations, making it difficult to predict the consequence of such errors on the reconstructed, demodulated bolometer signal. Such an INL effect has however been included in full mission simulations, and it reproduces qualitatively the gain variation features observed in real flight data, with an amplitude of about ±1%. This is larger than the required calibration precision of the 100 to 217 GHz channels.

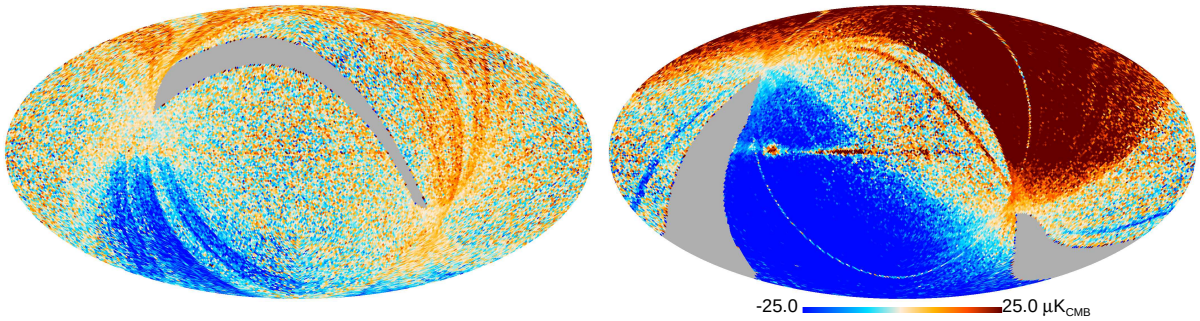

Figure 2.1: Differences between temperature maps built using data from detector 143-1a, for Surveys 1 and 3 (top) and 2 and 4 (bottom). In both cases, large-scale features appear. Their amplitude and disposition on the sky are compatible with residuals from the solar dipole, due to time variations of the detector gain, of the order of 1 to 2 %. These residuals should be compared to the amplitudes of the solar dipole, 3.353 mK$_{CMB}$, and to the orbital dipole that is about 10 times lower.

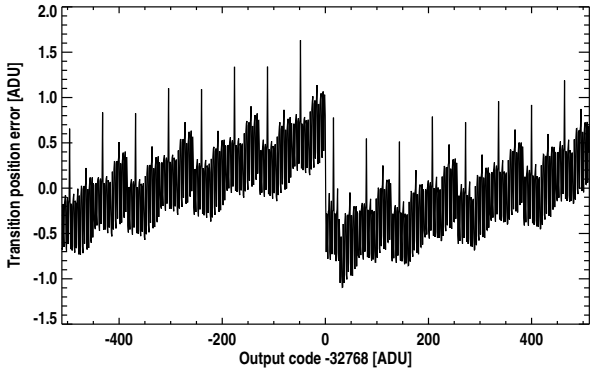

Figure 2.2: Error on transition code positions measured on one chip around the ADC mid-scale, on the ground on a spare ADC. The largest error occurs at the sign transition, but errors of about 1 ADU also occur regularly every 64 steps.

In order to precisely correct all the data for this effect, we need accurate measurements of all the ADC INLs, together with a good model for the bolometer raw signal (including systematics). Mapping the ADC response required more data than were acquired before the end of the HFI cold lifetime, so a dedicated campaign has been conducted over several months, at a focal plane temperature of about 4 K, to obtain a clean ADC characterization on Gaussian noise. Correcting this effect needs to be carried out prior to the TOI processing steps, and will require thorough checks of any products. At the time of writing, correction procedures are being intensively tested but they have not been included in the 2013 *Planck* data release.

In the absence of a full correction procedure, we had to develop an effective method to address the apparent bolometer gain variations that arise from the ADC non-linearities. In this method, the absolute scale is fixed by the solar dipole, to ensure a better robustness against higher-order non-linearities, as described in Sect. 2.3.2. Relative gains are determined using the scanning redundancies, as explained in Sect. 2.3.3.

2.3.2 Solar dipole calibration

The photometric calibration of the 100–353 GHz bolometers is based on the CMB dipole. We estimate one value of the detector gain for each ring through a template fit of the HPR data. We fit the coefficients of a linear combination of dipole, Galactic signal, and noise, neglecting the CMB and the polarization:

$$\mathbf{d} = g_r^{\mathrm{D}}.\mathbf{t}_{\mathrm{D}}+g_r^{\mathrm{G}}.\mathbf{t}_G+c_r+\mathbf{n}. \tag{2.3}$$

Here $\mathbf{d}$ represents the HPR samples from ring r, $\mathbf{t}_{\mathrm{D}}$ is the value of the total (Solar and orbital) kinematic dipole, $\mathbf{t}_{\mathrm{G}}$ is a model for the Galactic emission, and $\mathbf{n}$ is the white component of the noise. For simplicity, we used a non-relativistic approximation. We do not take into account the smearing of the dipole by the instrumental beam in our procedure. We simultaneously fit three parameters: g_r^{D}, the gain of the kinematic dipole; g_r^{G}, the gain of the Galactic model; and c_r, a constant accounting for the low-frequency noise.

As the satellite scans circles on the sky, the ratio of the dipole and Galactic signal amplitudes varies. We use a Galactic model to obtain a measurement of the dipole gain, even in rings where the dipole amplitude is low. However, imperfection of that model may lead to bias in the dipole gain. To reduce this bias, we exclude pixels with a Galactic latitude lower

than 9°. Because we calibrate on the kinematic dipole, we do not use the gain g_r^G in what follows. Pixels contaminated by point sources listed in the *Planck* Catalogue of Compact Sources (Planck Collaboration XXVIII 2014) are also excluded. The best model we have for the sky emission at the HFI frequencies being HFI measurements themselves, we use HFI sky maps at the detector frequency as a Galactic model.
Results of the gain estimation for each ring are shown in Fig. 2.3 for one detector (143-1a) . We can see that the gain estimate is less accurate on some ring intervals. This is due to the *Planck* scanning strategy: these intervals correspond to epochs when the *Planck* spin axis is orthogonal to the dipole direction. We can also see the apparent ring-by-ring gain variations, of the order of ±1%, explained in Sect.2.3.1. To show this more clearly, the figure compares the ring-by-ring variations reconstructed in Surveys 1 and 2 with those from Surveys 3 and 4.
The final gain value for each detector, hereafter denoted by $\tilde{G}^{SD}$, is defined as the average of these estimates between rings 2000 and 6000, between which the individual measurements for each ring have a dispersion of less than 1%.

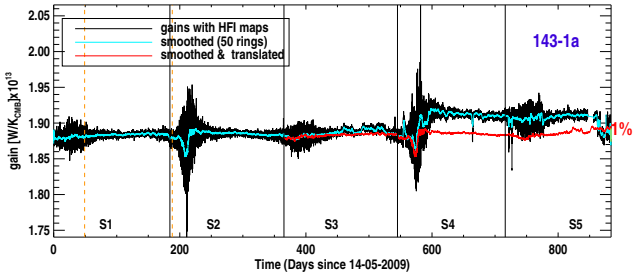

Figure 2.3: Solar dipole gain reconstructed ring-by-ring for one HFI bolometer. The thin black line represent the raw values, and the thick cyan line is a smoothed rendition with a width of 50 rings (about 2 days). We have indicated the conventional boundaries of the surveys as black vertical lines. The orange vertical dashed lines indicate the interval in which we compute the gain $\tilde{G}^{SD}$ (computed between rings 2000 and 6000, or approximately days 60 and 190). The red curve shows the smoothed gain variation shifted to match the repetition in Surveys 3 and 4 of the scan strategy followed in Surveys 1 and 2 (note that the scan strategy for Survey 5 differs from that of Survey 3). The grey band highlights a ±0.5% excursion around the averaged gain $\tilde{G}^{SD}$. The observed ∼1% variations explain the large-scale residuals seen in Fig. 2.1.

2.3.3 Effective correction and characterization

In order to handle time variation of the bolometer gains, we set up an effective correction tool, called `bogopix` (Perdereau 2006). We start from Eq. 2.2, but take explicitly into account the orbital dipole $\mathbf{t}_{Do}$, which is time-variable, and also fit the gains $\mathbf{g}_r$ for each bolometer independently. The problem finally reads

$$\mathbf{d}=\mathbf{g}_r(\mathsf{A}\cdot\mathsf{T}+\mathbf{t}_{Do})+\Gamma\cdot\mathbf{o}_r+\mathbf{n}, \tag{2.4}$$

where r is the ring number. The unknowns are the offsets $\mathbf{o}_r$, the sky signal represented by T, and the gains $\mathbf{g}_r$, sampled using one value per ring. Since the orbital dipole is an absolute calibrator, the solution for $\mathbf{g}_r$ should also fix the absolute photometric calibration.
We take advantage of the low amplitude of the observed gain variations to linearize this nonlinear problem, following an iterative approach. Starting from an approximate solution for the gains $\mathbf{g}_r$ and sky maps T, we determine the variations with respect to these, $\delta\mathbf{g}_r$ and $\delta\mathsf{T}$, by solving :

$$\begin{aligned}\mathbf{d} &= (\mathbf{g}_r+\delta\mathbf{g}_r)(\mathsf{A}\cdot(\mathsf{T}+\delta\mathsf{T})+\mathbf{t}_{Do})+\Gamma\cdot\mathbf{o}_r+\mathbf{n} &(2.5)\\ &\approx \mathbf{g}_r(\mathsf{A}\cdot(\mathsf{T}+\delta\mathsf{T})+\mathbf{t}_{Do})+\delta\mathbf{g}_r(\mathsf{A}\cdot\mathsf{T}+\mathbf{t}_{Do})+\Gamma\cdot\mathbf{o}_r+\mathbf{n} &(2.6)\end{aligned}$$

The linearized Eq. 2.6 may then be solved for $\delta\mathbf{g}_r$, $\delta\mathsf{T}$ and $\mathbf{o}_r$ by a conjugate-gradient method. Using $\delta\mathbf{g}_r$ and $\delta\mathsf{T}$, the gains $\mathbf{g}_r$ and sky maps T can be updated. This process is iterated until a satisfactory solution is reached. To initialize the iterations, we start from the constant gain solution. We stop when the relative change in the χ^2 derived from Eq. 2.4 is low enough (in practice, when the change is less than 10^{-6}). This approach is similar to the one used for the LFI calibration (Planck Collaboration V 2014). It was successfully tested using the data set of Tristram et al. (2011), derived from simulated timelines with a *Planck*-like scanning strategy, realistic noise (both for the white and $1/f$ components), Gaussian beams, and delta-function bandpasses, for four 143 GHz polarization-sensitive bolometers over about 12000 rings. Figure 2.4 presents gains reconstructed with `bogopix` on simulated data, and compares them with the constant input gain values. From these results, we see that the precision of the gain value reconstructed for a single ring is about 0.5% (which is comparable with the global precision of 5×10^{-5} for a constant gain for 12000 rings found in Tristram et al. 2011).
We computed the gain variations using single-detector data, thus neglecting polarization. As in destriping (Tristram et al. 2011), gradients within the sky pixels used for T will limit the accuracy of the gain determination. These gradients increase with frequency. Moreover, the ADC non-linearity will induce biases in the signal used for the gain determination. As this

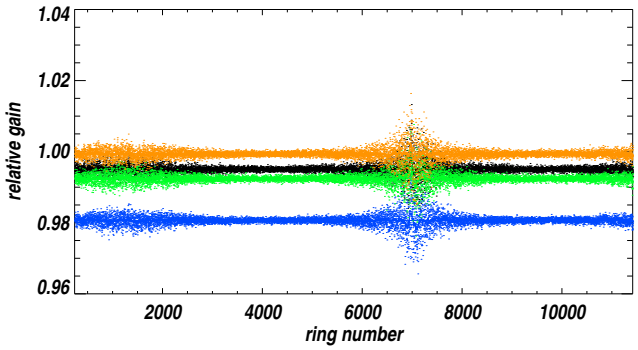

Figure 2.4: Example of results obtained with `bogopix` on the simulated data set used in Tristram et al. (2011), where constant gains biases were applied. The colours distinguish four different bolometers. Dots correspond to individual measurements, and the thick line is a smoothed representation of these results with a 50 ring width. We plot relative reconstructed gains, with respect to their unbiased value. In this simulation, each bolometer's data was biased by factors of respectively 1.98 (blue) , 0.77 (green), 0.50 (black) and 0.07 % (orange) respectively which is precisely reflected by the recovered `bogopix` value.

signal's dynamic range increases with frequency, we expect this bias also to increase with frequency. For these reasons, we used `bogopix` to determine an effective correction for the apparent gain variations only for frequencies ≤217 GHz. To avoid the central part of the Galactic plane and point sources, we used the mask used for destriping in the *Planck* Early Results paper (Planck HFI Core Team 2011b, Figure 32).
As shown in Fig. 2.5, the variations of the gains g_r found with `bogopix` follow nicely those from the solar dipole calibration ($g_r^{\rm D}$) in the regions where this signal is large. The lower level of fast variations from `bogopix` in the time intervals where the scan lies close to the Solar dipole equator and at the same time close to the Galactic plane, indicates that the `bogopix` results are less biased for these rings. We observe apparent gain variations on time scales of a few hour as well as months, with amplitudes of 1 to 2 % maximum, largely uncorrelated from one detector to another.

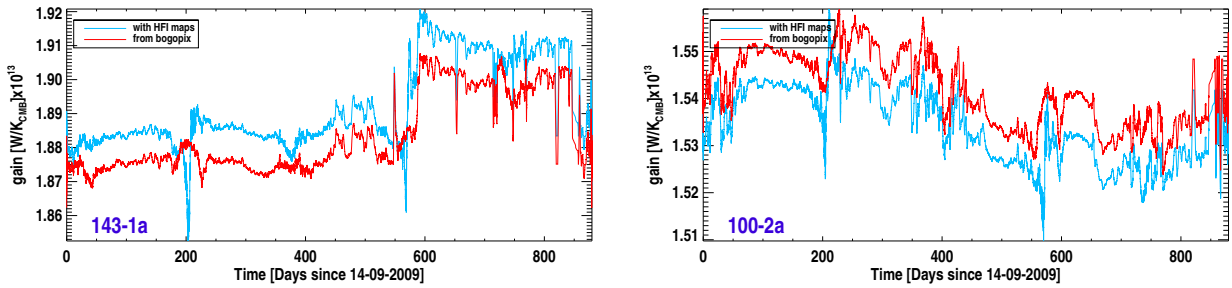

Figure 2.5: `bogopix` results for two HFI detectors, compared with those from the solar dipole calibration. Gain values for individual rings have been smoothed with a width of 50 rings (about 2 days), to increase the signal-to-noise ratio. There is good agreement of the relative gain variations between the `bogopix` results and those obtained from the HFI maps, except for the time intervals where the solar dipole amplitude is lower than the Galactic emission. The averaged value of the gains are, however, offset by factors (different from one detector to the other) of the order of 0.5 to 1 %.

The averaged gain level determined by the two methods are, however, different by 0.5 to 1 %, and the difference varies from one detector to another. We believe this is due to the different scales of the calibrating signals in the two methods: the absolute scale of `bogopix` results is set by that of the orbital dipole, a factor of 5 to 10 lower in amplitude that the solar dipole used in the other method. These signals are thus affected to different degrees by the ADC non-linearities. In the simplest case, the effect of the non-uniformity of the ADC digitization steps is a fixed offset (positive or negative) added on top of the signal, when this signal oversteps a given level, so the resulting calibration bias will be lower for the largest calibration signal.
We study the difference between the averaged solar dipole gain, $\tilde{G}^{\rm SD}$, and the average of the `bogopix` results, g_r, in the same ring interval, denoted by $\tilde{G}^{\rm bog}$. We introduce another calibration process, based on the orbital dipole as described in Tristram et al. (2011), together with `bogopix` gains, renormalized so that they average to 1 between rings 2000 and 6000 (corresponding to days 60 and 190 approximately), to correct for the apparent relative gain variations. This produces another estimate of the absolute gain, $G^{\rm OD}$. The relative differences, $(\tilde{G}^{\rm SD}-G^{\rm OD})/\tilde{G}^{\rm SD}$, are shown in Fig. 2.6 for each 143 GHz detector. Both methods agree with each other within 0.05 to 0.1 %. We conclude that the difference between $\tilde{G}^{\rm SD}$ and $\tilde{G}^{\rm bog}$ is genuine and it seems to be due to the use of the orbital dipole as the calibrator.
We showed in Tristram et al. (2011) that calibration errors induce large-scale features in the Q and U Stokes parameter

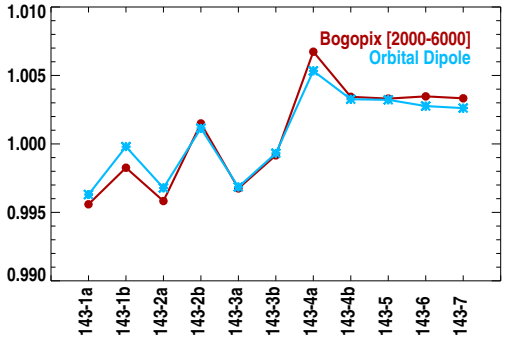

Figure 2.6: Relative differences of the orbital dipole calibration ($G^{\rm OD}$, blue) and the average of `bogopix` gains ($\tilde{G}^{\rm bog}$, red), with respect to the solar dipole calibration results($\tilde{G}^{\rm SD}$), for the 143 GHz HFI detectors. Both schemes produce gains within 0.1 % of each other, which shows that they are both affected by the same systematics (the ADC non-linearities).

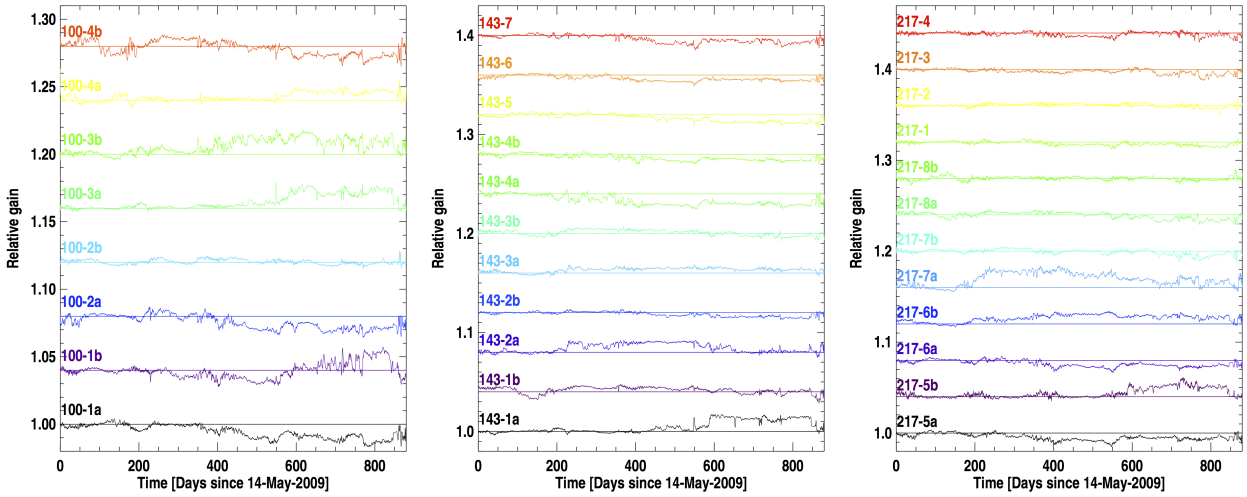

Figure 2.7: Relative gains reconstructed by `bogopix` for the 100, 143, and 217 GHz detectors as a function of time, smoothed with a width of 50 rings (about 2 days). Their overall amplitudes are of order 1 to 2 %, but both slow and fast (over a few tens of rings, i.e., a day) variations are observed. These variations are largely independent from one detector to the other. Relative gains for each detector have been vertically displaced by 3 % for clarity.

maps. When using the orbital-dipole-based calibration factors to build these maps, we indeed observe such large-scale patterns, which is further evidence that the latter factors are biased. We also observed a noticeable residual dipole in the reconstructed detector maps, after subtraction of the *WMAP* measured dipole, for the detectors where the difference between the solar and orbital dipole calibration was larger. We therefore conclude that, in the absence of an accurate correction for the ADC non-linearities, the orbital-dipole calibration scheme cannot be used to calibrate the HFI data.

2.3.4 Dipole calibration pipeline

We used the `bogopix` results only as to measure the *relative* gain variations, by normalizing to 1 on average between rings 2000 and 6000 (where the solar dipole calibration is computed). We show as an example a compilation of the relative gains reconstructed for the 100, 143, and 217 GHz detectors in Fig. 2.7. The absolute calibration scale of the CMB channels (100–353 GHz) is set by the solar dipole calibration, as in the HFI early data release (Planck HFI Core Team 2011a), which relied on *WMAP* solar dipole measurements (Hinshaw et al. 2009).

As a first example of the improvements that `bogopix` provides, we show in Fig. 2.8 the survey-difference maps (Survey 3 minus Survey 1, and Survey 4 minus Survey 2), for the detector used for Fig. 2.1. The differences obtained using `bogopix` are lower than $\sim 10 \mu K_{\rm CMB}$ outside the Galactic plane. The remaining residuals in that region, in particular in the Survey3−Survey1 difference, can be attributed to the nonlinear nature of the systematic error, only the first-order linear part of which is handled by `bogopix`.

For frequencies ≥353 GHz, `bogopix` results are not reliable, mainly because of the large spatial variation of the sky emission inside a pixel (we have used 1.72′ pixels here). Therefore, we do not correct the highest-frequency channels for any gain variations. This leads to calibration uncertainties of about 1% between maps from individual surveys.

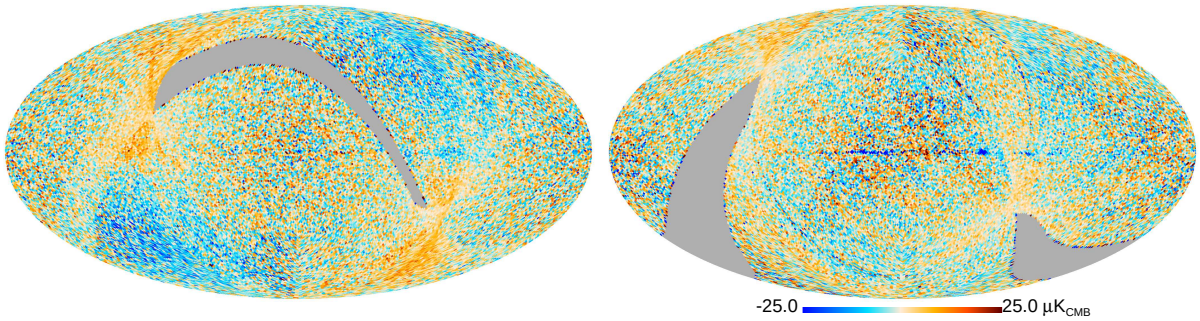

Figure 2.8: Residual differences between temperature maps built using data from detector 143-1a, for Surveys 1 and 3 (top) and Surveys 2 and 4 (bottom), derived using the `bogopix` results. The level of differences is much lower than in Fig. 2.1.

2.3.5 Dipole calibration uncertainties for single detector

For the dipole calibration scheme, the statistical uncertainties are estimated by propagating the TOI sample variances (NET) to the ring-by-ring gain estimation on the solar dipole, averaged between rings 2000 and 6000, for each detector. These uncertainties are much lower than the systematic uncertainties that dominate our calibration measurement. We estimate the size of these systematic uncertainties on the calibration of individual detectors by measuring the dispersion of these ring-by-ring gains. Both uncertainties are listed in Table 2.2, which gives their average at each frequency. The *WMAP* solar dipole amplitude uncertainty (0.24%, Hinshaw et al. 2009) is not included. The systematic errors given here should be considered as upper limits on the real systematics, as they have been derived from solar dipole ring-by-ring gains prior to the `bogopix` correction. We indicate the effect of the choice of a Galactic template by indicating a "worst case" scenario (second column of Table 2.2) in which a non-optimal template was used. When combining different detectors, some of these systematic errors should partially average out for temperature. The gain variation part, for example, is independent from one detector to another. To get a more precise estimation of the calibration accuracy for the frequency maps of this release, we have performed more elaborate tests, which are presented in Sect. 2.4.

Frequency [GHz]	Statistical error [%]	Systematic (worst case) [%]	Systematic [%]
100	0.004	0.64	0.37
143	0.002	0.53	0.29
217	0.002	0.69	0.41
353	0.010	2.53	1.81

Table 2.2: Statistical and systematic uncertainties on the dipole calibration, for single detectors from the lower-frequency HFI channels. The "worst case" column corresponds to a situation with a poorly matched sky template, whereas the third column is for the best case. In addition to each of these values, one has to take into account the *WMAP* solar dipole amplitude uncertainty, 0.24%, as this measurement is our primary calibrator.

2.4 Characterization and checks of calibration

In this section we present the various tests that have been carried out to assess the precision and stability of the calibration of the HFI data.

2.4.1 Time stability of the calibration

To evaluate the accuracy of the apparent gain variation correction coming from `bogopix` we compute, for each detector, the residual difference R between the HPR data d and a model including the destriping offsets o_r, the HFI I, Q and U maps, the dipoles t_D (orbital and solar) and the calibration parameters (relative ring-by-ring gains g_r from `bogopix`, overall gain $\tilde{G}^{\rm SD}$ based on the solar dipole, and zero point z derived as described above). This corresponds, for each HPR sample i of each ring r, and pixel p to:

$$R_i = (d_i - o_r)/(g_r \cdot \tilde{G}^{\rm SD}) - t_D - I_p - \frac{1-\eta}{1+\eta}\left(Q_p \cos 2\psi_i + U_p \sin 2\psi_i\right) - z \qquad (2.7)$$

We display these residuals as a function of the rotation phase, i.e., the angle between the direction of the pixel in the HPR and the satellite velocity, in Fig. 2.9. In this representation, the orbital dipole extrema will be found at fixed phases

0 and $\pm\pi$. The solar dipole will present a modulated pattern, also illustrated in Fig. 2.9. As the solar dipole is the brightest component of the sky emission, its pattern in the residuals is a good indication of inaccuracy of the gain variation correction. This may also capture additional time variable signals that would not be accounted for in our processing, for example the primary spillover pick-up. The areas where the Galactic emissions dominate show up as outliers in these residuals, for several reasons. First, they correspond to regions were intra-pixel gradients are large, and will leave some imprint due to the individual scanning trajectories of each detector. More importantly, they present emission spectra different from that of the CMB, on which we calibrate. Integrated over each detector's bandpass, this will translate into an apparent brightness difference. At this stage, we do not apply colour corrections to get rid of such effects, considering that they can be minimized by a proper selection of the sky area (i.e., avoiding the Galactic plane). Finally, imperfections in the time response of the detectors and in the pointing reconstruction will also induce larger residuals in the Galactic plane. Masking these regions, using a 40 % Galactic mask, we checked that, for all the 100–217 GHz detectors, the maximum level of the residuals we observe would correspond to a remaining gain variation lower than 0.3 % (i.e., residuals lower than 10 μK_{CMB}).

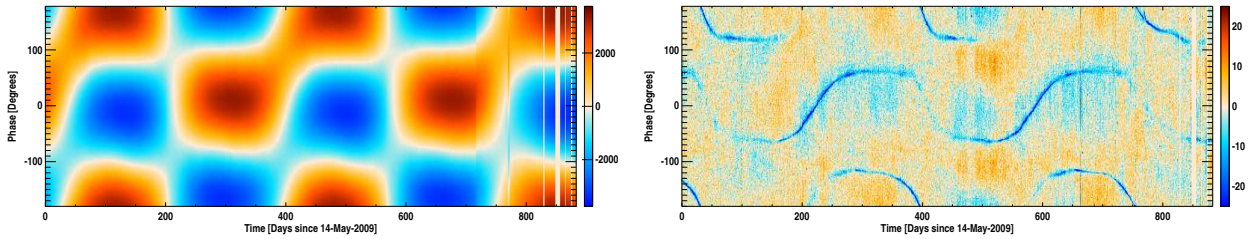

Figure 2.9: *Left:* Distribution of the residuals in μK_{CMB}, computed using Eq. 2.7, for detector 143-1a, plotted versus observation date and satellite rotation phase. *Right*: Expected pattern for the solar dipole, in μK_{CMB}. Comparison of the two plots provides a check of the level of residual gain variation after applying the `bogopix` gains. In the residuals the sharp features (dark blue) correspond to the Galaxy observations, where band-pass effects have not been corrected.

2.4.2 Intra-frequency calibration checks

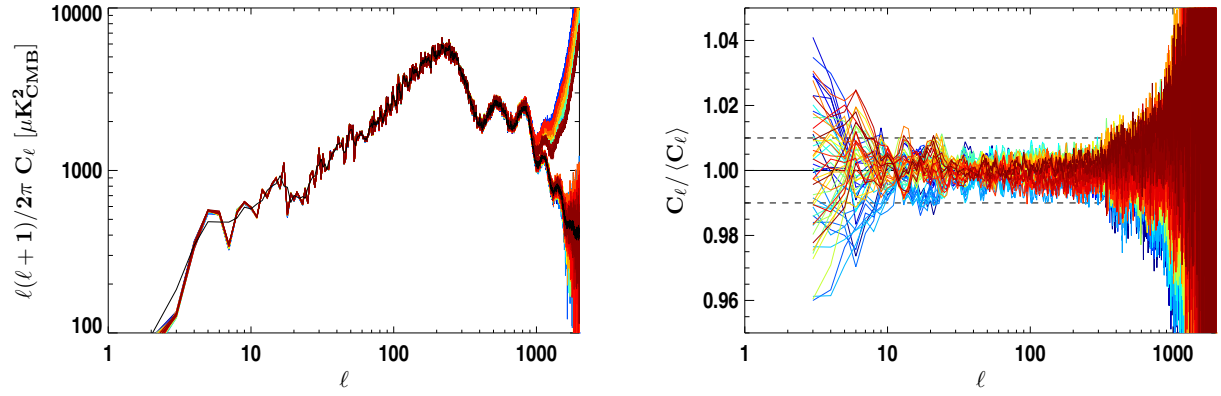

Figure 2.10: Auto- and pseudo-cross-spectra obtained from the eleven 143 GHz HFI detectors corrected for the beam (left) and their ratio with respect to the average of the pseudo-cross-spectra (right). This average is indicated in black in the top panel. Each detector pair is shown in a different colour. Note the noise suppression in the cross-spectra above $\ell \sim 800$.

We have checked the relative calibration of the detectors within a given frequency channel using pseudo-cross-power spectra. We start from the single-detector temperature maps, neglecting polarization. We mask sky areas where the Galactic emissions are large, keeping 40 % of the sky for frequencies lower than 300 GHz and 30 % above. We build the pseudo-cross spectra of this set of maps, using `Xspect` (Tristram et al. 2005). We correct each pseudo-spectrum for its beam window function (Planck Collaboration VII 2014). We then focus on the location of the first acoustic peak, so that results are not biased by beam uncertainties. For example, the set of spectra we obtain for the 143 GHz HFI detectors is shown in Fig. 2.10. Finally, we fit the recalibration coefficients that minimize the differences between these spectra, for ℓ in the range [25, 300]. For 545 and 857 GHz we apply a colour correction for the band-pass mismatch between detectors, assuming the *IRAS* spectral convention. The relative calibration coefficients found with this method should be considered as upper limits on the relative calibration precision of HFI, as we neglect polarization in this analysis. They are given for all frequencies in Table 2.3. For frequencies below 217 GHz the relative calibration accuracy is better than 0.4 %. These relative accuracies are consistent with the systematic uncertainties estimated in the previous section.

Frequency [GHz]	100	143	217	353	545	857
Calibration [%]	0.39	0.28	0.21	1.35	1.3	1.4

Table 2.3: Maximum absolute value of the relative calibration coefficients fitted on pseudo-spectra similar to those of Fig. 2.10, between detectors of each frequency. These values are upper limits on the relative calibration errors within each channel (i.e., between all bolometers of a given channel).

In Fig. 2.11, we compare the relative calibration coefficients derived from the pseudo-cross spectra, for all 100, 143 and 217 GHz detectors, with the relative differences between gains based on solar and orbital dipole calibration methods (see Sect. 2.3.3). Both orbital dipole methods are affected by the same systematics, namely the ADC non-linearities. CMB anisotropies are well intercalibrated between detectors, using solar dipole calibration. This reinforces the choice of the solar dipole calibration.

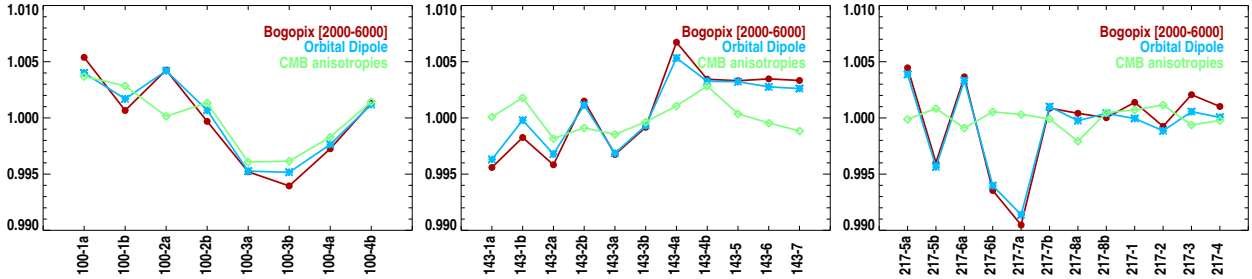

Figure 2.11: Relative calibration coefficients found when calibrating on the orbital dipole (constant gain, light blue, with `bogopix` in red) and using CMB anisotropies (see Sect. 2.4.2, in green), with respect to the Solar dipole gains, used to build the HFI maps. As ADC non-linearities are not corrected for, calibration systematics depend on the amplitude on the signal used to check for them. The amplitudes of such effects are within the systematic uncertainties quoted in Table 2.3.

2.4.3 Inter-frequency and absolute calibration checks for CMB-dominated channels

In this section, we describe the checks performed to study the calibration accuracy for CMB channels.

Pseudo-cross-power spectrum analysis

We applied a technique similar to that presented in Sect. 2.4.2 to assess the HFI inter-frequency relative calibration for combined maps, at frequencies where the CMB dominates at high Galactic latitudes. We built pseudo-power spectra from the temperature maps for 100, 143, and 217 GHz, applying the beam correction described in Planck Collaboration VII (2014). As above, we determined the cross-calibration coefficients that minimize the difference between the pseudo-cross-power spectra of the HFI maps for ℓ in the range [25, 300]. Results from this analysis are shown in Table 2.4. We see from these numbers that the internal relative calibration precision between the 100, 143 and 217 GHz channels is better than 0.15%.

Frequency [GHz]	100	143	217
Calibration	1.002	0.999	0.999

Table 2.4: Cross-calibration coefficients that minimize the dispersion of the HFI temperature cross-spectra around their common mean.

Solar-dipole parameter fits

We also studied the calibration accuracy using fits of the CMB dipole parameters on HFI maps. To perform this test, we used maps built without dipole subtraction. Such fits are likely to be biased in the presence of foregrounds, in particular due to the intrinsic dipole of the Galactic emissions. We therefore used a template fitting method to subtract dust emission; our dust template is based on *IRAS* data (Neugebauer et al. 1984). We masked 10% of the sky, based on Galactic dust and CO emission, as well as point sources, before fitting the amplitude and direction of the CMB dipole. We recover the *WMAP* dipole amplitude measurement at the level of 0.1 % or better in all cases (Table 2.5). The direction, perhaps more affected by foreground residuals or by uncertainties in the time response, is reconstructed within about 10′.

Frequency [GHz]	Amplitude [%]	Longitude [′]	Latitude [′]
100	-0.122	2.30	11.09
143	-0.074	3.00	11.91
217	-0.091	-5.10	12.79

Table 2.5: Differences between the CMB dipole parameters fitted on the HFI maps with those measured by *WMAP*. The typical statistical errors on these fits are ∼0.01% for the amplitude and less than 1′ for the direction.

Calibration checks using component separation methods

Finally, calibration consistency checks have been performed using component separation tools. In particular, the SMICA component separation method (Cardoso et al. 2008) has been used to fit relative calibration coefficients for each frequency (including LFI data) on the CMB anisotropies (Planck Collaboration XII 2014). The foreground model is a non-parametric 4-dimensional model, meaning that the foregrounds are represented by four templates with arbitrary emission laws, arbitrary angular spectra, and arbitrary correlations (2- and 3-dimensional fits were also performed with compatible results). Relative-calibration coefficients between frequency power spectra obtained using this method are summarized in Table 2.6. They agree, within errors, with the results shown in Tables 2.4 and 2.5. It should be noted that for frequencies >353 GHz, Rayleigh scattering, not included in such studies, will distort the CMB anisotropies used to derive such cross-calibrations, at the few percent level (Yu et al. 2001). Therefore cross-calibration coefficients found for 353 and 545 GHz, which are of the same order, should be considered as estimates of systematic cross-calibration uncertainties, rather than genuine corrections of our maps. Such studies are routinely incorporated in *Planck* likelihood minimizations (Planck Collaboration XV 2014), and more results are shown in Planck Collaboration XV (2014). Comparisons with LFI and *WMAP* are presented in Planck Collaboration XVI (2014).

Frequency [GHz]	Relative calibration	Fisher errors
100	0.999	0.2%
143	1	0.2%
217	1.000	0.2%
353	0.993	0.3%
545	1.05	3.5%

Table 2.6: Cross-calibration coefficients of the HFI sky maps at each frequency, with respect to the 143 GHz map, found with the SMICA component separation method, with errors derived from a Fisher matrix analysis.

2.4.4 Map noise level assessment

When combining detector data to build frequency maps, we apply an inverse noise weighting scheme. The weights we use are derived from the noise levels measured from clean TOIs together with the calibration coefficients. The resulting noise level in the combined maps is therefore a consistency check of the relative calibration between detectors, since a mis-calibration would result in additional noise, given the slightly different scanning path and redundancies of the detectors.

In Fig. 2.12 we show the intensity maps constructed for each of the HFI frequencies, together with the number of TOI samples per pixel; and difference-maps built with the first and second half of each rings, both as the raw differences, and as differences scaled by the square root of the number of TOI samples to pre-whiten them.

The detector noise estimate used for the detector's data weighting is slightly different for the 2013 data release than for the previous release (Planck HFI Core Team 2011b). As a consequence, the pixel covariances we compute are now consistent with noise levels estimated from the difference maps built from the first and second half of the rings.

Figure 2.13 presents pseudo-spectra of the null test difference maps, computed with a 15 % Galactic mask for frequencies up to 353 GHz, or 40 % for the higher frequencies, combined with a point source mask derived from the *Planck* catalogue of compact sources (Planck Collaboration XXVIII 2014). We compare these spectra in Fig. 2.13 with those from the half-difference of the maps reconstructed from Surveys 1 and 2, properly normalized to compensate for the lower integration time. As illustrated previously, in Fig. 2.1, such differences are sensitive to, among other things, time variations in the gains. As they compare observations made with roughly opposite scan directions, they may also exhibit residuals in regions where the sky signal is intense, and large gradients due to imperfect deconvolution of time response (Planck Collaboration VI 2014). As a consequence, their spectra, shown as dashed lines in Fig. 2.13, are higher at low multipoles than those of the half-ring differences. The fact that both half-difference spectra are very close to each other at high multipoles for frequencies lower than 353 GHz is an indication that these differences provide an estimate of the high spatial-frequency part of the noise included in the HFI 2013 data release. For the sub-millimetre channels, both spectra present a significant ℓ variation, showing that they are contaminated by systematic residuals.

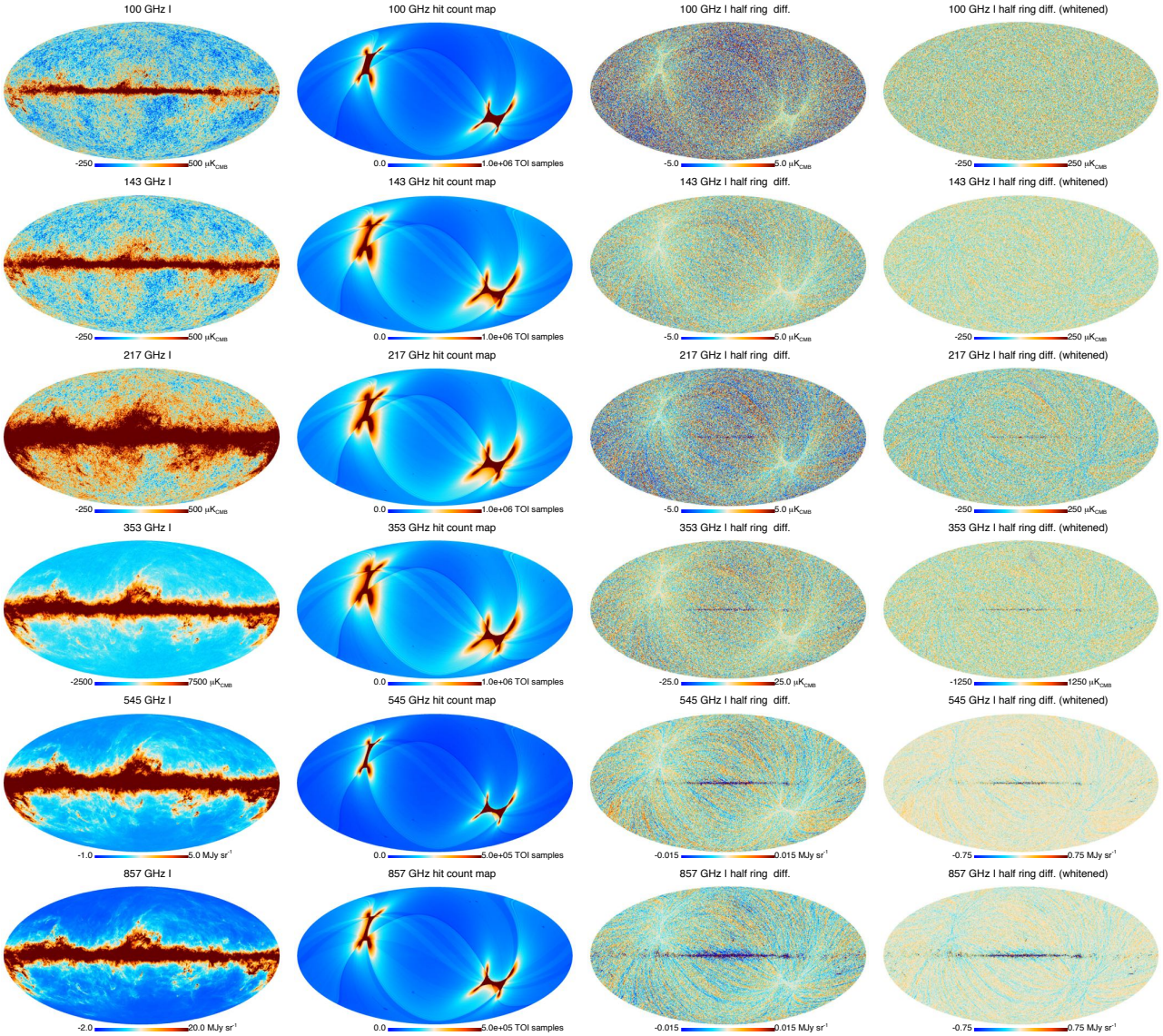

Figure 2.12: Signal (left), hit counts (second column) and half differences between maps built with only the first and second half of each ring (third column) for all HFI frequencies. The half ring differences are clearly correlated with the hit count maps. The last column shows the half-ring difference maps, scaled by the square root of the number of TOI samples, which largely removes this correlation.For the two highest frequencies, the differences show residual stripes and signal artefacts, at a low level (below 1 % of the sky signal). The difference maps have been degraded to *N*side=128 HEALPix resolution.

From these pseudo-spectra we estimate the noise level in the HFI maps by computing their average, after re-normalization by the sky coverage, in the ℓ range 100–6000. Using the averaged hit count per pixel, we convert these averages into an equivalent rms per TOI sample. We compare this estimate with two others: the rms of the half-ring map differences, properly whitened using the hit counts; and the averaged square-root of the variance computed in each pixel by the projection module, scaled to a dispersion per TOI sample using the averaged hit counts. These estimates are compared in Table 2.7. In general, they are in fair agreement for the three lowest frequencies, indicating that they are a good estimate of the noise level in the maps. At higher frequencies, however, signal residuals give a larger contributions. Therefore, such methods only provide an upper limit on the high-frequency noise in the maps.

2.5 Conclusions

In this paper we have presented the mapmaking and calibration procedures used for the *Planck* HFI data in the 2013 release. The calibrator for the CMB frequency data (100–353 GHz) is the solar dipole anisotropy as measured by *WMAP* (Hinshaw et al. 2009). This calibration is performed through a ring-by-ring template fit. Its limitations are largely a consequence of the non-ideal behaviour of the ADC from the bolometer read-out electronics. Tiny deviations from

Frequency [GHz]	Var. maps (a)	Diff. maps (b)	Spectra (c)	Units
100	1569	1546	1554	μK_{CMB}
143	777	775	826	μK_{CMB}
217	1109	1105	1212	μK_{CMB}
353	3671	3712	4101	μK_{CMB}
545	0.604	0.976	0.817	MJy sr^{-1}
857	0.695	2.58	0.920	MJy sr^{-1}

Table 2.7: Results of the three methods for deriving the TOI rms per sample from: (a) the variance maps; (b) the rms of the half ring difference maps; and (c) the pseudo spectra from Fig. 2.13 (as explained in the text) for each frequency. Units are μK_{CMB} for 100 to 353 GHz, and MJy sr^{-1} (νI_ν=constant) for the sub-mm channels. These results should be considered as rough estimates only. The higher the frequency, the larger are the contributions of systematics residuals in the half-differences, e.g., time constants and signal gradients.

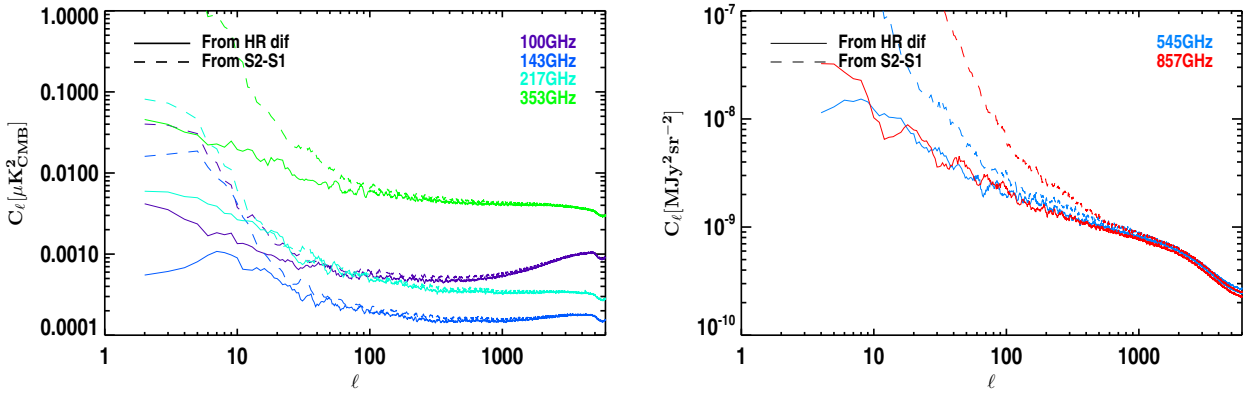

Figure 2.13: Pseudo-power spectra reconstructed from the half-differences between maps from the first and the second half of each ring (continuous lines) and the half-differences between maps restricted to Survey 1 and 2 (dashed lines) for, respectively, the dipole calibrated channels (right) and the sub-millimetre ones (right). These pseudo-spectra were computed using Galactic masks, removing 15 % ($\leq 353 GHz$) or 40 % of the sky (sub-mm channels), combined with the *Planck* point source mask. For high-frequency channels, power spectra are dominated by signal and destriping residuals, due to gradients inside the pixels, which are not scanned at exactly the same positions in the two data sets. In the survey differences, other systematics like time response, pointing drifts, and residual gain variations also induce larger residuals.

linearity in these devices cause apparent gain variation of the detector chain with time, which we have addressed using an effective gain correction, `bogopix`. We showed that this scheme reduces the apparent gain variation in time from 1–2 % to lower than 0.3 %, by studying the residuals of the map built for different time. Higher-order signal distortions induced by this systematic effect prevent us from using the more precise, orbital dipole-based calibration scheme presented in Tristram et al. (2011).

Correction for the ADC non-linearities should be made prior to any data reduction step. It requires precise measurements of each ADC response, which is currently taking place using data from the warm (4K) instrument. First tests of systematic corrections are also under way, with promising results. The time transfer functions used to deconvolve the data are derived from planets and galactic plane observations. These observations are not sensitive to time constant longer than 1s, that are observed by studying the thermal behaviour of the bolometers/bolometer plate system (Planck Collaboration II 2011). Such long time constant are shifting significantly the dipoles axis, and could thus affect the data at very low levels (below those of the ADC non-linearities correction), and contribute to the residual level of systematic inconsistencies observed in this paper.

The calibration for the 545 and 857 GHz channels is performed by comparing Uranus and Neptune flux densities with models of their emissivities. We had to switch to this scheme owing to apparent systematic effects in the FIRAS spectra we used in the HFI Early Data release. At those frequencies, time variations of the gain are lower than other systematic calibration uncertainties.

We revised our zero level-setting method, which now relies on the CIB monopole and the zero of the Galactic emission, defined as zero dust emission for a null HI column density.

At all frequencies, the statistical uncertainty of the calibration is negligible compared to the systematic uncertainty. The systematic uncertainty has been evaluated using several methods, presented in Sect. 2.4. We evaluated three types of systematic uncertainties:

(a) *Residual apparent variations of gains with time*. For the 100 to 217 GHz maps, we showed in Sect. 2.4.1 that, using `bogopix`, these variations were lower than 0.3 %, for each individual detector. As shown in Fig. 2.7 the

gain variations appear to be independent from one detector to the other, so such uncertainties should average out in the combined maps from this release. This 0.3 % uncertainty is therefore a conservative upper limit on the level of residual gain variations in the frequency maps. At higher frequencies, no estimation, nor correction for the apparent gain variation, is available. We choose to quote the level of variations we observed in the single detector measurements of `bogopix` at lower frequencies, which is 1 %; this is again an upper limit for combined maps. Given *Planck*'s scanning strategy, such uncertainties might be relevant for point-like sources studies, as these are observed in general once per survey, or globally when comparing sky maps from individual surveys.

(b) *Relative calibration uncertainties*, which should be used when combining different frequency maps, e.g., when reconstructing the SED of an object. We presented in Sect. 2.4.3 several methods to evaluate such uncertainties for 100 to 217 GHz channels. Both a direct comparison of pseudo-power spectra outside the Galaxy and results from the component separation method `SMICA` show that the inter-calibration between the 100, 143, and 217 GHz channels is better than 0.2 % (we keep the more conservative estimate, using `SMICA` for the reported errors). We complement these results with the upper limits extracted from `SMICA` at 353 and 545 GHz, using the central value (1 and 5%, respectively) as an upper limit on the uncertainty. For the relative calibration of the 857 GHz maps, we quote the 5 % uncertainty on the photometry used in the planet calibration.

(c) *Absolute calibration uncertainties* that should be considered when comparing with other data sets. This involves comparing *Planck* data with an external calibrator. Below 353 GHz, such uncertainties have been evaluated by two complementary approaches: reconstructing the dipole and comparing it with the *WMAP* measurements (Sect. 2.4.3); and evaluating the amplitude of residual dipoles in our maps, after foreground removal. From 100 to 217 GHz, both methods show consistency with *WMAP* at better than 0.3 %. The second approach shows agreement at 1 % for 353 GHz. As the data are calibrated on the *WMAP* dipole measurement, an additional uncertainty of 0.24% has to be combined with the HFI intrinsic uncertainties. Due to the nature of the calibrator, the absolute accuracies stated here only apply at very low ℓ. When studying smaller angular scale anisotropies, transfer functions, including that resulting from the - yet unaccounted for - very long time constants (see Section 2.3.1), should be taken into account.

Indeed the comparison of HFI with WMAP C_ℓ measurements at the level of the first and second peak show a discrepancy of 2.4 % in spectra, thus a possible calibration discrepancy of 1.2% (Planck Collaboration XVI 2014). Considering the relative calibration accuracy discussed above this must come from a common systematic effect on either the HFI CMB channels or on the WMAP V and W data, affecting the dipole calibrations and/or the transfer functions.

For the two highest frequencies, the absolute scale is limited by the accuracy of the planetary atmosphere models (5 %), combined with systematic uncertainties in our flux measurements (5 %), which results in a total uncertainty of 10 %. Such uncertainties are relevant for comparing *Planck* data with other data sets. When comparing with data sets sharing the same calibrator as HFI, the *WMAP* dipole or the planet models of Moreno (2010), the uncertainty on these calibrators should therefore be omitted in the comparison.

We summarize the calibration uncertainties for the HFI frequency maps in Table 2.8.

Frequency [GHz]	Time stability[a] [%]	Relative[b] [%]	Absolute[c] [%]	Model [%]
100	0.3	0.2	0.54	0.24
143	0.3	0.2	0.54	0.24
217	0.3	0.2	0.54	0.24
353	1.0	1.0	1.24	0.24
545	1.0	5.0	10.0	5.0
857	1.0	5.0	10.0	5.0

Table 2.8: Summary of the HFI systematic calibration uncertainties for the frequency maps of the 2013 data release. We indicate in the last column the uncertainties of the calibrators (*WMAP* dipole and models of planets) that are already included in the absolute uncertainties. These have to be taken into account when comparing with data sets relying on the same calibrators. (a) residual relative variation of calibration with time. (b) relative calibration uncertainty from one HFI channel to the other. (c) absolute calibration uncertainties of each HFI channel, including the uncertainty of the calibrators.

This work have been performed for the Planck-HFI collaboration. It has been presented in detail in many collaboration meetings and take advantage of interactions with the entire Planck collaboration.

Bibliography

Ashdown, M. A. J., Baccigalupi, C., Bartlett, J. G., et al. 2009, A&A, 493, 753
Cardoso, J., Martin, M., Delabrouille, J., Betoule, M., & Patanchon, G. 2008, IEEE Journal of Selected Topics in Signal Processing, 2, 735, special issue on Signal Processing for Astronomical and Space Research Applications
Górski, K. M., Hivon, E., Banday, A. J., et al. 2005, ApJ, 622, 759
Hinshaw, G., Weiland, J. L., Hill, R. S., et al. 2009, ApJS, 180, 225
Mather, J. C., Fixsen, D. J., Shafer, R. A., Mosier, C., & Wilkinson, D. T. 1999, ApJ, 512, 511
Moreno, R. 2010, Neptune and Uranus planetary brightness temperature tabulation. Tech. rep., ESA Herschel Science Center, available from ftp://ftp.sciops.esa.int/pub/hsc-calibration/PlanetaryModels/ESA2
Neugebauer, G., Habing, H. J., van Duinen, R., et al. 1984, ApJ, 278, L1
Perdereau, O. 2006, in CMB and Physics of the Early Universe
Planck HFI Core Team. 2011a, A&A, 536, A4
Planck HFI Core Team. 2011b, A&A, 536, A6
Planck Collaboration II. 2011, A&A, 536, A2
Planck Collaboration II. 2014, A&A, 571, A2
Planck Collaboration V. 2014, A&A, 571, A5
Planck Collaboration VI. 2014, A&A, 571, A6
Planck Collaboration VII. 2014, A&A, 571, A7
Planck Collaboration VIII. 2014, A&A, 571, A8
Planck Collaboration XII. 2014, A&A, 571, A12
Planck Collaboration XIV. 2014, A&A, 571, A14
Planck Collaboration XV. 2014, A&A, 571, A15
Planck Collaboration XVI. 2014, A&A, 571, A16
Planck Collaboration XXVIII. 2014, A&A, 571, A28
Tristram, M., Filliard, C., Perdereau, O., et al. 2011, A&A, 534, A88
Tristram, M., Macías-Pérez, J. F., Renault, C., & Santos, D. 2005, MNRAS, 358, 833
Yu, Q., Spergel, D. N., & Ostriker, J. P. 2001, ApJ, 558, 23

Chapter 3

Map-making for the 2015 release

extracted from Planck Collaboration VIII (2016)

"Planck 2015 results. VIII. High Frequency Instrument data processing: Calibration and maps"

For the 2015 release, we keep continue producing the maps at LAL for the Planck-HFI together with Olivier Perdereau. For each release (including the internal ones), we produced around 6500 maps from different set of Planck data (full or nominal mission, survey maps, half-ring or detsets maps, ...).
For the 2015 release, data were corrected with a first estimation of the ADC non-linearity in time-domain resolving for the apparent gain variation observed in 2013. However, residuals from ADC non-linear transfer function still induced a intensity-to-polarisation leakage that we corrected for, after map-making, using appropriate templates. I was in charge of the Planck map-making paper Planck Collaboration VIII (2016) which is copied in this chapter.

This chapter describes the processing applied to the cleaned, time-ordered information obtained from the *Planck* High Frequency Instrument (HFI) with the aim of producing photometrically calibrated maps in temperature and (for the first time) in polarization. The data from the entire 2.5-year HFI mission include almost five full-sky surveys. HFI observes the sky over a broad range of frequencies, from 100 to 857 GHz. To obtain the best accuracy on the calibration over such a large range, two different photometric calibration schemes have been used. The 545 and 857 GHz data are calibrated using models of planetary atmospheric emission. The lower frequencies (from 100 to 353 GHz) are calibrated using the time-variable cosmological microwave background dipole, which we call the orbital dipole. This source of calibration only depends on the satellite velocity with respect to the solar system. Using a CMB temperature of T_{CMB}=2.7255± 0.0006 K, it permits an independent measurement of the amplitude of the CMB solar dipole (3364.3±1.5 μK), which is approximatively 1σ higher than the *WMAP* measurement with a direction that is consistent between the two experiments. We describe the pipeline used to produce the maps of intensity and linear polarization from the HFI timelines, and the scheme used to set the zero level of the maps a posteriori. We also summarize the noise characteristics of the HFI maps in the 2015 *Planck* data release and present some null tests to assess their quality. Finally, we discuss the major systematic effects and in particular the leakage induced by flux mismatch between the detectors that leads to spurious polarization signal.

3.1 Introduction

Planck Collaboration VII (2016) describes how the time-ordered information (TOI) of each of the 52 bolometers is processed and flagged. Sampled at 5.544ms, the TOI is first corrected for the analog-to-digital converter (ADC) non-linearity, then it is demodulated and converted to the absorbed power with a simple non-linear bolometric correction. Glitches are flagged and glitch tails are removed from the TOI. Thermal fluctuations are removed on the 1 min timescale. Sharp lines in the temporal power spectrum of the TOI from the influence of the 4-K cooler are removed. Finally, the bolometer time response is deconvolved and the TOI is low-pass filtered. At this point, the TOIs are cleaned but not yet calibrated. The measurement of the beam is performed using a combination of observations of planets for the main beam and GRASP[1]

[1] TICRA, http://www.ticra.com/products/software/grasp

physical optics calculations for the sidelobes. The focal plane geometry, or the relative position of bolometers in the sky, is deduced from Mars observations.
This chapter describes how the prepared TOIs are used to make the calibrated maps for all *Planck* HFI bands. After a summary of the photometric definitions (Sect. 3.2), this paper gives a description of the main steps of the mapmaking processing, focusing on the changes made since the previous *Planck* releases (Planck Collaboration VI 2014; Planck HFI Core Team 2011). The major difference concerns the calibration (Sect. 3.3), which is now based on the orbital CMB dipole for the lower frequency channels (100, 143, 217, and 353 GHz, also called CMB channels) while the 545 and 857 GHz channels are photometrically calibrated using the signal from Uranus and Neptune. Section 3.4 explains the mapmaking upgrades, including the polarization treatment. Section 3.5 describes the maps, the solar dipole measurement, and the derivation of far sidelobes and zodiacal maps. Section 3.6 presents the noise characteristics and the null tests obtained by splitting the *Planck* HFI dataset into different groups based on ring period, time period, or detector sets. Consistency checks are performed in order to assess the fidelity of the maps. Finally, Sect. 3.7 is dedicated to the description of systematic effects, in particular in polarization. The major systematic residuals in *Planck* HFI data are due to the leakage from temperature to polarization induced by flux mismatch between associated bolometers. This is the result of either bandpass mismatch, or zero-level uncertainty, or calibration uncertainty. We present a first attempt to correct the maps for the intensity-to-polarization leakage. At lower frequencies, even after correction, the residuals are still higher than the noise level and thus the maps cannot yet be used for cosmological analysis.

3.2 Photometric equations

The power absorbed by a given detector at time t can be written as the sum of three terms corresponding to the first three Stokes parameters (I_p,Q_p,U_p) at the sampled pixel p of the beam-convolved sky,

$$P_t=G\Big[I_p+\rho\Big\{Q_p\cos2(\psi_t+\alpha)+U_p\sin2(\psi_t+\alpha)\Big\}\Big]+n_t, \tag{3.1}$$

where G encodes a photometric calibration factor, ρ is the detector polarization efficiency, ψ_t is the roll angle of the satellite, α is the detector polarization angle, and n_t represents all the noise contributions to the absorbed power (photon noise, phonon noise, glitch residuals, etc.). The polarization efficiency is derived from the cross-polarization coefficient η through $\rho=(1-\eta)/(1+\eta)$. It allows us to describe spider-web bolometers (SWB, $\rho\approx0$) as well as polarization-sensitive bolometers (PSB, $\rho\approx1$). According to the bolometer model and given the stability of the HFI operational conditions during the mission, the gain G is expected to be constant over the whole mission (see Sect. 1 of Planck Collaboration VII (2016)) once the bolometer non-linearities have been corrected.
For an axisymmetric beam response, the "smearing" and "pointing" operations commute, and one can solve directly for the pixelized beam-convolved map,

$$\begin{aligned} P_t &= G(1,\rho\cos2(\psi_t+\alpha),\rho\sin2(\psi_t+\alpha))^{\dagger}\cdot\Big(I_p,Q_p,U_p\Big)+n_t \\ &\equiv G\times A_{tp}T_p+n_t, \end{aligned} \tag{3.2}$$

where the direction of observation at the time t, (θ_t,ϕ_t), falls into pixel p and we define the map-pointing matrix A and the sky signal $\mathbf{T}=(I,Q,U)$.

3.3 Calibration

The bolometer signal measured through current-biasing is proportional to the small variation in the incoming power from the sky. To express the measurement in sky temperature units, one has to determine a gain per detector based on a known source in the sky. For the HFI low-frequency channels (100 to 353 GHz), we use the CMB orbital dipole as a primary calibrator. This signal fills the entire beam and is almost insensitive to the beam profile and only marginally affected by pointing errors, while its signal-to-noise is high enough thanks to the full-sky coverage. Moreover, it is a stronger signal than CMB anisotropies (by a factor of around 10), but not bright enough to cause non-linearities in the detectors, and has the same electromagnetic spectrum as the anisotropies. At higher frequencies (545 and 857 GHz), calibration is performed on planets.

3.3.1 CMB dipole conventions

The CMB dipole is induced by the Doppler effect of the relative motion of the satellite with respect to the CMB frame,

$$T_{\rm Doppler}(t,\hat{\mathbf{u}})=\frac{T_{\rm CMB}}{\gamma_t(1-\beta_t\cdot\hat{\mathbf{u}})}, \tag{3.3}$$

where $\beta_t=\mathbf{v}_t/c$ and $\gamma_t=(1-\beta_t^2)^{-1/2}$, $\mathbf{v}_t$ is the satellite velocity at time t, and $\hat{\mathbf{u}}$ is the unit vector along the line of sight.
The solar system motion with respect to the CMB frame, giving rise to what is referred to as the solar dipole, is the dominant component of the satellite velocity. A residual contribution (called the orbital dipole) is induced by the yearly

motion of the satellite with respect to the solar system barycentre. The solar dipole can be considered as sky-stationary during the observations and is thus projected onto the sky as an ℓ=1 component with amplitude previously measured by COBE and *WMAP*, 3355±8 μK (Hinshaw et al. 2009). Relativistic corrections to the solar dipole produce second-order anisotropies at multipoles $\ell \geq 1$ with amplitudes proportional to β^ℓ and, more importantly, couple the two dipole components, as will be discussed below. Although the orbital dipole velocity is typically an order of magnitude lower than the solar dipole, it is time dependent and its time-variability is precisely determined by the satellite velocity, which is known at the level of 10^{-4}km s^{-1}. Finally, to calibrate in temperature, we only rely on an external measurement of the CMB absolute temperature. We use T_{CMB}=2.7255 K (Fixsen 2009).
The expansion of Eq. (3.3) in β gives

$$\Delta(\hat{\mathbf{u}}) = \frac{T_{\rm Doppler}}{T_{\rm CMB}} - 1 \approx \beta\cdot\hat{\mathbf{u}} - \frac{\beta^2}{2} + (\beta\cdot\hat{\mathbf{u}})^2 + O(\beta^3). \tag{3.4}$$

If we decompose the velocity into a *solar* boost β_1 and an *orbital* boost β_2 then

$$\Delta = \Delta_1 + \Delta_2 - \beta_1\cdot\beta_2 + 2(\beta_1\cdot\hat{\mathbf{u}})(\beta_2\cdot\hat{\mathbf{u}}) + O(\beta^3), \tag{3.5}$$

where the first term corresponds to the solar dipole, the second term is the orbital dipole, and the third and fourth terms show the coupling between each term due to relativistic corrections.

3.3.2 Absolute calibration on orbital dipole

The calibration algorithm takes advantage of the orbital dipole not being fixed on the sky, unlike the solar dipole (during the length of the mission). In practice, relativistic corrections and second order in the development of the conversion from I_ν to T_{cmb} couple solar and orbital dipoles creating an additional non-stationary signal, which also depends on the frequency. We use the total CMB dipole computed using Eq. (3.3) as the calibration reference signal, assuming that it has the same scaling with frequency as the higher multipole CMB anisotropies. This approximation will leave in the HFI frequency maps the frequency dependent fraction of the kinematic quadrupole arising from the second-order term in the β expansion described in Kamionkowski & Knox (2003) and Quartin & Notari (2015). The amplitude of the kinematic quadrupole is expected to be lower than 0.5% on the CMB-calibrated *Planck*-HFI channels. However, it is not directly correlated to the orbital dipole on which we calibrate the data. Thus, we expect the systematic error induced on the gain estimation to be much smaller.
The orbital dipole signal is modulated on a one-year period. To take into account the time variation of this signal, we need to add a term in Eq. (3.2),

$$\mathbf{P} = G\times(\mathsf{A}\mathbf{T} + \mathbf{t}_{\rm orb}) + \mathbf{n}, \tag{3.6}$$

where $\mathbf{t}_{\rm orb}$ is the time-dependent orbital dipole signal, while in this formula the solar dipole is part of the sky signal $\mathbf{T}$. We note that we can arbitrarily set all or part of the solar dipole signal either in the calibration template or in the sky without changing the resulting gain estimation.
Since $\mathbf{t}_{\rm orb}$ is known, we can solve Eq. (3.6) for each bolometer independently, rewriting the system as

$$\mathbf{P} = \mathsf{A}\tilde{\mathbf{T}} + G\mathbf{t}_{\rm orb} + \mathbf{n}, \tag{3.7}$$

where the unknowns are the sky-signal in absorbed power units $\tilde{\mathbf{T}}$ and the gain G. The calibration problem is thus linear and can be solved directly. The maximum-likelihood estimate of the gain G is obtained by combining all available samples using the noise covariance matrix $\mathsf{N} = \langle n^\dagger n \rangle$ and marginalizing over $\tilde{\mathbf{T}}$, solving the equation

$$\left(\mathbf{t}_{\rm orb}^{\rm T}\mathsf{N}^{-1}\mathsf{Z}\mathbf{t}_{\rm orb}\right)\times G = \mathbf{t}_{\rm orb}^{\rm T}\mathsf{N}^{-1}\mathsf{Z}\mathbf{d}, \tag{3.8}$$

where $\mathbf{d}$ is the vector of input data P_t and we define

$$\mathsf{Z} = \mathsf{I} - \mathsf{A}\left(\mathsf{A}^{\rm T}\mathsf{N}^{-1}\mathsf{A}\right)^{-1}\mathsf{A}^{\rm T}\mathsf{N}^{-1}. \tag{3.9}$$

In practice, the noise is treated by assuming that the destriping reduces the matrix N to a diagonal one once the data $\mathbf{d}$ have been corrected for a constant offset (see Sect. 3.4.2). For the HFI, the mapmaking problem is degenerate for the reconstruction of polarization if we solve for a single detector at a time. Neglecting polarization in Eq. (3.8) for polarization-sensitive detectors biases the calibration solution. Moreover, we need a very accurate relative calibration between detectors that are combined to reconstruct polarization in order to minimize leakage from intensity to polarization (see Sect. 3.7.3). For this reason, for the *Planck* 2015 release we have extended the algorithm described in Tristram et al. (2011) to perform a multi-detector gain estimation for all bolometers at a given frequency together with the offsets (see Sect 3.4.2).

3.3.3 Long time-constant residuals

The observation strategy of Planck results in the path across a particular part of the sky being almost reversed six months later. As described in Planck Collaboration VII (2016), we take advantage of this to derive the time transfer function below one second. Nevertheless, longer time responses (larger than the second), even with low amplitudes, may bias the calibration estimation by distorting the dipole signal and causing some leakage of the solar into the orbital dipole. To take into account the systematic residuals after time-constant deconvolution into account, we built a simplified model describing a pure single-mode sinusoidal dipole signal (including solar and orbital dipole) convolved with an exponential decay in the time domain. In the frequency domain, this reads

$$\mathcal{T}_{\rm dip}=\mathcal{F}\left(t_{\rm dip}*Be^{-t/\tau}\right)=\frac{B}{1/\tau+2i\pi\nu}\delta_{\nu,\nu_{\rm spin}}, \tag{3.10}$$

where B and τ are the amplitude and the time constant, and $\nu_{\rm spin}$ is the spin frequency; $\mathcal{T}_{\rm dip}$ is a complex coefficient, the real part of which corresponds to the relative change in the gain G, while the imaginary part corresponds to the amplitude of the dipole mode shifted by 90°.

In practice, prior to the absolute calibration, we solve for the amplitude of a shifted-dipole template using single detector calibration,

$$\mathbf{P}=\mathbf{A}\tilde{\mathbf{T}}+G\mathbf{t}_{\rm dip}+C\mathbf{t}_{\rm dip}^{90^\circ}+\mathbf{n}, \tag{3.11}$$

where C gives the amplitude of the dipole mode shifted by 90°. With this toy model, we cannot reconstruct the amplitude and the time constant because we only fit for one coefficient C, but we trace the systematic effect on the dipoles due to the very long time response. Once the coefficient C has been determined, we correct the data for $C\mathbf{t}_{\rm dip}^{90^\circ}$ to account for this additional shifted mode coming from the residual time constant.

The effect on the gain G depends on the unknown value of the time constant τ. Figure 3.1 shows the impact on the gains for each bolometer when including the shifted-dipole correction. At higher frequencies (353 GHz and above), the signal is no longer dominated by a dipole and cannot be approximated by the model described above. For the 2015 release, we do not include any correction for time constant residuals in the mapmaking for those channels.

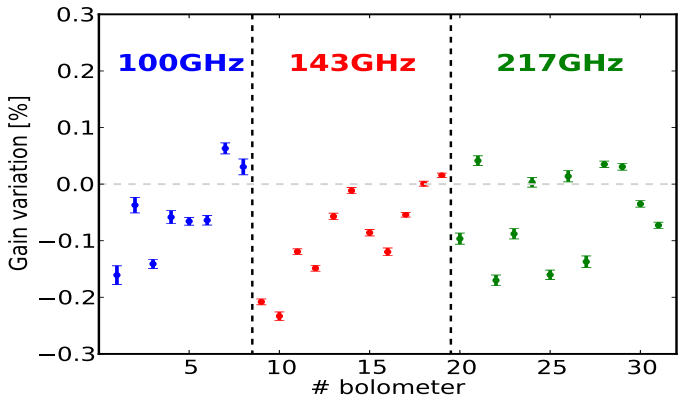

Figure 3.1: Effect on the gains when including the model for long time constant residuals.

3.3.4 Submillimetre calibration

Mars, Jupiter, Saturn, Uranus, and Neptune are all observed several times during the full length of the mission. The submillimetre channels of HFI (545 and 857 GHz) are calibrated on models of Uranus and Neptune. We do not use Jupiter and Saturn observations for calibration since both planets have strong absorption features at those frequencies, which complicate comparison with broadband measurements. The flux from Jupiter also leads to detector saturation at the highest HFI frequencies. Similarly, we choose not to use Mars as a calibrator because strong seasonal variations complicate the modelling.

Various methods are used to derive planet flux densities, including aperture photometry and point-spread function (PSF) fits. Planet measurements with *Planck* are studied fully in Planck Collaboration LII (2016). We focus here on calibration using aperture photometry in the time-ordered data from the submillimetre channels. The simulation pipeline used for the main beam reconstruction computes the reconstruction bias and the error budget (the mean and the variance) for each planet observation. The comparison of flux measurements of Neptune and Uranus with up-to-date models provides the calibration factors at 545 and 857 GHz.

Planet models

We use the ESA 2 model for Uranus and the ESA 3 model for Neptune (Moreno 2010). Both models quote absolute uncertainties of 5 %. Planet model spectra are produced from their modelled brightness temperatures using the planet solid angles at the time of observation and integrated under the individual 545 and 857 GHz bolometer bandpasses. Flux densities are colour-corrected to a reference spectrum defined by a constant νI_ν law so as to be directly comparable to HFI flux density measurements.
Planck Collaboration LII (2016) gives a detailed account of the ratio between the expected planet fluxes and the measured values at all HFI frequencies and for the five observed planets (Mars, Jupiter, Saturn, Uranus, and Neptune). They all fall within the 5 % model uncertainty range. This is a validation of the models at 100–353 GHz. Hence the models can be used with some confidence to calibrate the 545 and 857 GHz channels.

Aperture photometry in the timelines

We select all samples in a 2°×2° box around the planet positions and build time-ordered vector objects (hereafter timelines) for each bolometer and each planet scan. We use the first four scans of Neptune and Uranus (season 1 to 4). We build corresponding background timelines using all the samples in a 2°×2° box around the planet position when the planet is not there. The resulting background has a much higher spatial density than the planet timelines. We use this to build a background mini-map with 2′×2′ pixels that can then be interpolated at each sample position in the planet timelines in order to remove a local background estimate (see Appendix B in Planck Collaboration VII (2016) for details).
The aperture photometry measurement procedure applied to our planet timelines is an extension of the usual aperture photometry approach to irregularly gridded data. Flux is integrated in an aperture of radius 3 times the effective FWHM. Typically, aperture photometry is applied to maps of fixed-size pixels, which means integrating the flux in the aperture is equivalent to summing the pixel values. In our case, we have to take into account the inhomogenous spatial distribution of the samples. To do this we assume that the beam products perfectly describe the spatial light profile of Neptune and Uranus, and compute a spatial sampling correction factor as the ratio of the integrated flux in a highly spatially oversampled beam and the integrated flux in a beam sampled on the planet timelines. This sampling correction has to be computed for each bolometer and planet crossing, because the spatial sampling varies between planet observations. We estimate the statistical uncertainty of the measurements as the standard deviation of the samples in an annulus of radius 3 to 5 times the effective FWHM of the beam.
We find large variations between the individual planet measurements in each detector and at each season of the full mission survey (Fig. 3.2) which we attribute to the underestimation of the measurement uncertainty. The signal from Neptune and Uranus is not expected to vary in time apart from the differences in solid angle which are very small and already taken into account. While accurately corrected by the timeline aperture photometry algorithm presented here, the limited available spatial sampling of the planet signal at these frequencies could explain part of the variations. We therefore decided to include the seasonal rms of the measurements (we have four observations per bolometer per planet) in the measurement uncertainty.

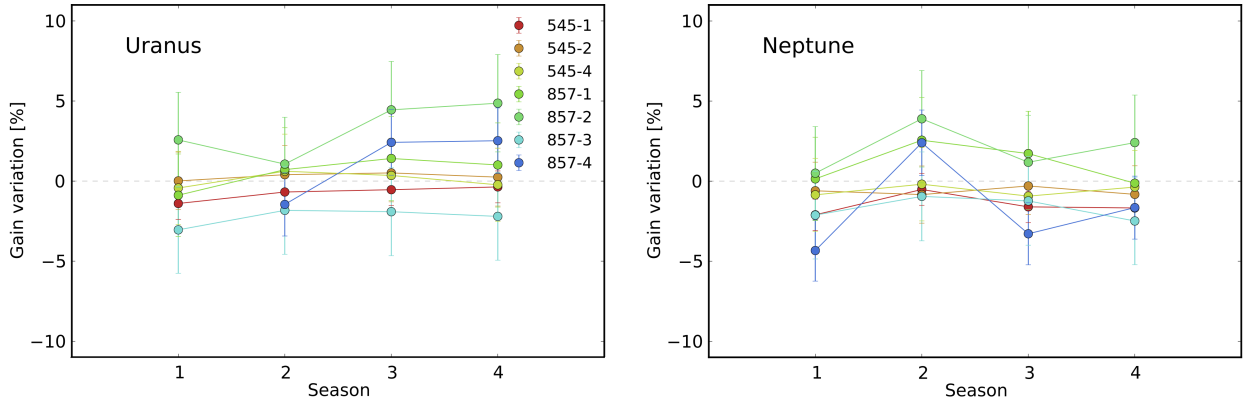

Figure 3.2: Dispersion of the planet-derived calibration factor per season around the planet calibration estimates for Uranus (*left*) and Neptune (*right*).

The averaged calibration factors for each detector for each planet are in very good agreement. The final calibration factors are the means of both planet estimates. We compare them to the 2013 *Planck* release in Fig. 3.3: the calibration factors changed by 1.9 and 4.1 % at 545 and 857 GHz, respectively, which is within the planet modelling uncertainty. Combined with other pipeline changes (such as the analog-to-digital converter non-linearity corrections), the 2015 frequency maps have decreased in brightness by 1.8 and 3.3 % compared to 2013.
Calibration uncertainties are given in Table 3.1. In order to produce the frequency maps, detectors are weighted by their inverse noise variance. We use the same weights to compute the corresponding calibration errors. We estimate combined statistical errors of 1.1 % and 1.4 % at 545 and 857 GHz, respectively, to which one should add linearly (as should be done

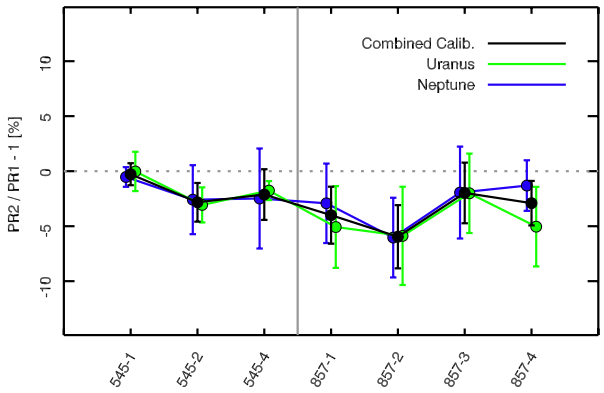

Figure 3.3: Comparison of the 2015 *Planck* release calibration to the 2013 release. We show the relative difference in percent per bolometer for Uranus (green), Neptune (blue), and both calibrators combined (black).

for systematics) the 5 % uncertainty arising from the planet models. Errors on absolute calibration are therefore 6.1 and 6.4 % at 545 and 857 GHz, respectively. Since the reported relative uncertainty of the models is of the order of 2 %, we find the relative calibration between the two HFI highest frequency channels to be better than 3 %.

Bolometer	Uncertainty Stat.	Uncertainty Syst.
545-1	1.0 %	5.0 %
545-2	1.8 %	5.0 %
545-4	2.3 %	5.0 %
857-1	2.6 %	5.0 %
857-2	2.9 %	5.0 %
857-3	2.8 %	5.0 %
857-4	2.0 %	5.0 %

Table 3.1: Uncertainties in the planet-derived calibration factor for each bolometer. The systematic uncertainty is the absolute uncertainty of the planet model.

3.4 Mapmaking

3.4.1 Summary

Each data sample is calibrated in K_{CMB} for the 100, 143, 217, and 353 GHz channels, or MJy sr^{-1} (assuming a constant νI_ν law) for the 545 and 857 GHz channels, using the calibration scheme described above. The bolometer gains are assumed to be constant throughout the mission, which was not the case for the 2013 release. The *Planck* total dipole (solar and orbital) is computed and subtracted from the data.

As in the *Planck* 2013 release, we average the measurements for each detector in each pixel visited during a stable pointing period (hereafter called a ring) while keeping track of the bolometer orientation on the sky. The subsequent calibration and mapmaking operations use this intermediate product as input. The calibrated TOIs are only modified by a single offset value per ring and per detector. The offsets are determined with the destriping method described in Tristram et al. (2011). Here, the size of the pixels where the consistency of different rings is tested is 8′ (N_{side}=512). Maps in intensity and polarization are used to assess the consistency of the destriper solution. The offsets are simultaneously determined for all bolometers at a given frequency using the full mission data. For all the maps produced using a given bolometer, the same offset per ring is used (except in the case of half-rings, see below).

The products of the HFI mapmaking pipelines are maps of I, Q, U together with their covariances (II, IQ, IU, QQ, QU, UU), pixelized according to the HEALPix scheme (Górski et al. 2005). The map resolution is N_{side}=2048, and the pixel size is 1.′7. The mapmaking method is a simple projection of each unflagged sample to the nearest grid pixel. In the case of polarization data with several detectors solved simultaneously, the polarization equation is inverted on a per-pixel basis (see Sect. 3.4.2). For each sky map, a hit count map is computed (number of samples per pixel; one sample has a duration of 5.544ms).

The zodiacal light component, which varies in time, is estimated using templates fitted on the survey-difference maps (see Sect. 3.5.4). We provide maps without zodiacal light for which these templates are systematically subtracted from the data of each bolometer prior to the mapmaking.

Unlike in the 2013 release, the far sidelobes are not removed from the maps. At most, this leaves residuals of the order of 0.5–1.5 μK in the 100–353 GHz maps with uncertainties on the residuals of roughly 100 % (Planck Collaboration VII 2016). At higher frequencies, Galactic pick-up from the far sidelobes produces significant residuals in about half of the detectors of the order of 0.03 MJy sr^{-1} at 545 and 0.3 MJy sr^{-1} at 857 GHz (see Planck Collaboration X 2016). The total solid angle in the spillover is a better known quantity, and we describe the effect of the far sidelobes on the calibration in Sect. 3.5.3.

3.4.2 Mapmaking method

In the same way as in Planck Collaboration VIII (2014), we use a destriping algorithm to deal with the HFI low-frequency noise. In this approach, the noise in a ring r is represented by an offset, denoted o_r, and a white noise part n, which is uncorrelated with the low-frequency noise. For a given bolometer, we can write Eq. (3.6) as

$$P_t = G\times(A_{tp}T_p + t_{\rm orb}) + \Gamma_{tr}o_r + n_t, \tag{3.12}$$

where Γ_{tr} is the ring-pointing matrix (which associates the data sample t with the ring number r). The unknowns are the gain G, the offsets for each ring o_r, and the sky signal for each pixel $T_p=(I_p,Q_p,U_p)$. As there is a degeneracy between the average of the offsets and the zero level of the maps, we impose the constraint $\langle o_r\rangle=0$. The absolute zero level of the maps is determined as described in Sect. 3.4.4.

For the production of the maps for the 2015 HFI data release, we first build the rings for all detectors. We apply the following frequency-dependent processing to these compressed data sets.

For CMB frequencies (100, 143, and 217 GHz) channels we proceed as follows:

1. we estimate a first approximation of the orbital dipole gain together with the offsets and the amplitude of the long-time-constant residuals for each bolometer independently, neglecting the polarization signal;
2. we then derive the gains and offsets for a fixed amplitude of the long-time-constant residuals using the multi-bolometer algorithm.

At 353 GHz, the long-time-constant residuals are more difficult to constrain. They are driven more by Galactic emission drifts than by the dipole, which dominates at lower frequencies, so that the model described in Sect. 3.3.3 is not relevant. Hence for this frequency we use a simpler pipeline without a long-time-constant residuals template:

1. we estimate the orbital dipole gain together with the offsets for each bolometer independently, neglecting the polarization signal;
2. we then estimate the final offsets using a destriping procedure for all bolometers at this frequency.

For the two highest frequencies, at 545 and 857 GHz, the pipeline is considerably different because we use the planets (Uranus and Neptune) as calibration sources:

1. we estimate a first approximation of the offsets for each bolometer independently;
2. we derive the gains from the planet flux comparison;
3. we then estimate the final offsets with a destriping procedure for all bolometers at a given frequency.

Finally, using the pre-computed gains and offsets, we project the ring data onto maps for each data set. For polarization, we invert the 3×3 system derived from Eq. (3.12) for each pixel independently with the criterion that the condition number be lower than 10^3,

$$\mathbf{T} = \left(\mathsf{A}^{\rm T}\mathsf{N}^{-1}\mathsf{A}\right)^{-1}\mathsf{A}^{\rm T}\mathsf{N}^{-1}\mathbf{d}, \tag{3.13}$$

where $\mathbf{d}$ are the calibrated, cleaned ring data (offsets and orbital dipole removed) $\mathbf{d}=(\mathbf{P}-\Gamma\mathbf{o})/G-\mathbf{t}_{\rm orb}$. We note that we use HEALPix (not IAU) conventions for the sign and normalization of the Q and U Stokes parameters.

For destriping, we use the same tool as before, `polkapix`, which was thoroughly validated in Tristram et al. (2011). Maps are built by simple co-addition in each pixel of the destriped, calibrated, and time-varying component-subtracted signal. We subtract the CMB dipole as measured by *Planck* (see Sect. 3.5.1).

We introduced the following modifications with respect to Planck Collaboration VIII (2014):

- we included polarization in the destriping for the channels that include polarization-sensitive bolometers;
- we enlarged the masked fraction of the sky from 10 to 15 %, based on Galactic emission, to avoid signal gradients leaking into offsets;
- to improve the offset accuracy, we computed one set of offsets combining all detectors, using full-mission data, and used them for all derived maps involving these detectors.

This last change induces a small noise correlation between detector-set maps (see Sect. 3.6.5). In 2013 we computed independent offsets for each detector or detector set, including the full mission.

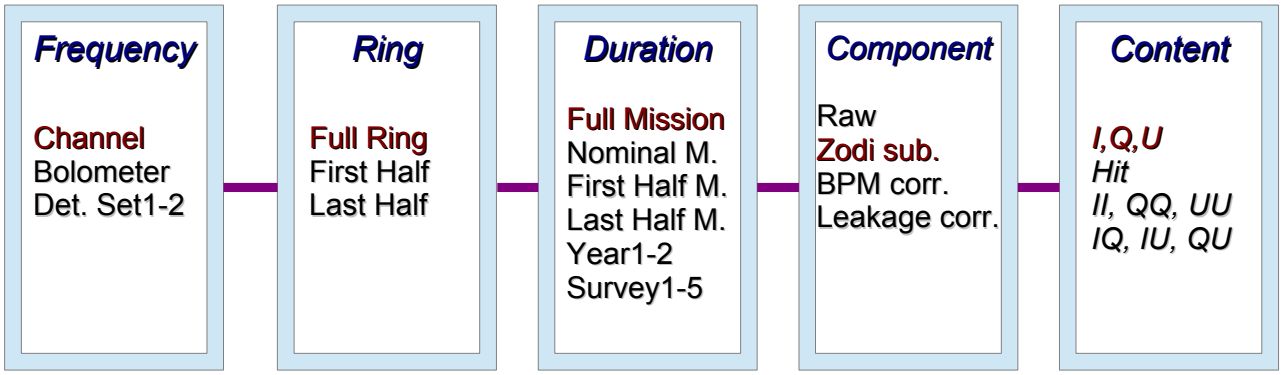

Figure 3.4: Map matrix. The HFI maps are released in different flavours. Not all combinations are released, but any map will correspond to a choice of lines in each box. The *Frequency* box is related to the use of all detectors at a given frequency (Channel), or individual bolometers, or sets of detectors. The *Ring* box is a way of splitting (or not) the data in equal halves at the ring level. The *Duration* box indicates the different ways of splitting data between surveys: years, full or nominal mission, first half mission, or last half mission. The *Component* box indicates the systematic corrections that can be applied at the map level. The recommended first choice map is highlighted in red.

3.4.3 Map products

The principal HFI final product consists of six maps that cover the six frequencies (100–857 GHz) for the full mission in intensity at high resolution ($N_{\rm side}$=2048). However, many more maps are needed to assess the noise and the consistency of the data. Figure 3.4 summarizes the various splits produced.
Maps from different halves of each ring period (first and last) are computed independently of each other, including the offset per half-ring. Thus, half-ring half-difference maps can give a quick account of the noise level in the maps.
For each frequency, we also produce temperature and polarization maps using detector sets (each set including four polarization-sensitive bolometers). In addition, we produce a temperature map for each spider-web bolometer.
The *Planck* scanning strategy samples almost all the sky pixels every six months, with alternating scan directions in successive six-month periods. The full cold HFI mission encompasses five surveys, each covering a large fraction of the sky. Surveys 1–2 and 3–4 are paired to produce Year 1 and Year 2 maps. Maps are produced for the full-mission dataset together with the survey, year, and half-mission maps. Each map is associated with a hit-count map and variance maps (II; and QQ, UU, IQ, IU, and QU when polarization is reconstructed). Overall, a total of about 6500 sky maps have been produced. We have used this data set to evaluate the performance of the photometric calibration by examining difference maps (see Sect. 3.6.2).

3.4.4 Zero levels

Planck-HFI cannot measure the absolute sky background. The mapmaking procedure does not change the mean value of the input TOI. We therefore adjust the monopole on the maps a posteriori in a similar manner to the method used in Planck Collaboration VIII (2014), which relies on external datasets. To achieve this, we need to take into account two major components of the monopole:

1. Galactic dust emission: we estimate the brightness in the HFI single-detector maps that corresponds to zero gas column-density (i.e. zero Galactic dust emission) by using the H I column density, which is assumed to be a reliable tracer of the Galactic gas column-density in very diffuse areas (see Planck Collaboration VIII 2014, Sect. 5.1). The offsets derived are then subtracted from each detector's data in the processing.
2. Extragalactic emission: the cosmic infrared background (CIB) monopole is taken into account by adding the levels from Béthermin et al. (2012) to the maps (see Table 3.6).

The sum of the two offsets is appropriate for total emission analysis. For Galactic studies, only the Galactic zero level has to be set which can be achieved by subtracting the CIB levels (Table 3.6) from the released maps. Unlike the previous release, in the 2015 maps the zero-level correction (both CIB and Galactic) has been applied.
Zodiacal light has not been accounted for in this procedure. The correction to be applied at each frequency to set the Galactic zero level using zodiacal-light-corrected maps are given in Table 3.6.

3.4.5 Polarization efficiency and orientation

The *Planck*-HFI bolometers were characterized on the ground before launch. Rosset et al. (2010) reported pre-flight measurements of the polarization efficiency of the HFI polarization-sensitive bolometers with an accuracy of 0.3 %. The

absolute orientation of the focal plane was measured at a level better than 0.°3. The relative orientation between bolometers is known with an accuracy better than 0.°9.
Spider-Web Bolometers are much less sensitive to polarization. Nonetheless, we take into account their polarization efficiency, which is between 1 and 9 %, although their orientations have been less accurately determined (errors can be up to a few percent), as described in Rosset et al. (2010).

3.5 HFI temperature and polarization maps

3.5.1 Solar dipole measurement

Frequency [GHz]	Threshold [MJy sr^{-1}]	d [μK]	lon [°]	lat [°]
100	2	3364.81±0.06	263.921±0.002	48.2642±0.0008
100	3	3364.76±0.05	263.922±0.002	48.2640±0.0006
100	4	3364.99±0.04	263.928±0.002	48.2631±0.0006
143	2	3364.05±0.03	263.908±0.001	48.2641±0.0004
143	3	3363.72±0.02	263.903±0.001	48.2653±0.0003
143	4	3363.39±0.02	263.905±0.001	48.2668±0.0003

Table 3.2: CMB solar dipole measurements for the 100 and 143 GHz channels estimated for different sky coverage levels (37, 50, and 58 %) corresponding to three thresholds in 857 GHz amplitude (2, 3, and 4 MJy sr^{-1}). Uncertainties include only statistical errors. Systematic errors are 0.8 μK for the amplitude, and (0.°024, 0.°0034) in Galactic (longitude, latitude).

The ℓ=1 mode of CMB anisotropy is unique in that its amplitude is dominated by a large component associated with our motion with respect to the CMB rest frame. In this section, we present the CMB solar dipole results based on *Planck*-HFI maps at the two lowest frequencies, 100 and 143 GHz. Low-frequency maps are dominated by CMB over a large fraction of the sky. Nevertheless, the inhomogeneous nature of the dust emission can bias CMB solar dipole estimates.
We cleaned the Galactic emission from the HFI maps using a local correlation with the 857 GHz map. We model each HFI map I_ν as

$$I_\nu - C = qI_{857} + D_{\rm res}, \tag{3.14}$$

where C is the CMB anisotropy (here we use the SMICA map, Planck Collaboration IX 2016, from which we remove any residual dipole component) and I_{857} is the *Planck* 857 GHz map that is assumed to have a negligible contribution from the solar dipole.[2] The term $D_{\rm res}$ includes the dipole and any systematic effects from both I_{857} and I_ν. In bright regions of the sky, $D_{\rm res}$ also contains extra emission that is uncorrelated or only partially correlated with I_{857}, for instance free-free emission or CO.
In order to capture any spatial variations of the dust spectral energy distribution (SED), we estimated q and $D_{\rm res}$ on an $N_{\rm side}$=64 grid. For each $N_{\rm side}$=64 pixel, we performed a linear regression of the $N_{\rm side}$=2048 pixels of I_ν vs I_{857}, assuming a constant dust SED over a 55′ area. We then fit for the dipole amplitude and direction in $D_{\rm res}$ using sky pixels where I_{857}<2, 3, or 4 MJy sr^{-1} (corresponding to 37, 50, or 58 % of the sky respectively) to limit the effect of Galactic-emission residuals (CO, free-free emission, and small-scale dust SED variations).
The results are given in Table 3.2. We measure a solar system peculiar velocity of 370.06±0.09 km s^{-1} with respect to the CMB rest frame. We use the CMB temperature from Fixsen (2009) (2.7255±0.0006 K) to convert that measurement into a CMB dipole measurement.
The error bars here only include statistical uncertainties, which are very low thanks to the *Planck*-HFI signal-to-noise ratio. We evaluate the additional systematic uncertainties from the variation of the results between independent bolometer maps. For the amplitude, the peak-to-peak variation between bolometers and combined maps is ±0.8 μK at 100 and 143 GHz. Variations with sky coverage are of the same order. We note that the uncertainty from the FIRAS temperature should be added to the budget (±0.74 μK). For the coordinates, we found variations of ±0.°013 in longitude and ±0.°0019 in latitude. These differences are observed when comparing results at different frequencies, and are likely to result from uncertainties in the foreground subtraction. This is also consistent with the magnitude of the direction shifts we observe when changing the sky fraction.
As an independent check, we also produce a cleaned CMB map using an internal linear combination (ILC) method. We used the HFI maps at 100, 143, and 217 GHz smoothed with a 1° FWHM Gaussian kernel. We note that smoothing the data with a 1° kernel reduces the solar dipole in the maps by 0.005 %, i.e. 0.2 μK, which we corrected for afterwards. We then estimate the solar dipole amplitude and direction using a Galactic mask that removes less than 15 % of the sky to avoid the inner Galactic plane where the residuals are most intense. The measurement is compatible with the results in Table 3.2.

[2] The amplitude of the solar dipole at 857 GHz is 0.0076 MJy sr^{-1}. At least 90 % of this is removed in the mapmaking process, leaving a residual that is well below the noise level and any systematic effects.

In the end, the amplitude (d) and direction (Galactic longitude, latitude) of the solar dipole measured by *Planck*-HFI is

$$\begin{aligned} d &= 3364.29\pm0.02(\mathrm{stat})\pm0.8(\mathrm{sys})\pm0.74(\mathrm{FIRAS})\ \mu\mathrm{K} \\ \begin{pmatrix} \mathrm{lon} \\ \mathrm{lat} \end{pmatrix} &= \begin{pmatrix} 263.^{\circ}914 & \pm0.^{\circ}001\ (\mathrm{stat}) & \pm0.^{\circ}013\ (\mathrm{sys}) \\ 48.^{\circ}2646 & \pm0.^{\circ}0003(\mathrm{stat}) & \pm0.^{\circ}0019(\mathrm{sys}) \end{pmatrix} \end{aligned}$$

This is to be compared to the official *Planck* solar dipole measurement obtained in combination with the *Planck*-LFI:

$$\begin{aligned} d &= 3364.5\pm2.0\ \mu\mathrm{K} \\ \begin{pmatrix} \mathrm{lon} \\ \mathrm{lat} \end{pmatrix} &= \begin{pmatrix} 264.^{\circ}00\pm0.^{\circ}03 \\ 48.^{\circ}24\pm0.^{\circ}02 \end{pmatrix} \end{aligned}$$

Compared to the *WMAP* five-year results (d,lon,lat)=(3355±8μK,263.$^{\circ}$99±0.$^{\circ}$14,48.$^{\circ}$26±0.$^{\circ}$03; Hinshaw et al. 2009), this is 9.3 μK (0.28 %) higher in amplitude while shifted by (0.′6,1.′2) in longitude and latitude. Part of the difference (0.6 μK) is due to the revised CMB monopole temperature compared to Mather et al. (1999) (2.725 K). This total dipole (solar, orbital, relativistic, and interactions thereof) is removed from the calibrated TOI before final mapmaking.

3.5.2 *Planck*-HFI maps

Frequency maps have been produced using inverse noise weighting. In Figs. 3.5 and 3.6 we show the six intensity frequency maps from 100 to 857 GHz at full resolution (N_{side}=2048). Figure 3.7 presents polarization maps at the first four frequencies (100, 143, 217, and 353 GHz), degraded to lower resolution (N_{side}=256) in order to enhance the signal-to-noise ratio. These maps have been corrected from bandpass leakage as will be discussed in Sect. 3.7.3. In both intensity and polarization, we clearly see the emission from the Galactic dust increasing with frequency. In intensity, CMB anisotropies are visible at high latitude in the low-frequency channels (between 100 and 217 GHz). In polarization, the 100 GHz maps are contaminated in the Galactic plane by residual CO leakage coming from bandpass mismatch between bolometers.

3.5.3 Far sidelobes

As noted in Planck Collaboration VII (2016), far sidelobes affect the response of the instrument to large-scale structures. In addition, the far sidelobes also affect the HFI calibration.

At low frequencies, HFI calibrates by fitting to the sinusoidal signal created by the dipole modulated by the *Planck* circular scanning strategy. As outlined in Appendix B of Planck Collaboration XXXI (2014), this effectively weights different parts of the beam in general, and the sidelobes in particular, by their angle from the spin-axis. For example, far sidelobe contributions close to the spin-axis actually affect the calibration very little. Similarly, since we are calibrating with signals that are "in phase" with the known phase of the main beam as it scans, the further a sidelobe contribution is in angle *around* the spin-axis from the main lobe, the less it contributes to the calibration. So, a sidelobe contribution that is 90° in scan phase from the main lobe, for example, would not contribute to the HFI calibration, while something close to the main beam would potentially have a large effect. The change of the gain due to the far sidelobes is calculated by fitting the dipole to full timeline simulations of the dipole convolved by the far sidelobes. The factors are 0.09 % at 100 GHz, 0.05 % at 143 GHz, 0.04 % at 217 GHz, and negligible at 353 GHz. The delivered 100–217 GHz maps have been scaled by these gain changes. It should be noted that these numbers are uncertain at the 20–30% level, depending on a multitude of details, such as how the telescope is modelled.

For the planet photometry, some level of knowledge of the amplitude of the far sidelobes is needed to correctly compare the reconstructed flux with the planet brightness. However, the relative far sidelobe power is lower than 0.3 % (Tauber et al. 2010) for all HFI frequencies, which is well below the systematic uncertainties of the planet emission models we are using, which are around 5 % (see Sect. 3.3.4). Therefore far sidelobes can safely be ignored in the 545 and 857 GHz calibration.

3.5.4 Zodiacal emission

Zodiacal emission is reconstructed and subtracted in the same fashion as that used for the 2013 *Planck* results (Planck Collaboration XIV 2014). The basic procedure for characterizing and removing zodiacal emission from the *Planck* maps is to

- make frequency maps for each horn and survey as described in previous sections;
- make survey difference maps for each horn and year;
- find the date ranges over which each N_{side}=256 pixel was observed, and veto those pixels that were observed over a time-span of more than one week;
- use the *COBE* model (Kelsall et al. 1998) to recreate the different zodiacal emission components, assuming black-body emissivities;

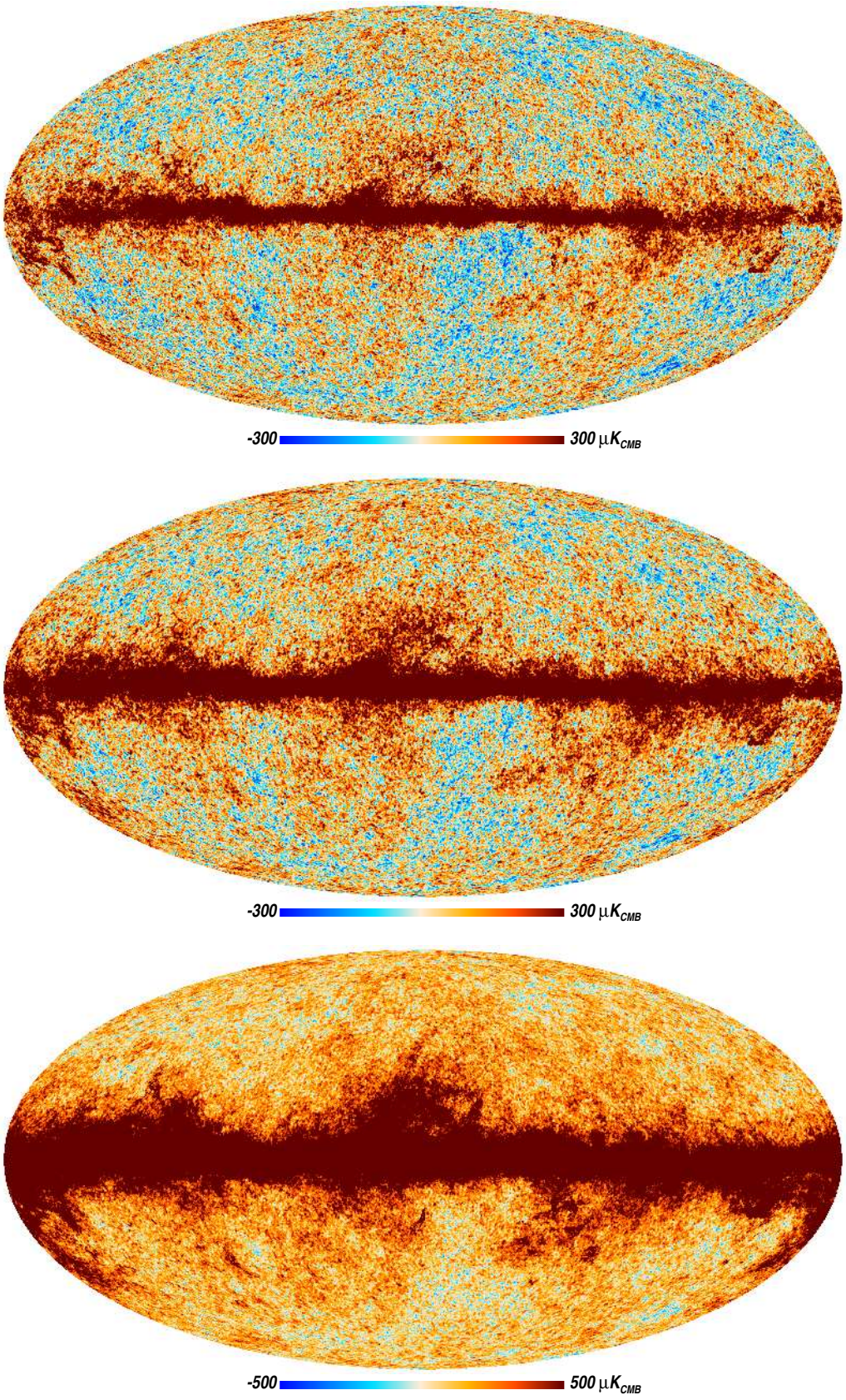

Figure 3.5: *Planck*-HFI full mission channel intensity maps at 100, 143, and 217 GHz (*from top to bottom*) after removal of zodiacal emission.

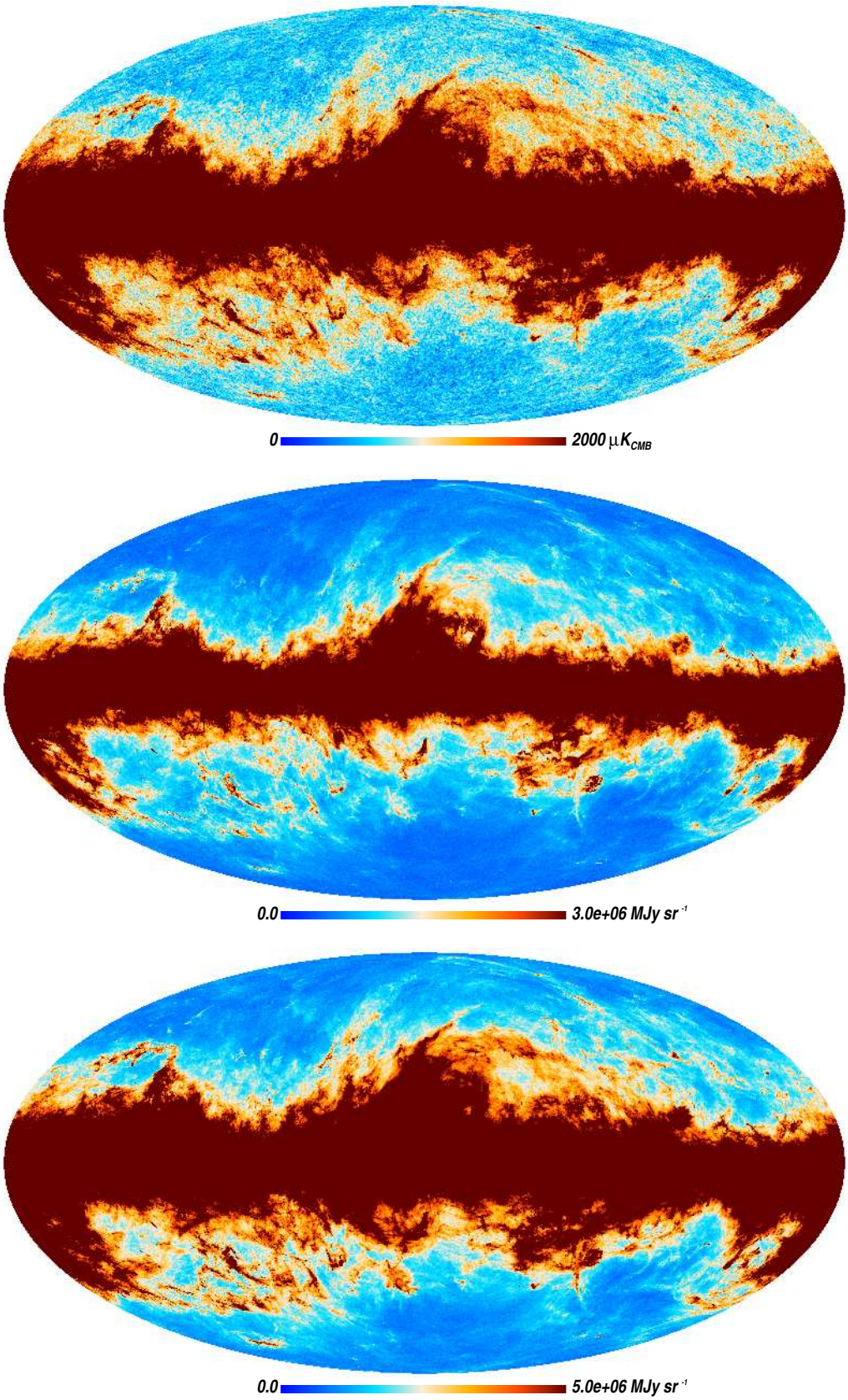

Figure 3.6: *Planck*-HFI full mission channel intensity maps at 353, 545, and 857 GHz (*from top to bottom*) after removal of zodiacal emission.

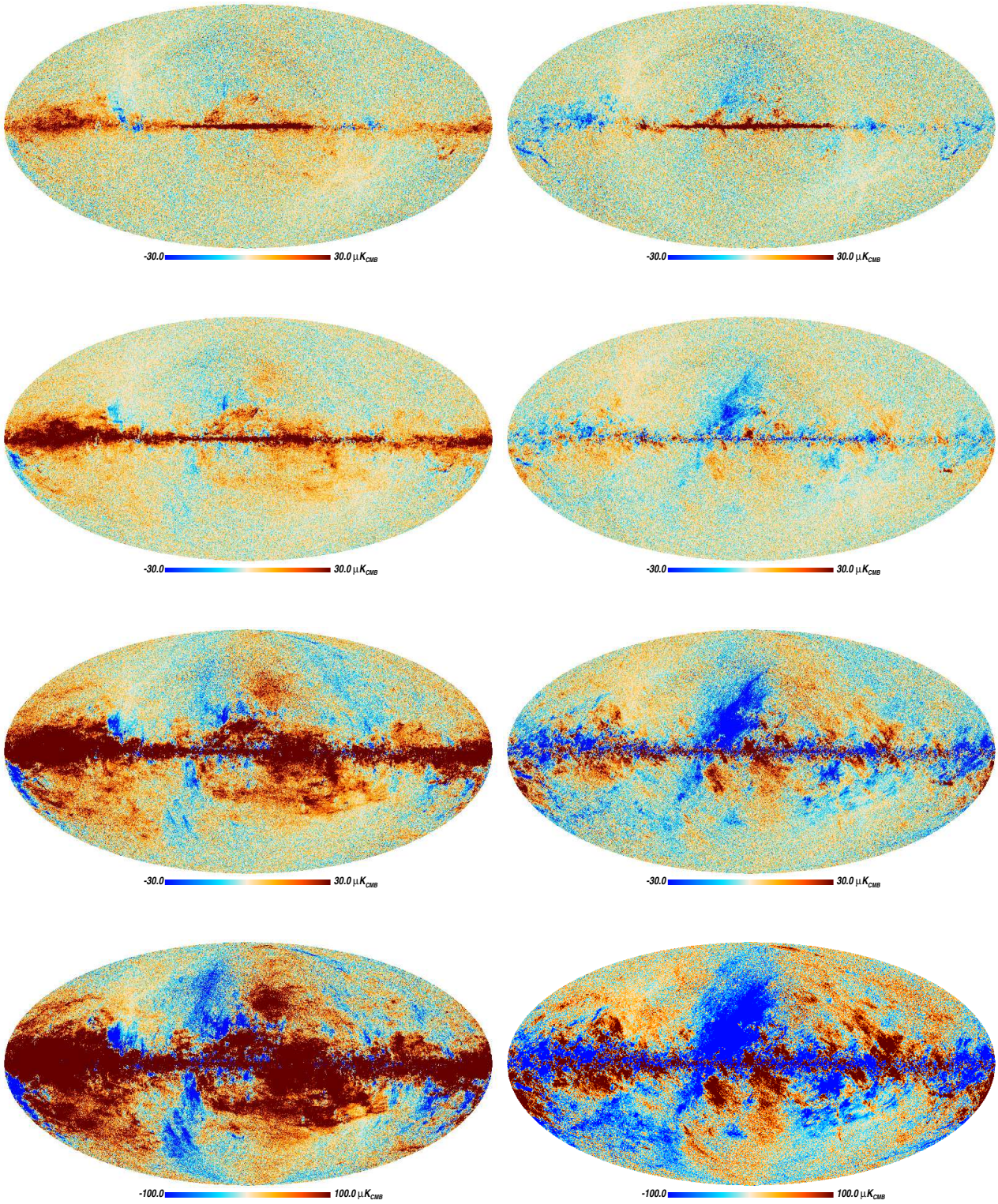

Figure 3.7: *Planck*-HFI full mission Q (*left*) and U (*right*) polarization maps corrected from bandpass leakage (see Sect. 3.7.3). *from top to bottom*: 100 GHz, 143 GHz, 217 GHz, and 353 GHz

- fit the components to the survey difference maps for each horn and year to extract the actual emissivities;
- use the average of the fitted emissivities to reconstruct the implied zodiacal emission seen during each pointing period, for each horn, and remove these from each detector.

Figure 3.8 shows the profiles for each HFI band for survey 3, made by differencing maps made without zodiacal emission

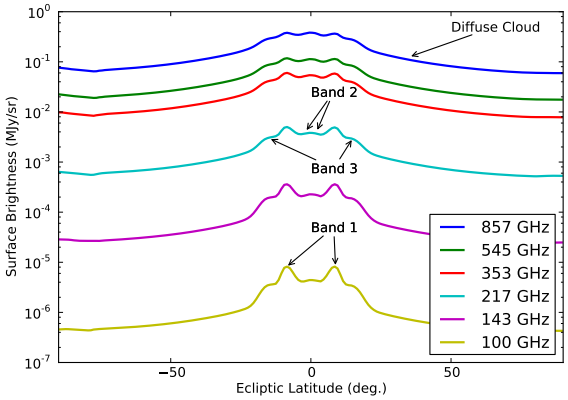

Figure 3.8: Zodiacal light profiles for each HFI band (survey 3) binned in ecliptic latitude. The diffuse cloud and bands are each marked only once, but exist at the same latitudes at each frequency in differing relative amounts.

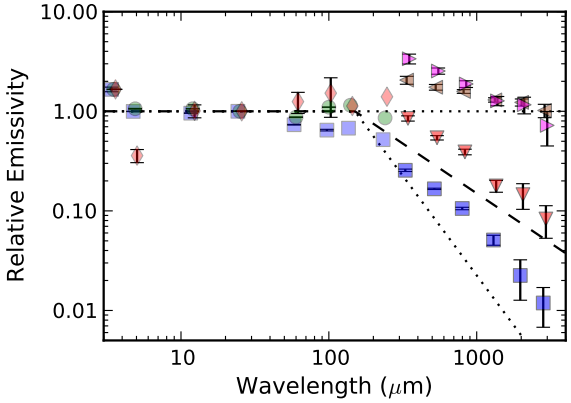

Figure 3.9: Zodiacal emissivities from COBE/DIRBE (λ<300μm, Kelsall et al. 1998) and *Planck* (λ>300μm, Table 3.3). The blue squares represent the emissivity of the Diffuse Cloud. For DIRBE, the red diamonds represent the fitted emissivity for all three IRAS Bands, and the green circles show the values for the Circumsolar Ring and Trailing Blob. Triangles are for *Planck*: IRAS Band 3 (pink right-pointing); IRAS Band 1 (the brown left-pointing); and IRAS Band 2 (red downward-pointing). For reference, the lines show emissivities that are unity at wavelengths less than 250 μm, but proportional to λ^{-2}, λ^{-1}, and λ^{0} at longer wavelengths.

Frequency [GHz]	Cloud	Band 1	Band 2	Band 3
857	0.256 ± 0.007	2.06 ± 0.19	0.85 ± 0.05	3.37 ± 0.38
545	0.167 ± 0.002	1.74 ± 0.11	0.54 ± 0.03	2.54 ± 0.18
353	0.106 ± 0.003	1.58 ± 0.07	0.39 ± 0.02	1.88 ± 0.14
217	0.051 ± 0.006	1.30 ± 0.07	0.15 ± 0.02	1.27 ± 0.14
143	0.022 ± 0.010	1.23 ± 0.10	0.15 ± 0.04	1.16 ± 0.22
100	0.012 ± 0.005	1.02 ± 0.16	0.08 ± 0.03	0.72 ± 0.27

Table 3.3: Frequency-averaged zodiacal emissivity values for the diffuse cloud and the three *IRAS* bands.

removal from those made with zodiacal emission removal and binning them in ecliptic latitude. The diffuse cloud and bands are each marked only once, but exist at the same latitudes at each frequency in differing relative amounts. These profiles also show some small offset effects near the ecliptic poles, which arise because the destriping is redone when zodiacal emission is removed.

The emissivities for each zodiacal component at each of the HFI frequencies are given in Table 3.3 and are plotted in Fig. 3.9. As noted in Planck Collaboration XIV (2014), there seems to be a jump between the emissivities for the bands at DIRBE wavelengths and the emissivities of Bands 1 and 3 at *Planck* wavelengths. This is being investigated, but is assumed to be a consequence of the assumption in the DIRBE analysis that all three bands have the same emissivities, while the *Planck* analysis allows them to be different. For the *Planck* cosmological studies this should be irrelevant, since the zodiacal analysis is being used only to remove the interplanetary dust contamination – the overall amplitudes of the emissivities, which are completely degenerate with the assumed particle density in the bands, are not being interpreted physically.

3.6 Noise description and subset differences

3.6.1 Map variance

As demonstrated in Planck Collaboration VII (2016), the noise spectra for the *Planck*-HFI bolometers show significant deviation from white noise, resulting in correlations between pixels after map projection. At large scales, the correlations are dominated by low-frequency noise, while at high resolution neighbouring pixels are correlated as a result of time-response deconvolution and filtering. The *Planck* 2015 release does not provide a pixel-pixel correlation matrix; only the variance per pixel is given for each delivered map. At first order, the variance maps are proportional to $1/N_{\rm hit}$, where $N_{\rm hit}$ is the number of samples per pixel.

The half-difference half-ring maps, projected using the same gain but destriped independently, are a good representation of the noise variance in the HFI maps. In the difference between the first and the second half of a ring, the sky signal vanishes almost completely. Moreover, most of the HFI systematics are scan-synchronous and thus also vanish in the difference.

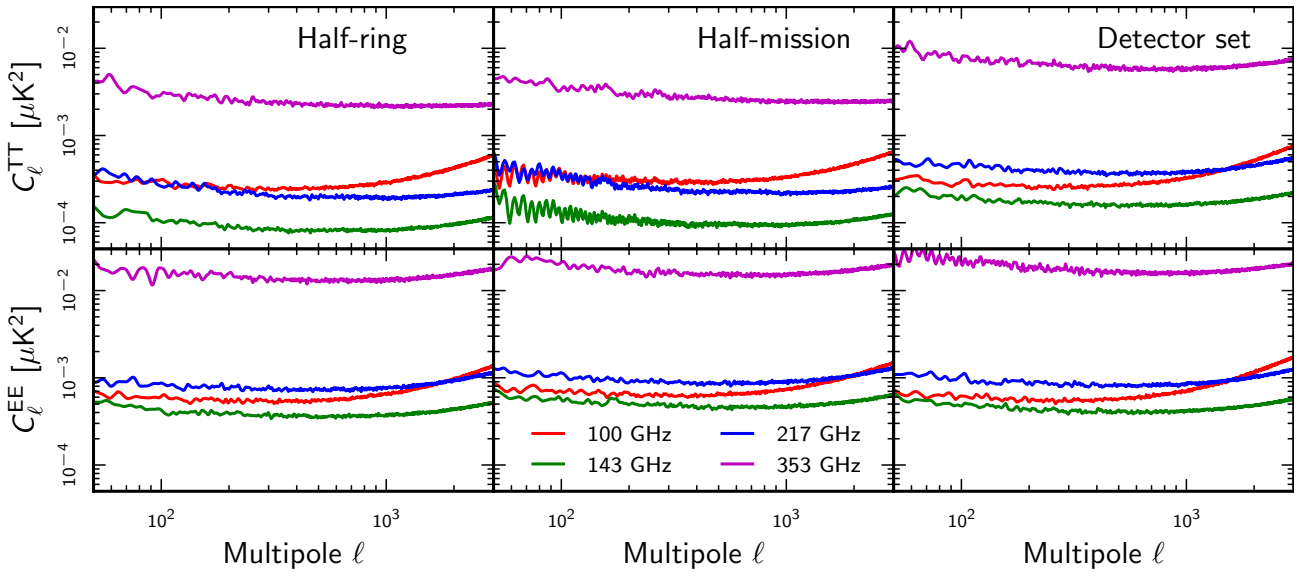

Figure 3.10: TT and EE power spectra reconstructed from the half-difference between data subset maps for the dipole-calibrated channels.

Table 3.4 compares the noise per sample from three estimators: (a) the mean value of the pre-whitened variance map (i.e. scaled using the hit counts), (b) the variance of the pre-whitened half-ring half-difference map, and (c) the average of the half-ring map power spectra in the ℓ range 100–5000 (see Sect. 3.6.2). For polarization, the numbers are averages over Q and U for the maps and E and B for the spectra. The different estimators are sensitive to different kinds of systematic effects, such as time-response residuals and signal gradient in pixels. Nevertheless, the three noise estimators give very consistent results.

Frequency [GHz]	Variance maps (a)	Diff. maps (b)	Pseudo-spectra (c)
100I	1538	1531	1410
100P	2346	2344	2131
143I	769	758	759
143P	1631	1618	1611
217I	1105	1098	1141
217P	2512	2486	2440
353I	3692	3459	3780
353P	10615	10141	10181
545I	0.612	0.619	0.779
857I	0.660	0.866	0.860

Table 3.4: Estimation of the noise per sample for intensity (I) and polarization (P) estimated from (a) the variance maps, (b) the half-ring difference maps, and (c) the pseudo-spectra. Units are μK_{CMB} for 100-353 GHz, and MJy sr^{-1} for the submm channels.

The variance maps (I–I, Q–Q, and U–U) are inhomogeneous owing to the *Planck* scanning (which have negligible wobbling), the relative position of the detectors in the focal plane, and the rejection of some rings or groups of rings (see Planck Collaboration VII (2016)). Moreover, the typical HEALPix pixel size is about 1.′7 at N_{side}=2048 resolution while *Planck* scans the sky on roughly (but not exactly) ecliptic meridians separated by 2.′5 (near the ecliptic equator). As a consequence, for single survey maps, lines of empty pixels appear between the scanning trajectories around (l,b)=(0°,±45°). Even when surveys are combined, inhomogeneities arise because the HEALPix pixels are elongated parallelograms. The axis of their elongation changes at the boundaries between the 12 primary HEALPix pixels. In the same regions of the sky and in Galactic coordinates, these elongations are parallel with the scanning trajectories, which induces moiré patterns in the coverage maps.
The degree of correlation between the Stokes parameters within each pixel reflects the distribution of the detector orientations, which results from the scanning strategy. The I–Q and I–U correlations are about 14, 9, 6, and 12 % at 100, 143, 217, and 353 GHz. The Q–U correlation is about 11, 2, 3, and 8 % at 100,143, 217, and 353 GHz).

3.6.2 Map differences

The redundancy of the *Planck* scanning history and focal plane layout provides numerous ways to check data consistency. We can create differences between maps built using data splits, as described in Sect. 3.4.3. In the limit that the signal is the

same in each data subset, the difference map should contain only noise. The TOI processing includes several operations that introduce correlations on various time scales; these are discussed below.
In the dipole-calibrated frequency channels (100–353 GHz), the signal differences are small enough that the data-split map differences can be evaluated at a spectral level, giving insight into the residual systematic errors. For high-frequency channels, we discuss the residuals in the map domain.
Given maps of two subsets of the data, M_A and M_B, we construct the half-difference as $\Delta M=(M_A-M_B)/2$. We compute the power spectrum in temperature and polarization of the half-difference, masking the sky with the *Planck* point source mask and the galaxy masks used in Planck Collaboration XI (2016), i.e. leaving 65, 59, 48, and 32 % of the sky unmasked at 100, 143, 217, and 353 GHz, respectively.
In order to use this half-difference map to assess noise in the full maps, we account for widely varying integration time in the two subsets using a pixel-by-pixel weight map, which is multiplied by the half-difference map ΔM prior to computing the angular power spectrum. The weight is constructed as $W=2/\sqrt{(1/n_A+1/n_B)(n_A+n_B)}$, where n_A is the hit count map for M_A and n_B is the hit count map for M_B. In the limit that the half-difference map consists entirely of white noise, this exactly accounts for the differences in the hit counts. The TT and EE spectra of the difference maps are plotted in Fig. 3.10 and are described in the sections below. The BB spectra are nearly the same as the EE spectra and are not shown.

Half-ring map differences

The half-ring difference is sensitive to high-frequency noise, since most low-frequency modes (on time scales longer than 1 h) are common to both data sets and thus vanish. In the harmonic domain, the noise is nearly white with an amplitude compatible with the noise estimated in the map domain (see Sect. 3.6.1). At large multipoles, the noise blows up because of the time transfer function deconvolution, before being cut off by the low-pass filter. At lower multipoles, half-ring differences show low-frequency noise residuals due to the destriping. Indeed, the destriping is performed independently for each half, or essentially half the data are used to solve the offsets for the full ring maps. The residuals from the offset determination are therefore expected to be twice as large as in the full-mission map.
In addition, the deglitching operation performed during the TOI processing uses the full data set to estimate the signal in each ring, thereby introducing some correlation between the two halves of each ring. Taking the difference between the two half-rings removes the correlated portion of the noise at the few percent level.

Half-mission map differences

With half-mission differences, we can check for long-time-scale variations and for apparent gain variation with time due to the analog-to-digital converter non-linearities. Moreover, because of the slightly shifted pointing between the first and second halves of the mission, the effect of a signal gradient within a pixel (especially on the Galactic plane where the signal is strong) is larger than for the half-ring map differences.
Because the number of observations in a given pixel can be very different between the two half-mission maps, using a weighting as described above is essential. Including the weighting, the half-mission differences give a power that is 10–20 % higher than the corresponding half-ring difference. This fraction of additional power is nearly the same in all the channels 100–353 GHz, and is the same in both temperature and polarization. We understand this small additional power to be due to effects from the TOI processing that introduce correlations in the noise between the subsets. The half-ring maps, as stated above, have correlations introduced by the deglitcher that are subsequently removed by the differencing. These correlations are not present between the half-mission data sets, so their difference shows a higher noise power.

Detector-set map differences

This difference probes systematic effects that are bolometer-dependent. In the case of 143, 217, and 353 GHz, we note that the detector-set split excludes the unpolarized detectors, and the noise in TT is correspondingly higher than in the half-mission and half-ring split. The 100 GHz channel has only polarization-sensitive bolometers and the TT spectrum of the difference is much closer to the spectrum seen for the other data splits.
There are several other effects that make the power spectrum of the detector-set difference stand apart. A unique time response function is deconvolved from each bolometer. In the half-ring and half-mission data splits, the deconvolved function is identical in the two halves. With the detector-sets, however, the time response is in general slightly different in the two halves. This effect leads to a tilt in the spectrum of the detector-set difference maps relative to the half-ring or half-mission split. Moreover, at 353 GHz, signal residuals are larger owing to relative calibration uncertainties between detectors.

Map differences at low-ℓ

At low multipoles, despite the huge progress in the control of the systematics, data are still contaminated by systematic residuals. Figure 3.11 shows the EE power spectra from the half-difference maps at 100, 143, and 217 GHz, and compared to the noise power spectrum from simulations (FFP8, described in Planck Collaboration XII 2016). While the half-ring differences are compatible with noise, at multipoles typically lower than 50 the detector-set and half-mission differences are dominated by excess power that is larger than the EE CMB signal. The origin of the excess power will be explored in a forthcoming publication.

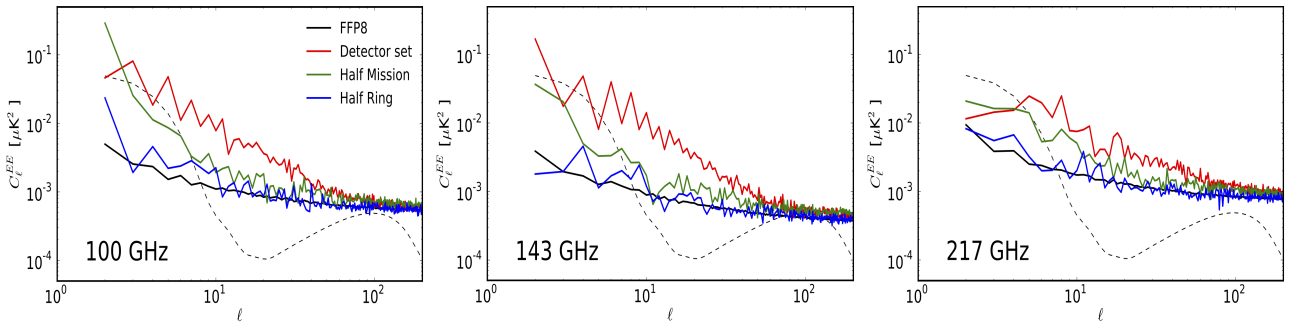

Figure 3.11: EE power spectra reconstructed from the half-difference between data subset maps for the dipole-calibrated channels at low multipoles compared to the noise estimation from the FFP8 simulations. CMB signal from *Planck* 2015 is plotted in dashed lines.

High-frequency channels

For the highest frequency channels (545 and 857 GHz) the data-split map differences are dominated by residual signals. Figure 3.12 shows the rms of the differences of intensity maps at 545 and 857 GHz for half-ring, half-mission, and year data splits compared to the same data split performed on a simulated noise map. At low signal, the difference is consistent with instrumental noise. At high signal levels, an additional residual appears in the difference map that is roughly proportional to the signal level. Part of this is due to pointing errors. For year and half-mission, the effect is enhanced by the combination of residual gain variations and the relative difference of pointing between the two splits. Over most of the sky, the signal is reproducible to better than 1 % for these frequencies. Bolometer map differences (not shown here) are, in addition, sensitive to the relative calibration error.

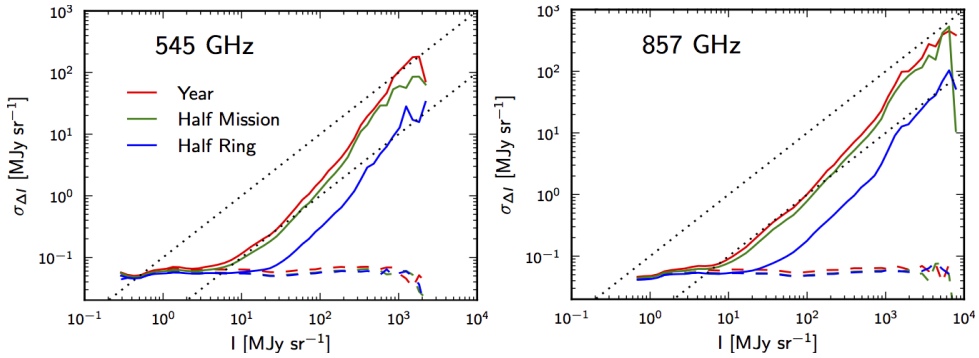

Figure 3.12: Rms of the residual signal in difference maps at 545 and 857 GHz, as a function of signal level in the full map. The solid coloured curves show the rms of the data, while dashed coloured curves show the rms of a simulated noise map. The diagonal dotted lines indicate 1 % and 10 % of the signal.

3.6.3 Noise cross-correlation

Here we check for correlations in the noise by computing cross-spectra between the difference maps described earlier. We look at 100 (Fig. 3.13), 143 (Fig. 3.14), and 217 GHz (Fig. 3.15) in comparison with the expectations from projecting noise realizations on the sky (using the FFP8 noise realizations described in Planck Collaboration XII 2016 and the end-to-end simulations described in Planck Collaboration VII (2016)).
When the half-mission cross-spectra of half-ring differences are computed, the results are roughly consistent with the FFP8 noise simulations. At 143 GHz in temperature, the end-to-end simulation produces a slight rise in power at low multipoles that is not seen in the data.
Large correlations are seen in the half-ring cross-spectra of half-mission differences. These are at least partially induced by our processing since the end-to-end simulations also show correlations that are not as large in amplitude as those seen in the data, but show a similar spectral shape. These correlations are mainly due to the deglitcher, as described above.

3.6.4 Temperature-polarization cross-variance

In absence of spatial correlations, noise correlations between temperature I and polarized Q and U modes vanish in the harmonic domain, thanks to the orthogonality of the spherical harmonic decomposition. Consequently the TE and TB auto-spectra are not biased by noise in the way that the TT, EE, and BB spectra are. In practice, transfer function deconvolution, filtering, and pixelization effects can produce spatial correlations at high multipoles, resulting in a noise

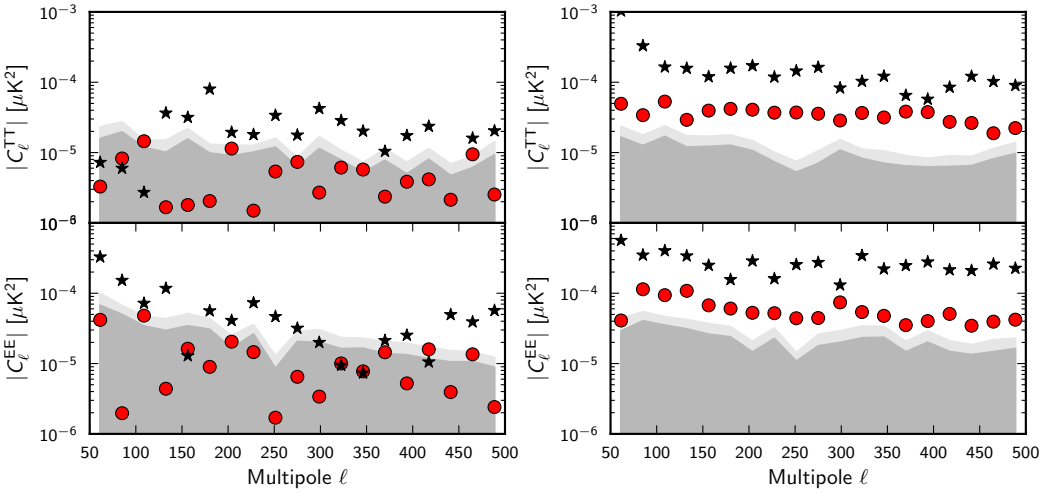

Figure 3.13: 100 GHz difference map cross spectra. *Left*: half-mission (HM) correlation of half-ring differences (HR). *Right*: half-ring (HR) correlation of half-mission difference (HM). The real data are red dots. The end-to-end simulation are black stars. One and two sigma contours from ten FFP8 noise realizations are shaded grey.

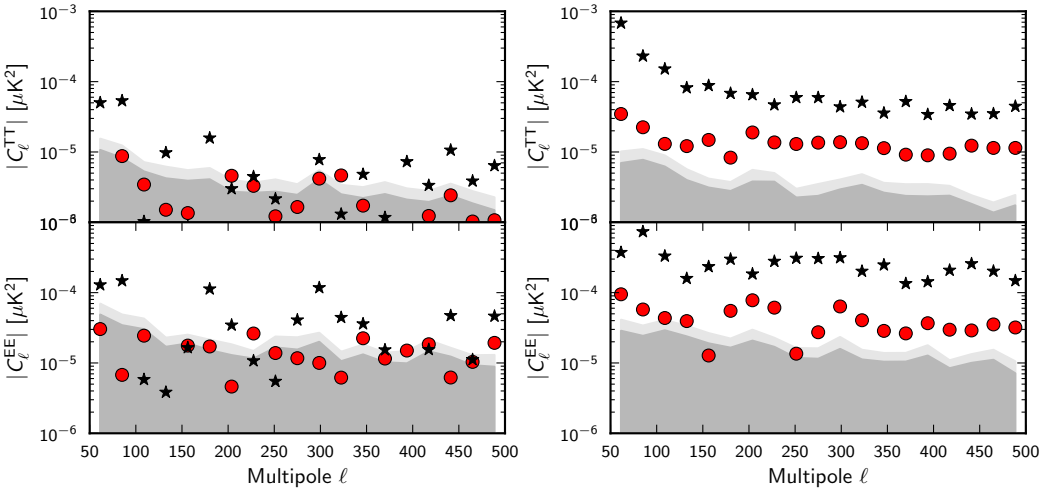

Figure 3.14: Same as Fig. 3.13 for 143 GHz difference map cross spectra.

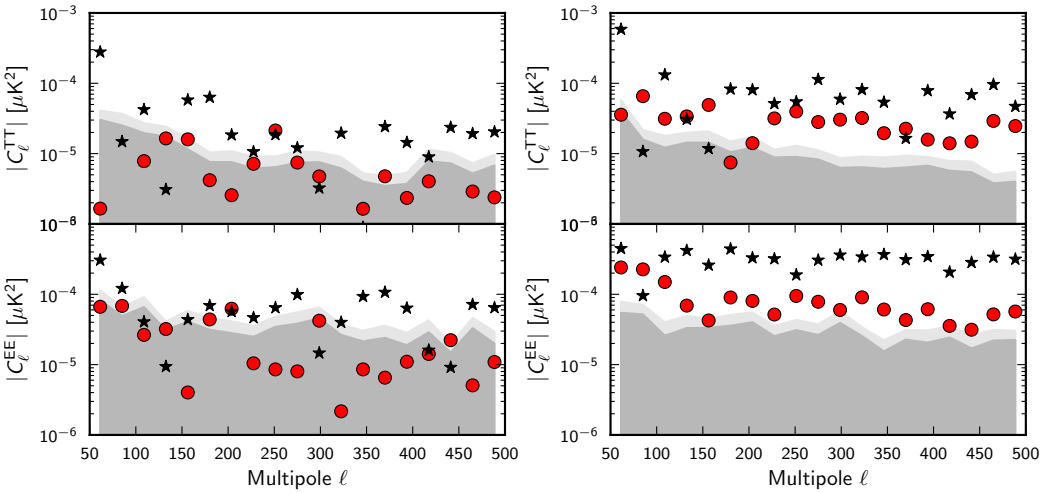

Figure 3.15: Same as Fig. 3.13 for 217 GHz difference map cross spectra.

bias that is observed in the TE and TB angular power spectra. In Fig. 3.16 we compare the auto and cross-spectra for the half-ring, half-mission, and detector set splits. These pseudo-spectra have been built by masking Galactic emission

and point sources (approximately 40 % of the sky). The auto-spectra are biased at high multipoles (starting at $\ell \approx 1500$). The amplitude of this bias and its sign depend on the frequency and on the mode considered. Nevertheless, none of the cross-spectra show significant departures from the null expectation.

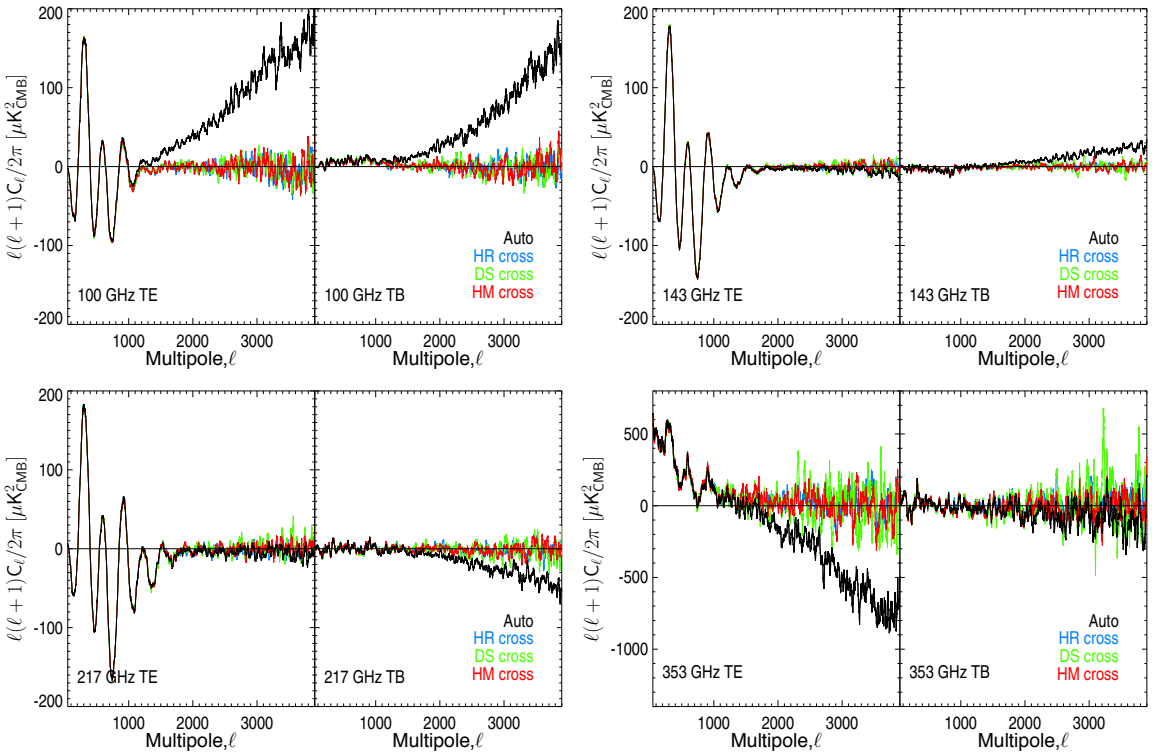

Figure 3.16: Pseudo-power spectra for TE (*left*) and TB (*right*) for each frequency (100, 143, 217, and 353 GHz). The auto-spectra are shown in black. Cross-spectra of half-ring (HR), half-mission (HM), and detector-set (DS) half-differences are shown in blue, red, and green, respectively. A Galaxy and point source mask, leaving 40 % of the sky, was used in all cases.

We observe that the amplitude of the noise bias in auto-spectra is mitigated when adding more independent data sets, such as detectors or surveys (survey maps show larger amplitude than half-mission and full-mission). These results are fully reproduced in the FFP8 simulations.

3.6.5 Subset map cross-covariance

When mapping subsets of the available data (selecting detectors and/or time spans) we have a choice between solving for independent baseline offsets for the subset in question or reusing full-mission, full-frequency baselines (as in the 2015 HFI map release). Full-mission baselines are more accurate, leaving less large-scale noise in the maps, but introduce noise correlation between detector-set maps.

We can measure the resulting bias in cross-spectra through noise simulations. Comparison between noise spectra from a Monte Carlo analysis at 100 GHz using both methods of destriping is shown in Fig. 3.17 for the case of detector sets. Noise spectra for each detector set show more large-scale power when using independent baselines than in the full mission case. On the other hand, the cross-power spectrum is biased by up to a few times $10^{-3}\mu K^2$ below ℓ=10; the same is true for the half-mission subset.

3.7 Systematic effects

We now describe the major systematic effects that could potentially affect the maps: the gain variations; errors in the absolute gain determination; errors in the polarization efficiency and orientation; and, most of all, the detector-to-detector gain mismatch. The latter includes bandpass mismatch (which affects the response to the foregrounds of the detectors at the same frequency) and relative gain uncertainties, both of which create intensity-to-polarization leakage. All these effects are constrained using tests involving the combination of maps, residuals in maps, cross-power spectra, and dedicated simulations.

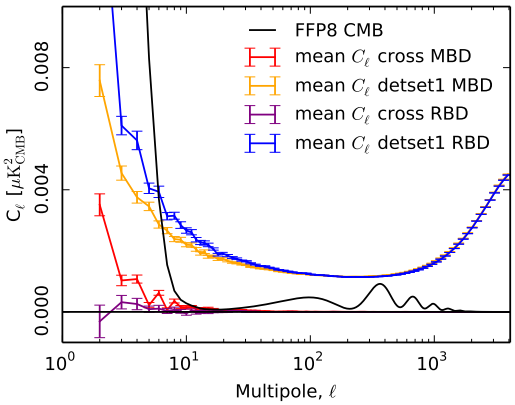

Figure 3.17: Average *EE* spectra obtained from 100 simulations of detector-set noise maps. The maps were produced using either the full-mission baseline destriping (MBD) or the destriping run on each subset independently (run baseline destriping or RBD). Both the increased low-ℓ noise in the RBD case and the increased cross-spectrum noise bias in the MBD case are apparent.

3.7.1 Gain stability

Gain stability has been significantly improved with respect to the *Planck* 2013 release. This is mainly due to the analog-to-digital converter non-linearity correction, combined with the new determination of the time transfer function (see Planck Collaboration VII (2016)). The amplitude of the apparent gain variation has been improved from 1–2 % to less than 0.5 % for all cases. Residual gain variations are compatible with zero when including the correction for the long-time-constant residuals, as discussed in Sect. 3.3.3.

We check the stability of the gain over time using the same tool as in Planck Collaboration VIII (2014) called `bogopix`. For each bolometer, the code fits simultaneously for the gain g_r and the offsets o_r for each ring, marginalizing over the sky signal T:

$$P_t = g_r \times (A_{tp} \cdot T_p + t_{\rm orb}) + o_r + n_t. \tag{3.15}$$

Given the low amplitude of the observed gain variations (less than 0.5 %), we linearize Eq. (3.15) and solve by iteration (see Planck Collaboration VIII 2014); one or two iterations are sufficient to ensure convergence. To initialize the iterations, we start from the constant gain solution G (see Sect. 3.3.2).

We compute the gain variations from single-bolometer data (neglecting polarization). Polarized signals will affect the gain determination. To reduce this bias, we ignore sky regions where the polarized emission is the strongest, which lie mostly in the Galactic plane.

Figure 3.18 shows the results of `bogopix` for bolometers at 100, 143, and 217 GHz, smoothed over a four-day period. At higher frequencies (353 GHz and above), the gain variations are much lower than the gain uncertainty. Owing to the *Planck* scanning strategy, the Galactic foreground is larger for some rings, while the orbital dipole amplitude is almost constant. This increases the dispersion around those regions and potentially induces some bias in the gain determination. In the end, we find gain variations with amplitudes lower than 0.3, 0.4, and 0.5 % at 100, 143, and 217 GHz, respectively.

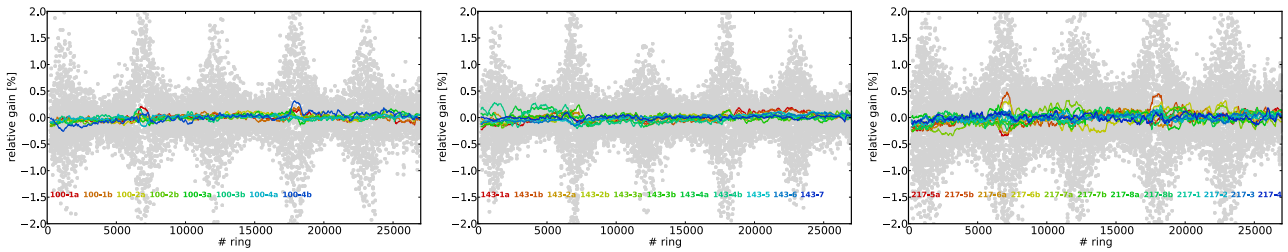

Figure 3.18: Gain variation with ring number for each bolometer estimated using `bogopix`. *From left to right:* 100, 143, and 217 GHz. Gain values for individual rings (grey dots) have been smoothed with a four-day width. The gain variations are lower than 0.3, 0.4, and 0.5 % at 100, 143, and 217 GHz, respectively.

The residual apparent gain variations are essentially coming from the uncertainty in the current analog-to-digital converter non-linearity correction, the uncertainty in the long-time-constant estimation, and the effect of long-term thermal variations on the bolometer and electronics response.

3.7.2 Calibration accuracy

Inter-frequency accuracy

The precision of the calibration can be assessed by looking for residual dipoles in the maps. If the calibration of a map is slightly incorrect, the removal of the solar dipole in the mapmaking process leaves a residual dipole. However, identifying such a residual dipole is difficult because of the presence of other sources of power at ℓ=1, mostly due to Galactic emission and zodiacal light, but also to imperfect correction of systematic effects such as far sidelobes.

Following the method presented in Sect. 3.5.1 used to estimate the solar dipole direction and amplitude, we cleaned the Galactic emission from the HFI maps using a local correlation with the 857 GHz map. Adding the solar dipole that was removed in the mapmaking process (Sect. 3.5.1) to $D_{\rm res}$ produces a map that contains the true solar dipole. We then fit for its amplitude, fixing its direction to the official *Planck* value (lon, lat =264.°00,48.°24) to limit the effect of other residuals still present in $D_{\rm res}$ (Galactic, systematic effects). The fit is done using sky pixels where I_{857}<2 (faintest 37 % of the sky) to limit the effect of Galactic emission residuals (CO, free-free emission, and small scale dust spectral energy distribution variations). Table 3.5 gives the ratio of fitted amplitude to the removed dipole found for the HFI maps at frequencies from 100 to 545 GHz. Because effects other than a miscalibration can contribute to a residual dipole in the maps, these ratios provide upper limits on the calibration accuracy at each frequency. The results indicate that the calibration at 100 and 143 GHz is precise at a level of few 10^{-4}. At 217 GHz, the fit is compatible with a residual dipole at the 0.2 % level. At higher frequencies, the fits indicates residuals at 0.52 % and 1.23 % at 353 and 545 GHz, respectively.

Frequency [GHz]	$A_{\rm fit}/A_{\rm rm}$	Statitiscal uncertainties	Systematic uncertainties
100	1.00010	±0.00006	±0.0001
143	0.99988	±0.00012	±0.0001
217	1.00184	±0.00027	±0.0003
353	1.00568	±0.00185	±0.0020
545	1.02515	±0.01627	±0.0190

Table 3.5: Ratio of amplitudes of the fitted dipole ($A_{\rm fit}$) and the removed dipole ($A_{\rm rm}$=3364.5 μK). The direction of the dipole removed from the data (lon=264.°00, lat=48.°24) was constrained here. The fit was computed for different sky fractions from 30 to 70 %. Statistical and systematic uncertainties are also indicated.

These results are in agreement with those obtained while performing component separation, as shown in Table 4 from Planck Collaboration IX (2016) and in Planck Collaboration X (2016). They are also in agreement with the results from the cosmological parameter determination, where intercalibration coefficients are also fitted for (see Planck Collaboration XI 2016). The agreement between these measurements computed over different multipole ranges highlights the quality of the *Planck*-HFI calibration, together with the accuracy of the transfer function reconstruction.

Intra-frequency accuracy

For polarization reconstruction with *Planck*-HFI data, we have to combine data from several detectors. Any relative calibration error will induce an intensity-to-polarization leakage (see Sect. 3.7.3). For the CMB channels, we have assessed the relative calibration accuracy for each detector at a given frequency using two complementary methods.

As in Sect. 6.2 (Fig. 14) of Planck Collaboration VIII (2014), we derive relative inter-calibration factors for each detector (for 100 to 353 GHz), rescaling their cross-pseudo-power spectra, estimated over 40 % of the sky (30 % for 353 GHz) in the ℓ range 25–300, which encompasses the first acoustic peak. We used colour-correction factors at 353 GHz, because even at high latitude the dust emission is large. As in 2013, we keep the maximum of these factors as a conservative estimate of the relative calibration accuracy. In 2015, we find 0.09, 0.07, 0.16, and 0.78 % for 100, 143, 217, and 353 GHz, respectively (compared to 0.39, 0.28, 0.21, and 1.35 % in 2013). Since single-detector maps are built ignoring polarization, these values should be considered as conservative upper limits on the relative detector-to-detector calibration accuracy.

We complemented these estimations by analysing the solar dipole residual on the differences of single detector maps. We fit the dipole amplitude fixing its direction while masking 30 % of the sky in the Galactic plane to avoid regions affected by band-pass differences. We find maximum amplitudes 0.5, 0.6, and 3.0 μK for 100, 143, and 217 GHz, respectively, which – relative to the solar dipole amplitude (3364.5μK, see Sect. 3.5.1) – gives accuracies of the same order as the aforementioned spectra analysis. As in this previous method, the main limitation comes from polarization which is ignored in the single detector maps.

While significantly better than for the 2013 release, calibration mismatch between bolometers at a given frequency is one of the main systematic residuals contaminating the HFI large angular scales in polarization, as explained in the next section.

3.7.3 Intensity-to-polarization leakage

Any gain mismatch between the measurements of detectors belonging to the same frequency channel will result in intensity-to-polarization and cross-polarization leakage in the channel maps. In *Planck*, the dominant leakage effect has three main origins:

- monopole mismatch from the uncertainty in the mean offset determination;
- gain mismatch that produces leakage from the whole intensity signal into polarization;
- bandpass mismatch that mainly generates intensity-to-polarization leakage from foreground emission (with a non-CMB spectrum). In the case of HFI, the leakage effect is dominated by CO and thermal dust emission.

All these leakage sources are especially important for the large angular scales. Beam-mismatch polarization leakage occurs at small angular scales and is discussed in Planck Collaboration VII (2016). Although the first two mismatches can be minimized by obtaining more accurate measurements of offsets and gains, respectively, the bandpass mismatch cannot be removed in the mapmaking process if we want to project CMB and foregrounds at the same time.
The power absorbed by a given bolometer b at time t is expressed using the Stokes parameters (I_p,Q_p,U_p), which characterize the emission in intensity and polarization in the corresponding sky pixel p. The polarized HFI channels are calibrated using the CMB orbital dipole and the total calibrated power absorbed by the bolometer b can be written as

$$\begin{aligned} m_t^b &= (1+\epsilon^b_{\rm gain}) \\ &\times \left\{\sum_k C_k(1+\epsilon^b_{{\rm BP},k})\left[I_p^k+\rho^b\left(Q_p^k\cos\phi_t^b+U_p^k\sin\phi_t^b\right)\right]\right\} \\ &+ \epsilon^b_{\rm offset}+n_t, \end{aligned} \tag{3.16}$$

where the polarization efficiency ρ^b and the polarization angle $\phi_t^b=2(\psi_t+\alpha^b)$ are explicitly dependent on the bolometer b, with the index k ranging over the different sky components. Additionally, we have the following definitions:

- $\epsilon^b_{\rm gain}$ encodes the gain mismatch of bolometer b with respect to the mean calibration of the channel;
- $\epsilon^b_{\rm offset}$ corresponds to the overall offset of bolometer b, which is small but not vanishing;
- $\epsilon^b_{{\rm BP},k}$ is the bandpass mismatch specific to bolometer b, which affects all sky components except the CMB (see description below);
- C_k is the average transmission of sky component k in a given channel.

Each of these ϵ terms is responsible for leakage from intensity to polarization in a manner that can in principle be quantified and corrected for, as described hereafter. We note that we only consider first-order terms in ϵ, as any higher-order contribution is negligible.

Bandpass mismatch

Each emission component k (where k = CMB, dust, synchrotron, etc.) is integrated over the bandpass of the detector according to a given spectrum $f_k(\nu)$. Since the polarized HFI channels are calibrated using the CMB orbital dipole, we define the transmission coefficients

$$\begin{aligned} C_k^b &= \frac{\int f_k(\nu)H_\nu^b d\nu}{\int f_{\rm CMB}(\nu)H_\nu^b d\nu} \\ &\equiv C_k(1+\epsilon^b_{{\rm BP},k}), \end{aligned} \tag{3.17}$$

where H_ν^b is the spectral response of bolometer b and $C_k=\sum_b C_k^b/N_{\rm bolo}$ is the average value of the C_k^b in a given channel. These transmission coefficients express the k-component emission in CMB units. If all bolometers had the same spectral responses then $\epsilon^b_{{\rm BP},k}$ would be equal to zero, i.e. $C_k^b=C_k$, in which case no leakage related to bandpass-mismatch would be produced.
Considering only bandpass mismatch corresponds to setting $\epsilon^b_{\rm gain}=0$ and $\epsilon^b_{\rm offset}=0$ in Eq. (3.16). Then, ordering all the data samples, m_t^b, for a bolometer observing a position p on the sky into a single vector $\mathbf{D}^b$, defining A to be the pointing matrix in temperature and polarization, and n the noise vector, Eq. (3.16) reads

$$\mathbf{D}^b=\sum_k C_k\mathsf{A}\begin{pmatrix} I_p^k \\ Q_p^k \\ U_p^k \end{pmatrix}+\sum_k C_k\epsilon^b_{{\rm BP},k}\mathsf{A}\begin{pmatrix} I_p^k \\ Q_p^k \\ U_p^k \end{pmatrix}+\mathbf{n}. \tag{3.18}$$

Using all bolometers b within a channel, the mapmaking procedure solves for the total signal Stokes parameters $(I_p^{\rm tot},Q_p^{\rm tot},U_p^{\rm tot})$ in pixel p, formally computing,

$$\begin{pmatrix} I_p^{\rm tot} \\ Q_p^{\rm tot} \\ U_p^{\rm tot} \end{pmatrix}=\left(\mathsf{A}^{\rm T}\mathsf{N}^{-1}\mathsf{A}\right)^{-1}\mathsf{A}^T\mathsf{N}^{-1}\mathbf{D}, \tag{3.19}$$

which becomes

$$\begin{pmatrix} I_p^{\rm tot} \\ Q_p^{\rm tot} \\ U_p^{\rm tot} \end{pmatrix} = \sum_k C_k \begin{pmatrix} I_p^k \\ Q_p^k \\ U_p^k \end{pmatrix} + \sum_k C_k \sum_{b=0}^{N_{\rm b}-1} \epsilon^b_{{\rm BP},k} \Gamma^b_p \begin{pmatrix} I_p^k \\ Q_p^k \\ U_p^k \end{pmatrix}, \tag{3.20}$$

where $\Gamma^b_p \equiv \left(\mathsf{A}^{\rm T}\mathsf{N}^{-1}\mathsf{A}\right)^{-1}\mathsf{A}^{\rm T}\mathsf{N}^{-1}\Delta^b\mathsf{A}$. We have introduced the matrix Δ^b, the elements of which are equal to zero except for the diagonal elements relevant to bolometer b, which are set to 1. The last term of Eq. (3.20) is the leakage term in pixel p, where intensity will leak into Q and U, Q into I and U, and U into I and Q, according to the mismatch coefficients $\epsilon^b_{{\rm BP},k}$ and the values of the 3×3 matrix

$$\Gamma^b_p = \begin{pmatrix} \Gamma_{II} & \Gamma_{QI} & \Gamma_{UI} \\ \Gamma_{IQ} & \Gamma_{QQ} & \Gamma_{UQ} \\ \Gamma_{IU} & \Gamma_{QU} & \Gamma_{UU} \end{pmatrix}^b_p . \tag{3.21}$$

Considering all pixels, the quantities Γ^b_{XX} correspond to nine sky maps for bolometer b. These maps can be fully determined from the mapmaking solution and may be understood as patterns of the mismatch leakage. In practice, cross-polarization leakage and polarization-to-intensity leakage are negligible compared to the intensity-to-polarization contribution and we therefore consider the latter only. The Γ_{IQ} and Γ_{IU} maps have been systematically produced by the mapmaking pipeline.[3] With these assumptions, the leakage induced by bandpass-mismatch in Q and U for the sky component k reads

$$L^{{\rm BP},k}_{IQ,IU} = C_k I^k \sum_{b=0}^{N_{\rm bolo}-1} \epsilon^b_{{\rm BP},k} \Gamma^b_{IQ,IU}. \tag{3.22}$$

In consequence, for a given calibrated intensity template of the sky component k (i.e. $I^k_{\rm template} = C_k I^k$) we can compute leakage correction maps as

$$L^{{\rm corr},k}_{IQ,IU} = I^k_{\rm template} \sum_{b=0}^{N_{\rm bolo}-1} \epsilon^b_{{\rm BP},k} \Gamma^b_{IQ,IU} = I^k_{\rm template} \sum_{b=0}^{N_{\rm bolo}-1} \frac{C^b_k}{C_k} \Gamma^b_{IQ,IU}, \tag{3.23}$$

where the last equality assumes $\sum_{b=0}^{N_{\rm bolo}-1} \Gamma^b_{IQ,IU} = 0$ by construction.
Leakage correction maps have been produced for all polarized HFI channels. The relevant foregrounds at these frequencies are dust (all channels) and CO (all channels except 143 GHz). To do so, the coefficients $C^b_{\rm dust}$ have been computed from Eq. (3.17), where the spectral responses of the bolometers $H^b(\nu)$ are those obtained from pre-launch ground-based measurements of the bandpasses (Planck Collaboration IX 2014). The dust spectrum is taken as a grey body with spectral index $\beta = 1.62$ and temperature $T = 19.7$ K, which are the all-sky average values found in Planck Collaboration XI (2014). For the intensity template required in Eq. (3.23), we use the thermal dust intensity maps at 353 GHz obtained from the *Planck* thermal dust model (Planck Collaboration XI 2014). Combining all these ingredients, the dust correction maps $L^{\rm corr(dust)}_{IQ,IU}$ are produced according to Eq. (3.23) and delivered in the 2015 HFI data release (Fig. 3.19).
We note, however, that the reliability of these corrections is limited by uncertainties both in the physical nature of the foreground components and in the determination of the bolometer spectral responses. For the sake of simplicity, a constant spectral index and a constant temperature across the sky have been assumed for the thermal dust emission. Furthermore, the calibrated thermal dust intensity templates are those derived from the 2013 *Planck* thermal dust model; although they are close, these templates do not strictly correspond to the calibration of the 2015 maps. Also, the leakage corrections are particularly sensitive to the differences in transmission between bolometers (i.e. the C^b_k coefficients); small uncertainties on those will yield large uncertainties in the final correction maps. In conclusion, the bandpass leakage corrections should not be taken at face value, but should be thought of as order-of-magnitude estimates only. We only advocate the use of these correction maps to test the stability and estimate uncertainties of any further results using the HFI polarization maps. A result solely obtained by applying the corrections will not be reliable.

Calibration and monopole mismatches

Using the same formalism as above, calibration mismatch is computed by setting $\epsilon^b_{{\rm BP},k} = 0$ and $\epsilon^b_{\rm offset} = 0$ in Eq. (3.16). Following closely Sect. 3.7.3, one finds that the total intensity-to-polarization leakage due to calibration mismatch is

$$\begin{aligned} L^{\rm gain}_{IQ,IU} &= \sum_k C_k I^k \times \sum_{b=0}^{N_{\rm bolo}-1} \epsilon^b_{\rm gain} \Gamma^b_{IQ,IU} \\ &\approx I^{\rm dipole} \times \sum_{b=0}^{N_{\rm bolo}-1} \epsilon^b_{\rm gain} \Gamma^b_{IQ,IU}, \end{aligned} \tag{3.24}$$

[3] The Γ_{II} pattern map quantifies the correction that should, in principle, be brought to the I channel map, given that some intensity has leaked into polarization. The correction is, however, negligible and is not taken into account here. The same is true for Γ_{QQ} and Γ_{UU}.

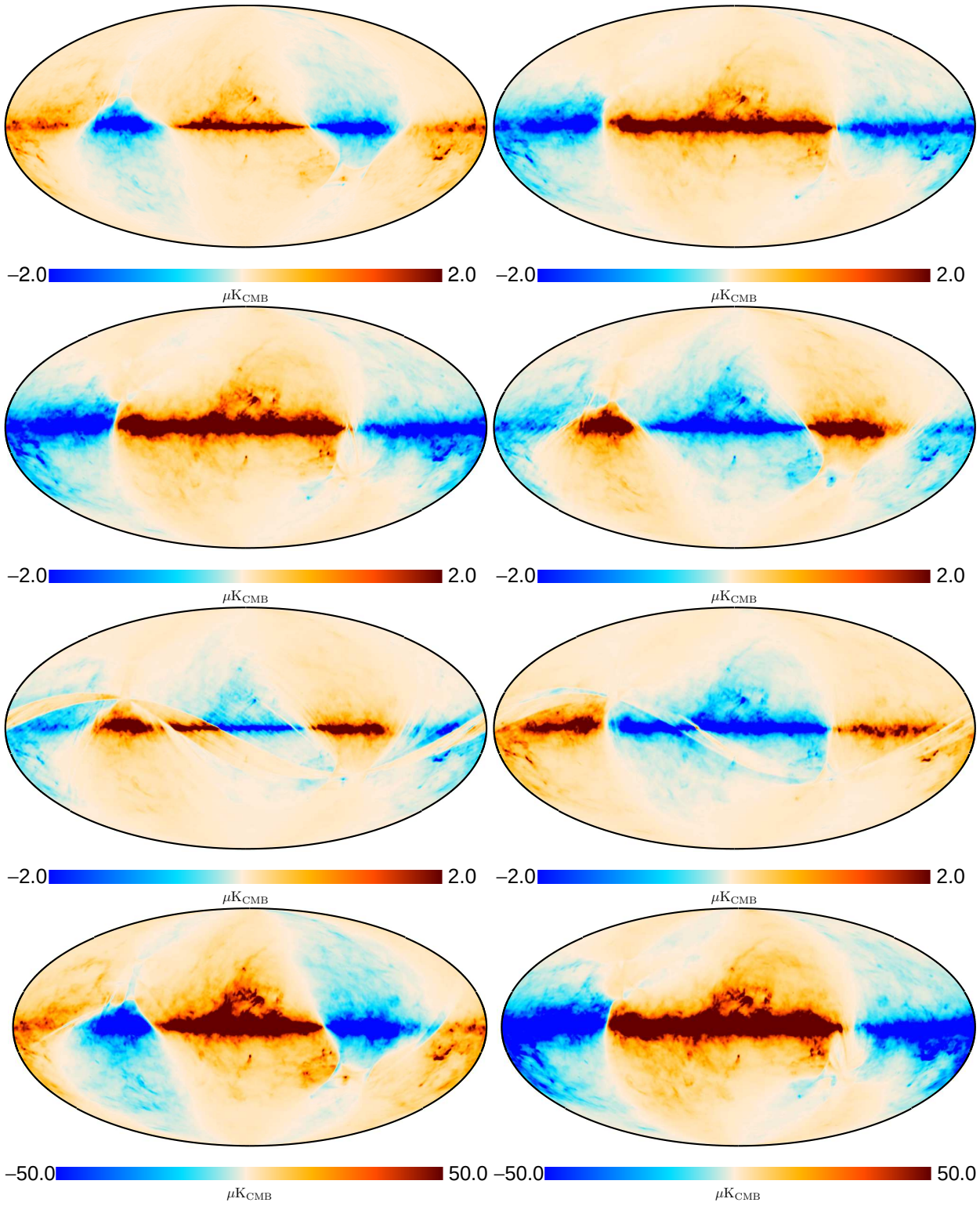

Figure 3.19: Dust leakage correction maps from ground-based measurements of the bandpass in Q (left) and U (right) at all HFI channels: 100, 143, 217, and 353 GHz (from top to bottom).

where at first order, for low-frequency maps, the solar dipole signal (k=dipole, $C_{\rm dipole}$=1 by construction) provides the dominant contribution to the calibration mismatch leakage effect.
Setting $\epsilon^b_{{\rm BP},k}$=0 and $\epsilon^b_{\rm gain}$=0 in Eq. (3.16), one shows in a similar fashion that the monopole intensity-to-polarization leakage is simply

$$L^{\rm mono}_{IQ,IU} = \sum_{b=0}^{N_{\rm bolo}-1} \epsilon^b_{\rm offset} \Gamma^b_{IQ,IU}, \tag{3.25}$$

where the monopole mismatch is modelled using a constant sky template $I^{\rm monopole}$=1, while the amplitude of the mismatch is encoded in $\epsilon^b_{\rm offset}$.
Although the bandpass mismatch coefficients $\epsilon^b_{\rm BP,dust}$ can be evaluated directly from foreground modelling (assuming a given spectrum of the dust and using the spectral responses of the detectors), this is not the case for $\epsilon^b_{\rm gain}$ and $\epsilon^b_{\rm offset}$. It is therefore not possible to provide correction maps for these leakage effects by computing Eq. (3.24) and (3.25) directly. However, one can consider the possibility of fitting these quantities from the maps themselves by using the $I^{\rm dipole}\times\Gamma^b_{IQ,IU}$ and $\Gamma^b_{IQ,IU}$ as templates of the gain and monopole leakages, respectively. Such a method, known as the generalized global fit (GGF), has been implemented.The leakage maps produced with this method for the 353 GHz channel are delivered in the 2015 release and have been corrected simultaneously for leakages induced by bandpass, calibration, and monopole mismatches.

3.7.4 In-flight validation of the polarimeter efficiency and orientation

As discussed in Sect. 3.4.5, the polarimeter efficiency and orientation used in this release are taken from ground measurements (Rosset et al. 2010). In order to validate these numbers in flight, we used the Crab nebula maps obtained with the IRAM 30 m telescope and the 90 GHz XPOL polarimeter (Aumont et al. 2010). These maps consist of I, Q, and U measurements with an angular resolution of 27″ of a 10′-wide region around the Crab nebula (Tau A, M1, or NGC 1952, at J2000 coordinates RA = $5^{\rm h}34^{\rm m}32^{\rm s}$ and Dec = 22°00′52″). The same region was observed by *Planck* once per survey, with different scan directions for odd and even surveys. We compared single survey, single bolometer maps of the Crab region with a model obtained from the IRAM maps, and solved for the best values of polarimeter angle and efficiency.
From single survey, single bolometer data we can only solve for an intensity map, which projects on the sky the total power P_t described in Eq. (3.1). This power depends on the true value of the polarization angle α specific to the detector. We compared the single bolometer, single survey maps with a model obtained with the following procedure:

- we pixelized the IRAM observations on a HEALPix grid with $N_{\rm side}$=2048, rotating to Galactic coordinates;
- we convolved these maps with the single bolometer, single survey effective beams using FEBeCoP (Mitra et al. 2011);
- using the Crab IRAM map as a template, and the polarization angles α, we modelled the intensity map described above in the Crab region as a function of an angular offset $\Delta\alpha$.

We then fitted for the values of the angular offset $\Delta\alpha$. To do that, we first removed the background from the single bolometer maps. We built a noise model combining the single detector pixel variance with the noise of the IRAM observation, taking into account the smoothing applied. We used the Rosset et al. (2010) values as a prior.
The resulting angular offsets are presented in Fig. 3.20. Corrections are compatible with zero, and this analysis does not favour an update of the ground-based parameters. We used the same procedure to fit the polarization efficiency ρ, but the result is completely dominated by the ground-based calibration prior.
If we assume that the CMB anisotropies have vanishing TB and EB power spectra, i.e. that there are no parity-violating physical mechanisms in the early Universe, we can also check whether the overall polarizer angle of *Planck*-HFI is compatible with zero. Planck Collaboration XLIX (2016) show that the CMB TB and EB spectra measured by HFI are consistent with zero. Their analysis gives a polarizer angle within 0.3° of zero, which is identical to the systematic error of the ground-based measurements. This is a factor of five improvement over the *WMAP* final results (Hinshaw et al. 2013) and is comparable with ACT (Naess et al. 2014; see also the review by Gubitosi & Paci 2013).

3.8 Conclusions

This paper has described the processing applied to construct the *Planck*-HFI maps delivered in the 2015 release. It has also assessed the main characteristics of the maps in terms of noise and systematics, in particular resulting from the analog-to-digital converter non-linearity correction and bolometer long time constants. Since the last release, the calibration has been upgraded and is now significantly more accurate. At low frequency, it is now independent and based on the orbital dipole signal, while the planets Uranus and Neptune are used to calibrate the high end of HFI, achieving 6.1 and 6.4 % absolute photometric calibration at 545 and 857 GHz, respectively. This has allowed us to measure a consistent CMB solar dipole with an unprecedented accuracy better than 10^{-3} and in agreement with the independent determination by LFI.

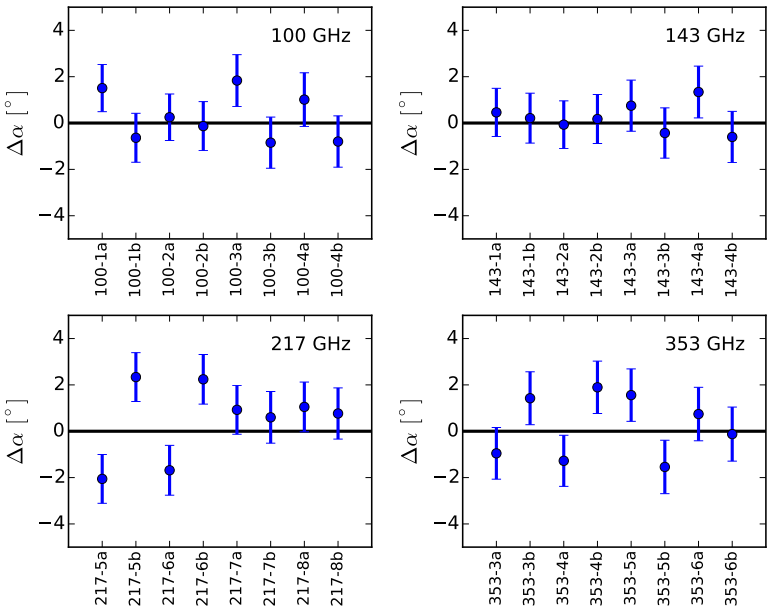

Figure 3.20: Estimated angular offset from comparison of the single bolometer, single detector maps with the IRAM Crab nebula maps, combining the first four surveys.

Table 3.6 gives a quantitative assessment of the main characteristics of the *Planck* HFI maps from the 2015 release. They now cover the entire *Planck* HFI cold mission (885 days). The HFI aggregated sensitivity (referring to a weighted average of the 100, 143, and 217 GHz channel maps) is $26\mu K_{CMB}$arcmin in temperature and $52\mu K_{CMB}$arcmin in polarization.
The noise in the maps shows some small low-frequency excess in addition to white noise prior to time constant deconvolution. The latter then naturally raises the higher part of the noise spectra in the multipole domain. We have identified a low-level noise correlation in particular between half-ring and detector subsets that is not directly reproduced by simulations, although the level is low compared to the CMB signal.
The raw sensitivity must be matched by a long list of constraints on any possible systematic effects. This list includes: an absolute calibration at a level from 0.1 % to 1.4 % depending on the frequency; a resulting apparent gain variation of less than 0.5 %; and a knowledge of the polarization angle and polarization absolute value respectively at the degree level and the 1 % level. The instrumental beam has been measured at the percent level by using multiple planet crossings.
Despite the huge progress made in the understanding of all the aforementioned systematic effects, *Planck*-HFI polarization maps are still dominated by systematic residuals at large scales. These are essentially coming from the temperature-to-polarization leakage resulting from the mismatch between the bolometers that are combined to reconstruct linear polarization maps. The origins of the leakage effects include mismatch of the zero level from uncertainty in the offset determination, mismatch from gain uncertainty (even at the 10^{-3} level), and bandpass mismatch. Corresponding first-order corrections for monopole, dipole, and bandpass mismatch are provided but residuals are still found to be larger than noise at very large scales. As a consequence, the *Planck*-HFI polarization maps at large scales cannot yet be directly used for cosmological studies.

Table 3.6: Main characteristics of HFI Full Mission Maps.

Quantity							Notes
Reference frequency ν [GHz]	100	143	217	353	545	857	*a1*
Number of bolometers	8	11	12	12	3	4	*a2*
Effective beam solid angle Ω [arcmin^2]	106.22	60.44	28.57	27.69	26.44	24.37	*b1*
Error in solid angle σ_Ω [arcmin^2]	0.14	0.04	0.04	0.02	0.02	0.02	*b2*
Spatial variation (rms) $\Delta\Omega$ [arcmin^2]	0.20	0.20	0.19	0.20	0.21	0.12	*b3*
Effective beam FWHM$_1$ [arcmin]	9.68	7.30	5.02	4.94	4.83	4.64	*b4*
Effective beam FWHM$_2$ [arcmin]	9.66	7.22	4.90	4.92	4.67	4.22	*b5*
Effective beam ellipticity ϵ	1.186	1.040	1.169	1.166	1.137	1.336	*b6*
Variation (rms) of the ellipticity $\Delta\epsilon$	0.024	0.009	0.029	0.039	0.061	0.125	*b7*
Sensitivity per beam solid angle [μK$_{\rm CMB}$]	7.5	4.3	8.7	29.7			*c1*
[kJy sr^{-1}]					9.1	8.8	*c1*
Temperature Sensitivity [μK$_{\rm CMB}$ deg]	1.29	0.55	0.78	2.56			*c2*
[kJy sr^{-1} deg]					0.78	0.72	*c2*
Polarization Sensitivity [μK$_{\rm CMB}$ deg]	1.96	1.17	1.75	7.31			*c3*
Calibration accuracy [%]	0.09	0.07	0.16	0.78	1.1(+5)	1.4(+5)	*d*
CIB monopole [MJy sr^{-1}]	0.0030	0.0079	0.033	0.13	0.35	0.64	*e1*
Zodiacal light level correction [K$_{\rm CMB}$]	4.3×10^{-7}	9.4×10^{-7}	3.8×10^{-6}	3.4×10^{-5}			*e2*
[MJy sr^{-1}]					0.04	0.12	*e2*

a1 Channel map reference frequency and channel identifier.
a2 Number of bolometers whose data were used in producing the channel map.
b1 Mean value over bolometers at the same frequency. See Sect. 4.2 in Planck Collaboration VII (2016).
b2 As given by simulations.
b3 Variation (rms) of the solid angle across the sky.
b4 FWHM of the Gaussian whose solid angle is equivalent to that of the effective beams.
b5 Mean FWHM of the elliptical Gaussian fit.
b6 Ratio of the major to minor axis of the best-fit Gaussian averaged over the full sky.
b7 Variability (rms) on the sky.
c1 Estimate of the noise per beam solid angle as given in *b1*.
c2 Estimate of the noise in intensity scaled to 1° assuming that the noise is white.
c3 Estimate of the noise in polarization scaled to 1° assuming that the noise is white.
d Calibration accuracy (at 545 and 857 GHz: the 5% accounts for the model uncertainty).
e1 According to the Béthermin et al. (2012) model, whose uncertainty is estimated to be at the 20 % level (also for constant νI_ν).
e2 Zero-level correction to be added on Zodical-light-corrected maps.

This work have been performed for the Planck-HFI collaboration. It has been presented in detail in many collaboration meetings and take advantage of interactions with the entire Planck collaboration. In particular, I have worked with B. Crill, G. Lagache, O. Perdereau.

Bibliography

Aumont, J., Conversi, L., Thum, C., et al. 2010, A&A, 514, A70
Béthermin, M., Daddi, E., Magdis, G., et al. 2012, ApJ, 757, L23
Fixsen, D. J. 2009, ApJ, 707, 916
Górski, K. M., Hivon, E., Banday, A. J., et al. 2005, ApJ, 622, 759
Gubitosi, G. & Paci, F. 2013, J. Cosmology Astropart. Phys., 2, 20
Hinshaw, G., Larson, D., Komatsu, E., et al. 2013, ApJS, 208, 19
Hinshaw, G., Weiland, J. L., Hill, R. S., et al. 2009, ApJS, 180, 225
Kamionkowski, M. & Knox, L. 2003, Phys. Rev. D, 67, 063001
Kelsall, T., Weiland, J. L., Franz, B. A., et al. 1998, ApJ, 508, 44
Mather, J. C., Fixsen, D. J., Shafer, R. A., Mosier, C., & Wilkinson, D. T. 1999, ApJ, 512, 511
Mitra, S., Rocha, G., Górski, K. M., et al. 2011, ApJS, 193, 5
Moreno, R. 2010, Tech. rep., ESA Herschel Science Center, available from ftp://ftp.sciops.esa.int/pub/hsc-calibration/PlanetaryModels/ESA2
Naess, S., Hasselfield, M., McMahon, J., et al. 2014, J. Cosmology Astropart. Phys., 10, 7
Planck HFI Core Team. 2011, A&A, 536, A6
Planck Collaboration VI. 2014, A&A, 571, A6
Planck Collaboration VIII. 2014, A&A, 571, A8
Planck Collaboration IX. 2014, A&A, 571, A9
Planck Collaboration XI. 2014, A&A, 571, A11
Planck Collaboration XIV. 2014, A&A, 571, A14
Planck Collaboration XXXI. 2014, A&A, 571, A31
Planck Collaboration VII. 2016, A&A, 594, A7
Planck Collaboration VIII. 2016, A&A, 594, A8
Planck Collaboration IX. 2016, A&A, 594, A9
Planck Collaboration X. 2016, A&A, 594, A10
Planck Collaboration XI. 2016, A&A, 594, A11
Planck Collaboration XII. 2016, A&A, 594, A12
Planck Collaboration XLIX. 2016, A&A, 596, A110
Planck Collaboration LII. 2016, ArXiv e-prints [arXiv:1612.07151]
Quartin, M. & Notari, A. 2015, ArXiv e-prints [arXiv:1504.04897]
Rosset, C., Tristram, M., Ponthieu, N., et al. 2010, A&A, 520, A13
Tauber, J. A., Norgaard-Nielsen, H. U., Ade, P. A. R., et al. 2010, A&A, 520, A2
Tristram, M., Filliard, C., Perdereau, O., et al. 2011, A&A, 534, A88

Chapter 4

Last map-making version

After the first release of the polarization maps from Planck in 2015, we worked on the map-making algorithm in order to take into account systematic residuals that prevent us from measuring the large scales using polarisation data. We upgraded the map-making algorithm in order to take into account instrumental effects using templates for which we fit the amplitudes while solving for the sky pixels. The resulting maps show less residuals at large scales but we still missed dedicated Monte-Carlos in order to characterize accurately the level of contamination from systematics in Planck data.

4.1 Introduction

Over the years working on map-making and calibration techniques for *Planck*-HFI, we have identified several systematics or instrumental effects that affect both the destriping and the calibration reconstruction. While for temperature, the effect is very tiny compare the strong signal-to-noise ratio offered by *Planck*, this is not the case in polarisation. Indeed, we have seen, in the 2013 releases (Planck Collaboration VIII 2014) and the 2015 releases (Planck Collaboration VIII 2016), strong intensity-to-polarisation leakage effect coming from the uncertainty in the gain recovery or the apparent gain variation coming from the ADC non-linearity (see Chapter 2 and 3).

More generally, any mismatch between detector signal falling into the same pixel will create I-Q-U mixing which is dramatic for the polarisation given the difference in the amplitude of the signals (in particular if you consider the dipole amplitude more than 10 times greater than the intensity anisotropies also roughly 10 times larger than the polarisation amplitude). For one detector, this mismatch arise from instrumental effect which vary with time (such as Far Side Lobes effects, long time constant residuals or ADC non-linearity) but also from time-varying foregrounds signals (such as Zodiacal light for exemple).

Moreover, we have demonstrated that destriping is more accurate when considering several detectors in the same minimization. This is also the case for calibration, while inter-calibration is then naturally taken into account. But adding more detectors means that we have to face more potential mismatch between signals falling into the same pixel. Indeed on top of varying signals, we also then add detector gain mismatch from calibration uncertainties but also from bandpass transmission mismatch. The latter is due to the particular shape of the bandpass transmission which differ from one bolometer to the other, inducing a different response to all signals which are not in CMB units (chosen for calibration) including foregrounds (essentially Dust and CO as far as HFI frequencies are concerned).

The differences in the bandpass functions will produce different detector response for sky emissions which are not CMB. At *Planck*-HFI frequencies, those include essentially Galactic Dust emission ($T^{\rm dust}$) and molecular lines emissions (CO, $T^{\rm CO}$).

4.2 Algorithm

To reduce the level of leakage, we added several time-variable (in time or ring domain) templates in the multi-detector map-making model. The power absorbed by a detector then reads

$$P_t = g(A_{tp} S_p + T_t^{\rm orb} + c_{\rm zodi} T_t^{\rm zodi} + c_{\rm FSL} T_t^{\rm FSL} + c_{\rm BP}^{\rm dust} T_t^{\rm dust} + c_{\rm BP}^{\rm CO} T_t^{\rm CO} + c_{\rm RLTC} T_t^{90^\circ} + \Gamma_{tr} o_r) + n_t. \quad (4.1)$$

The templates include:

- $T^{\rm orb}$, the orbital dipole (in practice the total dipole with relativistic corrections). It is a time-varying signal which can be accurately calculated from the satellite velocity knowing the CMB temperature. It is used as the reference to calibrate the data.
- $T^{\rm zodi}$, the Zodiacal light emission for each detector (as measured from the previous *Planck* data release);
- $T^{\rm FSL}$, the Far Side Lobe for each detector (based on a simulation with dipole+galaxy convoluted by the model of FSL). The FSL template account for the varying shape of the Far Side Lobe pattern depending on the orientation of the satellite with time. It is based on pre-launch optical measurements which have been checked to be consistent with in-flight data (see Planck Collaboration VII 2016).
- $T^{\rm dust}$, the Galactic dust intensity signal (accounting for the difference of dust emission between bolometers due to bandpass mismatch). The effect of bandpass-mismatch is largely dominated by intensity-to-polarization leakage while the polarization-to-polarization mixing can safely be neglected. In principle, to fit polarization-to-polarization, we would need to add a specific coefficient as the SED of dust in intensity and polarization slightly differ (Planck Collaboration Int. XXII 2015) and because the calibration of the polarized signals is affected both by the gain but also by the polarization efficiency associated to each detector. Moreover, we do not have accurate enough templates for polarization signal of the dust. Indeed, the 353 GHz channel from *Planck* is still contaminated by systematics and the noise is important, especially at high galactic latitude where the template dominates. As a consequence, we only consider intensity signal for the $T^{\rm dust}$ template which comes from the 353 GHz channel.
- $T^{\rm CO}$, the CO intensity signal (accounting for the difference of CO emission between bolometers due to bandpass mismatch). The emission from molecular lines is not expected to be significantly polarized. We use a signal from the component separation (Planck Collaboration X 2016).
- T^{90°, a 90° shifted-dipole. It allows to deal with the residual from long time-response (RLTC) uncertainties in the bolometer model. We use a first order expansion of a long time constant convolved by a dipole signal.

The map-making & calibration equation 4.1 can be written:

$$\mathbf{P}=\tilde{g}(\mathsf{A}\tilde{\mathbf{S}}+\tilde{\mathbf{c}}\cdot\mathsf{T}+\Gamma\tilde{\mathbf{o}})+\mathbf{n} \tag{4.2}$$

where we solve consistently for:

– the sky $\tilde{\mathbf{S}}$ in temperature and polarization (in each pixel),

– the gains $\tilde{g}$ (for each bolometer, either constant for the whole mission or one per ring),

– the offsets $\tilde{\mathbf{o}}$ (one per ring per bolometer),

– the template coefficients $\tilde{\mathbf{c}}$ (one per bolometer per template).

The coefficient for the orbital dipole is fixed to one as we use this signal as reference for the calibration. The Zodiacal light emission and the Far Side lobe signal are measured independently prior to the map-making. In practice, we fixed their coefficient and subtracted them from the input data prior to mapmaking. Effect of both emissions are negligible on the systematic budget. The difference between the procedure apply for the 2015 *Planck* release relies essentially in that we are now fitting altogether in the map-making procedure the amplitudes of bandpass-mismatch for the dust ($c^{\rm dust}_{\rm BP}$) and for CO ($c^{\rm CO}_{\rm BP}$) and the amplitude of residuals of long time-constant $c^{\rm RLTC}$ using all bolometers from the same frequency. We add a constraint on the bandpass coefficients (for dust and for CO) to be equal to 0 in mean so that we leave the average emission in the intensity sky signal S.
To solve this non-linear equation, we linearize at first order in g and use the same algorithm as for `bogopix` (presented in Chapter 3). As previously, we use a Galactic mask to avoid fitting the parameters on the inner part of the Galaxy where signal is strongly varying from one pixel to the other and where the model is not accurate enough. We also remove regions where we found strong CO emission. Once the gains g, the offsets o and the coefficients c are fitted, we then estimate the signal S on the entire sky (i.e. without mask).

For the post-2016 releases, the official *Planck*-HFI maps are produced at IAP using the code SRoll (see Planck Collaboration Int. XLVI 2016). The code implements exactly the same algorithm but uses an empirical model for RLTC including additional templates. Indeed, it is made of several harmonics of the signal rather than a 90° shifted dipole (in practice 3 bins including the harmonics from 1 to 3, harmonics from 4 to 7, and harmonics from 8 to 15). We think it is very dangerous to fit harmonics of the signal without demonstrating, through Monte Carlo simulations, the level of filtering associated to this procedure. Another difference, but with much smaller effect, is that the SRoll code does not fit the variable gains ring-by-ring but by bunch of rings such that the total dipole gain variance is constant over each period.

4.3 Results

Using the algorithm described in the previous section, we have produced maps for the three first frequencies of the *Planck*-HFI at 100, 143 and 217 GHz. We have checked the consistency of the recovered coefficients with previous results and external measurements. However, due to the lack of simulations available, we have not been able to study in details the

uncertainties on the recovered coefficients as well as the correlation between the different templates and the possible bias on the gain estimation.

4.3.1 Residuals of Long Time-Constants (RLTC)

We compared the amplitudes of the shifted-dipole c^{RLTC} with the values used in previous release (DX11d, *Planck* 2015). Up to now, the coefficients were estimated on bolometers independently prior to map-making. They are now part of the map-making procedure where we also reconstruct polarisation signal. Figure 4.1 shows that the impact on the coefficients increases with frequency (which indicates a correlation with foreground Galactic dust emission) and is related to polarisation (as suggested by the difference between *a* and *b* bolometers from the same horn). We also check the impact of the correction for the Zodiacal light and for the FSL which is found to be negligible.

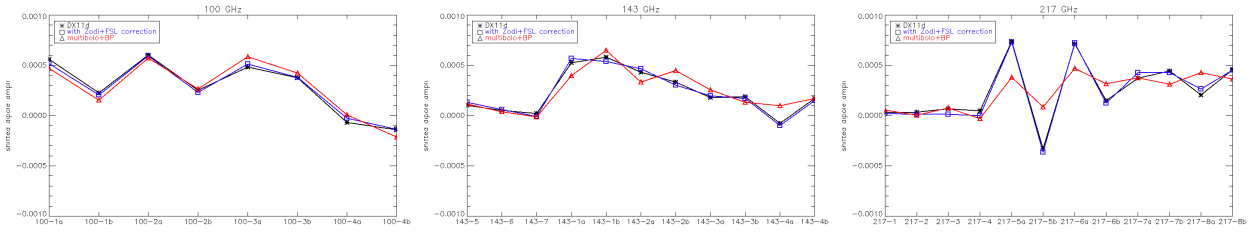

Figure 4.1: Coefficients for the residual of long time constant. *black:* for the DX11 release (where the coefficients were fitted for each bolometer independently prior to map-making); *blue:* with correction for FSL and Zodi signals; *red:* with the new map-making procedure.

4.3.2 Bandpass-mismatch

The dust bandpass-mismatch coefficients correspond to the integration of the dust SED into the passband of the detectors. Figure 4.2 shows the comparison between the bandpass-mismatch coefficients c^{BP} recovered in the map-making with the values expected from the ground-based pre-launch passband measurements (computed using a dust spectrum with β= −1.62 and T_{dust}=19.7K) (Planck Collaboration IX 2014). There are percent deviations with the sky-based measurement, but the ground-measurement suffer from complex error bars related to measurement of the higher part of the passband transmission. Nevertheless, the overall trend is well reproduced. The coefficients recovered are stable with respect to the FSL&Zodi correction, or the RLTC coefficients.
We have also check the consistency with measurement based on diffuse cloud emissions (not shown here) in which we directly compare the measured intensity between several detectors at the same frequency after having subtracted a CMB component.

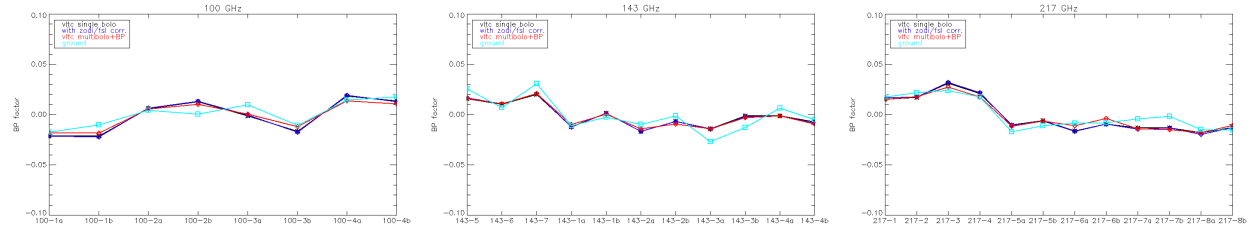

Figure 4.2: Coefficients for the bandpass-mismatch for dust. *black:* using RLTC coefficients from DX11; *blue:* with correction for FSL and Zodi signals; *red:* with the new map-making procedure; *cyan:* from the ground-based pre-launch measurements.

4.3.3 Gain

Requirement on the gain reconstruction is extremely strong for the *Planck* scanning strategy combining several detectors to recover polarization signal. As we have seen in Tristram et al. (2011) (Chapter 1), even with a statistical uncertainty of 5×10^{-5}, the intensity-to-polarisation leakage is only one order of magnitude below the CMB signal on *EE* angular power spectra. However, systematics residuals (from time-response uncertainties, bandpass-mismatch and ADC non-linearity) bias the reconstruction of the gain, increasing the leakage level.
We distinguish two cases here:

- a constant gain for each bolometer over the whole mission. This is what the instrument model predicts considering the fact extreme stability of the bolometer and electronics during the mission that have been checked comparing the optimization of the bolometer equilibrium at the beginning and at the end of the mission.

- a gain ring-by-ring gain variation to allow for apparent gain changes that might result from systematic residuals (such as ADC non-linearity residuals for exemple).

Figure 4.3 shows the relative change of constant gains with respect to the *Planck* 2015 release. We observe relative change of the order of a few 10^{-4}, with an asymmetry between bolometers *a/b* of the same pair which is related to a polarization effect. We also compare to the results obtained when using the previous coefficients for RLTC. The (though small) changes in amplitude of the c_{RLTC} affect the gain estimation from a few 10^{-4} level at 100 GHz up to 5.10^{-4} at 143 GHz.

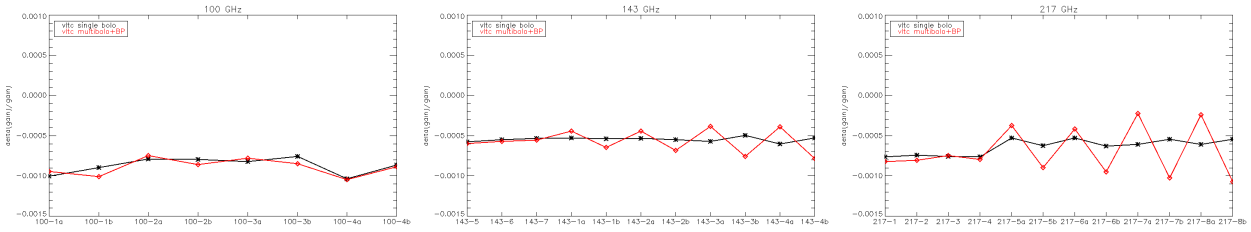

Figure 4.3: Relative change on the gain coefficients compared to *Planck* 2015 release. *black:* using RLTC coefficients from DX11; *red:* with the new map-making procedure.

Similarly to the last releases, the ring-by-ring gain reconstruction is dominated by noise (Planck Collaboration VIII 2016). In order to derive a correction to apply to the data on map projection, we smoothed the ring-by-ring estimation with a variable length adapted to the signal-to-noise level before projecting the final maps. Figure 4.4 shows the gain variations recovered with the new algorithm. Thanks to the ADC correction in time domain and to the use of templates for systematics in the map-making, they are now at the per-mile level. However, they still slightly increase the consistency between time splits, allowing the jackknives tests to pass.

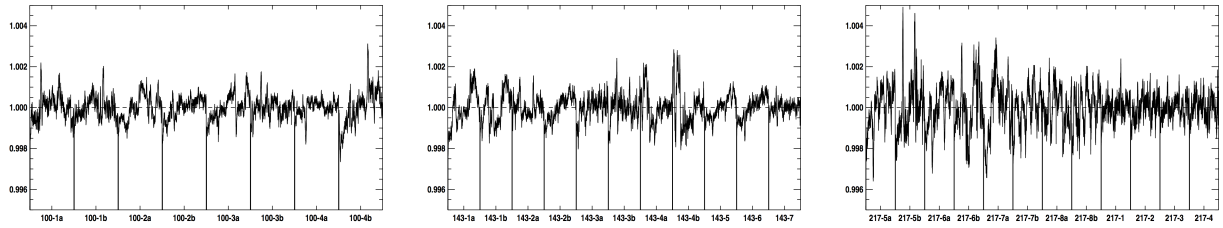

Figure 4.4: Gain estimation ring-by-ring after smoothing with a variable length adapted to the signal-to-noise level.

We have seen no effect of the Galactic mask used in the calibration process on the variable gains reconstruction.

4.4 Maps

After map projection, residual systematics are lower than the dust signal even if they can dominate on large angular scales. In Fig. 4.5, we plot the Q stokes residual maps after dust subtraction in different cases: the *Planck* 2015 release (DX11, Planck Collaboration VIII 2016); this analysis with constant gains over the mission; this analysis with ring-by-ring gains; the maps produced at IAP using the same kind of algorithm SRoll (RD12). To subtract the dust we simply used the 353 GHz channel as a template using a uniq coefficient on the sky. The residual maps include CMB polarization and systematic residuals. In order to focus on the large scales, the maps have been smoothed to 5°.

We can see by eye the significative improvement of the residuals compared to *Planck* 2015 release (DX11). Using variable gains increase the consistency between survey maps but the impact seems less important in the full-mission maps.

Compared to the RD12ll, the maps show less residuals at 100 and 143 GHz. At 217 GHz, we have still a large amount of residuals meaning that the actual systematic templates can not reproduce the residual systematics. Given the results obtained using SRoll algorithm, we think this comes from the residual long time-response systematic. Indeed the RLTC is stronger at high frequency and its impact is stronger due to higher level of Galactic dust emission. The SRoll algorithm, by filtering the lower frequency using additional templates from the harmonics of the signal, succeed in removing the large scale feature of the systematic resulting in a certainly better estimation of the gains at high frequency. However, due to the absence of simulations, we have not been able to confirm this hypothesis.

Note also that those residuals strongly depend on the 353 GHz map which is used to remove the dust contamination.

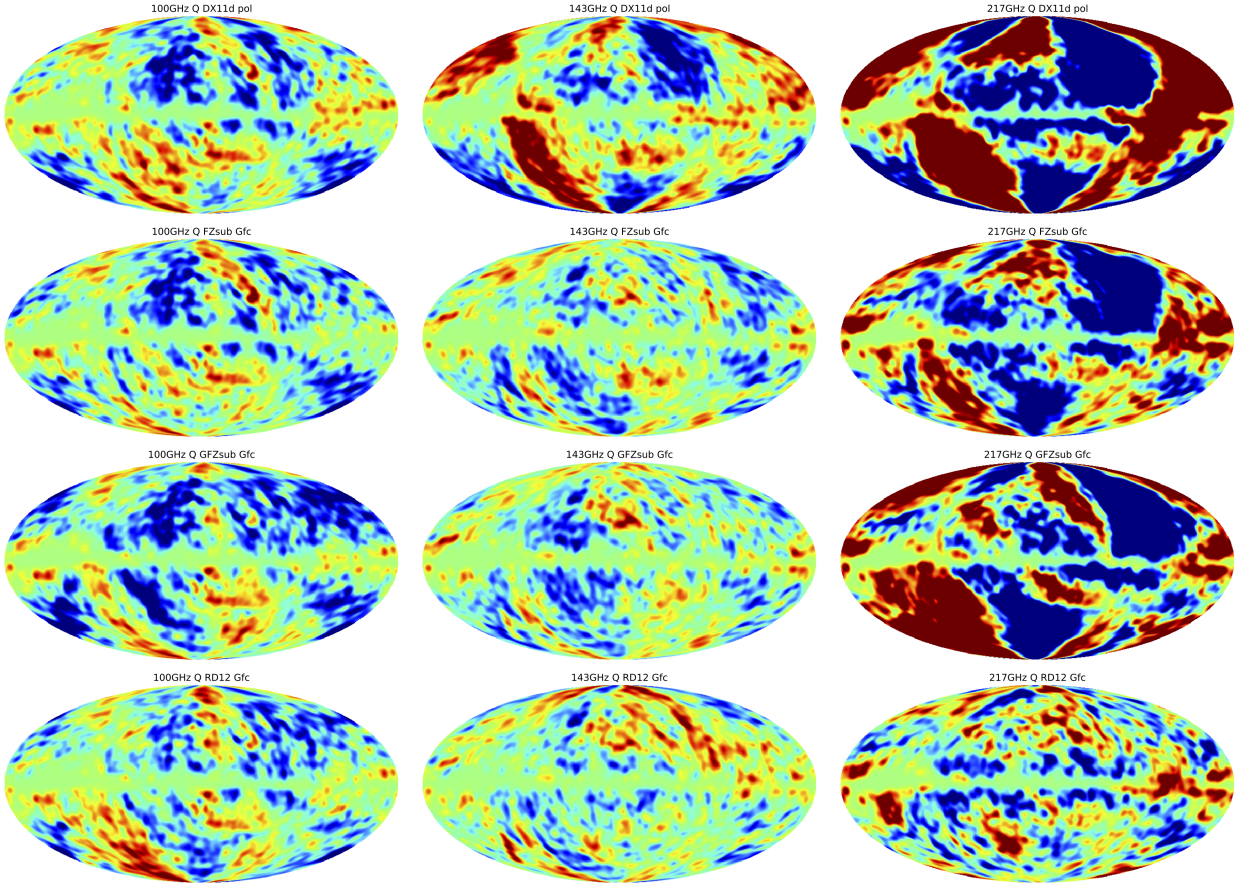

Figure 4.5: Maps of Q stokes parameter at 100, 143, and 217 GHz for the *Planck* 2015 release (DX11d, *raw 1*), the new map-making with constant gain (FZsub, *raw 2*), the new map-making with variable gains (GFZsub, *raw 3*) and SRoll (RD12ll, *raw 4*) respectively. The range is $\pm 1 \mu$K.

4.5 Conclusion

We have significantly improved the DPC map-making procedure by including systematic templates. Those includes Zodiacal light correction, Far Side Lobe signal as well as bandpass mismatch related to Galactic dust and CO emission and long time-response residuals. This allows for a significant decrease of the bias on the gain and offsets determination which consequently reduces the intensity-to-polarization leakage. Based on this work, the algorithm has been duplicated at IAP (renamed as `SRoll`). Results are comparable but for small differences coming from the template constructions.
In 2016, the *Planck*-HFI PI decided to use `SRoll` maps for the low-ℓ analysis and the final release. However, we have shown that the maps obtained with our updated version of `polkapix` are cleaner than the *Planck* 2015 maps and even cleaner than the one from `SRoll` (at least at 100 and 143 GHz).
To go further in the characterization of the maps and give a reliable estimation of residual systematics, we would need Monte Carlo simulations which are not available for now. This will allow both to check for potential bias in the parameter recovery (in particular the gains) and estimate the impact on the signal (as we think should happened in the case of `SRoll` when fitting for harmonics of the signal). Moreover, it is the only way to get an accurate estimation of the propagation of the systematic uncertainties which are currently neglected (as in Planck Collaboration Int. XLVI 2016).
This exercise is still missing in the *Planck* analysis and is absolutely needed in particular for the large scales interpretation where both the foregrounds and the systematics are by far dominant over the statistical noise.

No comment...

Bibliography

Planck Collaboration VIII. 2014, A&A, 571, A8
Planck Collaboration IX. 2014, A&A, 571, A9
Planck Collaboration VII. 2016, A&A, 594, A7
Planck Collaboration VIII. 2016, A&A, 594, A8
Planck Collaboration X. 2016, A&A, 594, A10
Planck Collaboration Int. XXII. 2015, A&A, 576, A107
Planck Collaboration Int. XLVI. 2016, A&A, 596, A107
Tristram, M., Filliard, C., Perdereau, O., et al. 2011, A&A, 534, A88

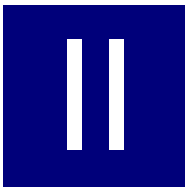

Likelihoods

Chapter 5

Lollipop: Low-ℓ Likelihood Polarized for Planck

extracted from Mangilli et al. (2015)

"Large-scale CMB temperature and polarization cross-spectra likelihoods"

For Planck purpose, I have worked on the large-scale polarised likelihood. I managed a small team dedicated to this within the Planck collaboration: lollipop *for* LOw-L LIkelihood Polarized On Planck. *Before applying to the Planck data, we worked with my post-doc Anna Mangilli and in collaboration with S. Plaszczynski on the statistics of the low multipoles and in particular on how we could build a cross-spectra likelihood for low-ℓ. This work was published in Mangilli et al. (2015) and is copied in this chapter.*

We present a cross-spectra based approach for the analysis of CMB data at large angular scales to constrain the reionization optical depth τ, the tensor to scalar ratio r and the amplitude of the primordial scalar perturbations A_s. With respect to the pixel-based approach developed so far, using cross-spectra has the unique advantage to eliminate spurious noise bias and to give a better handle over residual systematics, allowing to efficiently combine the cosmological information encoded in cross-frequency or cross-dataset spectra. We present two solutions to deal with the non-Gaussianity of the $\hat{C}_\ell$ estimator distributions at large angular scales: the first one relies on an analytical parametrization of the estimator distribution, while the second one is based on modification of the Hamimeche&Lewis likelihood approximation at large angular scales. The modified HL method (oHL) is powerful and complete. It allows to deal with multipole and mode correlations for a combined temperature and polarization analysis. We validate our likelihoods on numerous simulations that include the realistic noise levels of the *WMAP*, *Planck*-LFI and *Planck*-HFI experiments, demonstrating their validity over a broad range of cross-spectra configurations.

5.1 Introduction

One of the main challenges left for the present and future Cosmic Microwave Background (CMB) experiments is the high precision measurement of the CMB polarization anisotropies at large angular scales. This signal is extremely interesting because it encodes unique informations about the ionization history of the Universe and the inflationary epoch and it can be used as an independent and complementary probe to the small scale CMB information to constrain two important cosmological parameters: the optical depth to reionization τ and the tensor-to-scalar ratio parameter r which is related to the amplitude of the primordial tensor modes. Moreover, the large scales CMB signal is useful in breaking parameter degeneracies, in particular concerning the two parameters: τ and the amplitude of the primordial scalar density perturbations A_s which are strongly correlated through the amplitude of the first acoustic peak $\mathcal{A}_{TT}=A_s e^{-2\tau}$.
Current CMB experiments, in particular the ones that, as *Planck* (Planck Collaboration I 2015), targeted the accurate measurement of the CMB temperature anisotropies, have now reached a level of precision and resolution such that they have exploited all their statistical power, and are now limited by the systematic effects related to the instrument design and technology. An unprecedented accuracy and care at each step of the data analysis and its interpretation is therefore required to access the cosmological information encoded in the CMB polarization anisotropies at large angular scales. In

this paper we address this issue focusing on the importance of developing statistical methods specific to the analysis of CMB data at large angular scales that allow to minimize the impact of residual systematics related to the experimental configuration and design.

Given that the distribution of the CMB anisotropies is compatible with a Gaussian distribution, all the relevant statistical information is encoded in the two points correlation function of the CMB temperature and polarization anisotropies or, equivalently, its projection in harmonic space: the angular power spectrum of the CMB temperature and polarization fields. This is defined as $\hat{C}_\ell = \langle a_{\ell m} a^*_{\ell' m'} \rangle \delta_{\ell\ell'}$, where $a_{\ell m}$ are the coefficients of the spherical harmonic decomposition. The connection between the measured CMB data and the theory is done through the CMB likelihood function $\mathcal{L} = P(\mathbf{d}|C_\ell(\alpha))$ that quantifies the match between the CMB data $\mathbf{d}$ and a given theoretical model parametrized e.g. by a theoretical power spectrum $C_\ell(\alpha)$ defined in terms of a set of cosmological parameters α.

So far the analysis of the CMB anisotropies at large angular scales has mostly been based on methods that relies on low resolution maps in order to compute the exact CMB likelihood function in pixel space, $\mathcal{L} = P(\mathbf{d}|C_\ell(\alpha))$, with $\mathbf{d} \equiv M(\mathbf{p}) = \sum_{\ell m} a_{\ell m} Y_{\ell m}(\mathbf{p})$. This approach is based on the fact that, given that the CMB anisotropies are compatible with a gaussian distribution with random phases, the $a_{\ell m}$ follow a multi-variate Gaussian distribution. The likelihood function, written in pixel space or, equivalently, in terms of the $a_{\ell m}$ coefficients, is gaussian and therefore can be computed exactly (Gorski et al. 1994; Slosar et al. 2004; Page et al. 2007; Bennett 2013).

The problem of this approach is that, in the case of a real CMB experiment, the maps consist in a combination of signal, noise, instrumental systematics and must account for the incomplete sky coverage necessary to minimize the impact of the foregrounds contamination. In order to achieve the required accuracy at large angular scales, the noise matrix in pixel space must be reconstructed with extremely high accuracy to avoid spurious bias on the parameters reconstruction. However this accuracy can be extremely hard to achieve given the difficulty of the precise characterization not only of the noise but also of the residuals systematics related e.g. to the instrument, the scanning strategy and the residual foregrounds.

Alternatively, the likelihood function could be defined in the harmonic space as done e.g. in the small scales analysis where the data compression from CMB maps to angular power spectra is necessary for computational and numerical reasons. However, the complication of working in harmonic space at large angular scales (low-ℓ multipoles) is related to the fact that the distribution of the $\hat{C}_\ell$ estimators at low-ℓ is non-Gaussian. In harmonic space the $\hat{C}_\ell$ consist in the sum of the square of the harmonic coefficients $a_{\ell m}$ and they have a reduced-χ^2 distribution. Therefore the likelihood of a theoretical power spectrum as a function of the measured $\hat{C}_\ell$ is non-Gaussian. Contrary to the small-scales analysis, the CMB low-ℓ analysis is particularly concerned by this issue given that the central limit theorem cannot be invoked. Previous studies, (Percival & Brown 2006; Hamimeche & Lewis 2008), developed a CMB analysis on large angular scales based on the likelihood definition in harmonic space in terms of auto-spectra, that is to say CMB angular power spectra obtained from a given single frequency/dataset CMB map. This approach however shared problems similar to the pixel based likelihood approach, in particular in terms of the dependency to the noise and of the accurate characterization of the systematics effects at the auto-spectra levels.

In this paper we propose to extend the cross-spectra based approach for the analysis of the CMB temperature and polarization anisotropies to the large angular scales. We provide different solutions to deal with the non-Gaussianity of the cross-spectra estimators at large angular scales. Working in harmonic space using the cross-spectra allows to get rid of noise biases and to minimize the residuals systematics effects by exploiting the cross-correlation between different CMB maps, e.g. cross-frequency and cross-datasets. In this sense, the use of cross-spectra allows to access the cosmological information encoded in the CMB maps at different frequencies and to combine different CMB datasets in a more powerful way with respect to the pixel based or auto-spectra approach.

We present a detailed description of the cross-spectra statistics in Sect. 5.2. In Sect. 5.3 we describe the C_ℓ estimator that we use for the cross-spectra reconstruction and we define the specifications used to generate realistic cross-spectra simulations based on publicly available CMB data. Furthermore, in Sect. 5.3.2, we present the formalism to deal with the non-Gaussianity of the cross-spectra $\hat{C}_\ell$ estimators at large angular scales in the case of our realistic simulation settings. Based on this formalism, in Sect. 5.4 we construct two types of cross-spectra based likelihoods: in Sect. 5.4.1 we present an analytical solution based on the parametrization of the $\hat{C}_\ell$ estimator distribution that is useful for the simplest case of a single-field analysis where correlations can be neglected. In Sect. 5.4.2 we then define a more general method that allows to easily deal with a joint temperature and polarization analysis accounting for both correlations between multipoles and modes (TE, TB, EB). This more general method is based on the extension of the Hamimeche & Lewis (2008) (H&L) approach to the large angular scales analysis and it relies on a re-definition of the H&L variable transformation allowing to approximate the CMB likelihood function by a multivariate Gaussian at low multipoles and for cross-spectra. In Sect. 5.5 we present the likelihood results in the case of a single-field analysis, describing the validation tests and a comparison of the different methods. As the reference single-field we consider the E-modes polarization to constrain the optical depth to reionization parameter τ. The results for the general modified H&L solution (oHL) that accounts for the full temperature and polarization analysis including all correlations are described in Sec. 5.6 where we present constraints of the τ, r and A_s parameters. Also, we discuss the optimality of the oHL method with respect to the pixel based likelihood solutions. Finally in Sect. 5.7 we present our conclusions. We provide in the appendix 5.A the details of the analytic description of the cross-spectra distribution and in appendix 5.B we discuss the comparison of the auto-spectra and cross-spectra statistics.

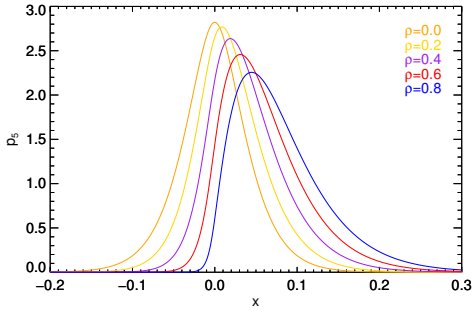

Figure 5.1: Examples of the full-sky cross-spectra distributions $p_N^{A\times B}(x{\equiv}\hat{C}_\ell^{\,A\times B})$ for N=5 modes (ℓ=2) with $\sigma_A\sigma_B$=0.1 and varying the degree of correlation (cf. Eq. 5.2).

5.2 Cross-spectra statistics

In order to gain some understanding of the underlying statistics, we start by presenting the analytical formalism to deal with CMB cross-spectra on the full sky, which will be generalized in Sect. 5.3 in particular to a cut-sky. We consider the CMB angular power spectrum obtained by combining the harmonic coefficients $a_{\ell m}$ of two different full-sky maps (A,B), measured with different noise spectra N_ℓ^A and N_ℓ^B. For a realistic experimental setting the harmonic coefficients are also convolved with the beam functions of the two maps A and B, b_ℓ^A and b_ℓ^B. The cross-spectra statistics is defined as:

$$\hat{C}_\ell^{\,A\times B}=\frac{1}{2\ell+1}\sum_{\ell=-m}^{m} a_{\ell m}^A a_{\ell m}^{B*} b_\ell^A b_\ell^B. \tag{5.1}$$

In the Eq. 5.1 and in the following we make the hypothesis that the noise and the residual systematics are not correlated between the maps so that the cross-spectra are unbiased estimate of the CMB signal. The cross-spectra distribution is given by (we refer to the Appendix Sect. 5.A for the details of this calculation):

$$p_N^{A\times B}(\hat{c})=\frac{N^{(N+1)/2}|\hat{c}|^{(N-1)/2}e^{(N\rho\hat{c}/z)}K_{(N-1)/2}\left(\frac{N|\hat{c}|}{z}\right)}{2^{(N-1)/2}\sqrt{\pi}\Gamma(N/2)\sqrt{z}(\sigma_A\sigma_B)^{N/2}}, \tag{5.2}$$

where $\hat{c}{=}\hat{C}_\ell^{\,A\times B}$, $z{=}(1{-}\rho^2)\sigma_A\sigma_B$, $N{=}2\ell{+}1$ is the number of modes, K_ν is the modified Bessel function of the second kind and order ν and:

$$\begin{cases}\sigma_A=\sqrt{C_\ell^{\rm th}+N_\ell^A}\\ \sigma_B=\sqrt{C_\ell^{\rm th}+N_\ell^B}\\ \rho=\dfrac{C_\ell^{\rm th}}{\sqrt{(C_\ell^{\rm th}+N_\ell^A)(C_\ell^{\rm th}+N_\ell^B)}}.\end{cases} \tag{5.3}$$

Some examples of the shapes for these distributions are shown on Fig. 5.1 where it is interesting to see how the distribution changes when varying the degree of correlation between the two maps (ρ). Note that, unlike for auto-spectra, the $p_N^{A\times B}(\hat{c})$ function can be negative since the negative exponential decay is compensated by the rise of the Bessel function, especially when the noise is important (large σ_A,σ_B).
From the characteristic function Eq. 5.38 we can compute the cumulant generating function $K(t){=}\ln\phi(t)$ and by Taylor-expanding it in powers of (it) around zero we obtain the first cumulants:

$$\kappa_1(\hat{C}_\ell^{\,A\times B}) = C_\ell^{\rm th} \tag{5.4}$$

$$\kappa_2(\hat{C}_\ell^{\,A\times B}) = \frac{2(C_\ell^{\rm th})^2+C_\ell^{\rm th}(N_\ell^A+N_\ell^B)+N_\ell^A N_\ell^B}{N} \tag{5.5}$$

$$\kappa_3(\hat{C}_\ell^{\,A\times B}) = C_\ell^{\rm th}\frac{8(C_\ell^{\rm th})^2+6C_\ell^{\rm th}(N_\ell^A+N_\ell^B)+6N_\ell^A N_\ell^B}{N^2}. \tag{5.6}$$

This generalize the results from Hamimeche & Lewis (2008, Appendix C)) obtained with identical noise. According to the Central Limit Theorem, the cumulants above κ_2 disappear with the number of modes N and the distribution approaches a Gaussian with a variance given by Eq. 5.5. Unlike for the auto-spectrum case (Eq. 5.41), the estimator κ_1 does not depend on the noise reconstruction. The clear advantage of using the cross-spectra is that the estimator is unbiased whatever knowledge we have of the noise spectra. Also, the statistical loss for using cross-spectra with respect to auto-spectra is small and minimized if the noise levels of the two maps involved are not too different, as shown in details in Sect. 5.B. Note that in general these conclusions hold true also when an incomplete sky coverage is considered.

5.3 Cross-spectra estimator

As in the auto-spectrum case (Wandelt et al. 2001), the inclusion of some cut on the sky and of anisotropic noise complicates the description of a cross-spectrum estimator by correlating modes between them (both in ℓ and m for a non azimuthal mask) and eventually distorting the marginal distributions. We then need to rely on realistic simulations to take into account the full complexity of the problem.

5.3.1 Angular power spectrum estimator

We use a pseudo-C_ℓ estimator (PCL), `Xpol` an extension to polarization of the `Xspect` algorithm (Tristram et al. 2005) to derive different sets of cross-spectra simulations.
At very low multipoles, the PCL estimator is known to be sub-optimal with respect to e.g. a Quadratic Maximum Likelihood estimator (QML) (Tegmark & de Oliveira-Costa 2001; Efstathiou 2006). This means that the variance and correlation of the PCL is expected to be slightly higher than for QML resulting in slightly larger distributions for the estimated $\hat{C}_\ell$. However, the implementation of cross-spectra for PCL estimators is straightforward and we can easily take into account the level of ℓ-by-ℓ correlations using Monte Carlo simulations. In any case, the definition and validation of the cross-spectra likelihood are independent on the choice of the cross-spectra estimator used.
We produced different sets of Monte-Carlo cross-spectra simulations. We generated simulated CMB maps on which we add anisotropic and correlated noise corresponding to four public datasets: WMAP (V band), *Planck*-LFI (70 GHz) and two *Planck*-HFI channels (100 GHz and 143 GHz). The CMB signal is constructed from the adiabatic ΛCDM model with cosmological parameters: $\Omega_b h^2$ (the baryon density), $\Omega_c h^2$ (the dark matter density), the amplitude and the spectral index of the primordial power spectrum A_s and n_s, θ (a parameter proportional to the ratio of the sound horizon and the angular diameter distance at recombination), the optical depth to reionization parameter τ or, equivalently, the redshift of reionization z_{re}. We also consider primordial tensor modes, parametrized by the tensor-to-scalar ratio of the amplitude of the primordial spectra r.
Our reference simulations are generated with a fiducial ΛCDM model based on the *Planck* 2015 best fit (Planck Collaboration XIII 2015) with τ=0.078. For the tensor-to-scalar ratio we choose r=0.1 as the fiducial input value. Since it is relevant for some validation tests, in particular to check the dependence on the fiducial model, we also generated two sets of simulations with different input cosmologies:

1. early reionization without tensor modes (*Planck* 2015 best-fit with τ=0.09, z_{re}=11.2, r=0)
2. late reionization with high level of tensor (*Planck* 2015 best-fit with τ=0.0566, z_{re}=8, r=0.2)

We estimate the noise angular power spectrum in temperature and polarization using the spectra of (I,Q,U) year map differences for *WMAP* and *Planck*-70. For *Planck*-HFI, we compute the temperature spectrum from available HFI intensity year map differences which we rescale according to the number of polarized detectors at each frequency to mimic the polarized noise power spectra. The latter ends up very close to what is published in Planck Collaboration VIII (2015). With this procedure, the noise power spectra used for simulations include realistic white noise level and low-frequency noise due to systematic and foreground residuals. From those power spectra, we derive constrained map realization of noise for each simulation. We then scale the noise map by the appropriate relative hit counts in each pixel to simulate the inhomogeneous scanning of each dataset.

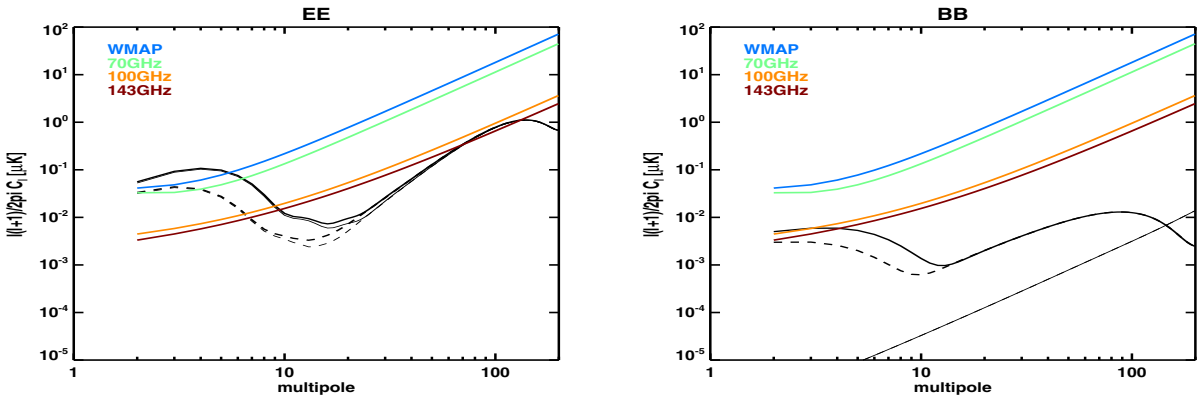

Figure 5.2: Polarized power spectra for E modes (*left*) and B modes (*right* for different reionization histories: late (dashed line) or early (solid line). B-mode spectrum are shown for r=0.2 (thick line) or r=0 (thin line). Noise level for the 4 considered data cases are overplotted (*WMAP*, *Planck*-70, *Planck*-100 and *Planck*-143).

We use our pseudo-C_ℓ estimator to produce the six cross-spectra corresponding to the four datasets: *WMAP*×*Planck*-70, *WMAP*×*Planck*-100, *WMAP*×*Planck*-143, *Planck*-70×*Planck*-100, *Planck*-70×*Planck*-143 and *Planck*-100×*Planck*-143. For each simulation, we construct the TT, EE, BB, TE, TB and EB cross-power spectra. The upper and lower panels of

Fig. 5.2 show the different noise levels corresponding to the four datasets for the E-modes and B-modes spectra, respectively and how the CMB polarized power at very low multipoles is directly scaled by the optical depth of reionization. The plots illustrate the effect of the change form early (z_{re}=11.2) to very late (z_{re}=8) reionization – which correspond to an optical depth of τ=0.09 and 0.566 respectively – for both E and B modes below ℓ=10. In addition, the tensor-to-scalar ratio rescales the overall amplitude of the primordial signal in BB.
We do not simulate the impact of foreground contaminations in map domain. However, residuals from foreground contaminations are statistically included in our estimate of the noise spectra. Moreover, we remove the Galactic plane for the power spectrum estimation. We use two sets of Galactic mask based on a threshold on the polarized power amplitude of dust emission and allowing for a sky coverage of 80% and 50% respectively.
The correlation matrices (Fig. 5.3) are directly derived from the Monte Carlo (MC). The level of correlation between multipoles depend on the sky cut and the dataset considered. For the *Planck*-100x*Planck*-143, using 80% sky coverage the correlations are weak (lower than 5%). As we will see in the next section (Sect. 5.3.2), for such a large sky coverage we can safely neglect the correlations and adapt the full-sky cross-spectra statistic. For the 50% sky, the correlations are significantly higher and can reach the level of 25%.

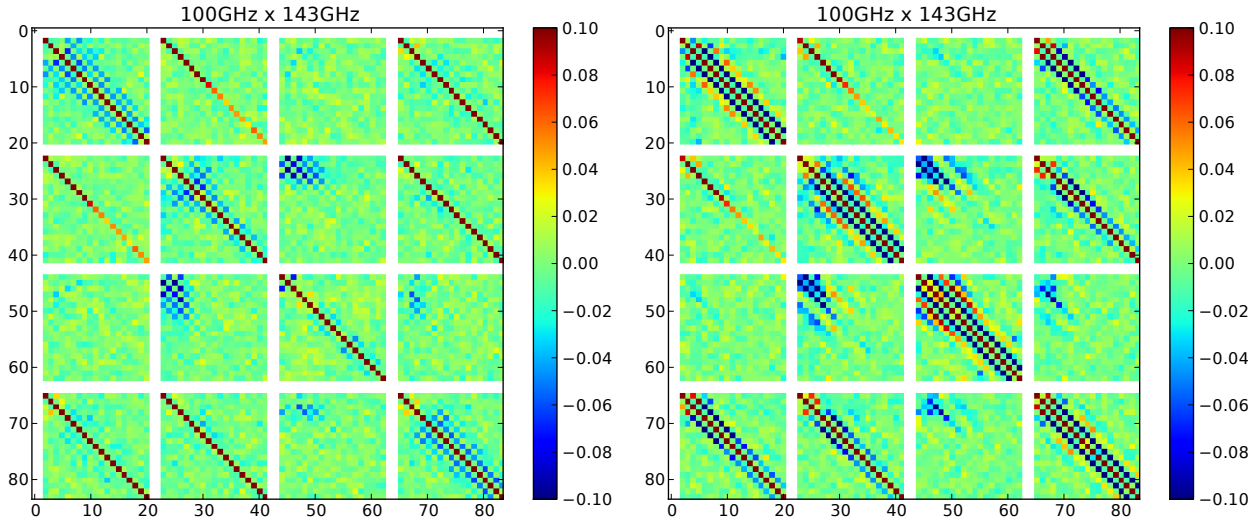

Figure 5.3: Correlation matrix for the cross-power spectra 100x143 with two different sky coverage: 80% (*left*) and 50% (*right*). Each block corresponds to TT, EE, BB, TE spectra respectively. ℓ=0 and ℓ=1 are not defined and set to zero.

5.3.2 Parametrization of the PCL marginals

The distribution of the PCL estimator is largely non-gaussian in the low-ℓ regime we are interested in (see examples in Fig. 5.16 and Fig. 5.17 in the Appendix 5.C) and all order moments actually depend on the noise powers and on the fiducial model. Leaving aside the complicated (and unnecessary) task of defining the full joint p.d.f $p(\mathbf{C}_\ell)$, we focus on how to parametrize analytically the individual (i.e. marginal) distributions by tweaking the results obtained on the full-sky in Sect. 5.2 in the case that a sky cut is applied. We propose two different approaches to achieve a satisfactory description.

Full-sky based approach

A somewhat heuristic argument used when masking some fraction $f_{\rm sky}$ of the sky, is to consider that the *number of degrees of freedom* of the associated χ^2 distribution N=$(2\ell+1)$ is reduced asymptotically by the $f_{\rm sky}$ factor (Hivon et al. 2002). When the mask is apodized by some window, we include the weighting factor w_2^2/w_4, where w_i is the i-th moment of the weighting scheme, in our definition of $f_{\rm sky}$.
Keeping in mind that cross-spectra do not follow any χ^2 distribution and that we are not in the asymptotic regime, we may still try to adapt this methodology based on our simulations. We then modify our number of modes by N=$(2\ell+1)f_{\rm sky}^{A\times B}$, keep the general full-sky shape of Eq. 5.2 and fit for the $f_{\rm sky}^{A\times B}$ factor for different masks, noise combinations and models.
The upper panel of Fig. 5.4 shows the $f_{\rm sky}^{A\times B}$ factor as a function of the multipole ℓ in the case of cross-spectra with different noise levels for the small ($f_{\rm sky}$ =0.77) and larger ($f_{\rm sky}$ =0.49) mask. As expected, there is a strong dependency of $f_{\rm sky}^{A\times B}$ on the mask size. The $f_{\rm sky}^{A\times B}$ is not a constant in the low-ℓ regime ($\lesssim$15) and it is asymptotically slightly different from the standard $f_{\rm sky}$ factor. This can be traced to the fact that we are dealing with polarization that involves different Wigner 3j functions than the ones derived from temperature. Despite this strong dependence on the mask, the $f_{\rm sky}^{A\times B}$ functions derived for the six cross-spectra show a very good consistency for all those different noise levels.

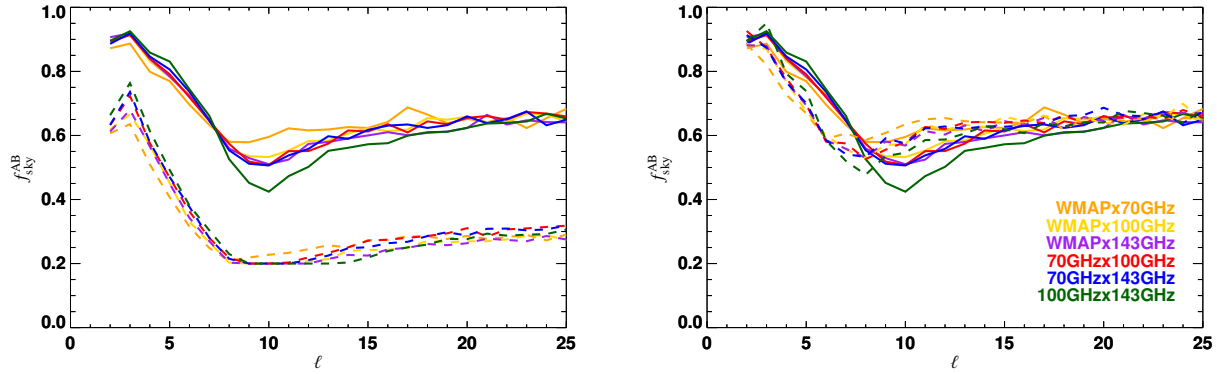

Figure 5.4: **Left panel:** *Dependence of the $f_{sky}^{A\times B}$ factor on the mask.* The two distinct groups (full and dashed lines) represents the $f_{\rm sky}^{A\times B}$ values fitted to the distributions obtained respectively on the small mask ($f_{\rm sky}$ =0.77) and large ($f_{\rm sky}$ =0.49) mask. **Right panel:** *Dependence of the $f_{sky}^{A\times B}$ factor on the fiducial model.* The plot shows the $f_{\rm sky}^{A\times B}$ factor as a function of the multipole when the early-reionization model (model 1, τ=0.09, solid lines) and the late-reionization model (model 2, τ=0.056, dashed lines) are used as input cosmology in the simulations.

In the lower panel of Fig. 5.4 we check the model dependency by comparing the $f_{\rm sky}^{A\times B}$ values reconstructed from two simulation sets generated with two different input cosmologies: the early reionization scenario (model 1, τ=0.09) and the late reionization scenario (model 2, τ=0.056). The reconstruction of the $f_{\rm sky}^{A\times B}$ factor is reasonably stable with respect to the change in the fiducial model used and will be considered in the following as independent.
The stability with respect to the choice of the fiducial model is further demonstrated in the Appendix 5.C (Fig. 5.16) which shows the excellent agreement of the p.d.f's for the *Planck*-100×*Planck*-143 cross-spectrum estimator *for both models* while $f_{\rm sky}^{A\times B}(\ell)$ is derived from *a single one*. Note that we choose to display our *worse* case: all other cross-spectra parametrisations are even better.

Edgeworth expansion

As an alternative to the reconstruction of the $f_{\rm sky}^{A\times B}(\ell)$ function, we also propose another approach, noticing that only the first three central moments contribute essentially to the estimator distribution above $\ell\gtrsim 4$. In this case we use the standard (constant) $f_{\rm sky}$ factor in $N=(2\ell+1)f_{\rm sky}$ and, to account for the fact that a fraction of the sky is masked, we modify the coefficients of the $C_\ell^{\rm th}$-polynomial of the full-sky cumulants (Eqs. 5.5 and 5.6) to match the ones reconstructed from the simulations. The new cumulants in this more general case take the form:

$$\begin{aligned}
\kappa_1(\hat{C}_\ell^{\,A\times B}) &= C_\ell^{\rm th} \\
\kappa_2(\hat{C}_\ell^{\,A\times B}) &= \frac{1.5(C_\ell^{\rm th})^2+2C_\ell^{\rm th}(N_\ell^A+N_\ell^B)+N_\ell^A N_\ell^B}{N} \\
\kappa_3(\hat{C}_\ell^{\,A\times B}) &= C_\ell^{\rm th}\frac{6(C_\ell^{\rm th})^2+12C_\ell^{\rm th}(N_\ell^A+N_\ell^B)+10N_\ell^A N_\ell^B}{N^2}.
\end{aligned} \tag{5.7}$$

Note that this parametrization just depends on constant values of the polynomial coefficients. Fig. 5.5 shows the κ_2 (variance) and κ_3 (skewness) reconstructed from the simulations for the two input fiducial models (early reionization model in blue and late reionization model in red). The agreement between the full-sky based approximation (dashed lines) and the parametrization of Eq. 5.7 derived from simulation (solid lines) is excellent. We emphasize that the κ_3 tuning is not mandatory (one may use the one from Eq. 5.6) since it drops rapidly.
The optimization of the cumulants was performed on a single cross-spectrum (*Planck*-100×*Planck*-143, model 2). It is however robust enough to be used in all other cases as will be demonstrated later in the likelihood tests (Sect. 5.5).
Now that we have a model-independent parametrization of the first cumulants, we proceed in writing an analytical description of the estimator p.d.f using an Edgeworth Series expansion (Kendall & Stuart 1963). Using the normalized variable $y=\dfrac{\hat{C}_\ell-\mu}{\sigma}$ where $\mu=\kappa_1$ and $\sigma=\sqrt{\kappa_2}$, the truncated expansion reads:

$$f(y|C_\ell^{\rm th},N_\ell^A,N_\ell^B)=\mathcal{N}(y)\left(1+\frac{\kappa_3}{6\sigma^3}H_3(y)\right), \tag{5.8}$$

where $\mathcal{N}$ denotes the normal distribution and H_3 is the 3rd order *probabilistic* Hermite polynomial (Kendall & Stuart 1963). Each μ,σ,κ_3 is computed from Eq. 5.7 and depends only on $C_\ell^{\rm th}$,N_ℓ^A,N_ℓ^B.

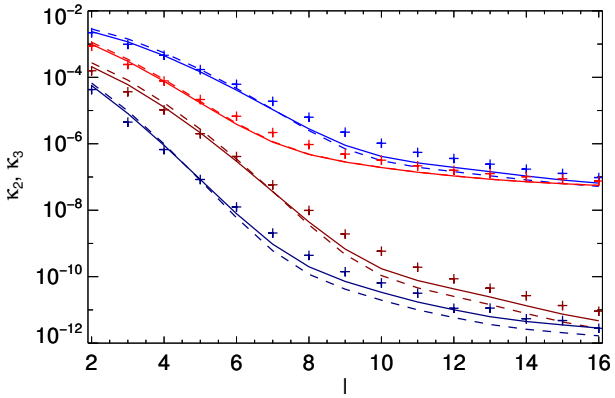

Figure 5.5: *Variance and skewness of the cross-spectra estimators.* The plot shows the second order cumulants, κ_2 (upper red and blue curves) and third order κ_3 (lower red and blue curves) of the PCL estimator. The blue lines correspond to results with the early reionization scenario (model 1) as fiducial model, the red when simulations has the late reionization scenario as input cosmology (model 2). The points refer to the cumulants reconstructed from the *Planck*-100×*Planck*-143 simulations. The dashed lines correspond to the analytic full-sky derived expressions Eqs. 5.5–5.6 with a rescaled $N=(2\ell+1)f_{\rm sky}$ factor. The solid lines refer to the parametrization of the cumulants based on the Edgeworth expansion defined in Eq. 5.7.

A classical issue when truncating an Edgeworth expansion is that, despite being properly normalized to one, it may lead to negative values so that Eq. 5.8 is not really a p.d.f and may lead to potential problems when constructing with it a log-likelihood function. We adopt the method proposed by Rocha et al. (2001) to alleviate this problem. Their idea is based on the solutions of the quantum harmonic oscillator, that exhibits non-Gaussianity above the ground level. For one extra-level the wave-function (i.e. a p.d.f) is of the form:

$$P(x)=\mathcal{N}(x)\left(\alpha_0+\frac{\alpha_3}{\sqrt{6}}H_3(x)\right)^2, \tag{5.9}$$

with $\alpha_0=\sqrt{1-\alpha_3^3}$. For a mild non-Gaussianity (small α_3), which is the case in our regime, we expand this equation:

$$P(x)=\mathcal{N}(x)\left(1+\frac{2\alpha_3}{\sqrt{6}}H_3(x)+O(\alpha_3^2)\right), \tag{5.10}$$

and equating terms to Eq. 5.8, we identify:

$$\alpha_3=\frac{\kappa_3}{2\sqrt{6}\sigma^3}. \tag{5.11}$$

In the following we will refer to *Edgeworth expansion* as this regularized form, namely Eq. 5.9 using Eq. 5.11.
Fig. 5.17 shows the agreement between the empirical estimator distributions obtained on simulations and our Edgeworth-based parametrization. The agreement is very satisfactory but for the ℓ=2,3 case which would require the use of higher order cumulants. On the other side, introducing some κ_4 (kurtosis) term brings some oscillations upon all the multipoles. This would not be desirable since the first two accessible multipoles have generally a very low SNR due to $1/f$ noise and large cosmic-variance and can be disregarded without a sizable loss of information.

5.4 Cross spectra-based likelihoods

With these tools in hand we now proceed in constructing the likelihood of a given model, which means inverting the (unknown) joint and possibly multi-field PCL estimator distribution given the true value $C_\ell^{\rm th}$. We first discuss the simple but frequent single-field case with a small mask for which we give analytical formulas. We then define a more general solution based on the modification of the H&L approximation to construct a general likelihood solution for the combination of the temperature and polarization fields accounting for correlations.

5.4.1 Single field approximations neglecting correlations

As a first solution, we can build our real-case likelihood from the parametrization of the marginalized estimator distribution $p(C_\ell)$ described in Sect. 5.3.2. This approximation is accurate when the masked sky-fraction is low (typically below 20%) so that the ℓ-by-ℓ correlations can be safely neglected. The likelihood function is defined as the product of the probability density functions $p_N^{A\times B}$ (cf. Eq. 5.2):

$$\mathcal{L}^{A\times B}(C_\ell^{\rm th}|\hat{C}_\ell,N_\ell^A,N_\ell^B)=\prod_{\ell=\ell_{\rm min}}^{\ell_{\rm max}} p_N^{A\times B}(\hat{C}_\ell), \tag{5.12}$$

where the $\hat{C}_\ell$ represent the values measured on data. The $p_N^{A\times B}$ functions are implicitly dependent on N_ℓ^A, N_ℓ^B, $C_\ell^{\rm th}$ and they can be defined according to the chosen analytical parametrization as described in Sect. 5.3.2 and Sect. 5.3.2.
Note that this approximation derived from the full sky formalism is easily defined for a single field, that is to say when the cross-spectra are derived from the combination of the same temperature or polarization field, e.g. the E-modes cross-spectra. A combined analysis that accounts for all the temperature and polarization fields is difficult to define analytically since correlations between different fields (TE, TB, EB) cannot be neglected and higher order moments of the $\hat{C}_\ell$ distribution must be accounted, making the analytical solution difficult to handle in this more general case.

5.4.2 General multi-field approximation

Here we present a more general formalism to define a cross-spectra likelihood for the analysis of the CMB data at large angular scales that allows to deal with realistic cases of incomplete sky coverage taking into account the $\ell-\ell$ correlations. This likelihood can also be easily generalized to a multi-fields likelihood that combines the temperature and polarization fields T, E and B, accounting for the field-field correlations TE, TB and EB.
In order to model the non-Gaussianity of the $\hat{C}_\ell$ estimators, the approximation that we propose is based on the modification of the Hamimeche & Lewis (2008) likelihood (H&L), adapted to work for the cross-spectra $C_\ell^{A\times B}$ and at low-ℓ.
The general form of the H&L likelihood is defined for auto-spectra at intermediate and small scales (ℓ>30) (Hamimeche & Lewis 2008):

$$-2ln\mathcal{L}(C_\ell^{th}|\hat{C}_\ell)=\sum_{\ell\ell'}[X_g]_\ell^T[M_f^{-1}]_{\ell\ell'}[X_g]_{\ell'}. \tag{5.13}$$

The $[M_f^{-1}]_{\ell\ell'}$ is the inverse of the C_ℓ-covariance matrix that allows to quantify the $\ell-\ell$ and the correlations of the T, E, B fields. The vector $[X_g]_\ell$ is the H&L transformed C_ℓ vector defined as:

$$[X_g]_\ell={\rm vecp}\Big(\mathbf{C}_{fid}^{1/2}\mathbf{U}(\mathbf{g}[\mathbf{D}(\mathbf{P})])\mathbf{U}^{\mathbf{T}}\mathbf{C}_{fid}^{1/2}\Big). \tag{5.14}$$

In eq.5.14, $\mathbf{C}_{fid}^{1/2}$ is the square root of the C_ℓ matrix:

$$\mathbf{C}_\ell=\begin{pmatrix} C_\ell^{TT} & C_\ell^{TE} & C_\ell^{TB} \\ C_\ell^{TE} & C_\ell^{EE} & C_\ell^{EB} \\ C_\ell^{TB} & C_\ell^{EB} & C_\ell^{BB} \end{pmatrix} \tag{5.15}$$

for a given fiducial model and the function ($\mathbf{g}[\mathbf{D}(\mathbf{P})]$) refers to the transformation:

$$g(x)=sign(x-1)\sqrt{(2(x-ln(x)-1))}, \tag{5.16}$$

applied to the eigenvalues of the matrix $\mathbf{P}=\mathbf{C}_{mod}^{-1/2}\hat{\mathbf{C}}_{data}\mathbf{C}_{mod}^{-1/2}$, where $\mathbf{C}_{mod}$ and $\hat{\mathbf{C}}_{data}$ are, respectively, the matrices of the sampled C_ℓ and the data. This approximation has been shown to be robust with respect to the choice of the fiducial model (Hamimeche & Lewis 2008). The problem is that for cross-spectra and at large angular scales the $\mathbf{P}$ matrix is no longer guaranteed to be positive definite. In fact, as shown in Eq. 5.2 that describes the distribution of the cross-spectra estimators $\hat{C}_\ell$, the $\hat{\mathbf{C}}_{data}$ can be negative. In order to solve for this issue, we propose a modification of the H&L likelihood that consists in adding an effective offset o_ℓ to the cross-spectra. This mimics the noise bias of the auto-spectra and makes the offset-cross-spectra distribution very similar to the auto-spectra distribution used in the H&L approximation. We re-define each $\mathbf{C}_\ell$ matrix (eq. 5.15) as:

$$\mathbf{C}_\ell^{A\times B}\rightarrow O(\mathbf{C}_\ell^{A\times B})=\begin{pmatrix} C_\ell^{TT}+o_\ell^{TT} & C_\ell^{TE} & C_\ell^{TB} \\ C_\ell^{TE} & C_\ell^{EE}+o_\ell^{EE} & C_\ell^{EB} \\ C_\ell^{TB} & C_\ell^{EB} & C_\ell^{BB}+o_\ell^{BB} \end{pmatrix} \tag{5.17}$$

so that:

$$[X_g(\mathbf{C}_\ell^{A\times B})]_\ell\rightarrow[OX_g]_\ell=[X_g(O(\mathbf{C}_\ell^{A\times B}))]_\ell. \tag{5.18}$$

The new offset H&L likelihood (oHL hereafter) reads:

$$-2ln\mathcal{L}(C_\ell|\hat{C}_\ell^{A\times B})=\sum_{\ell\ell'}[OX_g]_\ell^T[M_f^{-1}]_{\ell\ell'}[OX_g]_{\ell'}. \tag{5.19}$$

The variable transformation $g(x)$ is now modified for the cross-spectra to regularize the likelihood around zero so that Eq. 5.16 now reads:

$$g(x)\rightarrow sign(x)g(|x|). \tag{5.20}$$

The offset function o_ℓ^{XY} can be derived from simulations. We estimate the offsets from the MC distributions ensuring that the **P** matrix reconstructed is positive definite for more than 99% of our simulations.
Given that the offsets are needed to shift the C_ℓ distributions for each field T, E, B to avoid negative eigenvalues on the **P** matrix, the offset functions depend on the shape of the C_ℓ distribution at each ℓ. In particular, the offsets depend on the noise levels of the maps involved in the cross-spectra and on the mask used. In fact, the tails of the C_ℓ distributions at each ℓ are more negative when the noise is higher and when a larger mask is applied. The plot in Fig. 5.6 shows how the offset functions change for different combinations of noise levels in the case of the six cross-spectra considered: from the highest of the WMAP×*Planck*-70 in orange to the *Planck*-100×*Planck*-143 in green.

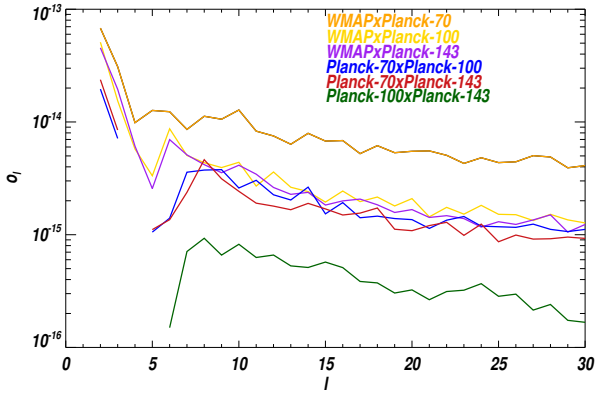

Figure 5.6: The offset functions $o_\ell^{A\times B}$ of the oHL likelihood for the E-modes cross-spectra and for the six different combinations of noise levels.

Moreover, the offsets also depend on the fiducial model, as, in general, an higher signal-to-noise implies that the C_ℓ distributions have a smaller shift to negative values. Fig. 5.7 shows the offset functions obtained from simulations generated with different fiducial models for the E-modes (dashed) and B-modes (solid) for the *Planck*-100×*Planck*-143 cross-spectra. The black lines refers to the early reionization scenario without tensor modes (model 1), the red lines to the late reionization scenario with tensors (model 2) and the blue lines to the *Planck* 2015 best fit with r=0.1. The shape of the offsets is consistent for the three different cases and, given the very different levels of signal considered, the dependence on the fiducial model is mild. As we will show in Sect. 5.5 and Sect. 5.6 the likelihood results on the cosmological parameters reconstruction are robust with respect to the choice of the fiducial model used to define the offset functions.

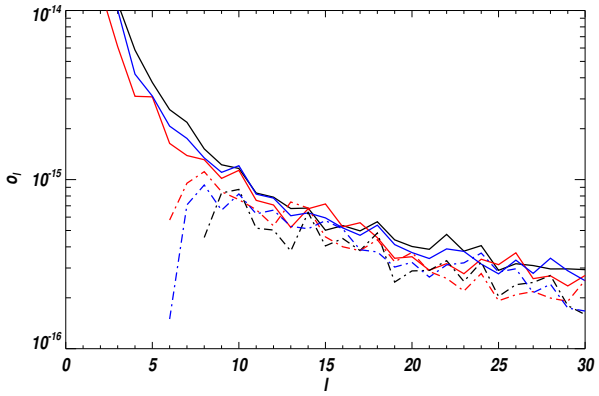

Figure 5.7: The offset functions $o_\ell^{A\times B}$ of the oHL likelihood for the *Planck*-HFI×*Planck*-143 B-modes cross-spectra (solid) and the E-modes cross-spectra (dashed). The different colors refers to the different fiducial models used in the simulations: black is the early reionization scenario without tensor modes (model 1), red is the late reionization scenario with tensors (model 2) and blue is the *Planck* 2015 best fit with r=0.1.

The $[M_f^{-1}]_{\ell\ell'}$ in Eq. 5.19 is the inverse of the cross-spectra $C_\ell^{A\times B}$-covariance matrix that can be estimated for a given theoretical fiducial model $C_\ell^{XY\,fid}$ through Monte Carlo simulations such that:

$$[M_f^{A\times B}]_{\ell\ell'}^{XY} = \langle \left((C_\ell^{XY})_{sim} - C_\ell^{XY\,fid}\right)\left((C_{\ell'}^{XY})_{sim} - C_{\ell'}^{XY\,fid}\right)\rangle_{MC}, \tag{5.21}$$

where $C_\ell^{XY} \equiv (C_\ell^{XY})^{A\times B}$, and $X,Y=\{T,E,B\}$.

Since it will be useful in the following, we also report the equations of the modified oHL likelihood in the case of the single field approximation. In particular, we are interested in applying the method to the polarization EE-only cross-spectra $C_\ell^{EE} \equiv (C_\ell^{EE})^{A\times B}$ for which the oHL likelihood is defined by

$$-2\ln\mathcal{L} = \sum_{\ell\ell'} [OX_g]_\ell^{EE} [M_f^{EE}]^{-1}_{\ell\ell'} [OX_g]_{\ell\ell'}^{EE} \tag{5.22}$$

where:

$$[X_g]_\ell^{EE} \rightarrow [OX_g]_\ell^{EE} = \sqrt{O(C_\ell^{EEfid})}\mathbf{g}\Big[\frac{O(\hat{C}_\ell^{EE})}{O(C_\ell^{EEmod})}\Big]\sqrt{O(C_\ell^{EEfid})}, \tag{5.23}$$

and:

$$O(C_\ell^{EE}) = (C_\ell^{EE} + o_\ell). \tag{5.24}$$

C_ℓ^{EEfid}, $\hat{C}_\ell^{EE}$ and C_ℓ^{EEmod} are, respectively, the spectra of the fiducial model, the data and the variable spectra for the likelihood sampling, and o_ℓ^{EE} is the effective offset. Also, the covariance matrix to account for the multipole coupling in this case is defined by:

$$[M_f]_{\ell\ell'} = \langle \Big((C_\ell^{EE})_{sim}^{A\times B} - C_\ell^{EEfid}\Big)\Big((C_{\ell'}^{EE})_{sim}^{A\times B} - C_{\ell'}^{EEfid}\Big)\rangle_{N_{sims}} \tag{5.25}$$

In practice, after publication of this article, we used offsets defined by analogy with auto-spectra statistics. Indeed, in the case of auto-spectra, the offsets in the likelihood approximation are replaced by the noise bias effectively present in the measured power-spectra. For cross-power spectra, the noise bias is null but noise spectra drive the C_ℓ variance. Thus, we use the effective offsets defined from the C_ℓ noise variance:

$$\Delta C_\ell \equiv \sqrt{\frac{2}{2\ell+1}} o_\ell \ . \tag{5.26}$$

5.5 Single field results

We first present the results in the case of the single field approximation. As single field we choose the E polarization and we build the EE cross-spectra likelihoods to constrain the τ parameter, since it is relevant for the analysis of present and future CMB data. We construct the three different single field cross-spectra likelihoods derived from the formulas in Sect. 5.4: the general analytical parametrization derived from full-sky based approach, the parametrization based on the Edgeworth expansion approximation to describe the cumulants of the cross-spectra distribution and the oHL single-field likelihood.

In order to compare the three methods, we focus on the small sky cut case, where the cross-spectra simulations are generated by applying a mask with $f_{\rm sky}$ =0.8. The ℓ-by-ℓ correlations are weak and the analytic approximations are reliable. This comparison is useful not only as a validation test of the different methods but also to demonstrate that correlations can indeed be neglected in the parametric case. To construct the single field oHL cross-spectra likelihood we use Eq. 5.22 where the ℓ-ℓ correlations are encoded in the cross-spectra covariance matrix of Eq. 5.25. For each of the six cross-spectra considered, the covariance matrix is computed from the Monte Carlo average of 10.000 E-modes simulations generated with a fiducial input cosmology corresponding to the *Planck* best-fit 2015 with τ=0.078 and tensor modes with r=0.1. We estimate the offsets $o_\ell^{EEA\times B}$ from our reference simulations as described in Sect. 5.4.2 and Fig. 5.6. Note that, as pointed out in Sect. 5.3.2 and Sect. 5.4.2, the parametrization used to define the analytical approximations and the definition of the offset functions of the oHL likelihood are both robust with respect to significative changes of the τ parameter in the fiducial model ($\Delta\tau_{fid} \simeq 0.03 >> \sigma_\tau$). However, in general, as it is the case for the HL likelihood analysis at smaller scales (Hamimeche & Lewis 2008), it is a good choice to use a fiducial model close to the "true" model to compute the covariance matrix.

The likelihood sampling is done by computing the C_ℓ^{EEmod} with the CAMB codevarying τ in the range [0.01,0.15] with a step $\Delta\tau$=0.001, fixing the other parameters to their *Planck* 2015 best-fit values and rescaling $A_s e^{-2\tau}$. The degeneracy between τ and the scalar amplitude parameter A_s is in fact broken by fixing accordingly the amplitude of the first peak of the TT spectrum A_{TT}=$A_s e^{-2\tau}$ at ℓ=200. More general results based on joint constraints of the τ and A_s are presented in Sect. 5.6.2.

To compare the three likelihoods, we choose events (i.e. one C_ℓ vector sample) at random from the set of *Planck*-100×*Planck*-143 simulations and construct for each ℓ independently the marginal likelihoods with the three different methods, setting each time all $C_\ell^{\rm th}$ values other than this multipole to their true values. Fig. 5.8 displays a typical case. Here are some comments that we derive from the observation of many samples: even-though the sample C_ℓ may get negative values, due to noise and low signal, the likelihood of any negative true power value is unphysical and is equal to 0. This case does not happen in practice since in cosmological parameter estimation the Boltzmann code always propose positive spectra. The Edgeworth-based method shows some oscillation for the very first multipoles, generally for ℓ=2,3. This is due to the very steep raising of the distributions at the very beginning (see Fig 5.16) which leads to some small negative *ringing* effect in the truncated expansion. The method introduced in Sect. 5.3.2 mitigates the effect but does

not completely cure for it and regarding this aspect the full-sky based method and the oHL likelihood gives a better approximation. Overall Fig. 5.8 shows the excellent agreement among the three likelihood methods in recovering the minimum $\Delta\chi^2$=$-2\ln[\mathcal{L}(C_\ell^{\rm th})/\mathcal{L}_{max}]$ for each multipoles with comparable accuracy.

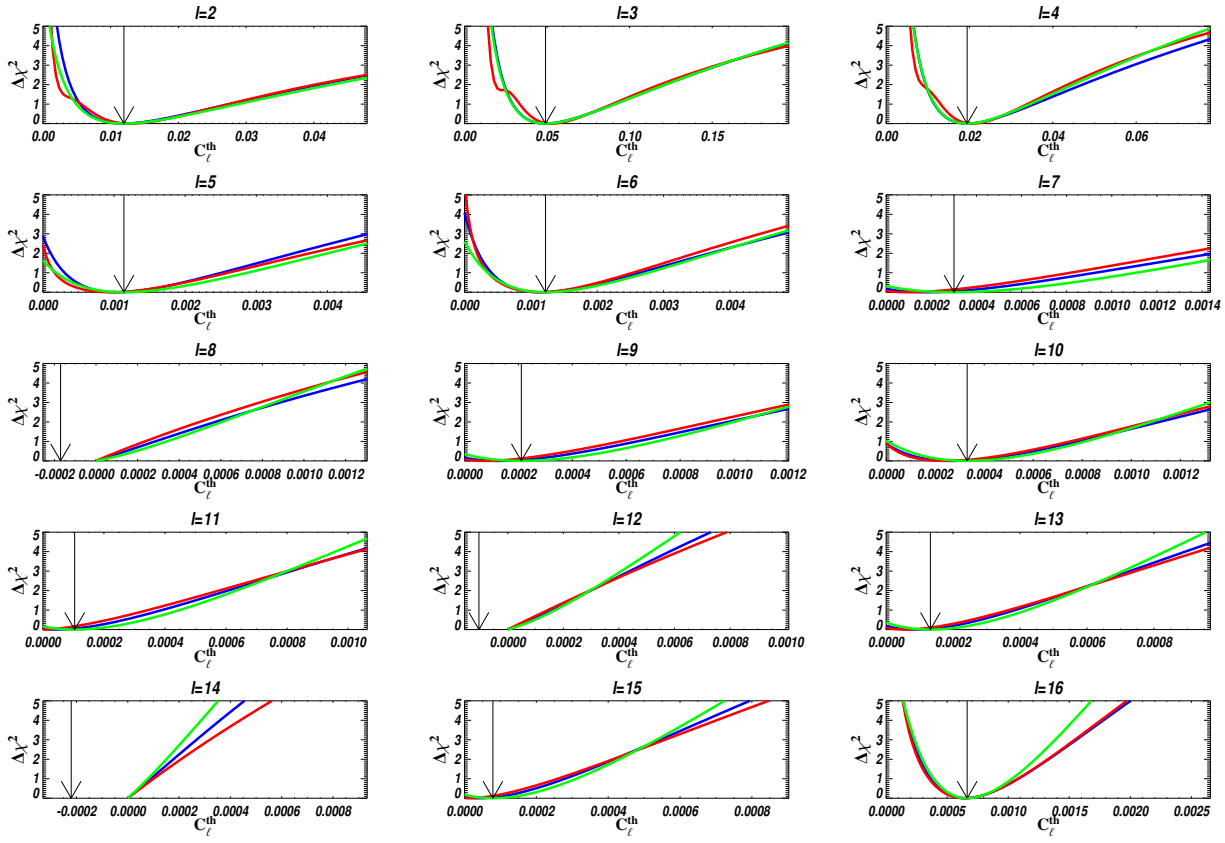

Figure 5.8: Comparisons of the three likelihoods methods developed for the low-correlations case ($f_{\rm sky}$= 0.8): red is for the Edgeworth expansion method, blue for the full-sky based method and green for the modified Hamimeche-Lewis approximation (oHL). The arrow represents where our random sample has fallen. Due to noise, it can be negative. The ordinate is $\Delta\chi^2$=$-2\ln[\mathcal{L}(C_\ell^{\rm th})/\mathcal{L}_{max}]$.

As a further validation test, we check the bias of the likelihood against our set of 10.000 Monte-Carlo simulations. For each simulation, we derive the distribution of the maximum likelihood of τ for ℓ<20. For the full sky based likelihood and for the Edgeworth expansion likelihood we remove multipoles 2 and 3 -which do not carry much information due to the cosmic variance level- since their p.d.f parametrization is less accurate, as shown in Sect. 5.3.2. For oHL we consider ℓ=[2,20].

Figure 5.9 shows the distribution of the maximum probability over the Monte Carlo simulations for the full sky based likelihood, the Edgeworth expansion likelihood and the oHL likelihood. All three approximations recover the input value τ_{fid}=0.078 used to generate our reference simulations, showing that the three likelihoods are unbiased. In Table 5.1 are reported the best fit values and the error bars on the estimation of the τ parameter. The error bars are computed as the standard deviation of the maximum probability $\tilde{\tau}$ for the three likelihoods. Since the oHL likelihood accounts for the ℓ-by-ℓ correlations while the full-sky based likelihood and the Edgeworth expansion approximation do not, the fact that the three methods give compatible results in terms of error bars confirm that the level of multipole correlations for a small sky cut is low and does not have an impact in the reconstruction of the τ parameter. Note however that both the analytical approximations are slightly sub-optimal with respect to the oHL likelihood, by a factor of $\simeq$4% for the full-sky based likelihood and by a factor of $\simeq$7% for the Edgeworth expansion likelihood. These results hold in general for all the cross-spectra considered.

Finally, it is useful to assess the stability of the results obtained with the oHL likelihood with respect to choice of the offset term. Indeed, changing the offsets both could bias the peak of the posterior distribution and change its width. As described in Eq. 5.23, the offset ensure the H&L transformation to be definite and too small offsets may leak to undefined likelihood. On the opposite, a overestimation of the offset value has limited effect on the peak distribution. Figure 5.10 shows that the impact of a factor of two in the estimation of the offsets amplitude is negligible on the posterior distribution of the τ parameter. The figure illustrates two representative cases of τ posteriors obtained with the highest and lowest noise configuration from our simulations. Note that a change in the offset of this type could arise if the fiducial model used to derive the offsets is very different from the best fit model, as illustrated in Fig. 5.6. The fact that this change has practically no effects on the posterior distributions demonstrates that the definition of the oHL likelihood is robust with

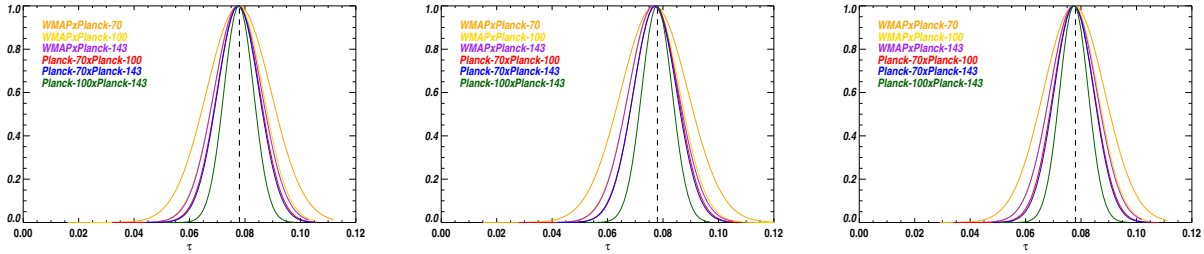

Figure 5.9: Distribution of the maximum probability for the analytic full-sky based likelihood (*left*), for the analytical parametrization based on the Edgeworth expansion (*middle*) and for the oHL likelihood (*right*) on each E-modes cross-spectra on 80% of the sky

Cross-spectra	$(\tilde{\tau}\pm\sigma_{\tilde{\tau}})^{fullsky}$	$(\tilde{\tau}\pm\sigma_{\tilde{\tau}})^{edgeworth}$	$(\tilde{\tau}\pm\sigma_{\tilde{\tau}})^{oHL}$
WMAP×*Planck*-70	0.0777±0.0116	0.0768±0.0121	0.0774±0.0110
WMAP×*Planck*-100	0.0777±0.0088	0.0768±0.0092	0.0773±0.0086
WMAP×*Planck*-143	.00774±0.0086	0.0765±0.0089	0.0772±0.0084
Planck-70×*Planck*-100	0.0776±0.0077	0.0773±0.0079	0.0774±0.0074
Planck-70×*Planck*-143	0.0775±0.0075	0.0771±0.0078	0.0774±0.0071
Planck-100×*Planck*-143	0.0777±0.0054	0.0778±0.0055	0.0781±0.0051

Table 5.1: Comparison of the best fit estimation of the reionization optical depth $\tilde{\tau}$ and error bars $\sigma_{\tilde{\tau}}$ for the three likelihood methods from simulations (see also Fig. 5.9). The errors are computed as the standard deviation of the maximum probability $\tilde{\tau}$ over a set of 2000 simulations. The input value used in the simulations is τ_{fid}=0.078 and $f_{\rm sky}$=0.8.

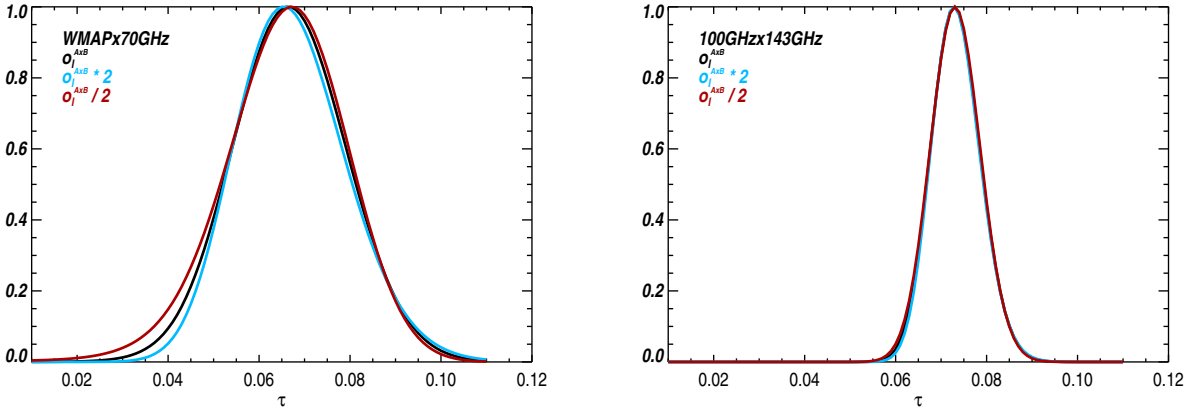

Figure 5.10: The plots show the effect of changing the offsets amplitude by a factor of two on the posterior distribution of the τ parameter. The left panel refers to the *WMAP*×*Planck*-70 cross-spectra, while the right panel to the *Planck*-100×*Planck*-143 cross-spectra.

respect to the offset reconstruction. Also, the effect on the width of a change in the offset is very weak, meaning that the offsets, as expected, do not affect the estimation of the error bars. The same results hold true for all the cross-spectra considered. In general, our offset terms are well defined and the oHL results are robust with respect to the offset choice.
For a smaller sky coverage, the three likelihoods remain unbiased even if the ℓ-by-ℓ correlations get larger. In this case, the parametric likelihoods are less optimal: their variance increase by about 10% compared to the oHL likelihood for the 50% mask.

5.6 Results for correlated fields

This section is dedicated to the results obtained with the full temperature and polarization oHL likelihood (Eq. 5.19). One of the main advantages of the oHL method relies in fact on the possibility to include in the analysis both the correlations between the [T,E,B] fields and the multipole correlations. Since the simulations used for each cross-spectrum are built with realistic noise levels as described in Sect. 5.3, the forecasted estimates on the τ, r and A_s parameters from the low-ℓ analysis presented here are realistic for current CMB experiments.
We build the {TT, EE, BB, TE, TB, EB} oHL likelihood for the six different cross-spectra: *WMAP*×*Planck*-70, *WMAP*×*Planck*-

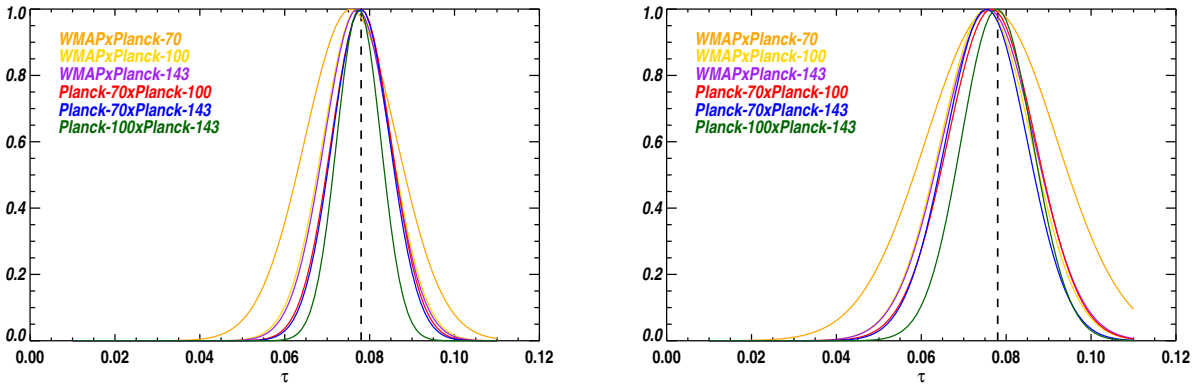

Figure 5.11: *Validation of the oHL multi-fields likelihood.* The plots show that the oHL likelihood computed combining the T, E and B fields and accounting for both multipole and fields correlations gives unbiased results on the estimation of the optical depth to reionization parameter τ. The left panel shows the τ posterior for the six different cross-spectra when 20% of the sky is masked (f_{sky}=0.8), while the right panel shows the results for a bigger mask with f_{sky}=0.5. The dashed line refers to the input value τ_{fid}=0.078 used in the simulations.

100, *WMAP*×*Planck*-143, *Planck*-70×*Planck*-100, *Planck*-70×*Planck*-143, *Planck*-100×*Planck*-143. For each cross-spectrum we construct the full [T,E,B] covariance matrix of Eq. 5.21 by computing the Monte Carlo average of 10.000 simulations generated with a fiducial input cosmology corresponding to our baseline *Planck* 2015 best fit with τ=0.078 and r=0.1. The offsets functions are derived from the same simulations as described in Sect. 5.4.2. For each cross-spectra we therefore add the offsets o_ℓ^{TT}, o_ℓ^{EE}, o_ℓ^{BB} to the diagonal elements of the C_ℓ matrix as defined in Eq. 5.17.

5.6.1 Constraints on τ

Firstly, we study the impact of including the T,E,B cross-spectra and their correlations on the estimation of the optical depth to reionization τ, compared to the single-field EE analysis described in the previous section Sect. 5.5. The sky fraction is f_{sky}=0.8 and the multipole range used is ℓ=[2,20]. As shown in Fig. 5.11 and Table 5.2, the combined analysis gives unbiased results on the estimation of τ. As expected, adding the temperature and the tensor modes and all the possible correlations gives results very close to the single-field EE analysis since the relevant physical information related to τ is essentially encoded in the EE-spectra. However, the full temperature and polarization analysis leads to a slight improvement in the estimation of the τ error bars, which is of about a few percent for the *Planck*-100×*Planck*-143 analysis.

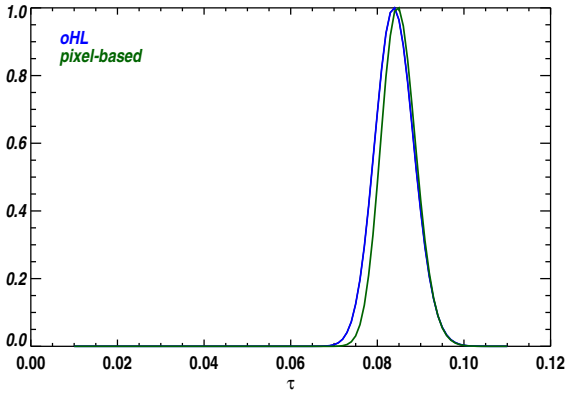

Figure 5.12: Comparison of the posterior distributions of the τ parameter obtained with the full temperature and polarization oHL likelihood (blue) and with the pixel-based likelihood (green). The plot shows a typical example from the *Planck*-HFI simulation set.

We compare the τ posterior distribution of the oHL likelihood to the one from the pixel-based likelihood. We implement a pixel-based likelihood by using a combination of the maps at *Planck*-100 and *Planck*-143 from the same simulation set that we used to generate the *Planck*-HFI cross-spectra. Both methods are therefore based on simulations with the same noise characterization. A typical case is given in Fig. 5.12. As expected, the oHL likelihood approximation is slightly sub-optimal with respect to the pixel-based likelihood which is not an approximation and is build to be statistically optimal. Note however that the error bars obtained with the oHL likelihood are comparable with the optimal estimate obtained by

Cross-spectra	$\tilde{\tau}\pm\sigma_{\tilde{\tau}}$ (f_{sky}=0.8)	$\tilde{\tau}\pm\sigma_{\tilde{\tau}}$ (f_{sky}=0.5)
WMAP×*Planck*-70	0.0750±0.0108	0.0761±0.0203
WMAP×*Planck*-100	0.0769±0.0075	0.0764±0.0121
WMAP×*Planck*-143	0.0769±0.0079	0.0770±0.0116
Planck-70×*Planck*-100	0.0783±0.0069	0.0776±0.0105
Planck-70×*Planck*-143	0.0784±0.0065	0.0763±0.0101
Planck-100×*Planck*-143	0.0780±0.0049	0.0788±0.0069

Table 5.2: Results on the estimation of the τ parameter with the full temperature and polarization oHL likelihood. The fiducial model used in the simulation is the *Planck* 2015 ΛCDM best fit with τ_{fid}=0.078. The table shows the comparison between the τ estimates (best fit $\tilde{\tau}$ and error bars $\sigma_{\tilde{\tau}}$) obtained with two set of simulations with different sky cuts: the small mask with with f_{sky}=0.8 and a bigger mask with f_{sky}=0.5.

using the pixel-based approach at better than 15%.
Finally, we use the combined oHL likelihood to test the results with a different sky cut. We consider a severe cut at 50% (f_{sky}=0.5). This is a more complicate case to deal with since the ℓ-by-ℓ correlations are stronger. Also, the shape of the distributions of the C_ℓ estimators at each ℓ is affected by the smaller sky coverage, leading to more negative tails. We generate the offset functions for each cross-spectra as described in Sect. 5.4.2, using our reference simulations masked at 50%. The results are summarized in Table 5.2 and in the bottom panel of Fig. 5.11 that shows the τ posteriors for each of the six cross-spectra. Even in this more complex case, the oHL likelihood analysis is unbiased. As expected, since we are considering a smaller sky fraction and non-negligible multipole correlations, we recover bigger error bars with respect to the $f_{\rm sky}$=0.8 analysis, with a degradation of ≃30% for the *Planck*-100×*Planck*-143.

5.6.2 Joint estimation of τ, r and A_s

Using the full combined analysis, we can construct multi-dimensional constraints on parameters. In particular, we focus on the correlations between the optical depth and the amplitude of the scalar fluctuations A_s and between the optical depth and the tensor-to-scalar ratio r which are relevant for the future analysis of CMB data at large angular scales from e.g. *Planck*. In both cases we perform the full analysis using the *Planck*-100×*Planck*-143 spectra which corresponds to the lowest noise frequency combination and it can be used to make realistic forecasts for current and future CMB experiments. We consider a sky cut with f_{sky}=0.8.

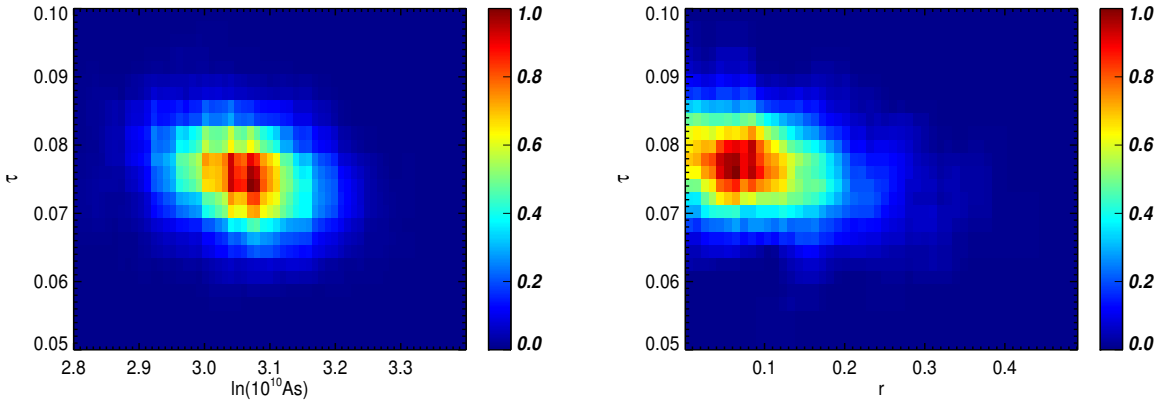

Figure 5.13: *2D-distribution of the maximum likelihood for τ-A_s (left panel)* and τ-r (right panel). The plots show the joint constraints obtained with the full temperature and polarization oHL likelihood on 2000 simulations of the *Planck*-100×*Planck*-143 cross-spectra. The fiducial input parameters used in the simulations are: τ_{fid}=0.078, r_{fid}=0.1 and $[ln(10^{10}A_s)]_{fid}$=3.09.

Joint estimation of τ and A_s

Using the temperature power spectrum only, A_s and τ are strongly degenerated. Indeed, the amplitude of the first acoustic peak of the CMB temperature power spectrum directly measures A_{TT}=$A_s e^{-2\tau}$. Using polarization data at large angular scale helps breaking this degeneracy. So far we fixed the degeneracy direction by rescaling the temperature spectrum, fixing A_{TT}, accordingly to the variation of τ in the likelihood sampling. Here we let A_s free to vary. The results from the simulations, using the *Planck*-100×*Planck*-143 full oHL likelihood are summarized in the left panel of Fig. 5.13. The plot shows the 2D histogram of the best fit values for the whole set of simulations in the τ-A_s projection. The full oHL likelihood correctly recovers the inputs values for τ and A_s as well as error bars compatible with the MC dispersion.

Joint estimation of τ and r

The CMB power spectra at large angular scales, in particular the E and B polarization modes, are affected by how the reionization process proceeded and lasted. Thus, as shown in Fig. 5.2, the power at large scales (low-ℓ) in the B-modes spectrum is directly related to the reionization optical depth. Indeed, the amplitude of the B-modes spectrum reionization bump scales with τ^2: $C^{BB}_{\ell<20}(\tau) \propto \tau^2 C^{BB}_{\ell<20}$. As the amplitude of the B-modes spectrum of course also depends on the amount of the primordial tensor perturbations, there is a degeneracy between the τ and r. It is therefore interesting to derive joint estimates of these parameters.
We compute the joint τ-r constraints with the full oHL likelihood on the set of 2000 simulations of the *Planck*-100×*Planck*-143 cross-spectra with an input cosmology corresponding to the *Planck* 2015 best fit for the base ΛCDM parameters with τ=0.078 and a tensor-to-scalar ratio of r=0.1. The multipole range used is, as usual, ℓ=[2,20]. The results of the oHL likelihood sampling on simulations are summarized in the right panel of Fig. 5.13. The plot shows the posterior in the τ-r plane from the oHL and from which we can see that the oHL likelihood correctly recovers the parameters τ and r compatible with the input values used in the simulations. As regarding the error bars, the forecasted 1σ error for τ in the case of the highest resolution channels of a *Planck*-like experiment is $\sigma_\tau^{100\times143}$=0.0051. For the tensor-to-scalar ratio in the multipole range considered, we find $\sigma_r^{100\times143}$=0.09. Note that in our analysis, we consider a correlated noise model. This noise characterization, which is more realistic with respect to a simpler white noise modeling, implies a rising of the noise level at low multipoles due to the $1/f$ noise correlations (see Fig. 5.2). Therefore, in particular in the case of a low signal scenario, the correlated noise at large scales can eventually dominate over the cosmic variance inducing a worsening of the constraining power proportional on how steep is the rising of the correlated noise at low multipoles.

5.7 Conclusions

In this paper we presented a new approach for the analysis of the CMB polarization data at large angular scales based on cross-correlation in spectra domain. Using cross-spectra with respect to the auto-spectra and, in general, to the pixel based approach used so far in the CMB analysis at large angular scales has many advantages, in particular in the case of a realistic CMB experiment that accounts for anisotropic noise and a sky cut needed to minimize the foreground contamination. In fact, by using cross-frequency/cross-dataset CMB spectra, the noise biases and the systematics specific to a given frequency/dataset are removed. Also, the possible foreground residuals can be minimized and the information encoded in different frequencies/datasets can be combined efficiently.
The cross-spectra estimators are non-Gaussian at low multipoles especially when applied on cut-sky. We generalized the approximation made in Hamimeche & Lewis (2008) to accommodate for cross-spectra at very low multipoles. This likelihood (oHL) can easily handle the correlation between CMB modes (TT, EE, BB, TE as well as TB and EB) and between multipoles and gives error bars less than 15% larger than the optimal pixel-based method. The oHL likelihood shares the same robustness with respect to the choice of the fiducial model as the H&L approximation (see discussion in Hamimeche & Lewis (2008)). We compared the oHL likelihood to the analytical parametrization of the estimator distribution which can be used as a quick likelihood solution in the case of a single field analysis with small sky cuts so that correlations can be safely neglected.
We generated different sets of simulations that we used to construct and validate the likelihoods, proving that all the methods are unbiased and can accurately constrain the optical depth to reionization parameter τ. Also, we showed that the oHL likelihood gives accurate constraints of the joint estimation of the τ parameter, the tensor-to-scalar ratio parameter r and the amplitude of the primordial scalar perturbations A_s. Our simulations account for anisotropic correlated noise, beam, mask with the characteristic of a realistic CMB experiment as *WMAP* and *Planck*. In order to validate our likelihoods for different noise levels, we generated simulations for cross-frequency spectra with different resolution, from the lowest, *WMAP*x*Planck*-70, to highest, i.e. *Planck*-100x*Planck*-143.
Optimal foreground cleaning is beyond the scope of this paper but foreground residuals, in particular synchrotron and dust, must be quantified in a realistic CMB analysis. In this paper we work with cleaned CMB maps but we account and propagate the uncertainties related to the foregrounds removal by using in our simulations realistic estimates derived from public data. The correlated noise term that we include in the simulations in fact is drown from real data and can be taken as a good proxy for a realistic combination of noise, systematics and foregrounds residuals, in particular at low multipoles.
The cross-spectra likelihood approach presented in this paper is a powerful and efficient tool for the analysis of the CMB data at large angular scales. It allows to minimize the impact of the experimental residual systematics (from both instruments and foreground contamination) while providing nearly-optimal constraints on the estimation of the τ, r and A_s cosmological parameters.

We acknowledge Antony Lewis for useful discussions on the cross-spectra statistics and likelihood. We acknowledge Olivier Perdereau, Marta Spinelli and Sophie Henrot-Versille for useful comments.

Appendix

5.A Cross-spectra distribution on the full sky

We consider the product of a pair of correlated central gaussian random variables:

$$x=z_a\times z_b \qquad (z_a,z_b)\sim\mathcal{N}_2(\mathbf{u};\mathbf{0},\mathbf{V}) \tag{5.27}$$

where $\mathbf{u}$ is a generic vector and the covariance matrix is written in the standard form:

$$\mathbf{V}=\begin{pmatrix}\sigma_A^2 & \rho\sigma_A\sigma_B\\ \rho\sigma_A\sigma_B & \sigma_B^2\end{pmatrix}. \tag{5.28}$$

Standard probability rules allow to compute its p.d.f (Grishchuk 1996):

$$f_x(x)=\frac{1}{\pi\sigma_A\sigma_B\sqrt{1-\rho^2}}e^{\frac{\rho x}{(1-\rho^2)\sigma_A\sigma_B}}K_0\left(\frac{|x|}{(1-\rho^2)\sigma_A\sigma_B}\right) \tag{5.29}$$

whose characteristic function (Fourier transform is):

$$\phi_x(t)=E\left[e^{ixt}\right]=\frac{1}{\sqrt{1-2i\rho\sigma_A\sigma_Bt+(1-\rho^2)\sigma_A^2\sigma_B^2t^2}}. \tag{5.30}$$

The sum of N such independent variables $X=\sum_{i=1}^N x_i$ has therefore the characteristic function:

$$\begin{aligned}\phi_X(t)=&\left[1-2i\rho\sigma_A\sigma_Bt+(1-\rho^2)\sigma_A^2\sigma_B^2t^2)\right]^{-N/2}\\ &\left[(1-\rho^2)\sigma_A^2\sigma_B^2(t-\frac{i}{(1-\rho)\sigma_A\sigma_B})(t+\frac{i}{(1+\rho)\sigma_A\sigma_B})\right]^{-N/2}.\end{aligned} \tag{5.31}$$

To obtain the X p.d.f we inverse-Fourier it:

$$\begin{aligned}f_X(x)=&\frac{1}{2\pi}\int_{-\infty}^{+\infty}\phi_X(t)e^{-ixt}dt\\ \propto&\int_{-\infty}^{+\infty}\frac{e^{-ixt}}{\left[(t-\frac{i}{(1-\rho)\sigma_A\sigma_B})(t+\frac{i}{(1+\rho)\sigma_A\sigma_B}))\right]^{N/2}}dt,\end{aligned} \tag{5.32}$$

and perform the change of variable $t\to t+\frac{i\rho}{(1-\rho^2)\sigma_A\sigma_B}$ to obtain

$$f_X(x)\propto e^{\frac{\rho x}{(1-\rho^2)\sigma_A\sigma_B}}\int_{-\infty}^{+\infty}\frac{e^{-ixt}}{\left[t^2+\frac{1}{(1-\rho^2)\sigma_A\sigma_B^2}\right]^{-N/2}}dt. \tag{5.33}$$

Then making use of the Basset integral (Olver et al. 2010, Eq.10.32.11) and reintroducing the normalization, we get:

$$f_X(x)=\frac{|x|^{(N-1)/2}e^{\frac{\rho x}{(1-\rho^2)\sigma_A\sigma_B}}K_{(N-1)/2}\left(\frac{|x|}{(1-\rho^2)\sigma_A\sigma_B}\right)}{2^{(N-1)/2}\sqrt{\pi}\Gamma(N/2)\sqrt{1-\rho^2}(\sigma_A\sigma_B)^{(N+1)/2}}, \tag{5.34}$$

where Γ refers to the gamma function and K_ν is the modified Bessel function of second kind and order $\nu=(N-1)/2$. We can check a-posteriori that we recover indeed Eq. 5.29 for the $N=1$ case, which justifies Eq. 5.30.

We now have all in hands to consider a full-sky $A\times B$ cross-spectrum $\hat{C}_\ell^{\,AB}=\frac{1}{2\ell+1}\sum_{l=-m}^{m}a_{lm}^Aa_{lm}^{B*}$ where for (isotropic) noise power (N^A,N^B) the covariance matrix reads

$$\mathbf{V}=\begin{pmatrix}C_\ell^{\rm th}+N_\ell^A & C_\ell^{\rm th}\\ C_\ell^{\rm th} & C_\ell^{\rm th}+N_\ell^B\end{pmatrix}. \tag{5.35}$$

Its p.d.f for a given ℓ therefore reads:

$$f_N(\hat{C}_\ell)=Nf_X(N\hat{C}_\ell) \tag{5.36}$$

where $N=2\ell+1$, and, in Eq. 5.34:

$$\begin{cases}\sigma_A=\sqrt{C_\ell^{\rm th}+N_\ell^A}\\ \sigma_B=\sqrt{C_\ell^{\rm th}+N_\ell^B}\\ \rho=\dfrac{C_\ell^{\rm th}}{\sqrt{(C_\ell^{\rm th}+N_\ell^A)(C_\ell^{\rm th}+N_\ell^B)}}.\end{cases} \tag{5.37}$$

This formula is similar to the one given (but not derived) in Percival & Brown (2006, Eq.19) for the TE distribution.
The characteristic function of the cross-spectrum estimator is:

$$\phi_{\hat{C}}(t)=\phi_X(\frac{t}{N}). \tag{5.38}$$

5.B Auto-spectra and cross-spectra statistics comparison

It is instructive to study the respective merits of the auto and cross spectra approaches to estimate a single field power-spectrum. We concentrate here on the full sky case where the auto and cross spectra estimators can be handled analytically. The main conclusions hold essentially on a cut-sky too.
Let us first recall some properties of power-spectrum estimation using auto-spectra. We consider the measurement of a Gaussian field (of power-spectrum $C_\ell^{\rm th}$) over the full sky with an instrument which has an isotropic noise (of power-spectrum N_ℓ^C) uncorrelated to the signal.
According to the spectral theorem, the decomposition of the map onto the (orthogonal) spherical harmonics basis yields a set of *independent* Gaussian random variables: $a_{\ell m}$'s. For a given multipole ℓ, this variable $x\equiv a_{\ell m}$ follows a Gaussian distribution of null mean and variance $\sigma_\ell^2=C_\ell^{\rm th}+N_\ell$. At a given ℓ , from a set of $N=2\ell+1$ measured harmonic coefficients $\{x_i\}$ the Maximum Likelihood estimator of $C_\ell^{\rm th}$ is the empirical variance:

$$\hat{C}_\ell=\frac{1}{N}\sum_{i=1}^{\ell}x_i^2-N_\ell^C \tag{5.39}$$

This estimator's distribution can be computed analytically by noticing that since x_i follows $\mathcal{N}(.;0,C_\ell^{\rm th}+N_\ell^C)$ it can be written as

$$\hat{C}_\ell=\frac{C_\ell^{\rm th}+N_\ell^C}{N}y-N_\ell^C \tag{5.40}$$

where y follows now a χ^2_N distribution. Then from the analytic χ^2 p.d.f and standard probability transformation rules one can obtain analytically the full $\hat{C}_\ell$ p.d.f (which is a Γ one). [1]
We do not need any elaborate expression to compute the first order moments. Instead we use the scaling property of the cumulants (which are equivalent to central moments up to the third order) which states that if X has some cumulants $\kappa_i(X)$, the cumulants of a linear transformation $Y=aX+b$ are $\kappa_i(Y)=a^i\kappa_i(X)+b\delta_i^1$. Since the first cumulants of a χ^2_N distribution are $\kappa=N(1,2,8...)$, Eq. 5.40 gives immediately:

$$\kappa_1(\hat{C}_\ell)=E\left[\hat{C}_\ell\right]=\frac{C_\ell^{\rm th}+N_\ell^C}{N}N-N_\ell^C=C_\ell^{\rm th} \tag{5.41}$$

$$\kappa_2(\hat{C}_\ell)={\rm Var}[\hat{C}_\ell]=\left(\frac{C_\ell^{\rm th}+N_\ell^C}{N}\right)^2 2N=\frac{2(C_\ell^{\rm th}+N_\ell^C)^2}{N} \tag{5.42}$$

$$\kappa_3(\hat{C}_\ell)=E\left[(\hat{C}_\ell-C_\ell^{\rm th})^3\right]=\left(\frac{C_\ell^{\rm th}+N_\ell^C}{N}\right)^3 8N=\frac{8(C_\ell^{\rm th}+N_\ell^C)^3}{N^2}, \tag{5.43}$$

Any error on the noise level estimation N_ℓ^C bias accordingly the estimator (κ_1) and we can recognize the cosmic variance expression (κ_2).
The clear advantage of using cross-spectra has already been emphasized: the estimator is unbiased whatever knowledge we have of the noise spectra, cf. Eq. 5.6 .
However in order to investigate its discriminating power, we also need to consider its variance, and to a lesser extent its higher order moments. What do we loose statistically using cross-spectra over using an auto-spectrum assuming a perfect knowledge of the noise? The answer depends on the relative levels of the signal ($C_\ell^{\rm th}$) and noise spectra (N_ℓ^A,N_ℓ^B) and on the ℓ range under consideration. To get some further insight, we consider the EE field from the *Planck* 2015 best-fit (Planck Collaboration XIII 2015) and variety of realistic maps noise-levels. We focused on three particular public datasets: *WMAP* (V band), *Planck*-70 (70GHz) and two *Planck*-HFI channels (100GHz and 143GHz).
We then consider the variance of the cross-spectrum estimator Eq. 5.5 and compare it to the one obtained on the auto-spectrum of an optimally inverse-variance combined map, i.e. with noise

$$\frac{1}{N_\ell^C}=\frac{1}{N_\ell^A}+\frac{1}{N_\ell^B} \tag{5.44}$$

We show the ratio of these quantities for the different noise-pair combinations on Fig. 5.14.
The variance increase is important in the case of two very different noise levels (for instance *WMAP*×*Planck*-HFI) and moderate when they are similar (*WMAP*×*Planck*-70, *Planck*-100×*Planck*-143). This can be understood from the variance formulas Eqs. (5.42) and (5.5) where when $N_\ell^B\gg N_\ell^A$,$N_\ell^C\simeq N_\ell^A$:

$${\rm Var}(\hat{C}_\ell^{\,A\times B})\simeq\frac{1}{N}\left(2(C_\ell^{\rm th})^2+N_\ell^BC_\ell^{\rm th}+N_\ell^AN_\ell^B\right) \tag{5.45}$$

$${\rm Var}(\hat{C}_\ell^{\,C})\simeq\frac{1}{N}\left(2(C_\ell^{\rm th})^2+4N_\ell^AC_\ell^{\rm th}+2(N_\ell^A)^2\right). \tag{5.46}$$

[1] We emphasize we are dealing for the moment with the estimator distribution, not the posterior or likelihood one.

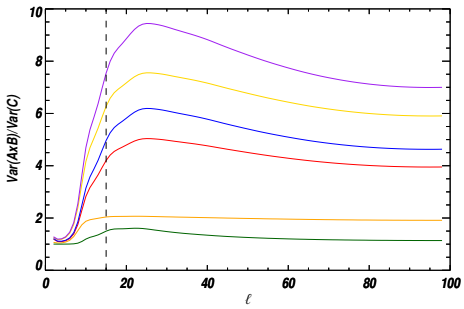

Figure 5.14: Ratio of the variance of the $A-B$ coss spectrum estimator to the one from the auto-spectrum of the optimally combined map. The colors indicate different noise combinations according to the following scheme: *WMAP*×*Planck*-70= orange, *WMAP*×*Planck*-100 = gold, *WMAP*×*Planck*-143 = purple, *Planck*-70×*Planck*-100 = red, *Planck*-70×*Planck*-143 = blue, *Planck*-100×*Planck*-143 = green. The dashed line recalls that most of the interesting information in EE about reinization is contained below $\ell \lesssim 15$.

Beyond the first term (the cosmic variance) which is dominant for low-ℓ's, the cross-spectrum picks up the noisiest of the two measurement while auto-spectra uses essentially the best one.

On the other side, when both measurements have similar noise levels, $N_\ell^A \simeq N_\ell^B, N_\ell^C \simeq \frac{N_\ell^A}{2}$, the variances become similar:

$$\mathrm{Var}(\hat{C}_\ell^{A\times B}) \simeq \frac{1}{N}\left(2(C_\ell^{\mathrm{th}})^2 + 2N_\ell^A C_\ell^{\mathrm{th}} + (N_\ell^A)^2\right) \tag{5.47}$$

$$\mathrm{Var}(\hat{C}_\ell^{C}) \simeq \frac{1}{N}\left(2(C_\ell^{\mathrm{th}})^2 + 2N_\ell^A C_\ell^{\mathrm{th}} + \frac{(N_\ell^A)^2}{2}\right). \tag{5.48}$$

Wether the linear term on C_ℓ^{th}dominates or not depends on the signal, the noise levels and the ℓ range. As a rule-of-thumb, the comparision of Eq. 5.45 to Eq. 5.46 suggests that the statistical loss for a cross-combination is *reasonable* when the two noise levels are within a factor ≃3. The same kind of conclusion holds for the third central moment, but one can get a smaller κ_3 value using cross-spectra for similar noise levels (Fig. 5.15).

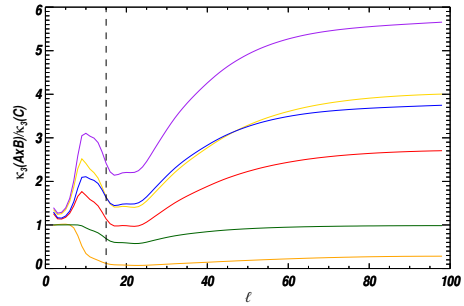

Figure 5.15: Ratio of the third order central moment (κ_3) for the $A\times B$ coss spectrum estimator to the one from the auto-spectrum of the optimally combined map. The colors indicate different noise combinations according to the following scheme: *WMAP*×*Planck*-70= orange, *WMAP*×*Planck*-100 = gold, *WMAP*×*Planck*-143 = purple, *Planck*-70×*Planck*-100 = red, *Planck*-70×*Planck*-143 = blue, *Planck*-100×*Planck*-143 = green. The dashed line recalls that most of the intresting information in EE about reoinization is contained below $\ell \lesssim 15$.

5.C p.d.f parametrization

In this section we show the excellent agreement that is obtained when comparing the parametrization of the EE PCL estimator distribution defined with the full sky based approach and the Edgeworth expansion method described in Sect. 5.3.2 and Sect. 5.3.2, respectively. We consider the small mask with f_{sky}=0.8 and the *Planck*-100×*Planck*-143 cross-spectrum simulations. Note that due to its low noise levels, this cross-spectrum is the most challenging to describe. All other cross-spectra show an even better agreement. The results are summarized in Fig. 5.16 and Fig. 5.17.

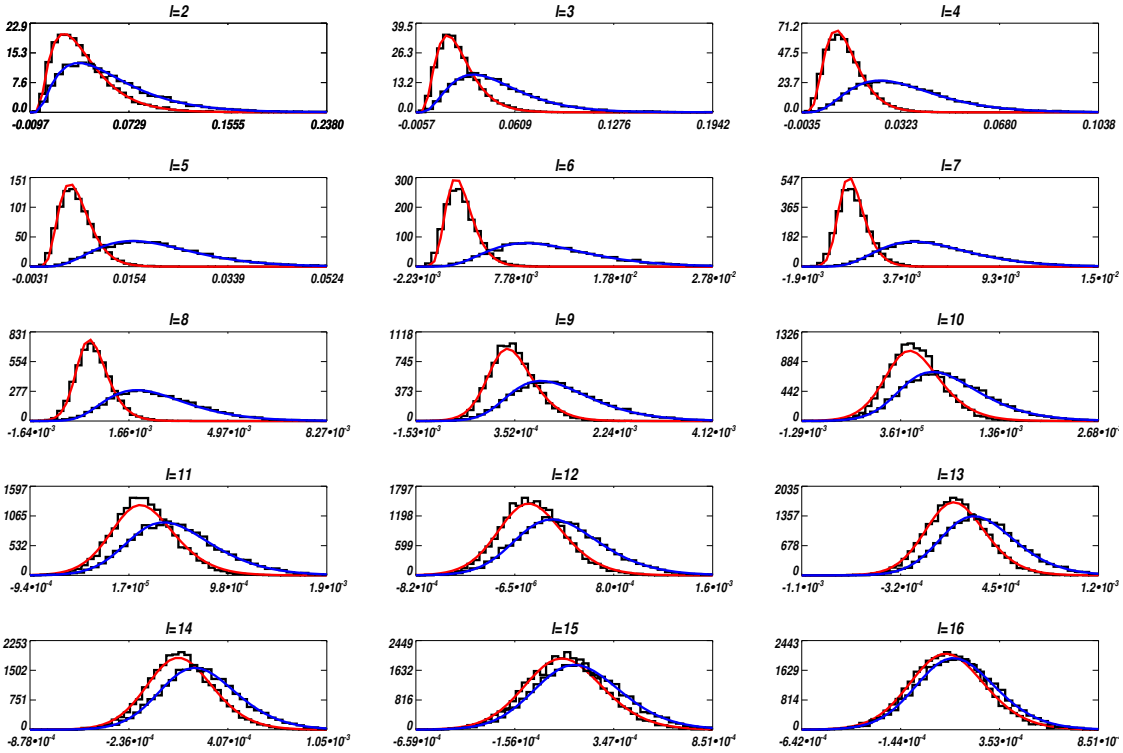

Figure 5.16: Normalized histograms (in black) of the 100×143 PCL estimator in the $\ell\in[2,16]$ range are compared to our analytic full-sky based description, for model1 (blue) and model2 (red). The number of degree of freedom $N(\ell)=(2\ell+1)f_{\rm sky}^{A\times B}(\ell)$ is reduced according to the values obtained on model 2 only (Fig. 5.4).

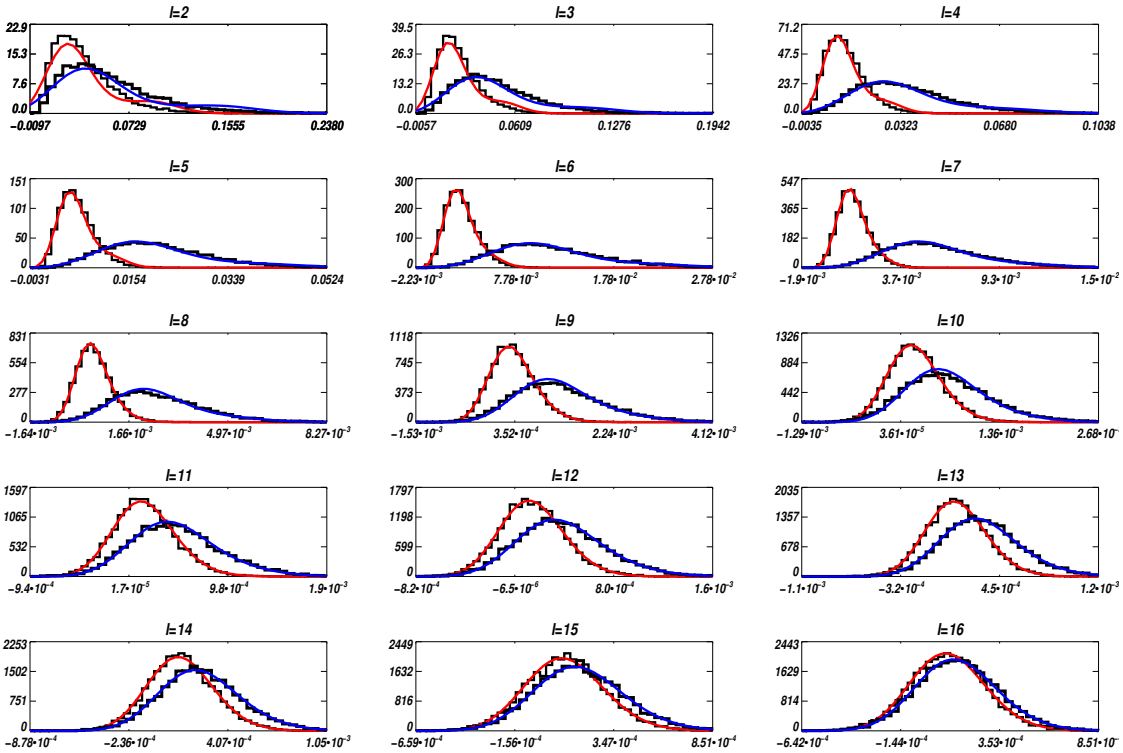

Figure 5.17: Normalized histograms (in black) of the 100×143 PCL estimator in the $\ell\in[2,16]$ range are compared to our analytical parametrization based on the Edgeworth expansion for model1 (blue) and model2 (red).

Bibliography

Bennett, C. L. e. 2013, ApJS, 208, 20
Efstathiou, G. 2006, MNRAS, 370, 343
Gorski, K. M., Hinshaw, G., Banday, A. J., et al. 1994, ApJ, 430, L89
Grishchuk, L. P. 1996, Phys. Rev. D, 53, 6784
Hamimeche, S. & Lewis, A. 2008, Phys.Rev., D77, 103013
Hivon, E., Górski, K. M., Netterfield, C. B., et al. 2002, ApJ, 567, 2
Kendall, M. & Stuart, A. 1963, The Advanced theory of statistics, Distribution theory No. vol. 1 (C. Griffin)
Mangilli, A., Plaszczynski, S., & Tristram, M. 2015, MNRAS, 453, 3174
Olver, F. W. J., Lozier, D. W., Boisvert, R. F., & Clark, C. W., eds. 2010, NIST Handbook of Mathematical Functions (New York, NY: Cambridge University Press)
Page, L. et al. 2007, Astrophys.J.Suppl., 170, 335
Percival, W. J. & Brown, M. L. 2006, Mon.Not.Roy.Astron.Soc., 372, 1104
Planck Collaboration I. 2015, A&A submitted, arXiv:1502.01582 [arXiv:1502.01582]
Planck Collaboration VIII. 2015, A&A submitted, arXiv:1502.01587 [arXiv:1502.01587]
Planck Collaboration XIII. 2015, A&A submitted, arXiv:1502.01589 [arXiv:1502.01589]
Rocha, G., Magueijo, J., Hobson, M., & Lasenby, A. 2001, Phys. Rev. D, 64, 063512
Slosar, A., Seljak, U., & Makarov, A. 2004, Phys.Rev., D69, 123003
Tegmark, M. & de Oliveira-Costa, A. 2001, Phys. Rev. D, 64, 063001
Tristram, M., Macias-Perez, J., Renault, C., & Santos, D. 2005, Mon.Not.Roy.Astron.Soc., 358, 833
Wandelt, B. D., Hivon, E., & Górski, K. M. 2001, Phys. Rev. D, 64, 083003

Chapter 6

Hillipop: High-ℓ Likelihood Polarized for Planck

extracted from Couchot et al. (2017b)

"Cosmology with the CMB temperature-polarization correlation"

In the context of Planck, I developed a likelihood for the small angular scales based on cross-spectra: High-ℓ Likelihood Polarized for Planck. *HiLLiPOP is one of the four high-ℓ likelihoods developed within the* Planck *consortium for the 2015 release and is briefly presented and compared to others in Planck Collaboration XIII (2016). With my post-doc Benjamin Rouillé d'Orfeuil, we worked in order to build an accurate estimation of the foreground residuals both for intensity and polarization. The major difference with the public* Planck *likelihood is that we use* Planck *measurements of the foregrounds residuals rather than relying on astrophysical models. In September 2013, we were the first team to present internally cosmological constraints based on polarized maps. Our results are compatible with the public* Planck *constraints while being more robust with respect to foregrounds (see Chapter 7) and with the lensing amplitude (see Chapter 8).*

This chapter describes in details the construction of the HiLLiPOP (*High-ℓ Likelihood Polarized for Planck*) based on cross-power spectra between CMB channels of the *Planck*-HFI and suitable in the multipole range from 50 to 2500. First we describe the maps and the sky region for the power spectra estimation (Sect. 6.1) and the CMB angular power spectra (Sect. 6.2) used in this analysis. Section 6.3 presents the likelihood functions both in temperature and in polarization. The covariance matrix is presented in Sect. 6.4. Then we address the model including the associated foreground emission (Sect. 6.5) and the additional priors (Sect. 6.6). Results on cosmological parameters are then discussed in Part III.

6.1 Maps and masks

The maps used in this analysis are taken from the Planck 2015 data release[1] and described in details in Planck Collaboration VIII (2016). We use two maps per frequency (A and B, one for each *half-mission*) at 100, 143, and 217 GHz. Beams associated to each maps are provided by the Planck collaboration (Planck Collaboration VII 2016). Figure 6.1 compares the signal with the noise of the Planck maps for each mode TT, EE, and TE.

Frequency-dependent apodized masks are applied to these maps in order to limit the foregrounds contamination in the power spectra. We use the same masks in temperature and polarization. The masks are constructed first by thresholding the total intensity maps of diffuse Galactic dust to exclude strong dust emission. In addition, we also remove regions with strong Galactic CO emission, nearby galaxies, and extragalactic point sources.

Diffuse Galactic dust emission is the main contaminant for CMB measurements in both temperature and polarization at frequencies above 100 GHz. We build Galactic masks using the Planck 353 GHz map as a tracer of the thermal dust emission in intensity. In practice, we smoothed the Planck 353 GHz map to increase the signal-to-noise before applying a threshold which depends on the frequency considered. Masks are then apodized using a 8° Gaussian taper for power spectra estimation. For polarisation, Planck dust maps show that the diffuse emission is strongly related to the Galactic

[1] Planck PLA: http://pla.esac.esa.int

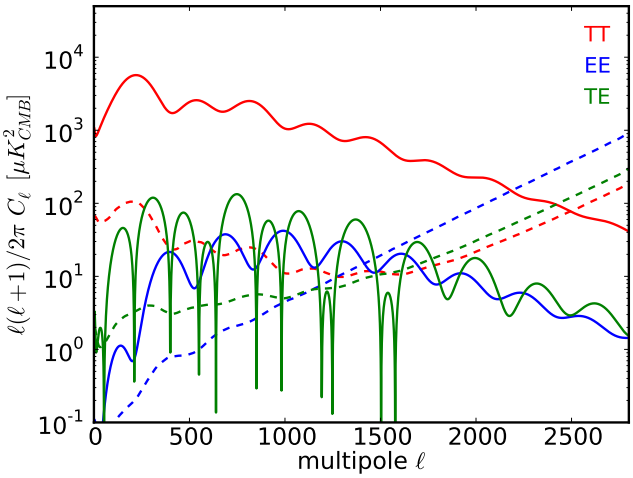

Figure 6.1: Signal (*solid line*) versus noise (*dashed line*) for the Planck cross-spectra for each mode TT, EE, and TE (in *red*, *blue*, and *green*, respectively).

magnetic field at large scales (Planck Collaboration Int. XIX 2015). However, at the smaller scales which matter here (ℓ>50), the orientation of dust grains is driven by local turbulent magnetic fields which produce a polarisation intensity proportional to the total intensity dust map. We thus use the same Galactic mask for polarisation as for temperature.
Molecular lines from CO produce diffuse emission on star forming region. Two major CO lines at 115 GHz and 230 GHz enter the Planck bandwidths at 100 and 217 GHz respectively (Planck Collaboration XIII 2014). We smoothed the Planck reconstructed CO map to 30 arcmin before applying a threshold at 2 K.km/s. The resulting masks are then apodised at 15 arcmin. In practice, the CO masks are almost completely included in the Galactic masks, decreasing the accepted sky fraction by only a few percents.
For point sources, the Planck 2013 and 2015 analyses mask the sources detected with a signal-to-noise above 5 in the Planck point-source catalogue (Planck Collaboration XXVI 2016) at each frequency (Planck Collaboration XVI 2014; Planck Collaboration XI 2016). On the contrary, the masks used in our analysis rely on a more refined procedure that preserves Galactic compact structures and ensures the completeness level at each frequency, but with a higher flux cut (340, 250, and 200 mJy at 100, 143, and 217 GHz, respectively). The consequence is that these masks leave slightly more unmasked extragalactic sources but preserve the power-spectra of the dust emission (as described in Planck Collaboration Int. XXX 2016). For each frequency, we mask a circular area around each source using a radius of three times the effective Gaussian beam width (σ=$FWHM$/ $\sqrt{\ln 8}$) at that frequency. We apodize these masks with a Gaussian taper of FWHM = 15 arcmin.
Finally, we also mask strong extragalactic objects including both point sources and nearby extended galaxies. The masked galaxies include the LMC and SMC and also M31, M33, M81, M82, M101, M51, and CenA.
The combined masks used are named M80, M70 and M55 (corresponding to effective $f_{\rm sky}$=72%,62%,48%), associated to the 100, 143, and 217 GHz channels, respectively (Fig. 6.2). Tests have been carried out using more conservative Galactic masks (with $f_{\rm sky}$ = 65%, 55% and 40% for 100, 143, and 217 GHz, respectively) showing perfectly compatible results than with the smaller masks. Compared to the masks used in the Planck 2015 analysis, the retained sky fraction is almost identical. Indeed, the Galactic masks used in Planck Collaboration XI (2016) retain 70%, 60%, and 50% respectively.

6.2 Power spectra

We use *Xpol* (an extension to polarisation of Tristram et al. 2005) to compute the cross-power spectra in temperature and polarisation (TT, EE, and TE). *Xpol* is a *pseudo-C_ℓ* method which also computes an analytical approximation of the C_ℓ covariance matrix directly from data. Using the six maps presented in Sect. 6.1, we derive the 15 cross-power spectra for each CMB mode: one for 100×100, 143×143, and 217×217; four for 100×143, 100×217, and 143×217 as outlined below.
From the coefficients of the spherical harmonic decomposition of the (I,Q,U) masked maps $\tilde{\mathbf{a}}^X_{\ell m}$=$\{\tilde{a}^T_{\ell m},\tilde{a}^E_{\ell m},\tilde{a}^B_{\ell m}\}$, we form the pseudo cross-power spectra between map i and map j:

$$\tilde{\mathbf{C}}^{ij}_\ell = \frac{1}{2\ell+1}\sum_m \tilde{\mathbf{a}}^{i*}_{\ell m}\tilde{\mathbf{a}}^{j}_{\ell m}, \tag{6.1}$$

where the vector $\tilde{\mathbf{C}}_\ell$ includes the 4 modes $\{\tilde{C}^{TT}_\ell,\tilde{C}^{EE}_\ell,\tilde{C}^{TE}_\ell,\tilde{C}^{ET}_\ell\}$. Note that the TE and ET cross-power spectra do not carry exactly the same information since computing T from the map i and E from the map j is not the same as computing E from the map j and T from i. They are computed independently and averaged afterwards using their relative weights for

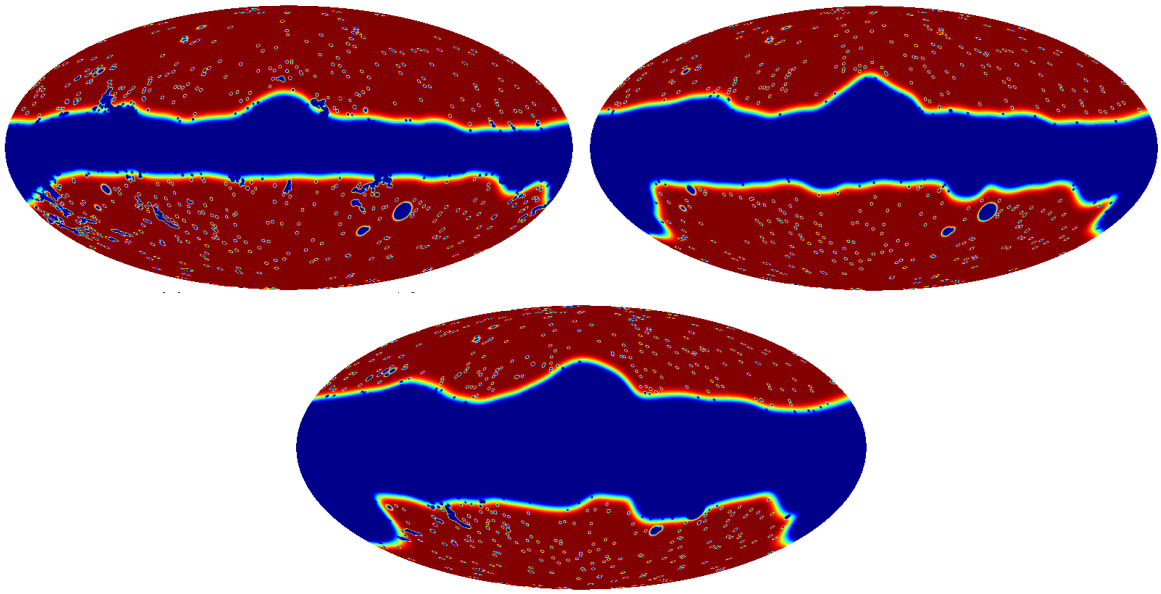

Figure 6.2: The M80, M70 and M55 masks. A combination of apodized Galactic mask and compact objects mask is used at each frequency (see text for details).

each cross-frequency. The pseudo-spectra are then corrected from beam and sky fraction using

$$\tilde{\mathbf{C}}_\ell^{ij}=(2\ell'+1)\mathsf{M}_{\ell\ell'}^{ij}\mathbf{C}_{\ell'}^{ij} \tag{6.2}$$

where the coupling matrix M depends on the masks used for each set of maps (Peebles 1973) and includes beam transfer functions usually extracted from Monte-Carlo simulations (Hivon et al. 2002).
The multipole ranges used in the likelihood analysis have been chosen to limit the contamination of the Galactic dust emission at low-ℓ and the noise at high-ℓ. Table 6.1 gives the multipole ranges, $[\ell_{\rm min},\ell_{\rm max}]$, considered for each of the six cross-frequencies in TT, TE, and EE. The spectra are cosmic-variance limited up to $\ell\simeq1500$ in TT and $\ell\simeq700$ in TE (outside of the troughs of the CMB signal). The EE mode is dominated by instrumental noise.

	TT	EE	TE
100×100	[50,1200]	[100,1000]	[100,1200]
100×143	[50,1500]	[100,1250]	[100,1500]
100×217	[500,1500]	[400,1250]	[200,1500]
143×143	[50,2000]	[100,1500]	[100,1750]
143×217	[500,2500]	[400,1750]	[200,1750]
217×217	[500,2500]	[400,2000]	[200,2000]
n_ℓ	9556	7256	8806

Table 6.1: Multipole ranges used in the analysis and corresponding number of multipole available ($n_\ell=\ell_{\rm max}-\ell_{\rm min}+1$). The total number of multipoles is 25618.

6.3 The likelihood function

On the full-sky, the distribution of auto-spectra is a scaled-χ^2 with $2\ell+1$ degrees of freedom. The distribution of the cross-spectra is slightly different (see Appendix A in Mangilli et al. 2015), however, above $\ell\geqslant50$, the number of modes is large enough so that we can safely assume that the C_ℓ are Gaussian distributed. When considering only a part of the sky, the C_ℓs get correlated so that for high multipoles, the resulting distribution can be approximated by a multi-variate Gaussian taking into account ℓ-by-ℓ correlations:

$$-2\ln\mathcal{L}=\sum_{\substack{i\leqslant j\\ i'\leqslant j'}}\sum_{\ell\ell'}\mathbf{R}_\ell^{ij}\left[\Sigma^{-1}\right]_{\ell\ell'}^{ij,i'j'}\mathbf{R}_{\ell'}^{i'j'}+\ln|\Sigma| \tag{6.3}$$

where $\mathbf{R}_\ell^{ij}=\mathbf{C}_\ell^{ij}-\hat{\mathbf{C}}_\ell^{ij}$ denotes the residual of the estimated cross-power spectrum $\mathbf{C}_\ell$ with respect to the model $\hat{\mathbf{C}}_\ell$ for each polarisation mode considered (TT,EE,TE) and each frequency ($\{i,j\}\in[100,143,217]$). The matrix $\Sigma=\left\langle\mathbf{R}\mathbf{R}^T\right\rangle$ is the

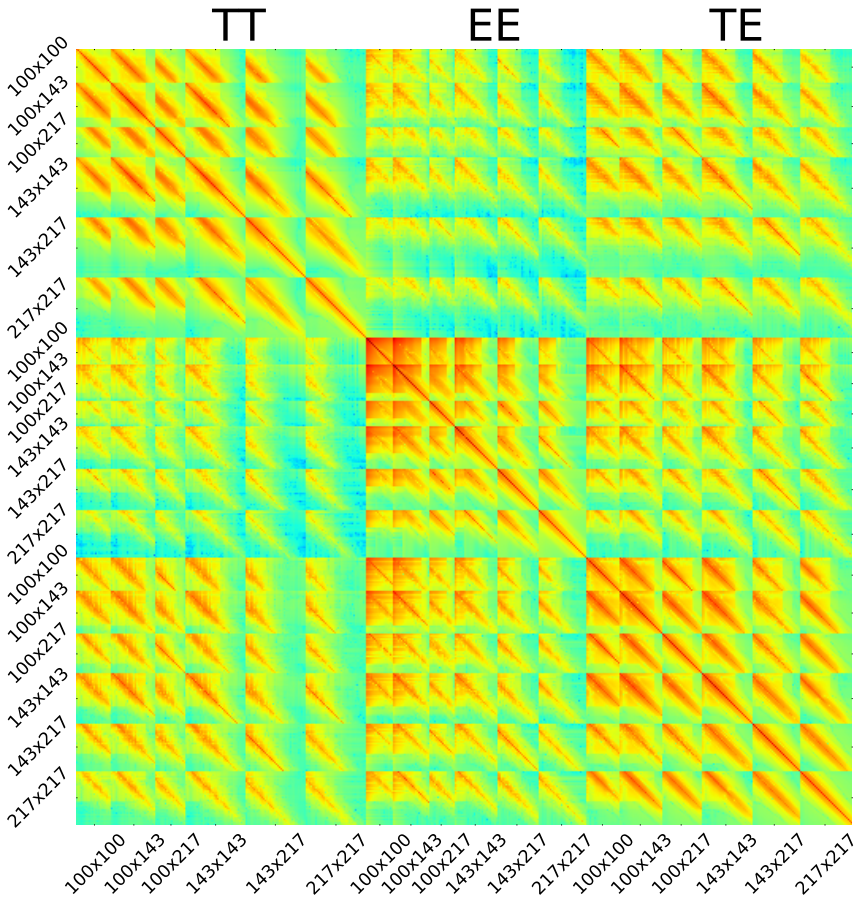

Figure 6.3: The full HiLLiPOP covariance matrix including all correlations in multipoles, between cross-frequencies and power spectra.

full covariance matrix which includes the instrumental variance from the data as well as the cosmic variance from the model. The latter is directly proportional to the model so that the matrix $\mathbf{\Sigma}$ should, in principle, depend on the model. In practice, given our current knowledge of the cosmological parameters, the theoretical power spectra typically differ from each other at each ℓ by less than they differ from the observed C_ℓ so that we can expand $\mathbf{\Sigma}$ around a reasonable fiducial model. As described in Planck Collaboration XV (2014), the additional terms in the expansion are small if the fiducial model is accurate and its absence do not bias the likelihood. Using a fixed covariance matrix $\mathbf{\Sigma}$, we can drop the constant term $\ln|\mathbf{\Sigma}|$.We therefore expect the likelihood to be χ^2-distributed with a mean equal to the number of degree of freedom $n_{\rm dof}=n_\ell-n_{\rm p}$ (where n_ℓ is reported in Table 6.1 and $n_{\rm p}$ is the number of fitted parameters) and a variance equal to $2n_{\rm dof}$.
We define several likelihood functions based on the information used: `HillipopT` for TT cross-spectra, `HillipopE` for EE cross-spectra, `HillipopX` for TE cross-spectra, and `HillipopTXE` for the combination of all cross-spectra. The `HillipopX` likelihood combines information from TE and ET cross-spectra.
The next two sections describe the computation of the covariance matrix and the building of the model, insisting on the differences with the Planck public likelihood.

6.4 Semi-analytical covariance matrix

We use a semi-analytical estimation of the C_ℓ covariance matrix computed using *Xpol*. The matrix encloses the ℓ-by-ℓ correlations between all the power spectra involved in the analysis. The computation relies directly on data estimates. It follows that contributions from noise (correlated and uncorrelated), sky emission (from astrophysical and cosmological origin) and the *cosmic variance* are implicitly taken into account in this computation without relying on any model or simulations.
The covariance matrix $\mathbf{\Sigma}$ of cross-power spectra is directly related to the covariance $\tilde{\mathbf{\Sigma}}$ of the pseudo cross-power spectra through the coupling matrices:

$$\Sigma^{ab,cd}_{\ell_1\ell_2}\equiv\left\langle\Delta C^{ab}_\ell\Delta C^{cd*}_{\ell'}\right\rangle=\left(M^{ab}_{\ell\ell_1}\right)^{-1}\tilde{\Sigma}^{ab,cd}_{\ell_1\ell_2}\left(M^{cd*}_{\ell'\ell_2}\right)^{-1} \tag{6.4}$$

with $(a,b,c,d)\in\{T,E\}$ for each map A,B,C,D.
We compute $\tilde{\mathbf{\Sigma}}$ for each cross-spectra blocks independently that includes ℓ-by-ℓ correlation and 4-spectra mode correlation $\{TT,EE,TE,ET\}$. Both TE and ET blocks are computed individually and finally averaged. The matrix $\tilde{\mathbf{\Sigma}}$ that gives the correlations between the pseudo cross-power spectra (ab) and (cd) is a N-by-N matrix (where $N=n_\ell^{TT}+n_\ell^{EE}+n_\ell^{TE}+n_\ell^{ET}$) and reads:

$$\begin{aligned}\tilde{\Sigma}^{ab,cd}_{\ell\ell'} &\equiv \left\langle \Delta\tilde{C}^{ab}_{\ell}\Delta\tilde{C}^{cd*}_{\ell'}\right\rangle = \left\langle \tilde{C}^{ab}_{\ell}\tilde{C}^{cd*}_{\ell'}\right\rangle - \tilde{C}^{ab}_{\ell}\tilde{C}^{cd*}_{\ell'} \\ &= \sum_{mm'}\frac{\left\langle \tilde{a}^{a}_{\ell m}\tilde{a}^{c*}_{\ell' m'}\right\rangle\left\langle \tilde{a}^{b*}_{\ell m}\tilde{a}^{d}_{\ell' m'}\right\rangle + \left\langle \tilde{a}^{a}_{\ell m}\tilde{a}^{d*}_{\ell' m'}\right\rangle\left\langle \tilde{a}^{b*}_{\ell m}\tilde{a}^{c}_{\ell' m'}\right\rangle}{(2\ell+1)(2\ell'+1)}\end{aligned}$$

by expanding the 4-point Gaussian correlation using the Isserlis' formula (or Wick theorem).
Each 2-point correlation of pseudo-$a_{\ell m}$ can be expressed as the convolution of $\mathbf{C}_\ell$ with a kernel which depends on the polarisation mode considered:

$$\begin{aligned}\left\langle \tilde{a}^{T_a*}_{\ell m}\tilde{a}^{T_b}_{\ell' m'}\right\rangle &= \sum_{\ell_1 m_1} C^{T_aT_b}_{\ell_1} W^{0,T_a}_{\ell m \ell_1 m_1} W^{0,T_b*}_{\ell' m' \ell_1 m_1} \\ \left\langle \tilde{a}^{E_a*}_{\ell m}\tilde{a}^{E_b}_{\ell' m'}\right\rangle &= \frac{1}{4}\sum_{\ell_1 m_1}\left\{C^{E_aE_b}_{\ell_1} W^{+,E_a*}_{\ell m \ell_1 m_1} W^{+,E_b}_{\ell' m' \ell_1 m_1} + C^{B_aB_b}_{\ell_1} W^{-,E_a*}_{\ell m \ell_1 m_1} W^{-,E_b}_{\ell' m' \ell_1 m_1}\right\} \\ \left\langle \tilde{a}^{T_a*}_{\ell m}\tilde{a}^{E_b}_{\ell' m'}\right\rangle &= \frac{1}{2}\sum_{\ell_1 m_1} C^{T_aE_b}_{\ell_1} W^{0,T_a*}_{\ell m \ell_1 m_1} W^{+,E_b}_{\ell' m' \ell_1 m_1}\end{aligned}$$

in which the kernels W^0, W^+, and W^- are defined as linear combination of products of $Y_{\ell m}$ of spin 0 and ±2 (see Appendix 6.A). As suggested in Efstathiou (2006), neglecting the gradients of the window function and applying the completeness relation for spherical harmonics (Varshalovich et al. 1988), we can reduce the products of four W into kernels similar to the coupling matrix M defined in Eq. 6.2. In the end, the blocks of $\mathbf{\Sigma}$ matrices reads:

$$\begin{aligned}\Sigma^{T_aT_b,T_cT_d} &\simeq C^{T_aT_c}_{\ell\ell'}C^{T_bT_d}_{\ell\ell'}\mathsf{M}_{TT,TT} + C^{T_aT_d}_{\ell\ell'}C^{T_bT_c}_{\ell\ell'}\mathsf{M}_{TT,TT} \\ \Sigma^{E_aE_b,E_cE_d} &\simeq C^{E_aE_c}_{\ell\ell'}C^{E_bE_d}_{\ell\ell'}\mathsf{M}_{EE,EE} + C^{E_aE_d}_{\ell\ell'}C^{E_bE_c}_{\ell\ell'}\mathsf{M}_{EE,EE} \\ \Sigma^{T_aE_b,T_cE_d} &\simeq C^{T_aT_c}_{\ell\ell'}C^{E_bE_d}_{\ell\ell'}\mathsf{M}_{TE,TE} + C^{T_aE_d}_{\ell\ell'}C^{E_bT_c}_{\ell\ell'}\mathsf{M}_{TT,TT} \\ \Sigma^{T_aT_b,T_cE_d} &\simeq C^{T_aT_c}_{\ell\ell'}C^{T_bE_d}_{\ell\ell'}\mathsf{M}_{TT,TT} + C^{T_aE_d}_{\ell\ell'}C^{T_bT_c}_{\ell\ell'}\mathsf{M}_{TT,TT} \\ \Sigma^{T_aT_b,E_cE_d} &\simeq C^{T_aE_c}_{\ell\ell'}C^{T_bE_d}_{\ell\ell'}\mathsf{M}_{TT,TT} + C^{T_aE_d}_{\ell\ell'}C^{T_bE_c}_{\ell\ell'}\mathsf{M}_{TT,TT} \\ \Sigma^{E_aE_b,T_cE_d} &\simeq C^{E_aT_c}_{\ell\ell'}C^{E_bE_d}_{\ell\ell'}\mathsf{M}_{TE,TE} + C^{E_aE_d}_{\ell\ell'}C^{E_bT_c}_{\ell\ell'}\mathsf{M}_{TE,TE}\end{aligned}$$

which are thus directly related to the measured auto- and cross-power spectra (see Appendix 6.A for details). In practice, to avoid any correlation between C_ℓ estimates and their covariance, we use a smoothed version of each measured power spectrum (using a Gaussian filter with σ_ℓ=5) to estimate the covariance matrix.
The analytical full covariance matrix (Fig. 6.3) has 25618×25618 elements, is symmetric and positive definite. Its condition number is $\sim 10^8$.
This semi-analytical estimation have been tested against Monte-Carlo simulations. In particular, we tested how accurate the approximations are in the case of: non-ideal Gaussian signal (due to the presence of small foregrounds residuals); Planck realistic (low) level of pixel-pixel correlated noise; and apodization length used for the mask. We have found no deviation to the sample covariance estimated from the 1000 realizations of the Full-focal Plane Planck simulations (FFP8, see Planck Collaboration XII 2016) including anisotropic correlated noise and foreground residuals. To go further and check the detailed impact from the sky mask (including the choice of the apodization length), we simulated CMB maps from the Planck 2015 best-fit ΛCDM angular power spectrum, on which we added realistic anisotropic Gaussian noise (but without correlation) corresponding to each of the six dataset maps. We then computed their cross-power spectra using the same foreground masks as for the data. A total of 15000 sets of cross-power spectra have been produced.
When comparing the diagonal of the covariance matrix from the analytical estimation with the corresponding simulated variance, a precision better than a few percents is found (Fig. 6.4). The residuals show some oscillations, essentially in temperature, which are introduced by the compact objects mask. Indeed, the large number of small holes with short apodization length of the latter induces structures in the harmonic window function which break the hypothesis used in the semi-analytical estimation of the C_ℓ covariance matrix. However, the refined procedure used to construct our specific point source mask allows to keep the level of the impact to less than a few percent.
Since we are using a Gaussian approximation of the likelihood, the uncertainty of the covariance matrix will not bias the cosmological parameters estimation. The percent precision obtained here will then only propagates into a percent error on the variance of the recovered cosmological model.

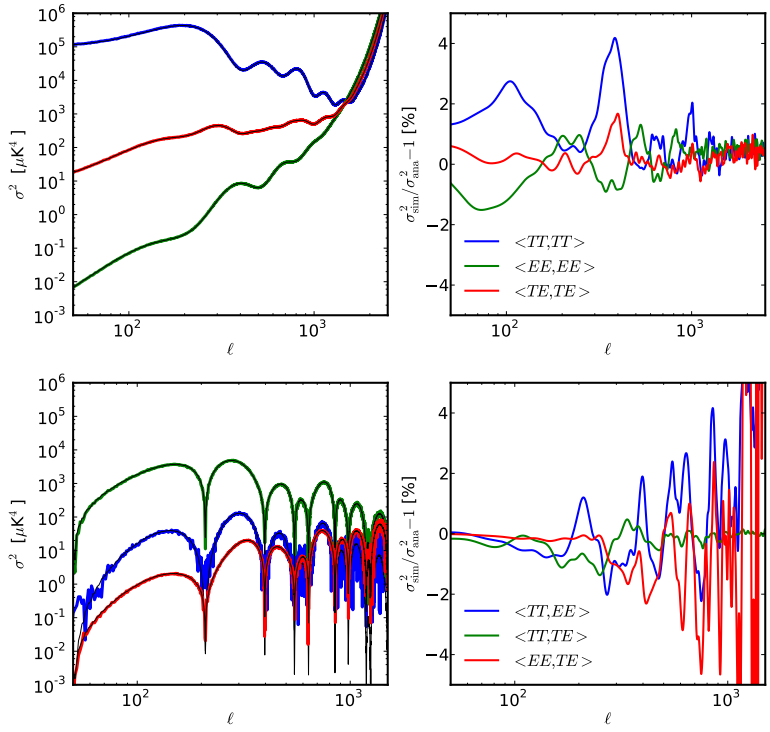

Figure 6.4: Diagonals of the C_ℓ covariance matrix $\mathbf{\Sigma}$ for the block 143A×143B computed using the semi-analytical estimation (*color lines*) compared with the Monte-Carlo (*black line*). *Top:* spectra auto-correlation. *Bottom:* spectra cross-correlation.

6.5 Model

We now present the model ($\hat{\mathbf{C}}_\ell$) used in the likelihood (Eq. 6.3). The foreground emissions are mitigated by applying the masks (defined in Sect. 6.1) and using an appropriate choice of multipole range. However, our likelihood function explicitly takes into account residuals of foreground emissions in power spectra together with CMB model and instrumental systematic effects. The model finally reads:

$$\hat{\mathbf{C}}^{ij}_\ell = A^2_{\rm pl} c_i c_j \left(1+\beta^{ij}\mu^{ij}_\ell\right)^2 \left(\mathbf{C}^{\rm CMB}_\ell + \sum_{\rm fg} A^{ij}_{\rm fg} \mathbf{C}^{ij,{\rm fg}}_\ell\right) \tag{6.6}$$

where $A_{\rm pl}$ is an absolute calibration factor, c_i represents the inter-calibration of each map (normalized to the 143A map), β is the amplitude of the beam uncertainty μ_ℓ, and $\mathsf{A}_{\rm fg}$ are the amplitudes of the foregrounds components $\mathbf{C}^{\rm fg}_\ell$.
The model for CMB, $\mathbf{C}^{\rm CMB}_\ell$, is computed solving numerically the background+perturbation equations for a specific cosmological model. In this paper, we consider a ΛCDM model with 6 free parameters describing: the density of baryons (Ω_b) and Cold Dark Matter (Ω_{cdm}) today; the angular size of sound horizon at recombination (θ); the reionization optical depth (τ); and the index and the amplitude of the primordial scalar spectrum ($n_{\rm s}$ and $A_{\rm s}$).
We include in the sum of the foregrounds for the temperature likelihood contributions from: Galactic dust, cosmic infrared background (CIB), thermal (tSZ) and kinetic (kSZ) Sunyaev-Zeldovich, Poisson point sources (PS), and correlation between infra-red galaxies and the tSZ effect (tSZxCIB). Only Galactic dust is considered in polarization. Synchrotron emission is known to be significantly polarized but it is subdominant in the Planck-HFI channels and we can neglect its contribution in power-spectra above ℓ=50. The contribution from polarized point sources is also negligible in the ℓ range considered for polarized spectra (Tucci & Toffolatti 2012).
In HiLLiPOP, we use physically motivated templates of foreground emissions power spectra, based on Planck measurements. We assume a C_ℓ template for each foreground with a fixed frequency spectrum and rescale it using a free parameter $\mathsf{A}^{\rm fg}$ normalized to one.
The model is a function of the cosmological ($\mathbf{\Omega}$) and nuisance (p) parameters: $\hat{\mathbf{C}}^{\rm model}_\ell(\mathbf{\Omega},p)$. The latter include instrumental parameters accounting for instrumental uncertainties and scaling parameters for each astrophysical foreground models as described in the following sections. At the end, we have a total of 6 instrumental (only calibration is considered, see Sect. 6.5.1), 9 astrophysical (7 for TT, 1 for TE, 1 for EE) and 6+ cosmological (ΛCDM and extensions) i.e. a total of 21+ free parameters in the full likelihood function (see Table 6.2). Note that the Planck public likelihood depends on more nuisance parameters: 15 for TT (compared to 13 for `HillipopT`), 9 for TE (compared to 7 for `HillipopX`), and 9 for EE (compared to 7 for `HillipopE`).

name	definition	prior (if any)
	instrumental	
c_0	map calibration (100-A)	0.000±0.002
c_1	map calibration (100-B)	0.000±0.002
c_2	map calibration (143-A)	fixed
c_3	map calibration (143-B)	0.000±0.002
c_4	map calibration (217-A)	0.002±0.002
c_5	map calibration (217-B)	0.002±0.002
$A_{\rm pl}$	absolute calibration	1±0.0025
	foreground modelling	
$A_{\rm PS}^{\rm radio}$	scaling parameter for radio sources in TT	
$A_{\rm PS}^{\rm IR}$	scaling parameter for IR sources in TT	
$A_{\rm SZ}$	scaling parameter for the tSZ in TT	
$A_{\rm CIB}$	scaling parameter for the CIB in TT	1.00±0.20
$A_{\rm dust}^{\rm TT}$	scaling parameter for the dust in TT	1.00±0.20
$A_{\rm dust}^{\rm EE}$	scaling parameter for the dust in EE	1.00±0.20
$A_{\rm dust}^{\rm TE}$	scaling parameter for the dust in TE	1.00±0.20
$A_{\rm kSZ}$	scaling parameter for the kSZ effect	
$A_{\rm SZxCIB}$	scaling parameter for cross correlation SZ and CIB	

Table 6.2: Nuisance parameters for the HiLLiPOP likelihood

6.5.1 Instrumental systematics

The instrumental parameters of the HiLLiPOP likelihood are the inter-calibration coefficients (c, which are measured relatively to the 143A map), and the amplitudes (β) of the beam error modes (μ_ℓ). In practice, we have linearized Eq. 6.6 for the coefficients c and fit for small deviations around zero ($c_i \rightarrow 1+c_i$) while fixing c_2=0 for normalization. The uncertainty in the absolute calibration is propagated through a global rescaling factor $A_{\rm pl}$.
The effective beam window functions B_ℓ account for the scanning strategy and the weighted sum of individual detectors performed to obtained the combined maps (Planck Collaboration VII 2016). It is constructed from MonteCarlo (MC) simulations of CMB convolved with the measured beam on each time-ordered data sample. The uncertainties in the determination of the HFI effective beams come directly from simulations and is described in terms of the MC eigenmodes μ_ℓ (Planck Collaboration XV 2014). In the Planck 2013 analysis, it was found that, in practice, only the first beam eigenmode for the 100×100 spectrum was relevant (Planck Collaboration XVI 2014). For the 2015 analysis, (Planck Collaboration XI 2016) found no evidence for beam error in their multipole range thanks to higher accuracy in the beam estimation allowing to reduce the amplitude of the beam uncertainty. As a consequence, in our analysis, we fixed their contribution to zero (β=0).

6.5.2 Galactic dust

The TT, EE, and TE Galactic dust C_ℓ templates are obtained from the cross-power spectra between half-mission maps at 353 GHz (as in Planck Collaboration Int. XXX 2016). This is repeated for each mask combination associated to the map dataset. The estimated power spectra are then accordingly rescaled to each of the six cross-frequencies considered in this analysis. We compute the 353 GHz cross-spectra $\hat{\mathbf{C}}_\ell^{M_iM_j}$ for each pair of masks (M_i,M_j) associated to the cross-spectra $i\times j$ (Fig. 6.5). We then subtract the Planck best-fit CMB power spectrum. For TT, we also subtract the CIB power spectrum (Planck Collaboration XXX 2014). Besides Galactic dust, unresolved point sources contribute to the TT power spectra at 353 GHz. To construct the dust templates $\mathbf{C}_\ell^{M_iM_j,\rm dust}$ for our analysis, we thus fit a power-law model with a free constant $A\ell^\alpha+B$ in the range ℓ=[50,2500] for TT, while a simple power-law is used to fit the EE, TE power-spectra in the range ℓ=[50,1500].
Thanks to the use of the point source mask (described in Sect. 6.1), our Galactic dust residual power spectrum is much simpler than in the case of the Planck official likelihood. Indeed, the masks used in the Planck analysis remove some Galactic structures and bright cirrus which induces an artificial knee in the residual dust power spectra around $\ell\sim$200 (Sect. 3.3.1 in Planck Collaboration XI 2016). In contrast, our Galactic dust power spectra are directly comparable to the ones derived in Planck Collaboration Int. XXX (2016). Moreover, here we do not assume that the dust power spectra have the same spatial dependence across masks.
For each polarisation mode (TT,EE,TE), we then extrapolate the dust templates at 353 GHz for each cross-mask to the cross-frequency considered:

$$\mathbf{C}_\ell^{ij,\rm dust} = A_{\rm dust} a_{\nu_i}^{\rm dust} a_{\nu_j}^{\rm dust} \mathbf{C}_\ell^{M_iM_j,\rm dust} \tag{6.7}$$

where the $a_\nu^{dust}=f^{dust}(\nu)/f^{dust}(353\,\rm GHz)$ extrapolated factors are estimated for intensity or polarisation maps. We use a greybody emission law with a mean dust temperature of 19.6 K and spectral indices β^T=1.59 and β_P=1.51 as measured in Planck Collaboration Int. XXII (2015). The resulting a_ν^{dust} factors are (0.0199,0.0387,0.1311) for total intensity and (0.0179,0.0384,0.1263) for polarization at 100, 143, and 217 GHz, respectively.
In HiLLiPOP, this results in three free parameters ($A_{\rm dust}^{TT}$, $A_{\rm dust}^{EE}$, $A_{\rm dust}^{TE}$) describing the amplitude of the dust residuals in each mode. This model based on Planck internal measurements is simpler than what is plugged in the Planck official likelihood which allows the amplitude of each cross-frequency to vary (ending with a total of 16 free parameters) and puts constraints on the dust SED through the use of strong priors.

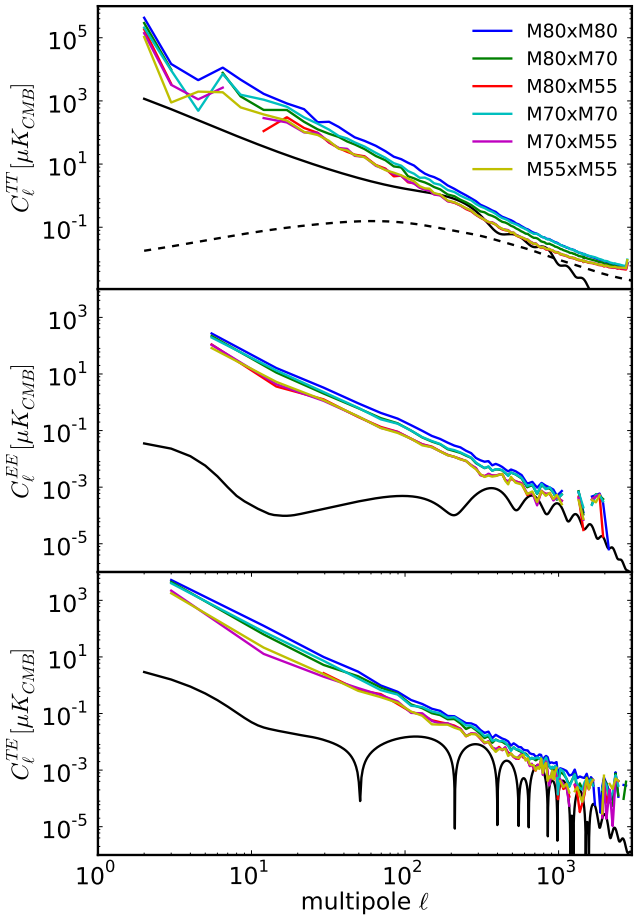

Figure 6.5: Dust power-spectra at 353 GHz for TT (*top*), TE (*middle*), and EE (*bottom*). The power spectra are computed from cross-correlation between half-mission maps for different sets of masks as defined in Sect 6.1 and further corrected for CMB power spectrum (*solid black line*) and CIB power spectrum (*dash black line*).

6.5.3 Cosmic Infrared Background

The thermal radiation of dust heated by UV emission from young stars produces an extragalactic infrared background which emission law is very close to the Galactic dust emission. The Planck Collaboration has studied the Cosmic Infrared Background (CIB) in detail in Planck Collaboration XXX (2014) and provides templates based on a model that associates star-forming galaxies with dark matter halos and their subhalos, using a parametrized relation between the dust-processed infrared luminosity and (sub-)halo mass. This model provides an accurate description of the Planck and IRAS CIB spectra from 3000 GHz down to 217 GHz. We extrapolate this model here, assuming it remains appropriate in describing the 143 GHz and 100 GHz data.
The halo model formalism, that is also used for the tSZ and the tSZ×CIB models (see Sect. 6.5.4 and 6.5.5) has the general expression (Planck Collaboration XXIII 2016)

$$C_\ell = C_\ell^{\mathrm{AB,1h}} + C_\ell^{\mathrm{AB,2h}}, \tag{6.8}$$

where A and B stand for tSZ effect or CIB emission, $C_\ell^{\mathrm{AB,1h}}$ is the 1-halo contribution, and $C_\ell^{\mathrm{AB,2h}}$ is the 2-halo term. The 1-halo term $C_\ell^{\mathrm{AB,1h}}$ is computed as

$$C_\ell^{\mathrm{AB,1h}} = 4\pi \int \mathrm{d}z \frac{\mathrm{d}V}{\mathrm{d}z\mathrm{d}\Omega} \int \mathrm{d}M \frac{\mathrm{d}^2\mathrm{N}}{\mathrm{d}M\mathrm{d}V} W_{\mathrm{A}}^{\mathrm{1h}} W_{\mathrm{B}}^{\mathrm{1h}}, \tag{6.9}$$

where $\frac{\mathrm{d}^2\mathrm{N}}{\mathrm{d}M\mathrm{d}V}$ is the dark-matter halo mass function from Tinker et al. (2008), $\frac{\mathrm{d}V}{\mathrm{d}z\mathrm{d}\Omega}$ the comoving volume element, and $W_{\mathrm{A,B}}^{\mathrm{1h}}$ is the window function that accounts for selection effects and total halo signal. The contribution of the 2-halo term, $C_\ell^{\mathrm{AB,2h}}$, accounts, instead, for correlation in the spatial distribution of halos over the sky.
For the CIB, the 2-halo term (i.e. the term that considers galaxies belonging to two different halos), is dominant at low and intermediate multipoles and is very well constrained by Planck. The 1-halo term is flat in C_ℓ and not well measured as it is degenerated with the shot noise. Hence, in Planck Collaboration XXX (2014) strong priors on the shot noises

have been used to get the 1-halo term. In HiLLiPOP, we did not include any shot-noise term in the CIB template to avoid degeneracies with the amplitude of infra-red sources (see Sect. 6.5.6).
The power spectra template for each cross-frequency in $\mathrm{Jy}^2\mathrm{sr}^{-1}$ (with the IRAS convention $\nu I(\nu)$=cst) are then converted in $\mu\mathrm{K}^2_{\mathrm{CMB}}$ using a slightly revised version of Table 6 in Planck Collaboration IX (2014): a^{conv}_{100}=1/244.06, a^{conv}_{143}=1/371.66 and a^{conv}_{217}=1/483.48 $\mathrm{K_{CMB}/MJy.sr^{-1}}$ at 100, 143, and 217 GHz, respectively. Those coefficients account for the integration of the CIB emission law in the Planck bandwidth.
The CIB templates used in HiLLiPOP (Fig. 6.6) are then rescaled with a free single parameter A_{CIB}:

$$\mathbf{C}_\ell^{ij,\mathrm{CIB}}=A_{\mathrm{CIB}}a^{\mathrm{conv}}_{\nu_i}a^{\mathrm{conv}}_{\nu_j}C_\ell^{\nu_i\nu_j,\mathrm{temp}}. \tag{6.10}$$

The same parametrization was finally adopted in the Planck official analysis for the 2015 release.

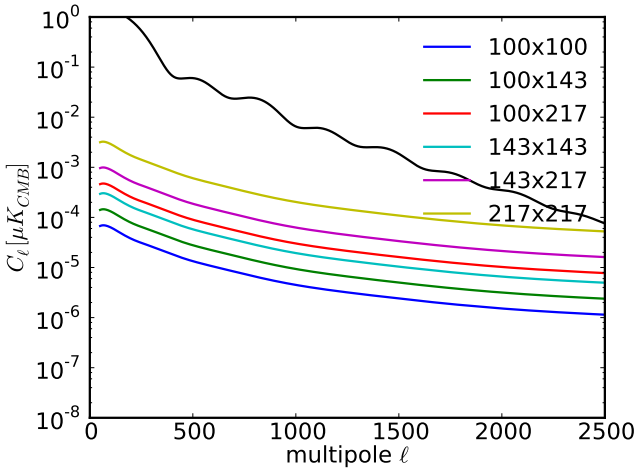

Figure 6.6: The CIB power spectra templates. The SED and the angular dependence is given by Planck Collaboration XXX (2014). The CMB TT power spectrum is plotted in black.

6.5.4 Sunyaev-Zel'dovich effect

The thermal Sunyev-Zel'dovich emission (tSZ) is also parameterized by a single amplitude and a fixed template measured in Planck Collaboration XXI (2014) at 143 GHz,

$$\mathbf{C}_\ell^{ij,\mathrm{tSZ}}=A_{\mathrm{tSZ}}a^{\mathrm{tSZ}}_{\nu_i}a^{\mathrm{tSZ}}_{\nu_j}C_\ell^{\mathrm{tSZ}}, \tag{6.11}$$

where $a^{\mathrm{tSZ}}_\nu=f^{\mathrm{tSZ}}(\nu)/f^{\mathrm{tSZ}}(143)$ is the thermal Sunyaev-Zeldovich spectrum normalized at 143 GHz. We recall that, ignoring the bandpass corrections, the tSZ spectrum is given by

$$f^{\mathrm{tSZ}}(\nu)=\left(x\coth\left(\frac{x}{2}\right)-4\right)\quad\text{with } x=\frac{h\nu}{k_{\mathrm{B}}T_{\mathrm{cmb}}}. \tag{6.12}$$

After integrating over the instrumental bandpass, we obtain f^{tSZ}=−4.031,−2.785,0.187 at 100, 143, and 217 GHz, respectively (see Table 1 in Planck Collaboration XXII 2016). The Planck official likelihood uses the same parametrization but with an empirically motivated template power spectrum (Efstathiou & Migliaccio 2012).
The kinetic Sunyev-Zel'dovich (kSZ) is produced by the peculiar velocities of the clusters containing hot electron gas. We use power spectra extracted from reionization simulations. We supposed that the kSZ follows the same SED as the CMB and only fit a global free amplitude, A_{kSZ}. We choose a combination of templates coming from homogeneous and patchy reionization.

$$\mathbf{C}_\ell^{ij,\mathrm{kSZ}}=A_{\mathrm{kSZ}}\left(C_\ell^{\mathrm{hKSZ}}+C_\ell^{\mathrm{pKSZ}}\right). \tag{6.13}$$

For the homogeneous kSZ, we use a template power spectrum given by Shaw et al. (2012) calibrated with a "cooling and star formation" simulation. For the patchy reionisation kSZ we use the fiducial model of Battaglia et al. (2013). Both templates are shown in Fig. 6.7. The Planck official likelihood considers a template from homogeneous reionization only but the impact on the cosmology is completely negligible.

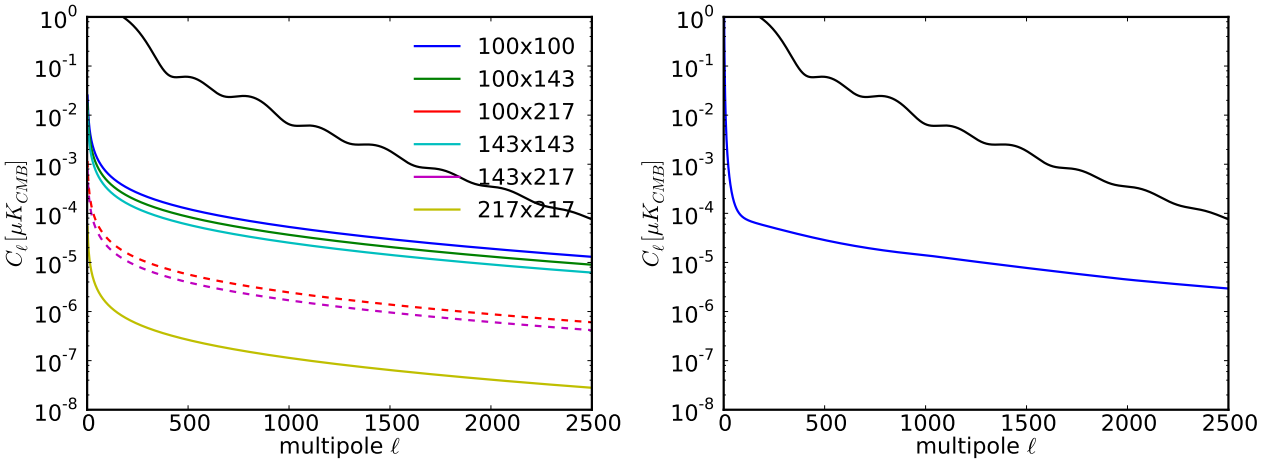

Figure 6.7: Top: the tSZ power spectra templates at each cross-frequency. Dashed-lines are negative. SED are fixed and we fit the overall amplitude $A_{\rm tSZ}$. Bottom: frequency independent kSZ template. The black line is the CMB power-spectrum.

6.5.5 tSZxCIB correlation

The halo model can naturally account for the correlation between two different source populations, each tracing the underlying dark matter but having different dependence on host halo properties (Addison et al. 2012). An angular power spectrum can thus be extracted for the correlation between unresolved clusters contributing to the tSZ effect, and the dusty sources that make up the CIB. While the latter has a peak in redshift distribution between $z\simeq1$ and $z\simeq2$, and is produced by galaxies in dark matter halos of 10^{11}-10^{13} $M_\odot$, tSZ is mainly produced by local ($z<1$) and massive dark matter halos (above 10^{14} $M_\odot$). This implies that the CIB and tSZ distributions present a very small overlap for the angular scales probed by Planck, and it is thus hard to detect (Planck Collaboration XXIII 2016).
We use the templates shown in Fig. 6.8, computed using a tSZ power spectrum template based on Efstathiou & Migliaccio (2012) and a CIB template as described in Sect. 6.5.3. The power spectra templates in $\mathrm{Jy^2sr^{-1}}$ (with the convention $\nu I(\nu)$=cst) are then converted in $\mu\mathrm{K}^2_{\rm CMB}$ using the same coefficients as for the CIB (Sect. 6.5.3).
As for the other foregrounds, we then allow for a global free amplitude, $A_{\rm tSZxCIB}$ and write

$$\mathbf{C}_\ell^{i,j,\rm tSZxCIB} = A_{\rm tSZxCIB} a_{\nu_i}^{\rm conv} a_{\nu_j}^{\rm conv} C_\ell^{\nu_i\nu_j,\rm temp}. \tag{6.14}$$

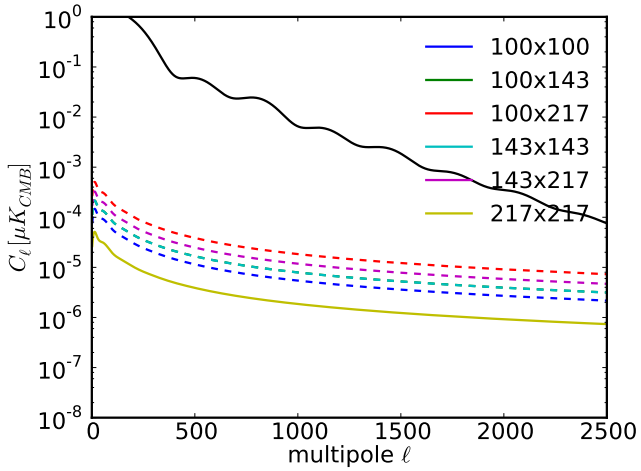

Figure 6.8: The tSZxCIB power spectra templates. The SED and the angular dependence is fixed. Dashed-lines are negative.

6.5.6 Unresolved PS

At Planck frequencies, unresolved point sources signal incorporates contribution from extragalactic radio and infrared (IR) dusty galaxies (Tucci et al. 2005). We use a specific mask for each frequency to mitigate the impact of strong sources (see Sect. 6.1). Planck Collaboration XI (2016) gives the expected amplitudes for the Poisson shot noise from

theoretical models that predict number counts dN/dS for each frequency. Their analyses takes into account the details of the construction for the point source masks, such as the fact that the flux cut varies across the sky or the "incompleteness" of the catalogue from which the masks are built at each frequency. We computed the expectation at each cross-frequency for the point source amplitudes ($a^{radio}_{\nu_i,\nu_j}$ and $a^{IR}_{\nu_i,\nu_j}$) based on the flux-cut considered for our own point sources masks using a model from Tucci et al. (2011) for the radio sources and from Béthermin et al. (2012) for dusty galaxies. We consider a flat Poisson-like power spectrum for each component and rescale by two free amplitudes $A^{\rm radio}_{\rm PS}$ and $A^{\rm IR}_{\rm PS}$:

$$\mathbf{C}_\ell^{ij,\rm PS} = A^{\rm radio}_{\rm PS} a^{radio}_{\nu_i,\nu_j} + A^{\rm IR}_{\rm PS} a^{IR}_{\nu_i,\nu_j}. \tag{6.15}$$

In polarization, we neglect the point source contribution from both components (Tucci et al. 2004).
Note that it is difficult to build a reliable multi-frequency model for the unresolved sources which depend on the flux-cut used to construct each mask but also on the procedure used to identified spurious detection of high-latitude Galactic cirrus as point sources in the catalog. The uncertainty on the flux-cut estimation is particularly important in the case of radio sources as the flux-cuts considered for CMB analysis (typically around 200 mJy) are close to the peak of the number count. That is the main reason why the Planck public likelihood analysis does consider one amplitude for point sources per cross-spectrum.

6.6 Additional Priors

The various parameters considered in the model described in this section are not all well constrained by the CMB data themselves. We complement our model with additional priors coming from external knowledge.
For the instrumental nuisances, Gaussian priors are applied on the calibration coefficients based on uncertainty estimated in Planck Collaboration VIII (2016): c_0=c_1=c_3=0±0.002, c_4=c_5=0.002±0.004 (Table 5) and $A_{\rm pl}$=1±0.0025.
Given its angular resolution, Planck is not equally able to constrain the different astrophysical emissions. We choose to apply Gaussian priors on the dominant ones, including galactic dust, CIB, thermal-SZ and point sources. The width of the priors is driven by the uncertainty of the foreground modeling. We recall that this modeling tries to capture residuals from highly non-gaussian and non-isotropic emissions using template in C_ℓ with fixed spectral energy densities (SED). As a consequence, it is difficult to derive an accurate estimation of the expected amplitudes. We used Gaussian centered on one and with 20% width (1.0±0.2) as priors for the rescaling amplitudes of the five foregrounds ($A_{\rm dust}$, $A_{\rm CIB}$, $A_{\rm tSZ}$, $A^{\rm radio}_{\rm PS}$, and $A^{\rm IR}_{\rm PS}$).
The Planck collaboration suggests the addition of a 2D prior on both amplitudes of tSZ and kSZ in order to mimic the constraints from the high-resolution experiments ACT and SPT (see Planck Collaboration XI 2016). As demonstrated in Couchot et al. (2017c), this is not strictly equivalent, in particular for results on $A_{\rm L}$. We choose to let the correlation free.

6.7 Conclusion

Building a coherent likelihood for CMB data given Planck sensitivity is difficult due to the complexity of the foreground emissions modeling. In this paper, we have presented a full temperature and polarization likelihood based on cross-spectra (including TT, TE, and EE) over a wide range of multipoles (from ℓ=50 to 2500). We have described in details the foreground parametrization which relies on the Planck measurements for astrophysical modeling.
In Chapter 7, we describe in more details the results we obtained on ΛCDM cosmology. We found results on the ΛCDM cosmological parameters consistent between the different likelihoods (`HillipopT`, `HillipopX`, `HillipopE`). The cosmological constraints from this work are directly comparable to the Planck 2015 cosmological analysis (Planck Collaboration XIII 2016), despite the differences in the foreground modeling adopted in HiLLiPOP. Both instrumental and astrophysical nuisance parameters are compatible with expectations, with the exception of the point source amplitudes in temperature for which we found a small tension with the astrophysical expectations. This tension may be the sign of potential systematic residuals in Planck data and/or uncertainty in the foreground model in temperature (especially on the dust SED or the various ℓ-shape of the foreground templates).

The authors thank G. Lagache for the work on the point source mask and the estimation of the infra-red sources amplitude; M. Tucci for the estimation of the radio point source amplitude; P. Serra for the work on the CIBxtSZ power spectra model.
This work represents a large part of my work in the period 2012-2016. It has been used to derive scientific results described in three papers (Couchot et al. 2017c,b,a).

Appendix

6.A Semi-analytical covariance matrix

Harmonic decomposition

Following notations from Hivon et al. (2002), the decomposition into spherical harmonics reads

$$T(\hat{\mathbf{n}}) = \sum_{\ell m} a^T_{\ell m} Y_{\ell m}(\hat{\mathbf{n}}) \tag{6.16}$$

$$Q(\hat{\mathbf{n}}) \pm iU(\hat{\mathbf{n}}) = \sum_{\ell m} {}_{\mp 2}a_{\ell m}\, {}_{\mp 2}Y_{\ell m}(\hat{\mathbf{n}}) \tag{6.17}$$

$$\left\{ \begin{array}{lcl} {}_{2}a_{\ell m} & = & a^E_{\ell m} + i a^B_{\ell m} \\ {}_{-2}a_{\ell m} & = & a^E_{\ell m} - i a^B_{\ell m} \end{array} \right. \tag{6.18}$$

with :

$$a^E_{\ell m} \equiv \frac{1}{2}\int \Big\{ (Q(\hat{\mathbf{n}}) - iU(\hat{\mathbf{n}}))\, {}_2Y^*_{\ell m}(\hat{\mathbf{n}}) + (Q(\hat{\mathbf{n}}) + iU(\hat{\mathbf{n}}))\, {}_{-2}Y^*_{\ell m}(\hat{\mathbf{n}}) \Big\} d\hat{\mathbf{n}} \tag{6.19}$$

$$a^B_{\ell m} \equiv -\frac{i}{2}\int \Big\{ (Q(\hat{\mathbf{n}}) - iU(\hat{\mathbf{n}}))\, {}_2Y^*_{\ell m}(\hat{\mathbf{n}}) - (Q(\hat{\mathbf{n}}) + iU(\hat{\mathbf{n}}))\, {}_{-2}Y^*_{\ell m}(\hat{\mathbf{n}}) \Big\} d\hat{\mathbf{n}} \tag{6.20}$$

When including a sky window function (or mask) w, then

$$T_{\ell m} = \sum_{\ell_1 m_1} a^T_{\ell_1 m_1} \sum_{\ell_2 m_2} w^T_{\ell_2 m_2} \int {}_0Y^*_{\ell m}(\hat{\mathbf{n}})\, {}_0Y_{\ell_1 m_1}(\hat{\mathbf{n}})\, {}_0Y_{\ell_2 m_2}(\hat{\mathbf{n}}) d\hat{\mathbf{n}} \tag{6.21}$$

$$E_{\ell m} = \frac{1}{2}\sum_{\ell_1 m_1} \Big\{ (a^E_{\ell_1 m_1} + i a^B_{\ell_1 m_1}) \sum_{\ell_2 m_2} w^E_{\ell_2 m_2} \int {}_2Y^*_{\ell m}(\hat{\mathbf{n}})\, {}_2Y_{\ell_1 m_1}(\hat{\mathbf{n}})\, {}_0Y_{\ell_2 m_2}(\hat{\mathbf{n}}) d\hat{\mathbf{n}} + (a^E_{\ell_1 m_1} - i a^B_{\ell_1 m_1}) \sum_{\ell_2 m_2} w^E_{\ell_2 m_2} \int {}_{-2}Y^*_{\ell m}(\hat{\mathbf{n}})\, {}_{-2}Y_{\ell_1 m_1}(\hat{\mathbf{n}})\, {}_0Y_{\ell_2 m_2}(\hat{\mathbf{n}}) \Big\} \tag{6.22}$$

$$B_{\ell m} = -\frac{i}{2}\sum_{\ell_1 m_1} \Big\{ (a^E_{\ell_1 m_1} + i a^B_{\ell_1 m_1}) \sum_{\ell_2 m_2} w^B_{\ell_2 m_2} \int {}_2Y^*_{\ell m}(\hat{\mathbf{n}})\, {}_2Y_{\ell_1 m_1}(\hat{\mathbf{n}})\, {}_0Y_{\ell_2 m_2}(\hat{\mathbf{n}}) d\hat{\mathbf{n}} - (a^E_{\ell_1 m_1} - i a^B_{\ell_1 m_1}) \sum_{\ell_2 m_2} w^B_{\ell_2 m_2} \int {}_{-2}Y^*_{\ell m}(\hat{\mathbf{n}})\, {}_{-2}Y_{\ell_1 m_1}(\hat{\mathbf{n}})\, {}_0Y_{\ell_2 m_2}(\hat{\mathbf{n}}) \Big\} \tag{6.23}$$

where the window function is decomposed into spin-0 spherical harmonics ($w = \sum_{\ell m} a^W_{\ell m}\, {}_0Y_{\ell m}$).
Let's define ${}_sK^X_{\ell_1 m_1 \ell_2 m_2}$ with $s \in \{-2,0,2\}$ (X=T,E,B):

$${}_sK^X_{\ell_1 m_1 \ell_2 m_2} \equiv \int {}_sY^*_{\ell_1 m_1}(\hat{\mathbf{n}})\, {}_sY_{\ell_2 m_2}(\hat{\mathbf{n}}) w^X(\hat{\mathbf{n}}) d\hat{\mathbf{n}} = \sum_{\ell_3 m_3} w^X_{\ell_3 m_3} \int {}_sY^*_{\ell_1 m_1}(\hat{\mathbf{n}})\, {}_sY_{\ell_2 m_2}(\hat{\mathbf{n}})\, {}_0Y_{\ell_3 m_3}(\hat{\mathbf{n}}) d\hat{\mathbf{n}} \tag{6.24}$$

we can then rewrite $E_{\ell m}$ and $B_{\ell m}$ as:

$$T_{\ell m} = \sum_{\ell_1 m_1} a^T_{\ell_1 m_1}\, {}_0K^T_{\ell m \ell_1 m_1} \tag{6.25}$$

$$E_{\ell m} = \frac{1}{2}\sum_{\ell_1 m_1} \Big\{ a^E_{\ell_1 m_1} \big[{}_2K^E_{\ell m \ell_1 m_1} + {}_{-2}K^E_{\ell m \ell_1 m_1} \big] + i a^B_{\ell_1 m_1} \big[{}_2K^E_{\ell m \ell_1 m_1} - {}_{-2}K^E_{\ell m \ell_1 m_1} \big] \Big\} \tag{6.26}$$

$$B_{\ell m} = -\frac{i}{2}\sum_{\ell_1 m_1} \Big\{ a^E_{\ell_1 m_1} \big[{}_2K^B_{\ell m \ell_1 m_1} - {}_{-2}K^B_{\ell m \ell_1 m_1} \big] + i a^B_{\ell_1 m_1} \big[{}_2K^B_{\ell m \ell_1 m_1} + {}_{-2}K^B_{\ell m \ell_1 m_1} \big] \Big\} \tag{6.27}$$

Let's define $W_{\ell_1 m_1 \ell_2 m_2}$:

$$\left\{ \begin{array}{lcl} W^{0,X}_{\ell_1 m_1 \ell_2 m_2} & \equiv & {}_0K^X_{\ell_1 m_1 \ell_2 m_2} \\ W^{\pm,X}_{\ell_1 m_1 \ell_2 m_2} & \equiv & {}_2K^X_{\ell_1 m_1 \ell_2 m_2} \pm {}_{-2}K^X_{\ell_1 m_1 \ell_2 m_2} \end{array} \right. \tag{6.28}$$

Thus finally

$$\begin{pmatrix} T_{\ell m} \\ E_{\ell m} \\ B_{\ell m} \end{pmatrix} = \sum_{\ell_1 m_1} \begin{pmatrix} W^{0,T}_{\ell m \ell_1 m_1} & 0 & 0 \\ 0 & \frac{1}{2}W^{+,E}_{\ell m \ell_1 m_1} & \frac{i}{2}W^{-,E}_{\ell m \ell_1 m_1} \\ 0 & -\frac{i}{2}W^{-,B}_{\ell m \ell_1 m_1} & \frac{1}{2}W^{+,B}_{\ell m \ell_1 m_1} \end{pmatrix} \begin{pmatrix} a^T_{\ell_1 m_1} \\ a^E_{\ell_1 m_1} \\ a^B_{\ell_1 m_1} \end{pmatrix} \tag{6.29}$$

Power-spectra (first order $\mathbf{a_{\ell m}}$ correlation)

We suppose independent datasets (i,j) for which we have (I,Q,U) maps and compute the spherical transform to obtain $X_{\ell m}$ (for $X \in \{T,E,B\}$) coefficients. The cross-power spectra are thus define as

$$\tilde{C}^{X_a Y_b}_\ell = \frac{1}{2\ell+1}\sum_{m=-\ell}^{\ell} \left\langle X^a_{\ell m} Y^{b*}_{\ell m} \right\rangle \tag{6.30}$$

We have to compute $\left\langle X^a_{\ell m} Y^{b*}_{\ell' m'} \right\rangle$ for each set of $(X,Y) \in T,E,B$ using (6.29). In this section, we will neglect the terms in EB and TB with respect to other mode correlation.

temperature

$$\left\langle T^a_{\ell m} T^{b*}_{\ell' m'} \right\rangle = \sum_{\ell_1 m_1} \sum_{\ell_2 m_2} \left\langle a^{T_a}_{\ell_1 m_1} a^{T_b *}_{\ell_2 m_2} \right\rangle W^{0,T_a}_{\ell m \ell_1 m_1} W^{0,T_b *}_{\ell' m' \ell_2 m_2}$$

with :

$$\left\langle a^{X_a}_{\ell_1 m_1} a^{X_b *}_{\ell_2 m_2} \right\rangle = \delta_{\ell_1 \ell_2} \delta_{m_1 m_2} C^{X_a X_b}_{\ell_1} \qquad (x=T,E,B) \tag{6.31}$$

Thus :

$$\boxed{\left\langle T^a_{\ell m} T^{b*}_{\ell' m'} \right\rangle = \sum_{\ell_1 m_1} C^{T_a T_b}_{\ell_1} W^{0,T_a}_{\ell m \ell_1 m_1} W^{0,T_b *}_{\ell' m' \ell_1 m_1}} \tag{6.32}$$

polarization

$$\left\langle E^{a*}_{\ell m} E^b_{\ell' m'} \right\rangle = \frac{1}{4} \sum_{\ell_1 m_1} \sum_{\ell_2 m_2} \left\langle \left\{ a^{E_a *}_{\ell_1 m_1} W^{+,E_a *}_{\ell m \ell_1 m_1} - i a^{B_a *}_{\ell_1 m_1} W^{-,E_a *}_{\ell m \ell_1 m_1} \right\} \times \left\{ a^{E_b}_{\ell_2 m_2} W^{+,E_b}_{\ell' m' \ell_2 m_2} + i a^{B_b}_{\ell_2 m_2} W^{-,E_b}_{\ell' m' \ell_2 m_2} \right\} \right\rangle$$

using (6.31):

$$\begin{aligned} \left\langle E^{a*}_{\ell m} E^b_{\ell' m'} \right\rangle \quad = \quad & \frac{1}{4} \sum_{\ell_1 m_1} \left\{ C^{E_a E_b}_{\ell_1} W^{+,E_a *}_{\ell m \ell_1 m_1} W^{+,E_b}_{\ell' m' \ell_1 m_1} + i C^{E_a B_b}_{\ell_1} W^{+,E_a *}_{\ell m \ell_1 m_1} W^{-,E_b}_{\ell' m' \ell_1 m_1} \right. \\ & \left. - i C^{B_a E_b}_{\ell_1} W^{-,E_a *}_{\ell m \ell_1 m_1} W^{+,E_b}_{\ell' m' \ell_1 m_1} + C^{B_a B_b}_{\ell_1} W^{-,E_b *}_{\ell m \ell_1 m_1} W^{-,E_b}_{\ell' m' \ell_1 m_1} \right\} \end{aligned}$$

We neglect C^{EB}_ℓ, so that $\left\langle E^{a*}_{\ell m} E^b_{\ell' m'} \right\rangle$ is real and reads:

$$\boxed{\left\langle E^{a*}_{\ell m} E^b_{\ell' m'} \right\rangle = \frac{1}{4} \sum_{\ell_1 m_1} \left\{ C^{E_a E_b}_{\ell_1} W^{+,E_a *}_{\ell m \ell_1 m_1} W^{+,E_b}_{\ell' m' \ell_1 m_1} + C^{B_a B_b}_{\ell_1} W^{-,E_a *}_{\ell m \ell_1 m_1} W^{-,E_b}_{\ell' m' \ell_1 m_1} \right\}} \tag{6.33}$$

With the same idea,

$$\left\langle B^{a*}_{\ell m} B^b_{\ell' m'} \right\rangle = \frac{1}{4} \sum_{\ell_1 m_1} \sum_{\ell_2 m_2} \left\langle \left\{ a^{B_a *}_{\ell_1 m_1} W^{+,B_a *}_{\ell m \ell_1 m_1} + i a^{E_a *}_{\ell_1 m_1} W^{-,B_a *}_{\ell m \ell_1 m_1} \right\} \times \left\{ a^{B_b}_{\ell_2 m_2} W^{+,B_b}_{\ell' m' \ell_2 m_2} - i a^{E_b}_{\ell_2 m_2} W^{-,B_b}_{\ell' m' \ell_2 m_2} \right\} \right\rangle$$

$$\boxed{\left\langle B^{a*}_{\ell m} B^b_{\ell' m'} \right\rangle = \frac{1}{4} \sum_{\ell_1 m_1} \left\{ C^{B_a B_b}_{\ell_1} W^{+,B_a *}_{\ell m \ell_1 m_1} W^{+,B_b}_{\ell' m' \ell_1 m_1} + C^{E_a E_b}_{\ell_1} W^{-,B_a *}_{\ell m \ell_1 m_1} W^{-,B_b}_{\ell' m' \ell_1 m_1} \right\}} \tag{6.34}$$

cross modes

$$\left\langle T^{a*}_{\ell m} E^b_{\ell' m'} \right\rangle = \frac{1}{2} \sum_{\ell_1 m_1} \sum_{\ell_2 m_2} \left\langle \left\{ a^{T_a *}_{\ell_1 m_1} W^{0,T_a *}_{\ell m \ell_1 m_1} \right\} \times \left\{ a^{E_b}_{\ell_2 m_2} W^{+,E_b}_{\ell' m' \ell_2 m_2} + i a^{B_b}_{\ell_2 m_2} W^{-,E_b}_{\ell' m' \ell_2 m_2} \right\} \right\rangle$$

We neglect C^{TB}_ℓ null, so that $\left\langle T^{a*}_{\ell m} E^b_{\ell' m'} \right\rangle$ is real and reads:

$$\boxed{\left\langle T^{a*}_{\ell m} E^b_{\ell' m'} \right\rangle = \left\langle E^{b*}_{\ell m} T^a_{\ell' m'} \right\rangle = \frac{1}{2} \sum_{\ell_1 m_1} \left\{ C^{T_a E_b}_{\ell_1} W^{0,T_a *}_{\ell m \ell_1 m_1} W^{+,E_b}_{\ell' m' \ell_1 m_1} \right\}} \tag{6.35}$$

And

$$\left\langle T^{a*}_{\ell m} B^b_{\ell' m'} \right\rangle = \frac{1}{2} \sum_{\ell_1 m_1} \sum_{\ell_2 m_2} \left\langle \left\{ a^{T_a *}_{\ell_1 m_1} W^{0,T_a *}_{\ell m \ell_1 m_1} \right\} \times \left\{ a^{B_b}_{\ell_2 m_2} W^{+,B_b}_{\ell' m' \ell_2 m_2} - i a^{E_b}_{\ell_2 m_2} W^{-,B_b}_{\ell' m' \ell_2 m_2} \right\} \right\rangle$$

$$\boxed{\left\langle T^{a*}_{\ell m} B^b_{\ell' m'} \right\rangle = \left\langle B^{b*}_{\ell m} T^a_{\ell' m'} \right\rangle = \frac{1}{2} \sum_{\ell_1 m_1} \left\{ C^{T_a B_b}_{\ell_1} W^{0,T_a *}_{\ell m \ell_1 m_1} W^{+,B_b}_{\ell' m' \ell_1 m_1} - i C^{T_a E_b}_{\ell_1} W^{0,T_a *}_{\ell m \ell_1 m_1} W^{-,E_b}_{\ell' m' \ell_1 m_1} \right\}} \tag{6.36}$$

$$\left\langle E^{a*}_{\ell m} B^b_{\ell' m'} \right\rangle = \frac{1}{4} \sum_{\ell_1 m_1} \sum_{\ell_2 m_2} \left\langle \left\{ a^{E_a *}_{\ell_1 m_1} W^{+,E_a *}_{\ell m \ell_1 m_1} - i a^{B_a *}_{\ell_1 m_1} W^{-,E_a *}_{\ell m \ell_1 m_1} \right\} \times \left\{ a^{B_b}_{\ell_2 m_2} W^{+,B_b}_{\ell' m' \ell_2 m_2} - i a^{E_b}_{\ell_2 m_2} W^{-,B_b}_{\ell' m' \ell_2 m_2} \right\} \right\rangle$$

$$\boxed{\begin{aligned} \left\langle E^{a*}_{\ell m} B^b_{\ell' m'} \right\rangle = \left\langle B^{b*}_{\ell m} E^a_{\ell' m'} \right\rangle = \frac{1}{4} \sum_{\ell_1 m_1} & \left\{ C^{B_a E_b}_{\ell_1} W^{-,E_a *}_{\ell m \ell_1 m_1} W^{-,B_b}_{\ell' m' \ell_1 m_1} - C^{E_a B_b}_{\ell_1} W^{+,E_a *}_{\ell m \ell_1 m_1} W^{+,B_b}_{\ell' m' \ell_1 m_1} \right\} \\ - i & \left\{ C^{E_a E_b}_{\ell_1} W^{+,E_a *}_{\ell m \ell_1 m_1} W^{-,B_b}_{\ell' m' \ell_1 m_1} + C^{B_a B_b}_{\ell_1} W^{-,E_a *}_{\ell m \ell_1 m_1} W^{+,B_b}_{\ell' m' \ell_1 m_1} \right\} \end{aligned}} \tag{6.37}$$

Application to C_ℓ

For Eq. 6.30, we need to compute the product of 2 $W^{\oplus,X}_{\ell m \ell' m'}$ as in Eqs (6.32,6.33,6.34,6.35,6.36,6.37).
Here, we wrote integrals as 3j-wigner symbols using

$$\int d\hat{n}\ {}_s Y^*_{lm}(\hat{n})\ {}_{s'} Y_{\ell' m'}(\hat{n})\ {}_{s''} Y_{\ell'' m''}(\hat{n}) \quad = \quad (-1)^{s+m} \left[\frac{(2\ell+1)(2\ell'+1)(2\ell''+1)}{4\pi} \right]^{1/2} \begin{pmatrix} \ell & \ell' & \ell'' \\ -s & s' & s'' \end{pmatrix} \begin{pmatrix} \ell & \ell' & \ell'' \\ -m & m' & m'' \end{pmatrix} \tag{6.38}$$

and make use of the orthogonally for the spinned-harmonics :

$$\begin{cases} \sum_{\ell m}(2\ell+1)\begin{pmatrix} \ell_1 & \ell_2 & \ell \\ m_1 & m_2 & m \end{pmatrix}\begin{pmatrix} \ell_1 & \ell_2 & \ell \\ m'_1 & m'_2 & m \end{pmatrix} = \delta_{m_1 m'_1}\delta_{m_2 m'_2} \\ \sum_{m_1 m_2}(2\ell+1)\begin{pmatrix} \ell_1 & \ell_2 & \ell \\ m_1 & m_2 & m \end{pmatrix}\begin{pmatrix} \ell_1 & \ell_2 & \ell' \\ m_1 & m_2 & m' \end{pmatrix} = \delta_{\ell\ell'}\delta_{mm'} \end{cases} \tag{6.39}$$

We then define

$$\begin{cases} \mathsf{M}_{TT,TT}(\ell_1,\ell_2;a,b) \equiv L_{\ell_1\ell_2}\sum_{m_1 m_2} W^{0,a}_{\ell_1 m_1 \ell_2 m_2} W^{0,b*}_{\ell_1 m_1 \ell_2 m_2} = \frac{1}{4\pi}\sum_{\ell_3}(2\ell_3+1)C^{W_a,W_b}_{\ell_3}\begin{pmatrix} \ell_1 & \ell_2 & \ell_3 \\ 0 & 0 & 0 \end{pmatrix}^2 \\ \mathsf{M}_{TE,TE}(\ell_1,\ell_2;a,b) \equiv \frac{L_{\ell_1\ell_2}}{2}\sum_{m_1 m_2} W^{0,a}_{\ell_1 m_1 \ell_2 m_2} W^{+,b*}_{\ell_1 m_1 \ell_2 m_2} = \frac{1}{8\pi}\sum_{\ell_3}(2\ell_3+1)C^{W_a,W_b}_{\ell_3}(1+(-1)^L)\begin{pmatrix} \ell_1 & \ell_2 & \ell_3 \\ 0 & 0 & 0 \end{pmatrix}\begin{pmatrix} \ell_1 & \ell_2 & \ell_3 \\ -2 & 2 & 0 \end{pmatrix} \\ \mathsf{M}_{EE,EE}(\ell_1,\ell_2;a,b) \equiv \frac{L_{\ell_1\ell_2}}{4}\sum_{m_1 m_2} W^{+,a}_{\ell_1 m_1 \ell_2 m_2} W^{+,b*}_{\ell_1 m_1 \ell_2 m_2} = \frac{1}{16\pi}\sum_{\ell_3}(2\ell_3+1)C^{W_a,W_b}_{\ell_3}(1+(-1)^L)^2\begin{pmatrix} \ell_1 & \ell_2 & \ell_3 \\ -2 & 2 & 0 \end{pmatrix}^2 \\ \mathsf{M}_{EE,BB}(\ell_1,\ell_2;a,b) \equiv \frac{L_{\ell_1\ell_2}}{4}\sum_{m_1 m_2} W^{-,a}_{\ell_1 m_1 \ell_2 m_2} W^{-,b*}_{\ell_1 m_1 \ell_2 m_2} = \frac{1}{16\pi}\sum_{\ell_3}(2\ell_3+1)C^{W_a,W_b}_{\ell_3}(1-(-1)^L)^2\begin{pmatrix} \ell_1 & \ell_2 & \ell_3 \\ -2 & 2 & 0 \end{pmatrix}^2 \end{cases} \tag{6.40}$$

with $L_{\ell\ell'}\equiv\frac{1}{(2\ell+1)(2\ell'+1)}$, $L=\ell_1+\ell_2+\ell_3$, which depend only on the scalar cross-power spectrum of the masks $C_\ell^{W_a,W_b}=\sum_m w^a_{\ell m} w^{b*}_{\ell m}/(2\ell+1)$.
Finally, for $\mathbf{C}_\ell^{ab}=\left(C_\ell^{T_aT_b},C_\ell^{E_aE_b},C_\ell^{B_aB_b},C_\ell^{T_aE_b}\right)$, the relation between pseudo-c_ℓ ($\tilde{\mathbf{c}}_\ell$) and $\mathbf{c}_\ell$ is given using the general coupling matrix:

$$\boxed{\tilde{\mathbf{C}}_\ell^{ab}=(2\ell'+1)\mathsf{M}^{a\times b}_{\ell\ell'}\mathbf{C}^{ab}_{\ell'}} \tag{6.41}$$

and the coupling matrix M that translate pseudo spectra to power spectra reads (see Kogut et al. 2003):

$$\mathsf{M}^{a\times b}_{\ell\ell'}=\begin{pmatrix} \mathsf{M}_{TT,TT} & 0 & 0 & 0 \\ 0 & \mathsf{M}_{EE,EE} & \mathsf{M}_{EE,BB} & 0 \\ 0 & \mathsf{M}_{EE,BB} & \mathsf{M}_{EE,EE} & 0 \\ 0 & 0 & 0 & \mathsf{M}_{TE,TE} \end{pmatrix}(\ell,\ell';w_a,w_b) \tag{6.42}$$

Covariance matrix (second order $\mathbf{a}_{\ell\mathbf{m}}$ correlation)

We want write the correlation matrix $\Sigma^{ab,cd}_{\ell\ell'}$ that gives the correlation between cross-spectra (ab) and (cd) and between multipoles ℓ and ℓ':

$$\Sigma^{ab,cd}_{\ell\ell'}\equiv\left\langle\Delta\mathbf{C}^{ab}_\ell\Delta\mathbf{C}^{cd*}_{\ell'}\right\rangle=\left(\mathsf{M}^{ab}_{\ell\ell_1}\right)^{-1}\left\langle\Delta\tilde{\mathbf{C}}^{ab}_{\ell_1}\Delta\tilde{\mathbf{C}}^{cd*}_{\ell_2}\right\rangle\left(\mathsf{M}^{cd*}_{\ell'\ell_2}\right)^{-1} \tag{6.43}$$

with the *pseudo*-covariance matrix $\tilde{\Sigma}$:

$$\tilde{\Sigma}^{ab,cd}_{\ell\ell'}=\left\langle\Delta\tilde{\mathbf{C}}^{ab}_\ell\Delta\tilde{\mathbf{C}}^{cd*}_{\ell'}\right\rangle=\left\langle\tilde{\mathbf{C}}^{ab}_\ell\tilde{\mathbf{C}}^{cd*}_{\ell'}\right\rangle-\mathbf{C}^{ab}_\ell\mathbf{C}^{cd*}_{\ell'} \tag{6.44}$$

Let's write the 4-$a_{\ell m}$ correlations :

$$\left\langle\tilde{\mathbf{C}}^{X_aX_b}_\ell\tilde{\mathbf{C}}^{X_cX_d*}_{\ell'}\right\rangle=\frac{1}{(2\ell+1)(2\ell'+1)}\sum_{mm'}\left\langle X^a_{\ell m}X^{b*}_{\ell m}X^{c*}_{\ell'm'},X^d_{\ell'm'}\right\rangle\qquad(X_{\ell m}=T_{\ell m},E_{\ell m},B_{\ell m}) \tag{6.45}$$

We use the Isserlis' formula (or Wick theorem) which gives for gaussian variables:

$$\left\langle x_ix_jx_kx_l\right\rangle=\left\langle x_ix_j\right\rangle\langle x_kx_l\rangle+\langle x_ix_k\rangle\left\langle x_jx_l\right\rangle+\langle x_ix_l\rangle\left\langle x_jx_k\right\rangle \tag{6.46}$$

Thus (6.45) reads

$$\begin{aligned} \left\langle\tilde{C}^{X_aX_b}_\ell\tilde{C}^{X_cX_d*}_{\ell'}\right\rangle &= L_{\ell\ell'}\sum_{mm'}\left\{\left\langle X^a_{\ell m}X^{b*}_{\ell m}\right\rangle\left\langle X^{c*}_{\ell'm'}X^d_{\ell'm'}\right\rangle+\left\langle X^a_{\ell m}X^{c*}_{\ell'm'}\right\rangle\left\langle X^{b*}_{\ell m}X^d_{\ell'm'}\right\rangle+\left\langle X^a_{\ell m}X^d_{\ell'm'}\right\rangle\left\langle X^{b*}_{\ell m}X^{c*}_{\ell'm'}\right\rangle\right\} \\ &= C^{X_aX_b}_\ell C^{X_cX_d*}_{\ell'}+L_{\ell\ell'}\sum_{mm'}\left\{\left\langle X^a_{\ell m}X^{c*}_{\ell'm'}\right\rangle\left\langle X^{b*}_{\ell m}X^d_{\ell'm'}\right\rangle+\left\langle X^a_{\ell m}X^d_{\ell'm'}\right\rangle\left\langle X^{b*}_{\ell m}X^{c*}_{\ell'm'}\right\rangle\right\} \end{aligned} \tag{6.47}$$

$$\left\langle\Delta\tilde{C}^{X_aX_b}_\ell\Delta\tilde{C}^{X_cX_d*}_{\ell'}\right\rangle = L_{\ell\ell'}\sum_{mm'}\left\{\left\langle X^a_{\ell m}X^{c*}_{\ell'm'}\right\rangle\left\langle X^{b*}_{\ell m}X^d_{\ell'm'}\right\rangle+\left\langle X^a_{\ell m}X^d_{\ell'm'}\right\rangle\left\langle X^{b*}_{\ell m}X^{c*}_{\ell'm'}\right\rangle\right\} \tag{6.48}$$

We know that :

$$X^*_{\ell m}=(-1)^mX_{\ell-m} \tag{6.49}$$

We can thus replace m' by $-m'$ in the sum of the rhs of (6.48) and use (6.49) :

$$\left\langle X^a_{\ell m}X^d_{\ell'm'}\right\rangle\left\langle X^{b*}_{\ell m}X^{c*}_{\ell'm'}\right\rangle=(-1)^{-2m'}\left\langle X^a_{\ell m}X^{d*}_{\ell'm'}\right\rangle\left\langle X^{b*}_{\ell m}X^c_{\ell'm'}\right\rangle$$

And finally, elements of the pseudo-covariance matrix $\tilde{\Sigma}$ reads:

$$\boxed{\left\langle\Delta\tilde{\mathbf{C}}^{X_aX_b}_\ell\Delta\tilde{\mathbf{C}}^{X_cX_d*}_{\ell'}\right\rangle=L_{\ell\ell'}\sum_{mm'}\left\{\left\langle X^a_{\ell m}X^{c*}_{\ell'm'}\right\rangle\left\langle X^{b*}_{\ell m}X^d_{\ell'm'}\right\rangle+\left\langle X^a_{\ell m}X^{d*}_{\ell'm'}\right\rangle\left\langle X^{b*}_{\ell m}X^c_{\ell'm'}\right\rangle\right\}} \tag{6.50}$$

Basic properties

We recall some basic properties :

$$ {}_sY_{\ell m}=(-1)^{s+m}\ {}_{-s}Y^*_{\ell -m} \tag{6.51}$$

which leads to:

$$\begin{aligned}\left[\int {}_sY^*_{\ell_1 m_1}(\hat{\mathbf{n}})\ {}_sY_{\ell_2 m_2}(\hat{\mathbf{n}})\ {}_0Y_{\ell_3 m_3}(\hat{\mathbf{n}})d\hat{\mathbf{n}}\right]^* &= \int {}_sY_{\ell_1 m_1}(\hat{\mathbf{n}})\ {}_sY^*_{\ell_2 m_2}(\hat{\mathbf{n}})\ {}_0Y^*_{\ell_3 m_3}(\hat{\mathbf{n}})d\hat{\mathbf{n}}\\ &= (-1)^{(s+s+0)}\int {}_{-s}Y^*_{\ell_1 -m_1}(\hat{\mathbf{n}})\ {}_{-s}Y_{\ell_2 -m_2}(\hat{\mathbf{n}})\ {}_0Y_{\ell_3 -m_3}(\hat{\mathbf{n}})d\hat{\mathbf{n}}\\ &= \int {}_{-s}Y^*_{\ell_1 -m_1}(\hat{\mathbf{n}})\ {}_{-s}Y_{\ell_2 -m_2}(\hat{\mathbf{n}})\ {}_0Y_{\ell_3 -m_3}(\hat{\mathbf{n}})d\hat{\mathbf{n}}\end{aligned}$$

From this we deduce that

$$\left({}_{\pm 2}K^X_{\ell_1 m_1 \ell_2 m_2}\right)^* = {}_{\mp 2}K^X_{\ell_1 -m_1 \ell_2 -m_2}$$

Thus for $W^{\oplus,X}_{\ell_1 m_1 \ell_2 m_2}$ we have $\left(W^{0,X}_{\ell_1 m_1 \ell_2 m_2}\right)^*=W^{0,X}_{\ell_1 -m_1 \ell_2 -m_2}$, $\left(W^{+,X}_{\ell_1 m_1 \ell_2 m_2}\right)^*=W^{+,X}_{\ell_1 -m_1 \ell_2 -m_2}$, and $\left(W^{-,X}_{\ell_1 m_1 \ell_2 m_2}\right)^*=-W^{-,X}_{\ell_1 -m_1 \ell_2 -m_2}$. We recall also that the spin-lower and spin-raising derivative reads like:

$$ {}_sY_{\ell m} = \sqrt{\frac{(\ell-s)!}{(\ell+s)!}}\ \eth^s Y_{\ell m},\ 0\le s\le \ell \tag{6.52}$$

$$ {}_sY_{\ell m} = \sqrt{\frac{(\ell+s)!}{(\ell-s)!}}\ (-1)^s\bar{\eth}^{-s} Y_{\ell m},\ -\ell\le s\le 0 \tag{6.53}$$

And

$$(\eth^s)^*=\bar{\eth}^s \tag{6.54}$$

Other important properties include the following:

$$\eth({}_sY_{\ell m}) = +\sqrt{(\ell-s)(\ell+s+1)}\ {}_{s+1}Y_{\ell m} \tag{6.55}$$

$$\bar{\eth}({}_sY_{\ell m}) = -\sqrt{(\ell+s)(\ell-s+1)}\ {}_{s-1}Y_{\ell m} \tag{6.56}$$

Using spin-raising (resp. spin-lowering) operators (6.52) and (6.53) on ${}_{Y_{\ell m}(\hat{n}_j)}$ and then integrate two times by part we notice that :

$$\begin{aligned}\int {}_{-2}Y^*_{\ell' m'}(\hat{n}_j)\ {}_{-2}Y_{\ell_1 m_1}(\hat{n}_j) w_j d\hat{n}_j &= \int \sqrt{\frac{(\ell'-2)!}{(\ell'+2)!}}\left(\bar{\eth}^2\ Y_{\ell' m'}(\hat{n}_j)\right)^*\ {}_{-2}Y_{\ell_1 m_1}(\hat{n}_j)\ w_j\ d\hat{n}_j\\ &= \int \sqrt{\frac{(\ell'-2)!}{(\ell'+2)!}}\ \eth^2\Big(\ Y^*_{\ell' m'}(\hat{n}_j)\Big)\ {}_{-2}Y_{\ell_1 m_1}(\hat{n}_j)\ w_j\ d\hat{n}_j\\ &= \int \sqrt{\frac{(\ell'-2)!}{(\ell'+2)!}}\ Y^*_{\ell' m'}(\hat{n}_j)\ \eth^2\Big(\ {}_{-2}Y_{\ell_1 m_1}(\hat{n}_j)\ w_j\Big)\ d\hat{n}_j\\ &\simeq \int \sqrt{\frac{(\ell'-2)!}{(\ell'+2)!}}\ Y^*_{\ell' m'}(\hat{n}_j)\ \eth^2\Big(\ {}_{-2}Y_{\ell_1 m_1}(\hat{n}_j)\Big)\ w_j\ d\hat{n}_j\\ &= \int \sqrt{\frac{(\ell'-2)!}{(\ell'+2)!}}\ \sqrt{\frac{(\ell_1+2)!}{(\ell_1-2)!}}\ Y^*_{\ell' m'}(\hat{n}_j)\ Y_{\ell_1 m_1}(\hat{n}_j)\ w_j\ d\hat{n}_j\\ &= \int \sqrt{\frac{(\ell'-2)!}{(\ell'+2)!}}\ Y^*_{\ell' m'}(\hat{n}_j)\bar{\eth}^2\Big(\ {}_2Y_{\ell_1 m_1}(\hat{n}_j)\Big)\ w_j\ d\hat{n}_j\\ &\simeq \int \sqrt{\frac{(\ell'-2)!}{(\ell'+2)!}}\Big(\bar{\eth}^2\ Y^*_{\ell' m'}(\hat{n}_j)\ w_j\Big)\ {}_{+2}Y_{\ell_1 m_1}(\hat{n}_j)\ d\hat{n}_j\\ &= \int \sqrt{\frac{(\ell'-2)!}{(\ell'+2)!}}\Big(\eth^2\ Y_{\ell' m'}(\hat{n}_j)\Big)^*\ w_j\ {}_{+2}Y_{\ell_1 m_1}(\hat{n}_j)\ d\hat{n}_j\\ &\simeq \int {}_{+2}Y^*_{\ell' m'}(\hat{n}_j)\ {}_{+2}Y_{\ell_1 m_1}(\hat{n}_j)\ w_j\ d\hat{n}_j\end{aligned}$$

where we neglected gradients of the window function ${}_{w_j=w(\hat{n}_j)}$.
Finally, we also have the completeness relation for spherical harmonics (Varshalovich et al. 1988):

$$\sum_{\ell m} {}_sY_{\ell m}(\hat{n}_i)\,{}_sY^*_{\ell m}(\hat{n}_j)=\delta(\hat{n}_i-\hat{n}_j) \tag{6.57}$$

product of 2 $W^{\oplus,X}_{\ell_1 m_1 \ell_2 m_2}$

We neglect gradients of the window function and apply the completeness relation for spherical harmonics (Eq. 6.57).

$$\begin{aligned}\sum_{\ell_1 m_1} W^{0,X*}_{\ell m \ell_1 m_1} W^{0,Y}_{\ell' m' \ell_1 m_1} &= \sum_{\ell_1 m_1}\int_{ij} w^X_i w^Y_j d\hat{n}_i d\hat{n}_j Y_{\ell m}(\hat{n}_i) Y^*_{\ell_1 m_1}(\hat{n}_i) Y^*_{\ell' m'}(\hat{n}_j) Y_{\ell_1 m_1}(\hat{n}_j)\\ &= \int_i \left(w^X_i w^Y_i\right) d\hat{n}_i Y_{\ell m}(\hat{n}_i) Y^*_{\ell' m'}(\hat{n}_i)\\ &= W^0_{\ell m \ell' m'}(w^X w^Y)\equiv W^{0,XY}_{\ell m \ell' m'}\end{aligned} \tag{6.58}$$

$$\begin{aligned}
\sum_{\ell_1 m_1} W^{+,X*}_{\ell m \ell_1 m_1} W^{+,Y}_{\ell' m' \ell_1 m_1} &= \sum_{\ell_1 m_1} \int_{ij} w_i^X w_j^Y d\hat{n}_i d\hat{n}_j \Big[{}_{+2}Y_{\ell m}(\hat{n}_i)\, {}_{+2}Y^*_{\ell_1 m_1}(\hat{n}_i)\, {}_{+2}Y^*_{\ell' m'}(\hat{n}_j)\, {}_{+2}Y_{\ell_1 m_1}(\hat{n}_j) \quad + \quad {}_{+2}Y_{\ell m}(\hat{n}_i)\, {}_{+2}Y^*_{\ell_1 m_1}(\hat{n}_i)\, {}_{-2}Y^*_{\ell' m'}(\hat{n}_j)\, {}_{-2}Y_{\ell_1 m_1}(\hat{n}_j) \\
&\qquad + {}_{-2}Y_{\ell m}(\hat{n}_i)\, {}_{-2}Y^*_{\ell_1 m_1}(\hat{n}_i)\, {}_{+2}Y^*_{\ell' m'}(\hat{n}_j)\, {}_{+2}Y_{\ell_1 m_1}(\hat{n}_j) \quad + \quad {}_{-2}Y_{\ell m}(\hat{n}_i)\, {}_{-2}Y^*_{\ell_1 m_1}(\hat{n}_i)\, {}_{-2}Y^*_{\ell' m'}(\hat{n}_j)\, {}_{-2}Y_{\ell_1 m_1}(\hat{n}_j) \Big] \\
&\simeq 2 \sum_{\ell_1 m_1} \int_{ij} w_i^X w_j^Y d\hat{n}_i d\hat{n}_j \Big[{}_{+2}Y_{\ell m}(\hat{n}_i)\, {}_{+2}Y^*_{\ell_1 m_1}(\hat{n}_i)\, {}_{+2}Y^*_{\ell' m'}(\hat{n}_j)\, {}_{+2}Y_{\ell_1 m_1}(\hat{n}_j) + {}_{-2}Y_{\ell m}(\hat{n}_i)\, {}_{-2}Y^*_{\ell_1 m_1}(\hat{n}_i)\, {}_{-2}Y^*_{\ell' m'}(\hat{n}_j)\, {}_{-2}Y_{\ell_1 m_1}(\hat{n}_j) \Big] \\
&\simeq 2 \int_i \big(w_i^X w_i^Y\big) d\hat{n}_i \Big[{}_2Y_{\ell m}(\hat{n}_i)\, {}_2Y^*_{\ell' m'}(\hat{n}_i) + {}_{-2}Y_{\ell m}(\hat{n}_i)\, {}_{-2}Y^*_{\ell' m'}(\hat{n}_i) \Big] \\
&\simeq 2\, W^{+,XY}_{\ell m \ell' m'}
\end{aligned}$$

$$\begin{aligned}
\sum_{\ell_1 m_1} W^{-,X*}_{\ell m \ell_1 m_1} W^{-,Y}_{\ell' m' \ell_1 m_1} &= \sum_{\ell_1 m_1} \int_{ij} w_i^X w_j^Y d\hat{n}_i d\hat{n}_j \Big[{}_{+2}Y_{\ell m}(\hat{n}_i)\, {}_{+2}Y^*_{\ell_1 m_1}(\hat{n}_i)\, {}_{+2}Y^*_{\ell' m'}(\hat{n}_j)\, {}_{+2}Y_{\ell_1 m_1}(\hat{n}_j) \quad - \quad {}_{+2}Y_{\ell m}(\hat{n}_i)\, {}_{+2}Y^*_{\ell_1 m_1}(\hat{n}_i)\, {}_{-2}Y^*_{\ell' m'}(\hat{n}_j)\, {}_{-2}Y_{\ell_1 m_1}(\hat{n}_j) \\
&\qquad - {}_{-2}Y_{\ell m}(\hat{n}_i)\, {}_{-2}Y^*_{\ell_1 m_1}(\hat{n}_i)\, {}_{+2}Y^*_{\ell' m'}(\hat{n}_j)\, {}_{+2}Y_{\ell_1 m_1}(\hat{n}_j) \quad + \quad {}_{-2}Y_{\ell m}(\hat{n}_i)\, {}_{-2}Y^*_{\ell_1 m_1}(\hat{n}_i)\, {}_{-2}Y^*_{\ell' m'}(\hat{n}_j)\, {}_{-2}Y_{\ell_1 m_1}(\hat{n}_j) \Big] \\
&\simeq 0
\end{aligned}$$

$$\begin{aligned}
\sum_{\ell_1 m_1} W^{0,X*}_{\ell m \ell_1 m_1} W^{+,Y}_{\ell' m' \ell_1 m_1} &= \sum_{\ell_1 m_1} \int_{ij} w_i^X w_j^Y d\hat{n}_i d\hat{n}_j Y_{\ell m}(\hat{n}_i) Y^*_{\ell_1 m_1}(\hat{n}_i) \Big[{}_2Y_{\ell' m'}{}^*(\hat{n}_j)\, {}_2Y_{\ell_1 m_1}(\hat{n}_j) + {}_{-2}Y_{\ell' m'}{}^*(\hat{n}_j)\, {}_{-2}Y_{\ell_1 m_1}(\hat{n}_j) \Big] \\
&\simeq 2 \sum_{\ell_1 m_1} \int_{ij} w_i^X w_j^Y d\hat{n}_i d\hat{n}_j Y_{\ell m}(\hat{n}_i) Y^*_{\ell_1 m_1}(\hat{n}_i)\; Y_{\ell' m'}{}^*(\hat{n}_j)\; Y_{\ell_1 m_1}(\hat{n}_j) \\
&\simeq 2 \int_i (w_i^X w_i^Y) d\hat{n}_i Y_{\ell m}(\hat{n}_i)\; Y_{\ell' m'}{}^*(\hat{n}_i) \\
&\simeq 2\, W^{0,XY}_{\ell m \ell' m'} \qquad (6.59)
\end{aligned}$$

$$\begin{aligned}
\sum_{\ell_1 m_1} W^{0,X*}_{\ell m \ell_1 m_1} W^{-,Y}_{\ell' m' \ell_1 m_1} &= \sum_{\ell_1 m_1} \int_{ij} w_i^X w_j^Y d\hat{n}_i d\hat{n}_j Y_{\ell m}(\hat{n}_i) Y^*_{\ell_1 m_1}(\hat{n}_i) \Big[{}_2Y_{\ell' m'}{}^*(\hat{n}_j)\, {}_2Y_{\ell_1 m_1}(\hat{n}_j) - {}_{-2}Y_{\ell' m'}{}^*(\hat{n}_j)\, {}_{-2}Y_{\ell_1 m_1}(\hat{n}_j) \Big] \\
&\simeq 0 \qquad (6.60)
\end{aligned}$$

$$\begin{aligned}
\sum_{\ell_1 m_1} W^{+,X*}_{\ell m \ell_1 m_1} W^{-,Y}_{\ell' m' \ell_1 m_1} &= \sum_{\ell_1 m_1} \int_{ij} w_i^X w_j^Y d\hat{n}_i d\hat{n}_j \Big[{}_{+2}Y_{\ell m}(\hat{n}_i)\, {}_{+2}Y^*_{\ell_1 m_1}(\hat{n}_i)\, {}_{+2}Y^*_{\ell' m'}(\hat{n}_j)\, {}_{+2}Y_{\ell_1 m_1}(\hat{n}_j) \quad - \quad {}_{+2}Y_{\ell m}(\hat{n}_i)\, {}_{+2}Y^*_{\ell_1 m_1}(\hat{n}_i)\, {}_{-2}Y^*_{\ell' m'}(\hat{n}_j)\, {}_{-2}Y_{\ell_1 m_1}(\hat{n}_j) \\
&\qquad + {}_{-2}Y_{\ell m}(\hat{n}_i)\, {}_{-2}Y^*_{\ell_1 m_1}(\hat{n}_i)\, {}_{+2}Y^*_{\ell' m'}(\hat{n}_j)\, {}_{+2}Y_{\ell_1 m_1}(\hat{n}_j) \quad - \quad {}_{-2}Y_{\ell m}(\hat{n}_i)\, {}_{-2}Y^*_{\ell_1 m_1}(\hat{n}_i)\, {}_{-2}Y^*_{\ell' m'}(\hat{n}_j)\, {}_{-2}Y_{\ell_1 m_1}(\hat{n}_j) \Big] \\
&\simeq 2 \sum_{\ell_1 m_1} \int_{ij} w_i^X w_j^Y d\hat{n}_i d\hat{n}_j \Big[{}_{+2}Y_{\ell m}(\hat{n}_i)\, {}_{+2}Y^*_{\ell_1 m_1}(\hat{n}_i)\, {}_{+2}Y^*_{\ell' m'}(\hat{n}_j)\, {}_{+2}Y_{\ell_1 m_1}(\hat{n}_j) - {}_{-2}Y_{\ell m}(\hat{n}_i)\, {}_{-2}Y^*_{\ell_1 m_1}(\hat{n}_i)\, {}_{-2}Y^*_{\ell' m'}(\hat{n}_j)\, {}_{-2}Y_{\ell_1 m_1}(\hat{n}_j) \Big] \\
&\simeq 2 \int_i \big(w_i^X w_i^Y\big) d\hat{n}_i \Big[{}_2Y_{\ell m}(\hat{n}_i)\, {}_2Y^*_{\ell' m'}(\hat{n}_i) - {}_{-2}Y_{\ell m}(\hat{n}_i)\, {}_{-2}Y^*_{\ell' m'}(\hat{n}_i) \Big] \\
&\simeq 2\, W^{-,XY}_{\ell m \ell' m'}
\end{aligned}$$

Variance of pseudo-C_ℓ

We now write elements of the pseudo-covariance matrix $\tilde{\mathbf{\Sigma}}$ (Eq. 6.50). We consider approximation of high multipoles (greater than the width of the window function W_ℓ) for which, if the Galactic cut is sufficiently narrow, we can the replace the product $C^X_{\ell_1} C^Y_{\ell_2}$ by $C^X_{\ell\ell'} C^Y_{\ell\ell'} = \sqrt{C^X_\ell C^X_{\ell'} C^Y_\ell C^Y_{\ell'}}$ allowing the matrix to be symmetric. Then we apply relation on product of $W^{0,\pm,X}_{\ell m \ell' m'}$ (Section 6.A) on (ℓ_1, m_1) and (ℓ_2, m_2) successively. Finally, we identify the kernels $\mathsf{M}_{(\ell,\ell',a,b)}$ as defined in Eqs. (6.40).

$$\begin{aligned}
\Big\langle \Delta\tilde{C}_\ell^{T_a T_b} \Delta\tilde{C}_{\ell'}^{T_c T_d \star} \Big\rangle &= L_{\ell\ell'} \sum_{mm'} \Big\{ \Big\langle T^a_{\ell m} T^{c*}_{\ell' m'} \Big\rangle \Big\langle T^{b*}_{\ell m} T^d_{\ell' m'} \Big\rangle + \Big\langle T^a_{\ell m} T^{d*}_{\ell' m'} \Big\rangle \Big\langle T^{b*}_{\ell m} T^c_{\ell' m'} \Big\rangle \Big\} \qquad (6.61) \\
&= L_{\ell\ell'} \sum_{mm'} \sum_{\ell_1 m_1} \sum_{\ell_2 m_2} \Big\{ C^{T_a T_c}_{\ell_1} C^{T_b T_d}_{\ell_2} W^{0,T_a}_{\ell m \ell_1 m_1} W^{0,T_c \star}_{\ell' m' \ell_1 m_1} W^{0,T_b \star}_{\ell m \ell_2 m_2} W^{0,T_d}_{\ell' m' \ell_2 m_2} + C^{T_a T_d}_{\ell_1} C^{T_b T_c}_{\ell_2} W^{0,T_a}_{\ell m \ell_1 m_1} W^{0,T_d \star}_{\ell' m' \ell_1 m_1} W^{0,T_b \star}_{\ell' m' \ell_2 m_2} W^{0,T_c}_{\ell m \ell_2 m_2} \Big\} \\
&\simeq L_{\ell\ell'} C^{T_a T_c}_{\ell\ell'} C^{T_b T_d}_{\ell\ell'} \sum_{mm'} W^{0,T_a T_c}_{\ell m \ell' m'} W^{0,T_b T_d \star}_{\ell m \ell' m'} + L_{\ell\ell'} C^{T_a T_d}_{\ell\ell'} C^{T_b T_c}_{\ell\ell'} \sum_{mm'} W^{0,T_a T_d}_{\ell m \ell' m'} W^{0,T_b T_c \star}_{\ell m \ell' m'}
\end{aligned}$$

$$\boxed{\Big\langle \Delta\tilde{C}_\ell^{T_a T_b} \Delta\tilde{C}_{\ell'}^{T_c T_d \star} \Big\rangle \simeq C^{T_a T_c}_{\ell\ell'} C^{T_b T_d}_{\ell\ell'} \mathsf{M}_{TT,TT}(\ell,\ell';w_a^T w_c^T, w_b^T w_d^T) + C^{T_a T_d}_{\ell\ell'} C^{T_b T_c}_{\ell\ell'} \mathsf{M}_{TT,TT}(\ell,\ell';w_a^T w_d^T, w_b^T w_c^T)} \qquad (6.62)$$

$$\begin{aligned}
\Big\langle \Delta\tilde{C}_\ell^{E_a E_b} \Delta\tilde{C}_{\ell'}^{E_c E_d \star} \Big\rangle &= L_{\ell\ell'} \sum_{mm'} \Big\{ \Big\langle E^a_{\ell m} E^{c*}_{\ell' m'} \Big\rangle \Big\langle E^{b*}_{\ell m} E^d_{\ell' m'} \Big\rangle + \Big\langle E^a_{\ell m} E^{d*}_{\ell' m'} \Big\rangle \Big\langle E^{b*}_{\ell m} E^c_{\ell' m'} \Big\rangle \Big\} \qquad (6.63) \\
&= \frac{1}{16} L_{\ell\ell'} \sum_{mm'} \sum_{\ell_1 m_1} \sum_{\ell_2 m_2} \Big\{ C^{E_a E_c}_{\ell_1} C^{E_b E_d}_{\ell_2} W^{+,E_a}_{\ell m \ell_1 m_1} W^{+,E_c \star}_{\ell' m' \ell_1 m_1} W^{+,E_b \star}_{\ell m \ell_2 m_2} W^{+,E_d}_{\ell' m' \ell_2 m_2} + C^{E_a E_d}_{\ell_1} C^{E_b E_c}_{\ell_2} W^{+,E_a}_{\ell m \ell_1 m_1} W^{+,E_d \star}_{\ell' m' \ell_1 m_1} W^{+,E_b \star}_{\ell' m' \ell_2 m_2} W^{+,E_c}_{\ell m \ell_2 m_2} \Big\} \\
&\simeq \frac{1}{4} L_{\ell\ell'} C^{E_a E_c}_{\ell\ell'} C^{E_b E_d}_{\ell\ell'} \sum_{mm'} W^{+,E_a E_c}_{\ell m \ell' m'} W^{+,E_b E_d \star}_{\ell m \ell' m'} + \frac{1}{4} L_{\ell\ell'} C^{E_a E_d}_{\ell\ell'} C^{E_b E_c}_{\ell\ell'} \sum_{mm'} W^{+,E_a E_d}_{\ell m \ell' m'} W^{+,E_b E_c \star}_{\ell m \ell' m'}
\end{aligned}$$

$$\boxed{\left\langle \Delta\tilde{C}_\ell^{E_aE_b}\Delta\tilde{C}_{\ell'}^{E_cE_d\star}\right\rangle \simeq C_{\ell\ell'}^{E_aE_c}C_{\ell\ell'}^{E_bE_d}\mathsf{M}_{EE,EE}(\ell,\ell';w_a^Pw_c^P,w_b^Pw_d^P)+C_{\ell\ell'}^{E_aE_d}C_{\ell\ell'}^{E_bE_c}\mathsf{M}_{EE,EE}(\ell,\ell';w_a^Pw_d^P,w_b^Pw_c^P)} \tag{6.64}$$

$$\left\langle \Delta\tilde{C}_\ell^{B_aB_b}\Delta\tilde{C}_{\ell'}^{B_cB_d\star}\right\rangle = L_{\ell\ell'}\sum_{mm'}\left\{\left\langle B_{\ell m}^a B_{\ell' m'}^{c*}\right\rangle\left\langle B_{\ell m}^{b*}B_{\ell' m'}^d\right\rangle+\left\langle B_{\ell m}^a B_{\ell' m'}^{d*}\right\rangle\left\langle B_{\ell m}^{b*}B_{\ell' m'}^c\right\rangle\right\} \tag{6.65}$$

$$= \frac{1}{16}L_{\ell\ell'}\sum_{mm'}\sum_{\ell_1m_1}\sum_{\ell_2m_2}\left\{C_{\ell_1}^{B_aB_c}C_{\ell_2}^{B_bB_d}W_{\ell m\ell_1m_1}^{+,B_a}W_{\ell'm'\ell_1m_1}^{+,B_c\star}W_{\ell m\ell_2m_2}^{+,B_b\star}W_{\ell'm'\ell_2m_2}^{+,B_d}+C_{\ell_1}^{B_aB_d}C_{\ell_2}^{B_bB_c}W_{\ell m\ell_1m_1}^{+,B_a}W_{\ell'm'\ell_1m_1}^{+,B_d\star}W_{\ell'm'\ell_2m_2}^{+,B_b\star}W_{\ell m\ell_2m_2}^{+,B_c}\right\}$$

$$\simeq \frac{1}{4}L_{\ell\ell'}C_{\ell\ell'}^{B_aB_c}C_{\ell\ell'}^{B_bB_d}\sum_{mm'}W_{\ell m\ell'm'}^{+,B_aB_c}W_{\ell m\ell'm'}^{+,B_bB_d\star}+\frac{1}{4}L_{\ell\ell'}C_{\ell\ell'}^{B_aB_d}C_{\ell\ell'}^{B_bB_c}\sum_{mm'}W_{\ell m\ell'm'}^{+,B_aB_d}W_{\ell m\ell'm'}^{+,B_bB_c\star}$$

$$\boxed{\left\langle \Delta\tilde{C}_\ell^{B_aB_b}\Delta\tilde{C}_{\ell'}^{B_cB_d\star}\right\rangle \simeq C_{\ell\ell'}^{B_aB_c}C_{\ell\ell'}^{B_bB_d}\mathsf{M}_{EE,EE}(\ell,\ell';w_a^Pw_c^P,w_b^Pw_d^P)+C_{\ell\ell'}^{B_aB_d}C_{\ell\ell'}^{B_bB_c}\mathsf{M}_{EE,EE}(\ell,\ell';w_a^Pw_d^P,w_b^Pw_c^P)} \tag{6.66}$$

$$\left\langle \Delta\tilde{C}_\ell^{E_aE_b}\Delta\tilde{C}_{\ell'}^{B_cB_d\star}\right\rangle = L_{\ell\ell'}\sum_{mm'}\left\{\left\langle E_{\ell m}^a B_{\ell' m'}^{c*}\right\rangle\left\langle E_{\ell m}^{b*}B_{\ell' m'}^d\right\rangle+\left\langle E_{\ell m}^a B_{\ell' m'}^{d*}\right\rangle\left\langle E_{\ell m}^{b*}B_{\ell' m'}^c\right\rangle\right\} \tag{6.67}$$

$$= \frac{1}{16}L_{\ell\ell'}\sum_{mm'}\sum_{\ell_1m_1}\sum_{\ell_2m_2}\Big\{\begin{aligned}&C_{\ell_1}^{E_aE_c}C_{\ell_2}^{E_bE_d}W_{\ell m\ell_1m_1}^{+,E_a}W_{\ell'm'\ell_1m_1}^{-,B_c\star}W_{\ell m\ell_2m_2}^{+,E_b\star}W_{\ell'm'\ell_2m_2}^{-,B_d}\\&+C_{\ell_1}^{E_aE_c}C_{\ell_2}^{B_bB_d}W_{\ell m\ell_1m_1}^{+,E_a}W_{\ell'm'\ell_1m_1}^{-,B_c\star}W_{\ell m\ell_2m_2}^{-,E_b\star}W_{\ell'm'\ell_2m_2}^{+,B_d}\\&+C_{\ell_1}^{B_aB_c}C_{\ell_2}^{E_bE_d}W_{\ell m\ell_1m_1}^{-,E_a}W_{\ell'm'\ell_1m_1}^{+,B_c\star}W_{\ell m\ell_2m_2}^{+,E_b\star}W_{\ell'm'\ell_2m_2}^{-,B_d}\\&+C_{\ell_1}^{B_aB_c}C_{\ell_2}^{B_bB_d}W_{\ell m\ell_1m_1}^{-,E_a}W_{\ell'm'\ell_1m_1}^{+,B_c\star}W_{\ell m\ell_2m_2}^{-,E_b\star}W_{\ell'm'\ell_2m_2}^{+,B_d}\\&+C_{\ell_1}^{E_aE_d}C_{\ell_2}^{E_bE_c}W_{\ell m\ell_1m_1}^{+,E_a}W_{\ell'm'\ell_1m_1}^{-,B_d\star}W_{\ell m\ell_2m_2}^{+,E_b\star}W_{\ell'm'\ell_2m_2}^{-,B_c}\\&+C_{\ell_1}^{E_aE_d}C_{\ell_2}^{B_bB_c}W_{\ell m\ell_1m_1}^{+,E_a}W_{\ell'm'\ell_1m_1}^{-,B_d\star}W_{\ell m\ell_2m_2}^{-,E_b\star}W_{\ell'm'\ell_2m_2}^{+,B_c}\\&+C_{\ell_1}^{B_aB_d}C_{\ell_2}^{E_bE_c}W_{\ell m\ell_1m_1}^{-,E_a}W_{\ell'm'\ell_1m_1}^{+,B_d\star}W_{\ell m\ell_2m_2}^{+,E_b\star}W_{\ell'm'\ell_2m_2}^{-,B_c}\\&+C_{\ell_1}^{B_aB_d}C_{\ell_2}^{B_bB_c}W_{\ell m\ell_1m_1}^{-,E_a}W_{\ell'm'\ell_1m_1}^{+,B_d\star}W_{\ell m\ell_2m_2}^{-,E_b\star}W_{\ell'm'\ell_2m_2}^{+,B_c}\Big\}\end{aligned}$$

$$\simeq \begin{aligned}&\tfrac{1}{4}L_{\ell\ell'}(C_{\ell\ell'}^{E_aE_c}C_{\ell\ell'}^{E_bE_d}+C_{\ell\ell'}^{E_aE_c}C_{\ell\ell'}^{B_bB_d}+C_{\ell\ell'}^{B_aB_c}C_{\ell\ell'}^{E_bE_d}+C_{\ell\ell'}^{B_aB_c}C_{\ell\ell'}^{B_bB_d})\textstyle\sum_{mm'}W_{\ell m\ell'm'}^{-,E_aB_c}W_{\ell m\ell'm'}^{-,E_bB_d\star}\\&+\tfrac{1}{4}L_{\ell\ell'}(C_{\ell\ell'}^{E_aE_d}C_{\ell\ell'}^{E_bE_c}+C_{\ell\ell'}^{E_aE_d}C_{\ell\ell'}^{B_bB_c}+C_{\ell\ell'}^{B_aB_d}C_{\ell\ell'}^{E_bE_c}+C_{\ell\ell'}^{B_aB_d}C_{\ell\ell'}^{B_bB_c})\textstyle\sum_{mm'}W_{\ell m\ell'm'}^{-,E_aB_d}W_{\ell m\ell'm'}^{-,E_bB_c\star}\end{aligned}$$

$$\boxed{\begin{aligned}\left\langle \Delta\tilde{C}_\ell^{E_aE_b}\Delta\tilde{C}_{\ell'}^{B_cB_d\star}\right\rangle \simeq\ &(C_{\ell\ell'}^{E_aE_c}C_{\ell\ell'}^{E_bE_d}+C_{\ell\ell'}^{E_aE_c}C_{\ell\ell'}^{B_bB_d}+C_{\ell\ell'}^{B_aB_c}C_{\ell\ell'}^{E_bE_d}+C_{\ell\ell'}^{B_aB_c}C_{\ell\ell'}^{B_bB_d})\mathsf{M}_{EE,BB}(\ell,\ell';w_a^Pw_c^P,w_b^Pw_d^P)+\\&(C_{\ell\ell'}^{E_aE_d}C_{\ell\ell'}^{E_bE_c}+C_{\ell\ell'}^{E_aE_d}C_{\ell\ell'}^{B_bB_c}+C_{\ell\ell'}^{B_aB_d}C_{\ell\ell'}^{E_bE_c}+C_{\ell\ell'}^{B_aB_d}C_{\ell\ell'}^{B_bB_c})\mathsf{M}_{EE,BB}(\ell,\ell';w_a^Pw_d^P,w_b^Pw_c^P)\end{aligned}} \tag{6.68}$$

$$\left\langle \Delta\tilde{C}_\ell^{T_aE_b}\Delta\tilde{C}_{\ell'}^{T_cE_d\star}\right\rangle = L_{\ell\ell'}\sum_{mm'}\left\{\left\langle T_{\ell m}^a T_{\ell' m'}^{c*}\right\rangle\left\langle E_{\ell m}^{b*}E_{\ell' m'}^d\right\rangle+\left\langle T_{\ell m}^a E_{\ell' m'}^{d*}\right\rangle\left\langle E_{\ell m}^{b*}T_{\ell' m'}^c\right\rangle\right\} \tag{6.69}$$

$$= \frac{1}{4}L_{\ell\ell'}\sum_{mm'}\sum_{\ell_1m_1}\sum_{\ell_2m_2}\left\{C_{\ell_1}^{T_aT_c}C_{\ell_2}^{E_bE_d}W_{\ell m\ell_1m_1}^{0,T_a}W_{\ell'm'\ell_1m_1}^{0,T_c\star}W_{\ell m\ell_2m_2}^{+,E_b\star}W_{\ell'm'\ell_2m_2}^{+,E_d}+C_{\ell_1}^{T_aE_d}C_{\ell_2}^{E_bT_c}W_{\ell m\ell_1m_1}^{0,T_a\star}W_{\ell'm'\ell_1m_1}^{+,E_d}W_{\ell'm'\ell_2m_2}^{+,E_b}W_{\ell m\ell_2m_2}^{0,T_c\star}\right\}$$

$$\simeq \frac{1}{2}L_{\ell\ell'}C_{\ell\ell'}^{T_aT_c}C_{\ell\ell'}^{E_bE_d}\sum_{mm'}W_{\ell m\ell'm'}^{0,T_aT_c}W_{\ell m\ell'm'}^{+,E_bE_d\star}+L_{\ell\ell'}C_{\ell\ell'}^{T_aE_d}C_{\ell\ell'}^{E_bT_c}\sum_{mm'}W_{\ell m\ell'm'}^{0,T_aE_d}W_{\ell m\ell'm'}^{0,E_bT_c\star}$$

$$\boxed{\left\langle \Delta\tilde{C}_\ell^{T_aE_b}\Delta\tilde{C}_{\ell'}^{T_cE_d\star}\right\rangle \simeq C_{\ell\ell'}^{T_aT_c}C_{\ell\ell'}^{E_bE_d}\mathsf{M}_{TP,TP}(\ell,\ell';w_a^Tw_c^T,w_b^Pw_d^P)+C_{\ell\ell'}^{T_aE_d}C_{\ell\ell'}^{E_bT_c}\mathsf{M}_{TT,TT}(\ell,\ell';w_a^Tw_d^P,w_b^Pw_c^T)} \tag{6.70}$$

$$\left\langle \Delta\tilde{C}_\ell^{T_aT_b}\Delta\tilde{C}_{\ell'}^{T_cE_d\star}\right\rangle = L_{\ell\ell'}\sum_{mm'}\left\{\left\langle T_{\ell m}^a T_{\ell' m'}^{c*}\right\rangle\left\langle T_{\ell m}^{b*}E_{\ell' m'}^d\right\rangle+\left\langle T_{\ell m}^a E_{\ell' m'}^{d*}\right\rangle\left\langle T_{\ell m}^{b*}T_{\ell' m'}^c\right\rangle\right\} \tag{6.71}$$

$$= \frac{1}{2}L_{\ell\ell'}\sum_{mm'}\sum_{\ell_1m_1}\sum_{\ell_2m_2}\left\{C_{\ell_1}^{T_aT_c}C_{\ell_2}^{T_bE_d}W_{\ell m\ell_1m_1}^{0,T_a}W_{\ell'm'\ell_1m_1}^{0,T_c\star}W_{\ell m\ell_2m_2}^{0,T_b\star}W_{\ell'm'\ell_2m_2}^{+,E_d}+C_{\ell_1}^{T_aE_d}C_{\ell_2}^{T_bT_c}W_{\ell m\ell_1m_1}^{0,T_a\star}W_{\ell'm'\ell_1m_1}^{+,E_d}W_{\ell'm'\ell_2m_2}^{0,T_b}W_{\ell m\ell_2m_2}^{0,T_c\star}\right\}$$

$$\simeq L_{\ell\ell'}C_{\ell\ell'}^{T_aT_c}C_{\ell\ell'}^{T_bE_d}\sum_{mm'}W_{\ell m\ell'm'}^{0,T_aT_c}W_{\ell m\ell'm'}^{0,T_bE_d\star}+L_{\ell\ell'}C_{\ell\ell'}^{T_aE_d}C_{\ell\ell'}^{T_bT_c}\sum_{mm'}W_{\ell m\ell'm'}^{0,T_aE_d}W_{\ell m\ell'm'}^{0,T_bT_c\star}$$

$$\boxed{\left\langle \Delta\tilde{C}_\ell^{T_aT_b}\Delta\tilde{C}_{\ell'}^{T_cE_d\star}\right\rangle \simeq C_{\ell\ell'}^{T_aT_c}C_{\ell\ell'}^{T_bE_d}\mathsf{M}_{TT,TT}(\ell,\ell';w_a^Tw_c^T,w_b^Tw_d^P)+C_{\ell\ell'}^{T_aE_d}C_{\ell\ell'}^{T_bT_c}\mathsf{M}_{TT,TT}(\ell,\ell';w_a^Tw_d^P,w_b^Tw_c^T)} \tag{6.72}$$

$$\left\langle \Delta\tilde{C}_\ell^{T_aT_b}\Delta\tilde{C}_{\ell'}^{E_cE_d\star}\right\rangle = L_{\ell\ell'}\sum_{mm'}\left\{\left\langle T_{\ell m}^a E_{\ell' m'}^{c*}\right\rangle\left\langle T_{\ell m}^{b*}E_{\ell' m'}^d\right\rangle+\left\langle T_{\ell m}^a E_{\ell' m'}^{d*}\right\rangle\left\langle T_{\ell m}^{b*}E_{\ell' m'}^c\right\rangle\right\} \tag{6.73}$$

$$= \frac{1}{4}L_{\ell\ell'}\sum_{mm'}\sum_{\ell_1m_1}\sum_{\ell_2m_2}\left\{C_{\ell_1}^{T_aE_c}C_{\ell_2}^{T_bE_d}W_{\ell m\ell_1m_1}^{0,T_a}W_{\ell'm'\ell_1m_1}^{+,E_c\star}W_{\ell m\ell_2m_2}^{0,T_b\star}W_{\ell'm'\ell_2m_2}^{+,E_d}+C_{\ell_1}^{T_aE_d}C_{\ell_2}^{T_bE_c}W_{\ell m\ell_1m_1}^{0,T_a\star}W_{\ell'm'\ell_1m_1}^{+,E_d}W_{\ell'm'\ell_2m_2}^{0,T_b}W_{\ell m\ell_2m_2}^{+,E_c\star}\right\}$$

$$\simeq L_{\ell\ell'}C_{\ell\ell'}^{T_aE_c}C_{\ell\ell'}^{T_bE_d}\sum_{mm'}W_{\ell m\ell'm'}^{0,T_aE_c}W_{\ell m\ell'm'}^{0,T_bE_d\star}+L_{\ell\ell'}C_{\ell\ell'}^{T_aE_d}C_{\ell\ell'}^{T_bE_c}\sum_{mm'}W_{\ell m\ell'm'}^{0,T_aE_d}W_{\ell m\ell'm'}^{0,T_bE_c\star}$$

$$\boxed{\left\langle \Delta\tilde{C}_\ell^{T_aT_b}\Delta\tilde{C}_{\ell'}^{E_cE_d\star}\right\rangle \simeq C_{\ell\ell'}^{T_aE_c}C_{\ell\ell'}^{T_bE_d}\mathsf{M}_{TT,TT}(\ell,\ell';w_a^Tw_c^P,w_b^Tw_d^P)+C_{\ell\ell'}^{T_aE_d}C_{\ell\ell'}^{T_bE_c}\mathsf{M}_{TT,TT}(\ell,\ell';w_a^Tw_d^P,w_b^Tw_c^P)} \tag{6.74}$$

$$\left\langle \Delta\tilde{C}_\ell^{E_aE_b}\Delta\tilde{C}_{\ell'}^{T_cE_d\star}\right\rangle = L_{\ell\ell'}\sum_{mm'}\left\{\left\langle E_{\ell m}^a T_{\ell' m'}^{c*}\right\rangle\left\langle E_{\ell m}^{b*}E_{\ell' m'}^d\right\rangle+\left\langle E_{\ell m}^a E_{\ell' m'}^{d*}\right\rangle\left\langle E_{\ell m}^{b*}T_{\ell' m'}^c\right\rangle\right\} \tag{6.75}$$

$$= \frac{1}{8}L_{\ell\ell'}\sum_{mm'}\sum_{\ell_1m_1}\sum_{\ell_2m_2}\left\{C_{\ell_1}^{E_aT_c}C_{\ell_2}^{E_bE_d}W_{\ell m\ell_1m_1}^{+,E_a}W_{\ell'm'\ell_1m_1}^{0,T_c\star}W_{\ell m\ell_2m_2}^{+,E_b\star}W_{\ell'm'\ell_2m_2}^{+,E_d}+C_{\ell_1}^{E_aE_d}C_{\ell_2}^{E_bT_c}W_{\ell m\ell_1m_1}^{+,E_a}W_{\ell'm'\ell_1m_1}^{+,E_d\star}W_{\ell'm'\ell_2m_2}^{+,E_b\star}W_{\ell m\ell_2m_2}^{0,T_c}\right\}$$

$$\simeq \frac{1}{2}L_{\ell\ell'}C_{\ell\ell'}^{E_aT_c}C_{\ell\ell'}^{E_bE_d}\sum_{mm'}W_{\ell m\ell'm'}^{0,E_aT_c}W_{\ell m\ell'm'}^{+,E_bE_d\star}+\frac{1}{2}L_{\ell\ell'}C_{\ell\ell'}^{E_aE_d}C_{\ell\ell'}^{E_bT_c}\sum_{mm'}W_{\ell m\ell'm'}^{+,E_aE_d}W_{\ell m\ell'm'}^{0,E_bT_c\star}$$

$$\boxed{\left\langle \Delta\tilde{C}_\ell^{E_aE_b}\Delta\tilde{C}_{\ell'}^{T_cE_d\star}\right\rangle \simeq C_{\ell\ell'}^{E_aT_c}C_{\ell\ell'}^{E_bE_d}\mathsf{M}_{TP,TP}(\ell,\ell';w_a^Pw_c^T,w_b^Pw_d^P)+C_{\ell\ell'}^{E_aE_d}C_{\ell\ell'}^{E_bT_c}\mathsf{M}_{TP,TP}(\ell,\ell';w_a^Pw_d^P,w_b^Pw_c^T)} \tag{6.76}$$

Bibliography

Addison, G. E., Dunkley, J., & Spergel, D. N. 2012, MNRAS, 427, 1741
Battaglia, N., Natarajan, A., Trac, H., Cen, R., & Loeb, A. 2013, ApJ, 776, 83
Béthermin, M., Daddi, E., Magdis, G., et al. 2012, ApJ, 757, L23
Couchot, F., Henrot-Versillé, S., Perdereau, O., et al. 2017a, ArXiv e-prints [arXiv:1703.10829]
Couchot, F., Henrot-Versillé, S., Perdereau, O., et al. 2017b, A&A, 602, A41
Couchot, F., Henrot-Versillé, S., Perdereau, O., et al. 2017c, A&A, 597, A126
Efstathiou, G. & Migliaccio, M. 2012, MNRAS, 423, 2492
Efstathiou, G. P. 2006, MNRAS, 370, 343
Hivon, E., Górski, K. M., Netterfield, C. B., et al. 2002, ApJ, 567, 2
Kogut, A., Spergel, D. N., Barnes, C., et al. 2003, ApJS, 148, 161
Mangilli, A., Plaszczynski, S., & Tristram, M. 2015, MNRAS, 453, 3174
Peebles, P. J. E. 1973, ApJ, 185, 413
Planck Collaboration IX. 2014, A&A, 571, A9
Planck Collaboration XIII. 2014, A&A, 571, A13
Planck Collaboration XV. 2014, A&A, 571, A15
Planck Collaboration XVI. 2014, A&A, 571, A16
Planck Collaboration XXI. 2014, A&A, 571, A21
Planck Collaboration XXX. 2014, A&A, 571, A30
Planck Collaboration VII. 2016, A&A, 594, A7
Planck Collaboration VIII. 2016, A&A, 594, A8
Planck Collaboration XI. 2016, A&A, 594, A11
Planck Collaboration XII. 2016, A&A, 594, A12
Planck Collaboration XIII. 2016, A&A, 594, A13
Planck Collaboration XXII. 2016, A&A, 594, A22
Planck Collaboration XXIII. 2016, A&A, 594, A23
Planck Collaboration XXVI. 2016, A&A, 594, A26
Planck Collaboration Int. XIX. 2015, A&A, 576, A104
Planck Collaboration Int. XXII. 2015, A&A, 576, A107
Planck Collaboration Int. XXX. 2016, A&A, 586, A133
Shaw, L. D., Rudd, D. H., & Nagai, D. 2012, ApJ, 756, 15
Tinker, J., Kravtsov, A. V., Klypin, A., et al. 2008, ApJ, 688, 709
Tristram, M., Macías-Pérez, J. F., Renault, C., & Santos, D. 2005, MNRAS, 358, 833
Tucci, M., Martínez-González, E., Toffolatti, L., González-Nuevo, J., & De Zotti, G. 2004, MNRAS, 349, 1267
Tucci, M., Martinez-Gonzalez, E., Vielva, P., & Delabrouille, J. 2005, Mon.Not.Roy.Astron.Soc., 360, 935
Tucci, M. & Toffolatti, L. 2012, Advances in Astronomy, 2012, 52
Tucci, M., Toffolatti, L., de Zotti, G., & Martínez-González, E. 2011, A&A, 533, 57
Varshalovich, D. A., Moskalev, A. N., & Khersonskii, V. K. 1988, Quantum Theory of Angular Momentum (Singapore: World Scientific)

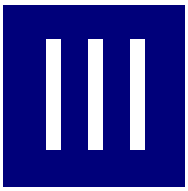

Cosmology

Chapter 7

ΛCDM results with Hillipop

extracted from Couchot et al. (2017b)

"Cosmology with the CMB temperature-polarization correlation"

With the HiLLiPOP likelihood, we derived constraints on the ΛCDM *model using CMB anisotropie measurements from Planck. We compared the CMB results obtained with the different angular power spectra TT, TE and EE. Given Planck sensitivities, most of the information is encoded in the temperature power spectrum. However, we have shown that the Planck TE cross-power spectrum can provide similar constraints on* ΛCDM *while being less sensitive to foregrounds. Our results are fully compatible with Planck 2015 constraints as described in Planck Collaboration XIII (2016). This study was published in Couchot et al. (2017b) and is reproduced here.*

We demonstrate that the CMB temperature-polarization cross-correlation provides accurate and robust constraints on cosmological parameters. We compare them with the results from temperature or polarization and investigate the impact of foregrounds, cosmic variance and instrumental noise. This analysis makes use of the Planck high-ℓ HiLLiPOP likelihood based on angular power spectra that takes into account systematics from the instrument and foreground residuals directly modeled using Planck measurements. The temperature-polarization correlation (TE) spectrum is less contaminated by astrophysical emissions than the temperature power-spectrum (TT) allowing to derive constraints that are less sensitive to foreground uncertainties. For ΛCDM parameters, TE gives very competitive results compared to TT.

7.1 Introduction

The results from the Planck satellite have recently demonstrated the consistency between the temperature and the polarisation data (Planck Collaboration XIII 2016). Adding to the measurement of the temperature fluctuations the information coming from the velocity gradients of the photon–baryon fluid through the polarization power spectra improves the constraints on cosmological parameters and helps breaking some degeneracies. One of the best example is the measurement of the reionization optical depth using the large-scale signature that reionization leaves in the EE polarization power spectrum (Planck Collaboration Int. XLVII 2016). Moreover, as suggested in Galli et al. (2014), for a cosmic variance limited experiment, polarization power spectra alone can provide tighter constraints on cosmological parameters than the temperature power spectrum while, for an experiment with Planck-like noise, constraints should be comparable.
In this paper, we discuss more in details the constraints on cosmological parameters obtained with the Planck 2015 polarization data (including foregrounds and systematic residuals). We find that the level of instrumental noise allows for an accurate reconstruction of cosmological parameters using temperature-polarization cross-correlation C_ℓ^{TE} only. Constraints from Planck EE polarization spectrum are dominated by instrumental noise. In addition, we investigate the robustness of the cosmological interpretation with respect to astrophysical residuals.
In the Planck analysis (Planck Collaboration XV 2014; Planck Collaboration XI 2016), the foreground contamination is mitigated using masks which are adapted to each frequency, reducing the sky fraction to the region where the foreground emissions are low. The residuals of diffuse foreground emissions are then taken into account using models at the spectrum level in the likelihood. Most of the results presented in Planck Collaboration XIII (2016) are based on TT angular power spectra which present the higher signal-to-noise ratio. However, foreground residuals in temperature combine several different emissions which are difficult to model in the power-spectra domain as they are both non-homogeneous

and non-gaussian. Any mismatch between the foreground model and the data can thus result in a bias on the estimated cosmological parameters and, in any case, will increase their posterior width. On the contrary, in polarisation, while the signal-to-noise is lower, the only foreground that affects the Planck data is the polarized emission of the Galactic dust. As we will show, this allows for a precise reconstruction of the cosmological parameters (especially with TE spectra) with less impact from foreground uncertainties.
The cosmological parameters reconstructed with TT spectra are compared to those obtained independently with TE and EE. In each cases, we detail the foreground modeling and the propagation of its uncertainties. We use the HiLLiPOP (High-ℓ Likelihood on Polarized Power-spectra) likelihood which is based on the Planck data in temperature and polarization. HiLLiPOP is one of the four high-ℓ likelihoods developed within the Planck consortium for the 2015 release and is briefly presented and compared to others in Planck Collaboration XIII (2016). It is a full temperature+polarization likelihood based on cross-spectra from Planck maps at 100, 143, and 217 GHz. It is based on a Gaussian approximation of the C_ℓ likelihood which is well suited for multipoles above ℓ=30. In contrary to the Planck **public** likelihood (Planck Collaboration XIII 2016), the foregrounds description in HiLLiPOP directly relies on the Planck astrophysical measurements. For the ΛCDM cosmology, using a τ prior, it gives results very compatible with the Planck **public likelihood** but for the (τ,A_s) pair which is more consistent with the low-ℓ data. Consequently, it also shows a better lensing amplitude A_L (see the discussion in Couchot et al. 2017c).
The chapter is organized as follows. We present in Sect. 7.2 the results for the ΛCDM cosmological model and check the impact of priors on the astrophysical parameters. Section 7.3 gives the results on the A_L parameter considered as a internal cross-check of the CMB likelihoods. Finally, in Sect. 7.4, we demonstrate the impact of the foreground parameters for the temperature likelihood and the TE likelihood in terms of both the bias and the precision of the cosmological parameters.

7.2 ΛCDM Results

This section is dedicated to the results derived with the HiLLiPOP likelihood functions (`HillipopTXE`, `HillipopT`, `HillipopE` and `HillipopX`). We discuss the cosmological parameters as well as the astrophysical foregrounds and instrumental nuisance. We pay particular attention to the difference between the results obtained with TT spectra (`HillipopT`) and the ones obtained with TE spectra (`HillipopX`).
We choose not to use any low-ℓ information and prefer to apply a simple prior on the optical reionization depth (τ= 0.058±0.012) as given by the *lollipop* likelihood in Planck Collaboration Int. XLVII (2016). We have checked that, for the ΛCDM model, the parameters are undistinguishable when using the corresponding Planck low-ℓ likelihood. We use the Gaussian priors on the inter-calibration coefficients and on astrophysical rescaling factors (dust, CIB, tSZ and point sources) as discussed in Chap.6 (Sect. 6.6).
The results described here have been obtained using the adaptative-MCMC algorithm implemented in the CAMEL toolbox[1]. We use the `CLASS`[2] software to compute spectra models for a given cosmology.

Likelihood	χ^2	n_{dof}	χ^2/n_{dof}
`HillipopTXE`	27888.3	25597	1.090
`HillipopT`	9995.9	9543	1.047
`HillipopX`	9319.9	8799	1.059
`HillipopE`	7304.5	7249	1.008

Table 7.1: χ^2 values compared to the number of degree of freedom (n_{dof}=n_ℓ−n_p).

The χ^2 values of the best-fit for each HiLLiPOP likelihood are reported in Table 7.1. Using our simple foreground model, we are able to fit the Planck data with reasonable χ^2 values and reduced-χ^2 comparable to the Planck public likelihood (the absolute values are not directly comparable since the Planck public likelihood uses binned cross-power spectra and different foreground modelization). Note that `HillipopT` and `HillipopX` show comparable χ^2 with a similar number of degrees of freedom.

7.2.1 ΛCDM cosmological results

Figure 7.1 shows the posterior distributions of the 6 ΛCDM parameters reconstructed from each likelihood and their combination which are summarized in Table 7.2. We find very consistent results for cosmology between all the likelihoods. For `HillipopE`, we find a ∼2σ tension on both n_s and Ω_b which is not related to the foregrounds, nor to the multipole range or the sky fraction.
Almost all parameters are compatible with the Planck results (Planck Collaboration XIII 2016) within 0.5σ when considering the temperature data only or the full likelihood. Error bars from the Planck public likelihood and HiLLiPOP as presented in this paper are nearly identical. As discussed in details in Couchot et al. (2017c), the difference in τ and A_s can be understood as a preference of the HiLLiPOP likelihood for a lower A_L (Sect. 7.3). The shifted value for A_L comes in

[1] available at camel.in2p3.fr
[2] http://class-code.net

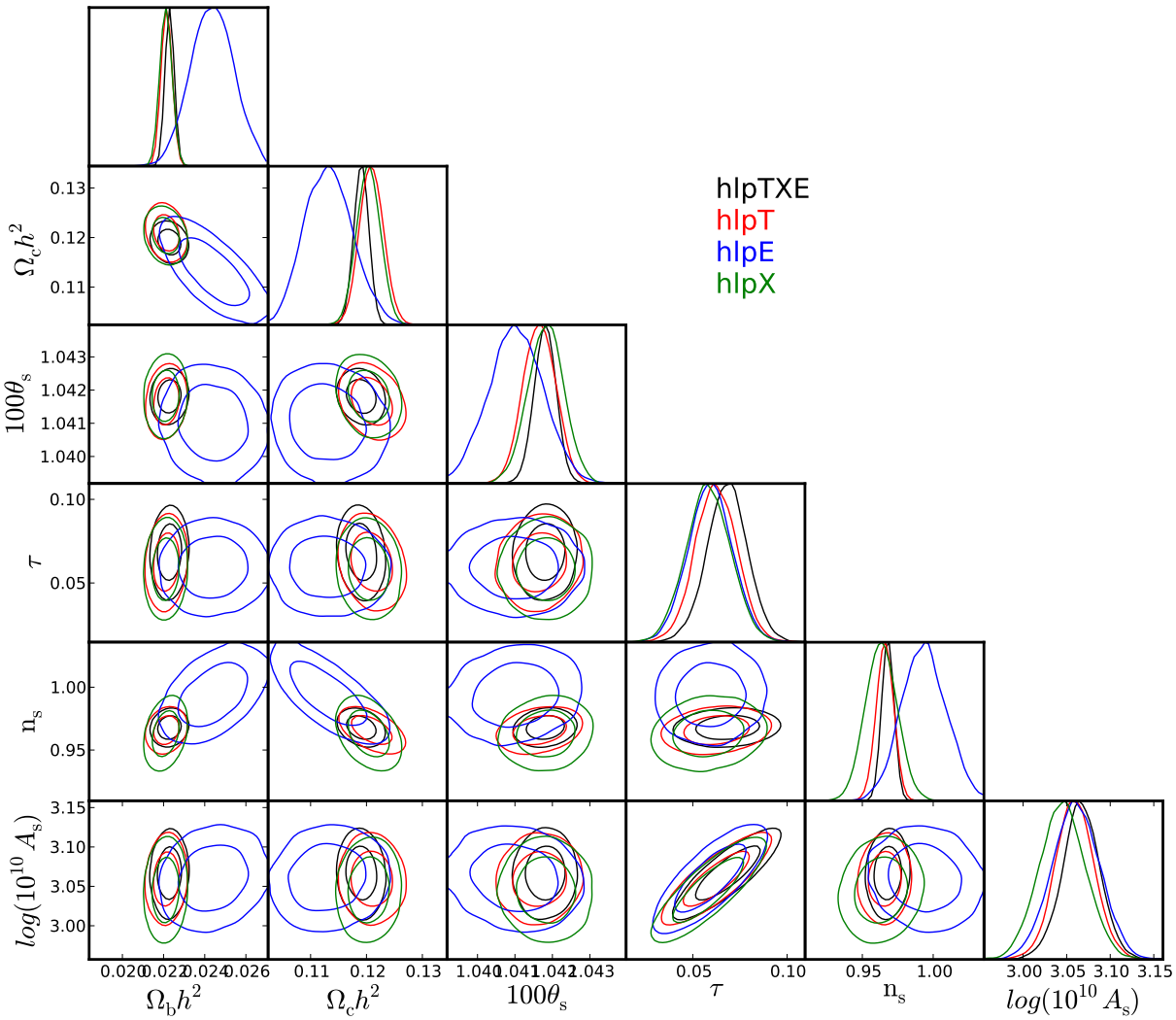

Figure 7.1: Posterior distribution for the 6 cosmological ΛCDM parameters for HiLLiPOP and a prior on τ (0.058±0.012).

Parameters	HillipopT	HillipopX	HillipopE	HillipopTXE
$\Omega_b h^2$	0.02212±0.00021	0.02210±0.00024	0.02440±0.00106	0.02227±0.00014
$\Omega_c h^2$	0.1209±0.0021	0.1204±0.0020	0.1130±0.0043	0.1191±0.0012
$100\theta_s$	1.04164±0.00043	1.04184±0.00047	1.04101±0.00074	1.04179±0.00028
τ	0.062±0.011	0.059±0.012	0.059±0.012	0.067±0.011
n_s	0.9649±0.0058	0.9631±0.0108	0.9939±0.0158	0.9672±0.0037
$log(10^{10} A_s)$	3.058±0.022	3.046±0.027	3.061±0.027	3.065±0.022

Table 7.2: Central value and 68% confidence limit for the base ΛCDM model with HiLLiPOP likelihoods with a prior on τ (0.058±0.012).

both cases from a tension between the high-ℓ and the τ constraint (either from lowTEB or from the prior), the likelihood for HiLLiPOP alone showing almost no constraint on τ when A_L is free.
The results are compatible with those presented in Couchot et al. (2017c), where we used low-ℓ data from Planck-LFI (instead of a tighter prior on τ from the last results of Planck-HFI). We also now impose a model for the point sources frequency spectrum (both radio sources and infra-red sources) which increased the sensitivity in n_s by ∼15%.
HillipopX is almost as sensitive as HillipopT to ΛCDM parameters, despite the fact that the signal-to-noise ratio is lower in the TE spectra. As we show and discuss in Sect. 7.4, this comes from the uncertainties on the foregrounds parameters which increase the width of the HillipopT posteriors. This is also the case for the Hubble parameter H_0 for which we find:

$$H_0 = 67.09\pm0.86 \quad \text{(HillipopT)} \tag{7.1a}$$
$$H_0 = 67.16\pm0.89 \quad \text{(HillipopX)}, \tag{7.1b}$$

compatible with the low value reported by the Planck collaboration (Planck Collaboration XIII 2016). The only parameter which is significantly less constrained by the TE data is n_s. Indeed, while, for a cosmic-variance limited experiment, TT and TE show comparable sensitivity for n_s, the Planck instrumental noise on TE spectra increases the posterior width by a factor almost 2 (Galli et al. 2014). As expected, the results based on the `HillipopE` likelihood are even less accurate.

7.2.2 Instrumental nuisances

In the likelihood function, the calibration uncertainties are modeled using an absolute rescaling $A_{\rm pl}$ and inter-calibration factors c_i. The parameter $A_{\rm pl}$ allows to propagate an overall calibration error at the cross-spectra level (which principally translate into a larger error on the amplitude of the primordial power spectrum A_s). We apply the same calibration factors for temperature and polarisation.
The constraints on inter-calibration coefficients from the Planck CMB data are much weaker than the external priors. Without priors, we found that the coefficients are recovered without any bias in all cases with posterior width of typically 1.5%, 2%, 7% and 5% for `HillipopTXE`, `HillipopT`, `HillipopE`, and `HillipopX`, respectively.

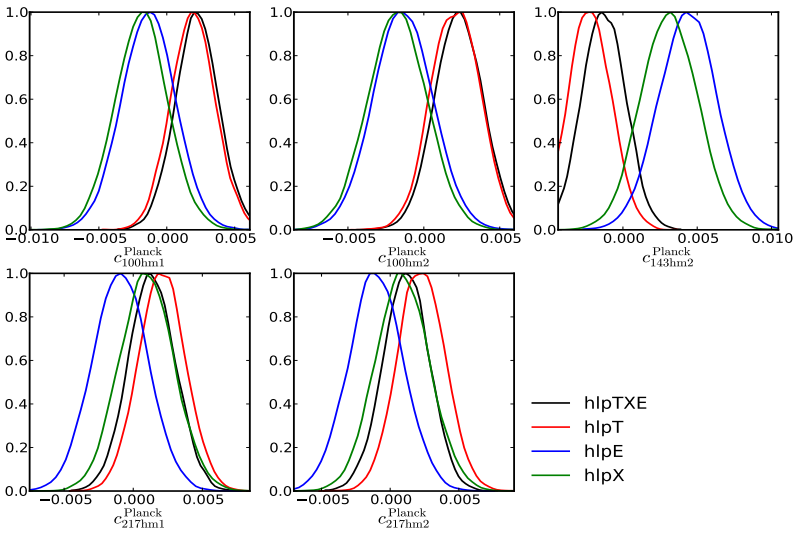

Figure 7.2: Posterior distribution of the 5 inter-calibration parameters for each of the HiLLiPOP likelihood (`HillipopTXE`, `HillipopT`, `HillipopE` and `HillipopX`).

Figure 7.2 shows the posterior distributions for the inter-calibration factors (including external priors described in Sect 6.6). We found a slight tension (less than 2σ) between the calibration factors recovered from temperature and for polarization. The relatively bad $\chi^2_{\rm min}$ value of the full likelihood configuration (Table 7.1) is certainly partially due to this disagreement between calibrations. We tried to take into account the difference between temperature and polarisation calibration. For that, we added, in the polarisation case, additional new parameters ϵ (corresponding to the polarisation efficiency) through the redefinition $c_i \rightarrow c_i(1+\epsilon_i)$ for the polarization maps. We checked the results with the `HillipopX` and `HillipopTXE` likelihoods. The calibrations in temperature are kept fixed and the ϵ_is are left free in the analysis. We did not see any improvement of the $\chi^2_{\rm min}$ for the full likelihood. The level of the calibration shifts is of the order of one per mil. We have checked that it has a negligible impact on both the cosmology and the astrophysical parameters.

7.2.3 Astrophysical results

We recall that the foregrounds in the HiLLiPOP likelihoods are modeled using fixed spectral energy densities (SED) and that, for each emission, the only free parameter is an overall rescaling amplitude (which should be one if the correct SED is used). The compatibility with one for all foreground amplitudes is thus a good test for the consistency of the internal Planck templates. Figure 7.3 shows the posterior distributions for the astrophysical foreground amplitudes. We discuss the results in details in the following sections. We check the stability of the cosmological results with respect to foreground parameters in Sect. 7.4.

dust

The emission of the galactic dust is the dominant residual foreground in the power spectra considered in this analysis.
The recovered amplitudes for each case (and, in parenthesis for the full likelihood) are:

$$A^{TT}_{\rm dust}=0.97\pm0.09 \quad (0.99\pm0.08) \tag{7.2a}$$
$$A^{TE}_{\rm dust}=0.86\pm0.12 \quad (0.80\pm0.11) \tag{7.2b}$$
$$A^{EE}_{\rm dust}=1.14\pm0.13 \quad (1.20\pm0.11) \tag{7.2c}$$

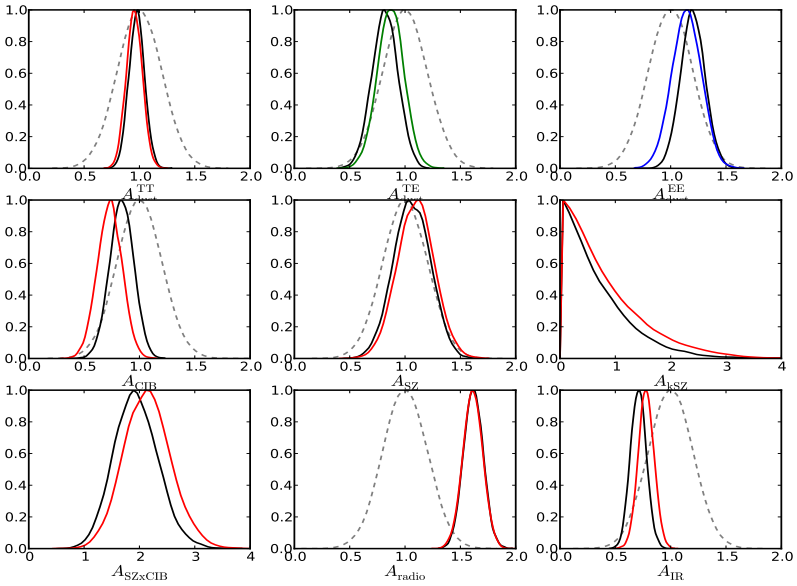

Figure 7.3: Astrophysical foreground amplitude posterior distributions for the HiLLiPOP likelihoods: `HillipopTXE` (*black*), `HillipopT` (*red*), `HillipopE` (*blue*) and `HillipopX` (*green*)). Priors are plotted in grey dashed line.

The dust amplitude in temperature is recovered perfectly. The amplitude for the EE polarisation mode is found slightly high at 1.5σ, while the TE polarisation mode is about 1.5σ low. When using the full HiLLiPOP likelihood, the tension on the dust polarisation modes EE and TE reaches 2σ which is directly related to the small tension on calibration discussed in Sect. 7.2.2.

CIB

The second emission on which Planck TT CMB power-spectra are sensitive is the CIB. The $A_{\rm CIB}$ recovered for `HillipopT` and `HillipopTXE` are respectively

$$A_{\rm CIB}=0.84\pm0.15 \quad (1.01\pm0.13), \tag{7.3}$$

which is perfectly compatible with the astrophysical measurement from Planck for `HillipopTEX` and at 1σ for `HillipopT`.

SZ

Planck data are only mildly sensitive to SZ components. In particular, we have no constraint at all on the amplitude of the kSZ effect ($A_{\rm kSZ}$) and the correlation coefficient between SZ and CIB ($A_{\rm tSZxCIB}$). When using astrophysical foregrounds information, the external prior on $A_{\rm tSZ}$ drives the final posterior:

$$A_{\rm SZ}=1.00\pm0.20 \quad (0.94\pm0.19). \tag{7.4}$$

Point Sources

We find more power in Planck power spectra for the radio sources than expected and a bit less for IR sources:

$$A^{\rm radio}_{\rm PS} = 1.61\pm0.09 \quad (1.62\pm0.09) \tag{7.5a}$$

$$A^{\rm IR}_{\rm PS} = 0.78\pm0.07 \quad (0.71\pm0.07), \tag{7.5b}$$

with no impact on cosmology (see Sect. 7.4). We have identified that the tension comes essentially from the 100 GHz map which dominates the constraints for the radio source amplitude. Table 7.3 shows the results when we fit one amplitude for each cross-spectra and compared to the model expectation.[3] The distribution of the posteriors for the point sources amplitudes are plotted in Fig. 7.4. We find relatively good agreement between the predictions from source counts and the HiLLiPOP results, with the exception of the 100×100 where the measurement differ by up to 4σ with the prediction. This is coherent with the results from the Planck collaboration (discussed in Sect. 4.3 of Planck Collaboration XI 2016). It could be a sign for residual systematics in the data but we recall that an accurate point source modeling is very hard to obtain for a large sky coverage with inhomogeneous noise as such of Planck. This is particularly important for the estimation of the radio sources amplitudes which are sensitive to both catalog completeness and flux cut estimation.

[3]Note that Table 17 in Planck Collaboration XI (2016) have incorrect prediction numbers for radio galaxies

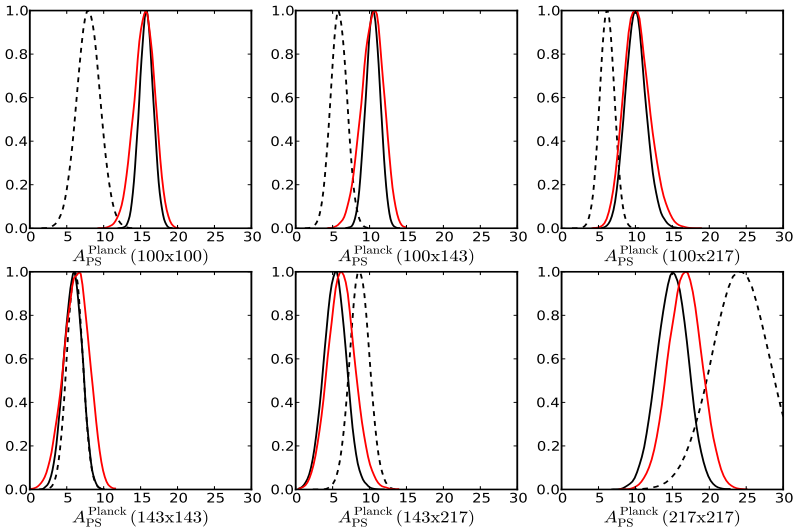

Figure 7.4: Posterior distributions for the six point sources amplitudes for `HillipopTXE` (*black line*) and `HillipopT` (*red line*) compared to model prediction (*dashed line*). Units: $\mathrm{Jy}^2.\mathrm{sr}^{-1}$ (νI_ν=*cte*).

	Radio	IR	Total	`HillipopT`	`HillipopTXE`
100×100	7.8±1.6	0.2±0.0	7.9±1.6	15.5±1.4	15.8±0.9
100×143	5.4±1.1	0.5±0.1	5.8±1.1	10.4±1.5	10.5±1.0
100×217	4.3±0.9	1.9±0.4	6.2±1.0	10.1±1.7	10.0±1.4
143×143	4.8±1.0	1.2±0.2	6.1±1.0	6.3±1.7	5.9±1.2
143×217	3.6±0.8	5.1±1.0	8.7±1.3	6.2±1.8	5.3±1.5
217×217	3.2±0.8	21.0±3.8	24.2±3.8	16.7±2.2	15.0±2.1

Table 7.3: Poisson amplitudes for radio galaxies (model from Tucci et al. 2011) and dusty galaxies (model from Béthermin et al. 2012) compared to HiLLiPOP results. Units: $\mathrm{Jy}^2.\mathrm{sr}^{-1}$ (νI_ν=*cte*).

7.3 $A_{\rm L}$ as a robustness test

As discussed in Couchot et al. (2017c), the measurement of the lensing effect in the angular power spectra of the CMB anisotropies provides a good internal consistency check for high-ℓ likelihoods. The Planck public likelihood shows an $A_{\rm L}$ discrepancy with one by up to 2.6σ.

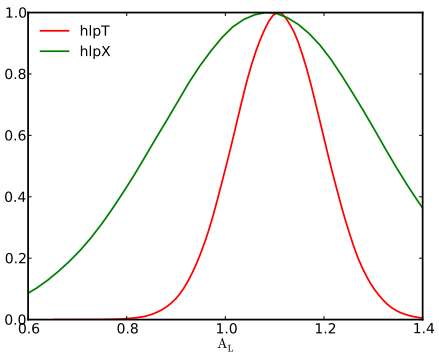

Figure 7.5: Posterior distribution for the $A_{\rm L}$ parameter for the temperature likelihood `HillipopT` (*red line*) and the temperature-polarization likelihood `HillipopX` (*green line*).

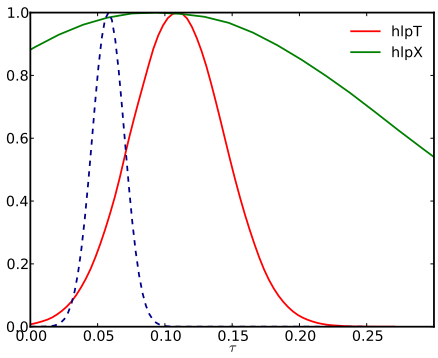

Figure 7.6: Posterior distribution for the reionization optical depth τ for `HillipopT` (*red line*) and `HillipopX` (*green line*) compared to the prior from Planck Collaboration Int. XLVII (2016) used throughout this analysis (*dashed darkblue line*).

With HiLLiPOP and the τ-prior, the best-fits for $A_{\rm L}$ (fig. 7.5) are

$$A_{\rm L} = 1.11\pm0.09 \quad (\texttt{HillipopT} + \tau \text{ prior}) \tag{7.6a}$$
$$A_{\rm L} = 1.08\pm0.21 \quad (\texttt{HillipopX} + \tau \text{ prior}), \tag{7.6b}$$

compatible with the standard expectation. While the relative variation of the theoretical power spectra with $A_{\rm L}$ is more important for TE than for TT, we find a weaker constraint for TE. This illustrates the fact that the noise level in the TE power spectrum from Planck is unable to capture the information from the lensing of the CMB TE at high multipoles.

In Couchot et al. (2017c), we have shown that the PLANCK tension on A_L is directly related to the constraint on τ. Indeed, the τ constraints from the HiLLiPOP likelihoods (Fig. 7.6) are less in tension with the PLANCK low-ℓ likelihoods. The HiLLiPOP only likelihoods give

$$\tau = 0.122\pm0.036 \quad (\texttt{HillipopT}) \tag{7.7a}$$
$$\tau = 0.103\pm0.081 \quad (\texttt{HillipopX}) \tag{7.7b}$$

which is, for HillipopT, at 1.7σ from the HFI low-ℓ analysis τ=0.058±0.012 (Planck Collaboration Int. XLVII 2016). The difference with the τ estimation derived in Couchot et al. (2017c) directly comes from the additional constraints in the point source sector. For HillipopX, the τ distribution is compatible with the PLANCK low-ℓ constraint but the constraint is weaker.
Note that when adding the information from the measurement of the power spectrum of the lensing potential (using the PLANCK lensing likelihood described in Planck Collaboration XV 2016) the constraints on τ from HillipopT and HillipopX become comparable and both compatible with PLANCK-HFI low-ℓ:

$$\tau = 0.077\pm0.028 \quad (\texttt{HillipopT} + \text{lensing}) \tag{7.8a}$$
$$\tau = 0.056\pm0.027 \quad (\texttt{HillipopX} + \text{lensing}). \tag{7.8b}$$

7.4 Foreground robustness: TT v.s. TE

In this section, we investigate the impact of foregrounds on the recovery of the ΛCDM cosmological parameters. We focus on the results from HillipopT and HillipopX.
First, we show in Fig 7.7, the posterior for the parameters with and without external foreground priors. These results demonstrate no impact of the priors on the final results, and suggest a low level of correlation between foreground parameters and cosmological parameters in the likelihood. Indeed, the statistics reconstructed from the MCMC samples (Fig. 7.8) exhibit less than 15% correlation between the two sets of parameters. In the case of temperature, we see strong correlations between the instrumental parameters on one side, and between the astrophysical ones on the other side. This is not the case for HillipopX, which, appart from the cosmological sector, exhibits less than 10% correlation.

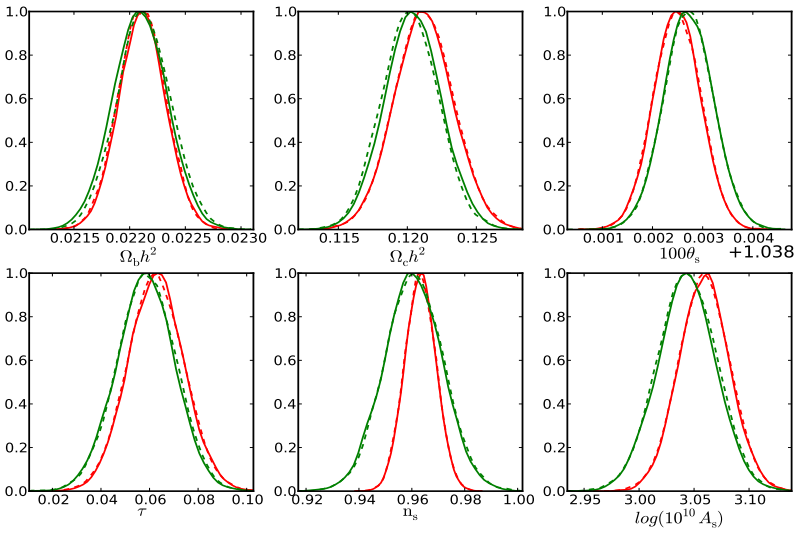

Figure 7.7: Posterior distributions for the six ΛCDM parameters with (*solid lines*) and without (*dashed lines*) astrophysical foregrounds priors in the case of HillipopT (*red*) and HillipopX (*green*).

In a second step, we have estimated the contribution of the foreground parameters to the error budget of the cosmological parameters (Table 7.4). This analysis assesses how much our uncertainties on the nuisance parameters impacts the cosmological error budget. A parameter estimation is performed to assess the full error for each parameter. Then another parameter estimation is performed with the foregrounds parameters fixed to their best-fit values. The confidence intervals recovered in this last case give the "statistical" uncertainties which are essentially driven by noise and cosmic variance (they correspond to the errors on parameters if we knew the nuisance parameters perfectly). Finally the "foreground" error is deduced by quadratically subtracting the "statistical" uncertainty from the total error following what was done in Planck Collaboration XI (2016).
In the temperature case, we see a strong impact of the nuisances on the error of $\Omega_b h^2$ and n_s. The posterior width of the reionization optical depth τ is strongly dominated by the prior so it is marginally affected by foregrounds uncertainties.

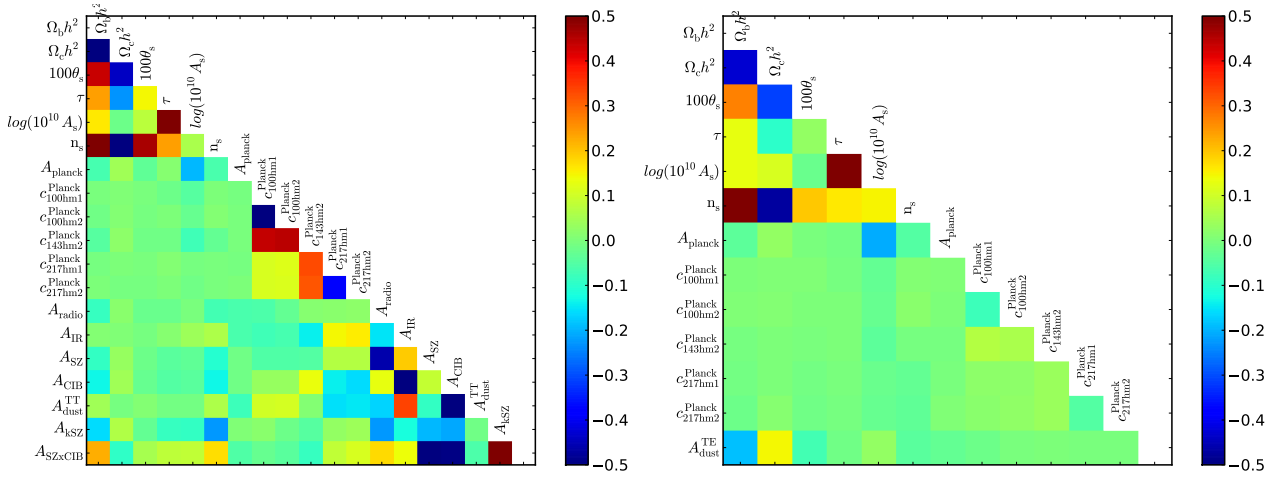

Figure 7.8: Correlation matrix of the likelihood parameters including ΛCDM and nuisance parameters for `HillipopT` (*top*) and `HillipopX` (*bottom*). Color scale is saturated at 50%.

Parameter	Estimate	Error			
		Full	"statistical"	"foreground"	
`HillipopT` parameters					
$\Omega_b h^2$	0.02212	0.00020	0.00018	0.00009	(27%)
$\Omega_c h^2$	0.1210	0.0021	0.0021	0.0003	(3%)
$100\theta_s$	1.04164	0.00043	0.00044	0.00000	(0%)
τ	0.062	0.011	0.011	0.002	(5%)
n_s	0.9649	0.0058	0.0052	0.0025	(24%)
$log(10^{10}A_s)$	3.058	0.022	0.022	0.003	(2%)
`HillipopX` parameters					
$\Omega_b h^2$	0.02209	0.00024	0.00024	0.00004	(3%)
$\Omega_c h^2$	0.1204	0.0020	0.0020	0.0005	(6%)
$100\theta_s$	1.04184	0.00047	0.00047	0.00003	(0%)
τ	0.058	0.012	0.012	0.000	(0%)
n_s	0.9630	0.0111	0.0107	0.0026	(6%)
$log(10^{10}A_s)$	3.046	0.026	0.027	0.000	(0%)

Table 7.4: Errors on cosmological parameters within the ΛCDM model for `HillipopT` and `HillipopX`. The full error is splitted between "statistical" and "foreground" errors. Errors are given at 68 % C.L.

Finally, even if the statistical uncertainty is larger in the case of TE, foregrounds uncertainties are negligible in the total error budget which makes them competitive with TT (except for n_s).
More important than increasing the error budget, nuisance uncertainties can also bias the cosmological parameters. Figure 7.9 shows the results on the ΛCDM parameters for `HillipopT` and `HillipopX` when nuisances are fixed either to their best-fit or to the value expected by the astrophysical constraints (i.e. scaling parameters fixed to 1). This corresponds to the extreme case for the potential bias, where we supposed an exact knowledge of the characteristics of the complex foregrounds spatial distribution and spectra. The attempt here is to give an idea of the impact of foreground uncertainties on cosmological parameters. Once again, we see a stronger impact on `HillipopT` than on `HillipopX`. In temperature, almost all parameters are shifted when changing the nuisance values, the strongest effect being for $\Omega_b h^2$, $\Omega_c h^2$, and n_s. On the contrary, we cannot see any impact of the $A^{TE}_{\rm dust}$ parameter shift even if its best-fit value is at 0.86 compared to 1.

7.5 Discussion

With the currently available CMB measurements, the sensitivity to ΛCDM cosmological parameters is dominated by the Planck data in the ℓ-range typically below ℓ=2000 both in TT and TE. For TE, adding higher multipoles coming from the measurements of the South Pole Telescope (Crites et al. 2015) or the Atacama Cosmology Telescope (Naess et al. 2014), we find almost identical results on ΛCDM cosmological parameters without any reduction of parameter uncertainties. This is different from the temperature data for which high-resolution experiments help reducing the uncertainty on foreground parameters which indirectly reduces the posterior width for cosmological parameters through their correlation (Couchot et al. 2017c). On the low-ℓ side, measurements of TE at $\ell < 20$ give information about the reionization optical depth τ (although not equivalent to the low-ℓ from EE) and a longer lever arm for n_s.
We checked the results of the temperature-polarization cross-correlation likelihood on some basic extensions to the ΛCDM

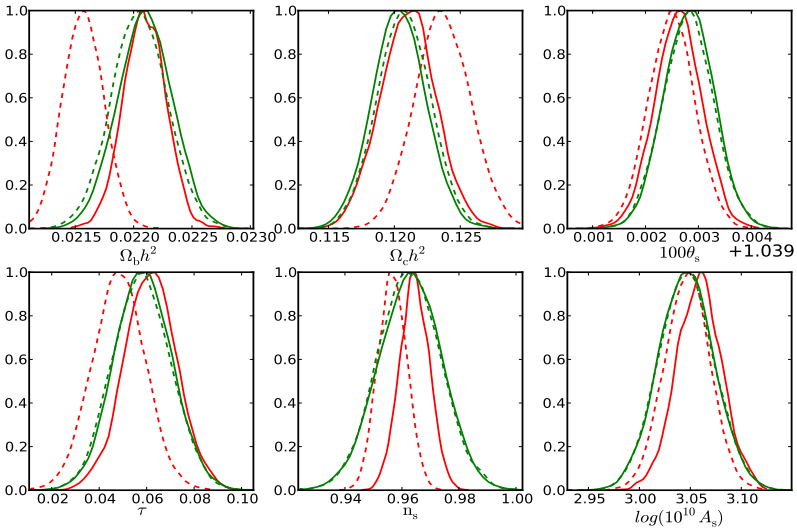

Figure 7.9: Posterior distribution for the cosmological parameters when foregrounds are fixed either to their bestfit value (*solid lines*) or to the expected astrophysical value (*dashed lines*) for `HillipopT` (*red*) and `HillipopX` (*green*).

model: essentially A_L, N_{eff} and $\sum m_\nu$. Given Planck sensitivity, we do not find any competitive constraints compared to the temperature likelihood. For exemple, we find an effective number of relativistic species N_{eff}=2.45±0.45 for `HillipopX` compared to N_{eff}=2.95±0.32 for `HillipopT`. Adding data from high-resolution experiments, we find N_{eff}=2.84±0.43, which does not help reducing the error down to the level of temperature data.
We combine CMB TE data with complementary information from the late time evolution of the Universe geometry, coming from the Baryon Acoustic Oscillations scale evolution (Alam et al. 2016) and the SNIa magnitude-redshift measurements (Betoule et al. 2014). We find very compatible results with a significantly better accuracy only on $\Omega_c h^2$.

7.6 Conclusion

We found results on the ΛCDM cosmological parameters consistent between the different likelihoods (`HillipopT`, `HillipopX`, `HillipopE`). The cosmological constraints from this work are directly comparable to the Planck 2015 cosmological analysis (Planck Collaboration XIII 2016), despite the differences in the foreground modeling adopted in HiLLiPOP. Both instrumental and astrophysical nuisance parameters are compatible with expectations, with the exception of the point source amplitudes in temperature for which we found a small tension with the astrophysical expectations. This tension may be the sign of potential systematic residuals in Planck data and/or uncertainty in the foreground model in temperature (especially on the dust SED or the various ℓ-shape of the foreground templates).
We investigated the robustness of the results with respect to the foreground and nuisance parameters. In particular, we demonstrated the impact of foreground uncertainties on the temperature power spectrum likelihood. We compared to the results from the likelihood based on temperature-polarization cross-correlation which involves less foreground residuals but is less sensitive. We found that foreground uncertainties have a stronger impact on TT than on TE with comparable final errors (except for n_s). Moreover, the `HillipopX` likelihood function does include less nuisance parameters (only 7 compared to 13 for `HillipopT`) and shows less correlation in the nuisance/foregrounds sectors which allows in practice much faster sampling.
This work illustrates the fact that TE spectra provides estimation of the cosmological parameters as accurate than TT while being more robust with respect to foreground contaminations. The results from Planck in polarization are still limited by instrumental noise in TE but, as suggested in Galli et al. (2014), future experiments only limited by cosmic variance over a wider range of multipoles will be able to constrain cosmology with TE even better than with TT.

This is part of a set of three scientific papers (Couchot et al. 2017c,b,a) produced by the Planck group at LAL.

Bibliography

Alam, S., Ata, M., Bailey, S., et al. 2016, ArXiv e-prints [arXiv:1607.03155]
Béthermin, M., Daddi, E., Magdis, G., et al. 2012, ApJ, 757, L23
Betoule, M., Kessler, R., Guy, J., et al. 2014, A&A, 568, A22
Couchot, F., Henrot-Versillé, S., Perdereau, O., et al. 2017a, ArXiv e-prints [arXiv:1703.10829]
Couchot, F., Henrot-Versillé, S., Perdereau, O., et al. 2017b, A&A, 602, A41
Couchot, F., Henrot-Versillé, S., Perdereau, O., et al. 2017c, A&A, 597, A126
Crites, A. T., Henning, J. W., Ade, P. A. R., et al. 2015, ApJ, 805, 36
Galli, S., Benabed, K., Bouchet, F., et al. 2014, Phys. Rev. D, 90, 063504
Naess, S., Hasselfield, M., McMahon, J., et al. 2014, J. Cosmology Astropart. Phys., 10, 007
Planck Collaboration XV. 2014, A&A, 571, A15
Planck Collaboration XI. 2016, A&A, 594, A11
Planck Collaboration XIII. 2016, A&A, 594, A13
Planck Collaboration XV. 2016, A&A, 594, A15
Planck Collaboration Int. XLVII. 2016, A&A, 596, A108
Tucci, M., Toffolatti, L., de Zotti, G., & Martínez-González, E. 2011, A&A, 533, 57

Chapter 8

Relieving tensions related to $A_{\rm L}$

extracted from Couchot et al. (2017c)

"Relieving tensions related to the lensing of the cosmic microwave background temperature power spectra"

Since the first release of Planck data, the CMB anisotropie likelihood function suffer from an internal "tension" related to the impact of gravitational lensing on the primordial CMB spectra. Indeed, the effect of gravitational lensing on spectra seems to be stronger than what ΛCDM *predict. Planck collaboration interpreted this small (less than 2.6σ) effect as a statistical flux. At LAL, we have studied more in details this tension and in particular had a look on foreground and systematic residuals that could affect the data. After we tried to convince the Planck consortium about our work, it have not received the agreement from the Planck Science Team and we decided to published it, after the Planck 2015 release, in Couchot et al. (2017c). It is copied in this chapter.*

The angular power spectra of the cosmic microwave background (CMB) temperature anisotropies reconstructed from Planck data seem to present 'too much' gravitational lensing distortion. This is quantified by the control parameter $A_{\rm L}$ that should be compatible with unity for a standard cosmology. With the `class` Boltzmann solver and the profile-likelihood method, for this parameter we measure a 2.6σ shift from 1 using the Planck public likelihoods. We show that, owing to strong correlations with the reionization optical depth τ and the primordial perturbation amplitude $A_{\rm s}$, a ~2σ tension on τ also appears between the results obtained with the low ($\ell \lesssim 30$) and high ($30 < \ell \lesssim 2500$) multipoles likelihoods. With `Hillipop`, another high-ℓ likelihood built from Planck data, this difference is lowered to 1.3σ. In this case, the $A_{\rm L}$ value is still in disagreement with unity by 2.2σ, suggesting a non-trivial effect of the correlations between cosmological and nuisance parameters.
To better constrain the nuisance foregrounds parameters, we include the VHL measurements of the Atacama Cosmology Telescope (ACT) and South Pole Telescope (SPT) experiments and obtain $A_{\rm L}$=1.03 ± 0.08. The combined `Hillipop`+ACT+SPT likelihood estimate of the optical depth is τ=0.052±0.035, which is now fully compatible with the low-ℓ likelihood determination. After showing the robustness of our results with various combinations, we investigate the reasons for this improvement that results from a better determination of the whole set of foregrounds parameters. We finally provide estimates of the ΛCDM parameters with our combined CMB data likelihood.

8.1 Introduction

The $A_{\rm L}$ control parameter attempts to measure the degree of lensing of the cosmic microwave background (CMB) power spectra. From a set of cosmological parameters (Ω), a Boltzmann solver, such as `class` (Blas et al. 2011) or `camb` (Lewis et al. 2000), computes the angular power spectra of the temperature/polarization anisotropies $C_\ell(\Omega)$ and of the CMB lensing potential $C_\ell^\Phi(\Omega)$. The latter is then used to compute the distortion of the CMB spectra by the gravitational lensing (Blanchard & Schneider 1987), which redistributes the power across multipoles while preserving the brightness in a non-trivial way (e.g Lewis & Challinor 2006): $\{C_\ell(\Omega), C_\ell^\Phi(\Omega)\} \rightarrow \tilde{C}_\ell(\Omega)$.
As originally proposed in Calabrese et al. (2008), a phenomenological parameter, $A_{\rm L}$, that re-scales the lensing potential, is introduced. This modifies the standard scheme into : $\{C_\ell(\Omega), A_{\rm L} \cdot C_\ell^\Phi(\Omega)\} \rightarrow \tilde{C}_\ell(\Omega, A_{\rm L})$. Sampling the likelihood, with this parameter left free, gives access to two interesting pieces of information:

1. from the A_L posterior distribution, one can check the consistency of the data with the model; it should be compatible with 1.0 for a standard cosmology.
2. by marginalizing over A_L, one can study the impact of neglecting (to first-order) the lensing information contained in the CMB spectra.

Since its first release, the *Planck* Collaboration reports a value of the A_L parameter that is discrepant with one by more than 2σ. The full-mission result, based on both a high and low-ℓ likelihood (Planck Collaboration XIII 2016, hereafter PCP15), is

$$A_L=1.22\pm0.10 \quad (\text{Planck TT+lowP}) \tag{8.1}$$

(all quoted errors are 68% CL intervals). As shown later, a profile likelihood analysis, as the one in Planck Collaboration Int. XVI (2014), rather points to a 2.6σ discrepancy.
This 'tension' may indicate a problem either on the model or the data side. The only solution for the model is to modify the computation of the geodesic deflection, i.e. to modify standard GR (Hu & Raveri 2015; Di Valentino et al. 2016). For the data, since Planck maps undergo a complicated treatment (for an overview see Planck Collaboration I 2016), one cannot exclude small residual systematic effects that could impact the details of the likelihood function in a different way from one implementation to the other.
The anomalously high A_L value directly affects the measurement of two ΛCDM parameters, the reionization optical depth τ and the primordial scalar perturbations amplitude A_s. Indeed, in the high-ℓ regime, only the $\mathcal{A}_T \equiv A_s e^{-2\tau}$ combination is constrained by the temperature power spectra amplitude. However this degeneracy is broken by the lensing distortion of the CMB anisotropies since $C_\ell^\Phi \propto A_s$ (more perturbations induce more lensing) so that both A_s and τ finally get constrained.
The aim of this work is twofold. First, to clarify the connection between the A_L tension with unity and the one that also appears on τ between the Planck public high and low-ℓ likelihoods, and also to show that this effect may be related to the details of the nuisance parametrization in the likelihoods. By using `Hillipop`, a high-ℓ likelihood that is built from Planck data, and better constraining the astrophysical foregrounds and the high-ℓ part of the CMB spectrum with the high-angular resolution data from ACT and SPT, we show that one can obtain a more self-consistent picture of the ΛCDM parameters. Section 8.2 provides an in-depth discussion about A_L using the Planck baseline likelihoods, `Plik` and `lowTEB`, and makes the link with the determination of τ explicit. Section 8.3 then recalls the main differences between `Plik` and `Hillipop` and discusses the first results with the latter. Then Sect. 8.4 describes how the inclusion of the ACT and SPT data was performed and, after various checks, discusses how their inclusion impacts the `Hillipop` results. Finally Sect. 8.5 discusses the results on the ΛCDM parameters using `Hillipop` in combination with other likelihoods.

8.2 The *Planck* A_L tension (and related parameters)

8.2.1 *Planck* likelihoods

Planck's baseline uses two different likelihood codes addressing different multipole ranges (see Planck Collaboration XI 2016, hereafter Like15):

1. the high-ℓ likelihood (`Plik`) is a Gaussian likelihood that acts in the multipole range $\ell\in[30,2500]$. Data consist of a collection of angular power spectra that are derived from cross-correlated Planck 100,143, and 217 GHz high frequency maps. For the results in this paper, we only use the temperature likelihood.
2. the low-ℓ likelihood (`lowTEB`) is a pixel-based likelihood that essentially relyies on the Planck low frequency instrument 70 GHz maps for polarization and on a component-separated map using all Planck frequencies for temperature. It acts in the $\ell\in[2,29]$ range.

In the Like15 terminology, 'Planck TT' refers to the combination of both the high and the low-ℓ temperature likelihoods. In this case, only the TT component of `lowTEB` is used. The 'Planck TT+`lowP`' notation combines `Plik` to the full `lowTEB` likelihood, which we label explicitly in this paper as `Plik+lowTEB`.
In the following, we will make use of the publicly available `Plik` likelihood code (`plik_dx11dr2_HM_v18_TT.clik`)[1] with the Gaussian priors on nuisance parameters suggested by the Planck collaboration[2], where the information on foregrounds from the ACT and SPT data is propagated by a single SZ prior (PCP15, Sect. 2.3.1).

8.2.2 Boltzmann solver

The results derived in this paper make use of the Boltzmann equations solver `class`[3] while *Planck*'s published results were derived using `camb`[4]. Both softwares have been compared previously (Lesgourgues 2011) and have produced spectra in excellent agreement when using their respective high precision settings. More recently, it was noticed in PCP15 that sampling from any of them gives very compatible results on ΛCDM cosmological parameters. The precise estimate of

[1] available in the Planck Legacy Archive (PLA): http://www.cosmos.esa.int/web/planck/pla
[2] Explanatory Supplement: http://wiki.cosmos.esa.int/planckpla2015
[3] CLASS: http://class-code.net
[4] CAMB: http://camb.info

the A_L parameter is more challenging since one is dealing with sub-percent effects on the spectra and thia requires extra care about differences between both softwares.
For this purpose, we sampled the `Plik+lowTEB` likelihoods in the ΛCDM+A_L model using `class v2.3.2` and obtain results almost identical to the published ones. In particular we measure

$$A_L=1.24\pm0.10 \quad (\texttt{Plik+lowTEB}, \texttt{class}/\text{MCMC}). \tag{8.2}$$

The tiny difference with respect to Eq. 8.1 can be traced down to a $O(1(\mu K)^2)$ difference on the high-ℓ part of the TT spectra (see Appendix A in Couchot et al. 2017c), but we consider that this general agreement is sufficient to perform reliable estimations. All further results will be derived consistently using `class`.

8.2.3 Profile likelihoods

In this paper, we also often make use of a statistical methodology based on profile-likelihoods for reasons that will be clearer in Sect. 8.2.5. For a given parameter θ, we perform several multi-dimensional minimizations of the $\chi^2 \equiv -2\ln\mathcal{L}$ function. Each time θ is fixed to a given $\theta(i)$ value, a minimization is performed with respect to all the other parameters, and the $\chi^2_{\rm min}(i)$ value is kept. The curve interpolated through the $\{\theta(i),\chi^2_{\rm min}(i)\}$ points and offset to 0, is known as the θ profile-likelihood: $\Delta\chi^2(\theta)$. We note that from the very construction procedure, the solution at the minimum of the profile always coincides with the complete best-fit solution, i.e the maximum likelihood estimate (MLE) of all the parameters. A genuine 68% CL interval is obtained by thresholding the profile at one even in non-Gaussian cases (e.g., James 2007).
This statistical method, an alternative to Monte-Carlo Markov Chain (MCMC) sampling, was discussed in Planck Collaboration Int. XVI (2014) and also used in Like15. Building a smooth profile from Planck data is computationally challenging since this approach requires an extreme precision on the $\chi^2_{\rm min}$ solution, typically better than 0.1 for values around 10^4. This goal can be achieved using the `Minuit` software[5] together with an increase of the `class` precision parameters.
This procedure leads to a so-called confidence interval (e.g., James 2007). In the frequentist approach, this represents a statement on the data: when repeating the experiment many times, the probability for the reconstructed interval to cover the true value is 68%. The Bayesian approach, as implemented through a MCMC method, leads to what is generally referred to as a 'credible interval' derived from the probability density function of the true value. In most cases (in particular Gaussian) both intervals are very similar. However, in some cases (typically so-called banana-shaped 2D posteriors), these intervals may differ significantly (Porter 1996). In this case, the mode (or mean) of the posterior distribution does not necessarily match the best fit solution and the existence of a difference between both values indicates what is referred to as likelihood volume effects. In this paper, we will mainly focus on the details of the region around the maximum likelihood and x will thus use the profile-likelihood method consistently.

8.2.4 A_L revisited

We first build the profile-likelihood for A_L (Fig. 8.1) and measure

$$A_L=1.26^{+0.11}_{-0.10} \quad (\texttt{Plik+lowTEB}, \texttt{class}/\text{profile}). \tag{8.3}$$

The shift with respect to Eq. 8.2 quantifies the size of the volume effects in the MCMC projection. It is of the same order of magnitude as the `camb`→`class` transition seen in Sect. 8.2.2. Using high-precision settings, we therefore find A_L at 2.6σ from 1.0.
Figure 8.1 also shows that the `Plik`-alone likelihood (in grey) gives

$$A_L=1.04^{+0.20}_{-0.10} \quad (\texttt{Plik}, \texttt{class}/\text{profile}), \tag{8.4}$$

which is compatible with 1.0. This difference from the Planck baseline result (Eq. 8.3) seems to come from a tension between the low and high-ℓ likelihoods. Moreover, using a prior of the kind $\tau=0.07\pm0.02$ (as in Like15) leads to $A_L=1.16\pm0.09$, which goes in the same direction as `Plik+lowTEB`. This connection with τ will be discussed in the following section.

8.2.5 High- vs. low-ℓ likelihood results on τ and A_s

We further investigate the high vs. low-ℓ likelihood tensions from the point of view of two other parameters that are strongly correlated to A_L: the reionization optical depth τ and the scalar perturbation amplitude A_s.
Figure 8.2 shows, in black, the τ profile-likelihood reconstructed with `Plik` only, which gives

$$\tau=0.172^{+0.038}_{-0.042} \quad (\texttt{Plik}). \tag{8.5}$$

This is higher than the maximum of the posterior reported in Like15 (Fig. 45) that is around 0.14 and is partly due to a volume effect (Sect. 8.2.3) and partly because of the `class`/`camb` difference highlighted in Appendix A of Couchot et al.

[5] http://seal.web.cern.ch/seal/work-packages/mathlibs/minuit/index.html

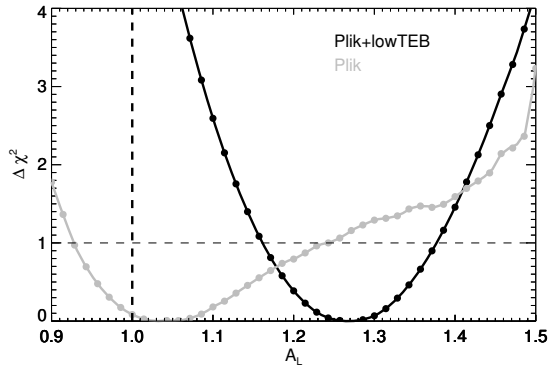

Figure 8.1: Profile-likelihoods of the A_L parameter reconstructed from the Plik high-ℓ likelihood alone (in grey) and when adding the lowTEB one (in black). The vertical dashed line recalls the expected ΛCDM value.

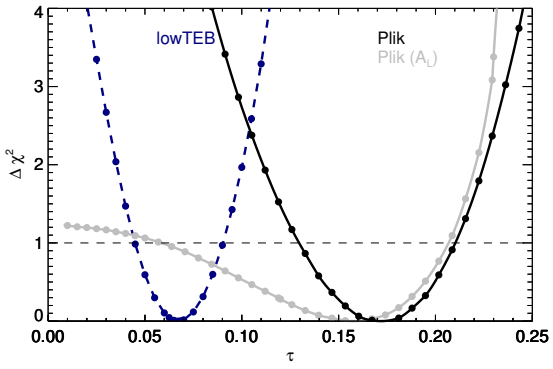

Figure 8.2: High vs. low-ℓ Planck likelihood constraints on τ. The high-ℓ result is obtained with Plik (only) and is shown in black while the low-ℓ one is in dashed blue. Both are obtained within the ΛCDM model. The grey profile shows the result for Plik when A_L is left free in the fits.

(2017c). Using consistently class and the same methodology, our result is 2.2σ away from the τ determination with the lowTEB likelihood for which the profile-likelihood gives the same results as the MCMC marginalization (Like15):

$$\tau=0.067^{+0.023}_{-0.021} \quad (\texttt{lowTEB}), \tag{8.6}$$

represented as a blue line on Fig. 8.2.
Without fixing A_L to 1 (grey curve on Fig. 8.2) the constraint on τ is much weaker, which illustrates the fact that the lensing of the CMB anisotropies in the high-ℓ likelihood is the main contributor to the τ measurement. Some constraining power still remains in particular for large τ values: this is due to the fact that the degeneracy between A_s and τ is broken for large τ when the reionisation bump at low ℓ enters the multipole range of Plik (ℓ>30) (see Hu & White 1997).
The discrepancy highlighted in Fig. 8.2 is directly related to the A_L problem (Fig. 8.1), but is simpler to study. The high-ℓ likelihood requires a large τ value that is in tension with the low-ℓ-based result. In the A_L test (Fig. 8.1) one combines both likelihoods.lowTEB pulls τ down. To match the spectra amplitude ($\mathcal{A}_T$), the high-ℓ likelihood pulls A_s down. Then A_L, being fully anti-correlated to A_s (since $C_\ell^\Phi \propto A_L A_s$), shifts to adjust the lensed model to the data again.
Because of the $\mathcal{A}_T$ degeneracy, the Plik-only estimate of A_s is also expected to be high. Indeed from a similar profile-likelihood analysis we obtain

$$\ln(10^{10}A_s)=3.270^{+0.058}_{-0.078} \quad (\texttt{Plik}), \tag{8.7}$$

again discrepant by more than 2σ with the results from Plik+lowTEB, 3.089±0.036 (PCP15).
In summary, the Plik high-ℓ likelihood alone converges to a consistent solution, $A_L \simeq 1$, but with large τ and A_s values. Constraining τ down by adding the lowTEB likelihood (or a low prior) is compensated in the fits by increasing A_L to match the data. To investigate the stability of those results, we will now use another *Planck* high-ℓ likelihoods.

8.3 The Hillipop likelihood

8.3.1 Description

Hillipop is one of the Planck high-ℓ likelihoods developed for the 2015 data release and is shorty described in Like15. Similarly to Plik, it is a Gaussian likelihood based on cross-spectra from the HFI 100, 143, and 217 GHz maps. The estimate of cross-spectra on data is performed using Xpol, a generalization of the Xspec algorithm (Tristram et al. 2005) to polarization. Figure 8.3 shows the combined TT spectrum with respect to the best-fit model that will be deepened later on.
The differences with Plik were mentioned in Like15. The most significant are:

- we use all the 15 half-mission cross-spectra built from the 100, 143, and 217 GHz maps while Plik uses only five of them;
- we apply inter-calibration coefficients at the map level, resulting in five free parameters (one is fixed) while Plik uses two at the spectrum level;
- we use point-sources masks that were obtained from a refined procedure that extracts Galactic compact structures;
- as a result, our galactic dust component follows closely and is parametrized by the power law discussed in Planck Collaboration Int. XXX (2016);

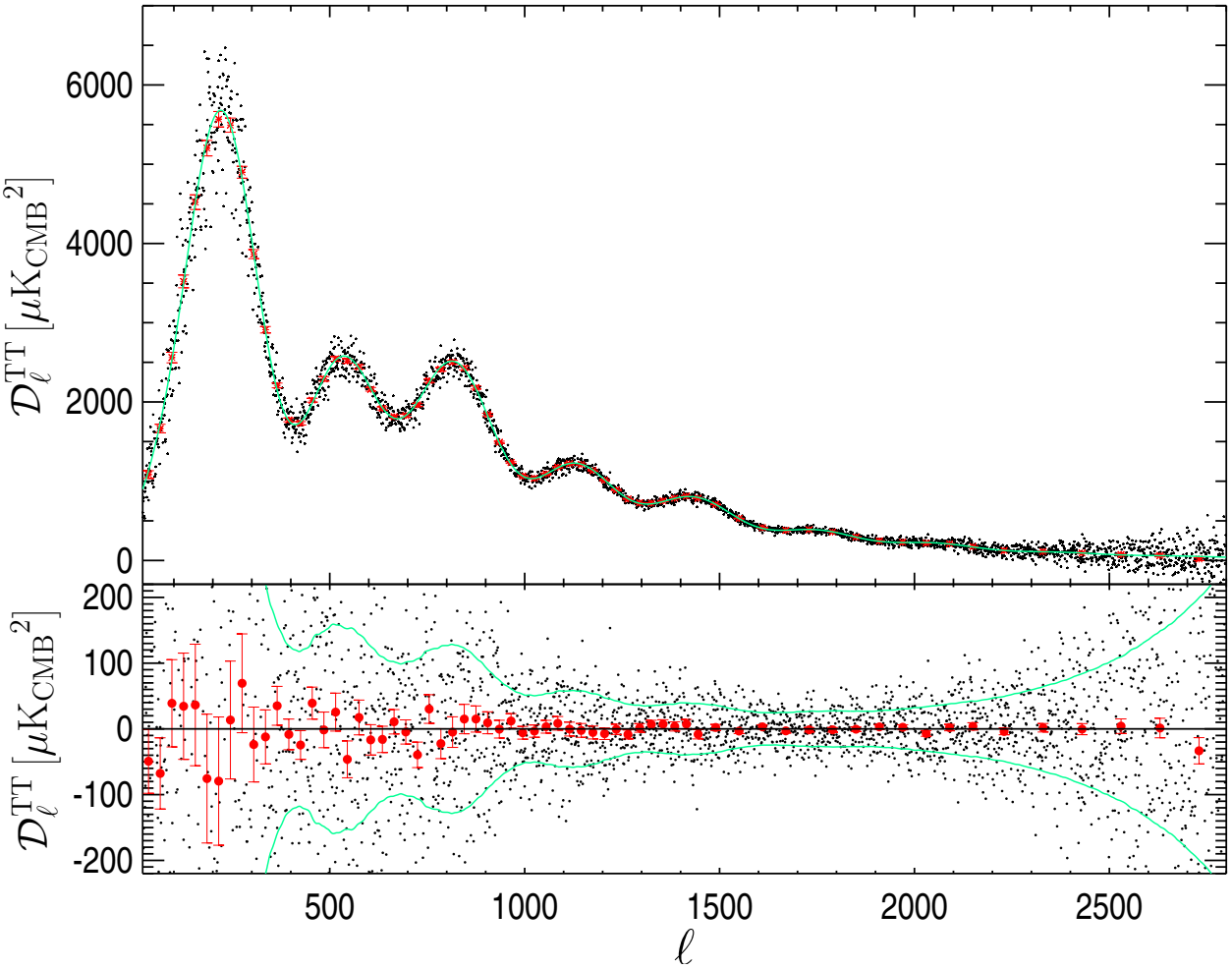

Figure 8.3: `Hillipop` foreground-subtracted combined power-spectrum ($\mathcal{D}_\ell=\ell(\ell+1)C_\ell/2\pi$) at each multipole (black points) and binned (red points) with respect to the best-fit model. The bottom plot shows the residuals. The green line shows the standard deviation as estimated from the covariance matrix.

- we use foreground templates derived from Planck Collaboration XXX (2014) for the CIB, and Planck Collaboration XXII (2016) for the SZ;
- we use all multipole values (i.e., do not bin the spectra).

Using `Hillipop` leads to ΛCDM estimates that are very compatible with the other Planck ones but on A_s and τ (Like15, Sect. 4.2). Using a prior on τ of 0.07±0.02, we obtain with `Hillipop` τ=0.075±0.019, while `Plik` gives a higher value τ=0.085±0.018 (Like15). Given the relation between τ and A_L discussed in Sect. 8.2.5, we can therefore expect different results on A_L.

8.3.2 Results

The profile-likelihoods of A_L derived from `Hillipop` with and without `lowTEB` is shown in Fig. 8.4. The `Hillipop`-alone profile is minimum near A_L=1.30 but is very broad : a 68% CL interval goes from .96 up to 1.42. We therefore conclude that `Hillipop` alone does not give a strict constraint on A_L. In combination with `lowTEB`, using the same procedure as described in Sect. 8.2.4, we obtain

$$A_L=1.22^{+0.11}_{-0.10} \quad (\texttt{Hillipop+lowTEB}). \tag{8.8}$$

This is slightly lower than the result obtained with `Plik` (Eq. 8.3) but still discrepant with one by about 2σ.
Within the ΛCDM model, Fig. 8.5 compares `Hillipop` vs. `lowTEB` results on τ. The `Hillipop` profile on τ gives

$$\tau=0.134^{+0.038}_{-0.048} \quad (\texttt{Hillipop}). \tag{8.9}$$

This is lower than the `Plik` result with similar error bars (Eq. 8.5) and lies within 1.3σ of the low-ℓ measurement (Eq. 8.6). In the ΛCDM+A_L case, `Hillipop` only gives an upper limit. The difference with `Plik` τ profile (Fig. 8.2) is the sign of different correlations between A_L and τ in these likelihoods.

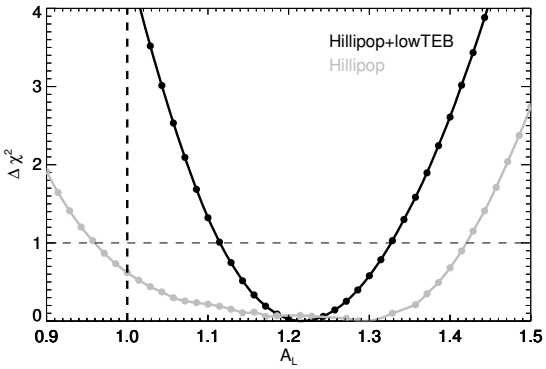

Figure 8.4: Profile-likelihoods of the A_L parameter reconstructed from the `Hillipop` likelihood alone (in grey) and when adding `lowTEB` (in black). The vertical dashed line recalls the expected ΛCDM value.

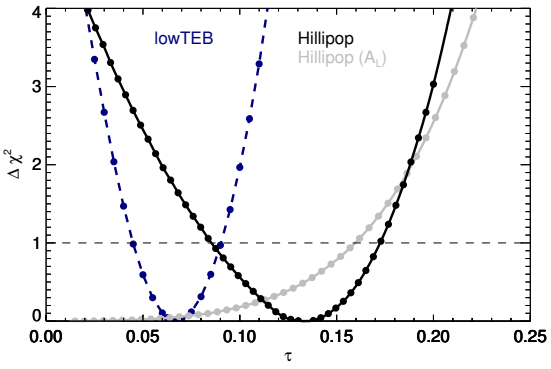

Figure 8.5: Profile-likelihoods of the τ parameter using only the high-ℓ `Hillipop` likelihood: ΛCDM+A_L free in the fits (in grey) and ΛCDM with fixed A_L=1 (in black).

One of the difference between the two likelihoods is in the definition of the foreground models. Moreover, with Planck data only, the accuracy on the foreground parameters is weak (especially for SZ and CIB amplitudes). In the next section, we will use the VHL datasets. This both adds constraints on lensing through the high multipoles and better determines the foregrounds parameters and possibly modifies the non-trivial correlations between nuisance and cosmological parameters.

8.4 Adding VHL data to constrain the foregrounds

8.4.1 Datasets

Atacama Cosmology Telescope. We use the final ACT temperature power spectra presented in Das et al. (2014). These are 148×148, 148×218, and 218×218 power spectra built from observations performed on two different sky areas (south and equatorial) and during several seasons, for multipoles between 1000 and 10000 (for 148×148), and 1500 to 10000 otherwise.

South Pole Telescope. We use two distinct datasets from SPT.
The higher ℓ part, dubbed `SPT_high`, uses results, described in Reichardt et al. (2012), from observations at 95, 150, and 220 GHz from the SPT-SZ survey. Their cross-spectra cover the ℓ range between 2000 and 10000. These measurements were calibrated using WMAP 7yr data. A more recent analysis from the complete ~2500 deg^2 area of the SPT-SZ survey is presented in George et al. (2015), dubbed `SPT_high2014` hereafter. In this later release, cross spectra cover a somewhat broader ℓ range, between 2000 and 13000. Both sets of cross spectra are however quite similar, but the later comes with a covariance matrix that includes calibration uncertainties. Its use makes our work harder since it was calibrated on the Planck 2013 data, which in turn had a calibration offset of 1% (at the map level) with respect to the Planck 2015 spectra. We thus prefer to use Reichardt et al. (2012) dataset as a baseline in our analyses, with free calibration parameters to match other datasets. We have checked that all results presented in this paper are stable when switching to George et al. (2015), in which case we have to set strict priors on recalibration parameters owing to the form of the associated covariance matrix.
We also include the Story et al. (2013) dataset, dubbed `SPT_low`, consisting of a 150 GHz power spectrum which ranges from ℓ=650 to 3000. Some concerns were raised in Planck Collaboration XVI (2014) about the compatibility of this dataset with Planck data. The tension was actually traced to be with the *WMAP*+SPT cosmology and the Planck and `SPT_low` power spectra were found to be broadly consistent with each other (Planck Collaboration XVI 2014). As will be shown later, we do not see any sign of tension between the Planck 2015 data and the `SPT_low` dataset, nor any reason to exclude it.

8.4.2 Foregrounds modelling

For the VHL astrophysical foregrounds, we chose to use a model as coherent as possible with what has been set-up for `Hillipop`, i.e., the same templates for tSZ, kSZ, CIB, and tSZ×CIB. Since they have been computed for the Planck frequencies and bandpasses, we have to extrapolate them to the ACT and SPT respective effective frequencies and bandpasses. For tSZ, we scale the template with the usual $f_\nu = x\coth x/2 - 4$ function (where $x = h\nu/k_B T_{CMB}$), using the effective frequencies for the SZ spectral distribution given in Dunkley et al. (2013). For CIB and tSZ×CIB, we start from templates in $Jy^2.sr^{-1}$ in the IRAS convention ($\nu I(\nu)$=cste spectrum) for Planck effective frequencies and bandpasses. For CIB, we use the conversion factors from Planck to the ACT/SPT effective frequencies and bandpasses, assuming the Béthermin

et al. (2012) SED for the CIB combined with unit conversion factors to K_{CMB}, for the ACT and SPT bandpasses (Lagache 2014). These factors are given in Table 8.1.

Dataset	Channel (GHz)	$MJy.sr^{-1}/K_{CMB}$	HFI freq. (GHz)	Conversion
ACT	148	401.936	143	0.85
	218	485.311	217	1.056
SPT	95	234.042	100	1.090
	150	413.540	143	0.7688
	220	477.017	217	1.061

Table 8.1: Conversion factors used for the foreground template extrapolation to ACT and SPT bandpasses with the CIB SED.

For the tSZ×CIB component of the $(\nu_1 \times \nu_2)$ cross-spectrum (from the ACT or SPT dataset), we scale the nearest HFI cross-spectrum $(\nu_1^P \times \nu_2^P)$ using the ratio

$$S_{\nu_1,\nu_2} = \frac{f_{\nu_1} C_{\nu_2} + f_{\nu_2} C_{\nu_1}}{f_{\nu_1^P} C_{\nu_2^P} + f_{\nu_2^P} C_{\nu_1^P}}, \tag{8.10}$$

and then convert it to K_{CMB} using the factors computed from the for the ACT and SPT bandpasses, as above. This scaling applies at the 15% level for the HFI cross-frequency templates, choosing the 143×143 one as a reference.
In addition, a few more specific templates have been added to each datasets:

- Point sources : to mask resolved point sources, ACT and SPT used their own settings to match each instrument's sensitivity and angular resolution. The unresolved point source populations in each case are thus different, so we introduce extra nuisance parameters to model them. We model the unresolved point source components in the ACT and SPT spectra with one amplitude $A_{PS}^{\nu_1 \times \nu_2}$ parameter per cross-spectrum. Consequently, this introduces six nuisance parameters for the ACT, six for the `SPT_high`, and one for the `SPT_low` datasets, respectively (see Table 8.2).
- Galactic dust : following Dunkley et al. (2013) and Das et al. (2014), we model the dust contribution in the ACT power spectra as a power law

$$\mathcal{D}_\ell^{dust}(i,j) = A_{\rm dust}^{\rm ACT} \left(\frac{\ell}{3000}\right)^{-0.7} \left(\frac{\nu_i \nu_j}{\nu_0^2}\right)^{3.8} \left[\frac{g(\nu_i) g(\nu_j)}{g(\nu_0)^2}\right]. \tag{8.11}$$

  We therefore introduce two nuisance parameters, one for each part of the ACT dataset, and set the reference frequency ν_0 at 150 GHz.

  For the SPT datasets, following Reichardt et al. (2012), we use a fixed template, with amplitudes 0.16, 0.21, and 2.19 μK_{CMB}^2 at 95, 150, and 218 GHz, respectively and an $\ell^{-1.2}$ spatial dependency.

8.4.3 Likelihoods

We compute one likelihood for each of the five VHL datasets following the method described in Dunkley et al. (2013). We use the respective published window functions to bin the (CMB + foregrounds) model, and the released covariance matrices to compute the likelihood. In all cases, these include beam uncertainties. Since we combine different datasets, we introduced nine additional nuisance parameters to account for their relative calibration uncertainties (at map level). Figure 8.6 shows a comparison of all the foreground-subtracted CMB spectra for the 150×150 component (which is almost common to all experiments), and Table 8.2 summarizes the characteristics of the datasets we use in the VHL likelihoods. A detailed inspection of all cross-spectra per frequency and component has been performed and does not reveal any inconsistency with the Planck data. More details are given in Appendix C of Couchot et al. (2017c).

Dataset	Freq (GHz)	#spectra	#nuisances
`SPT_low`	150	1	2
`SPT_high`	95,150,220	6	9
`ACT south/equat`	148,218	6	12

Table 8.2: Summary of the characteristics of the VHL data used in this analysis. Each experiment's likelihood includes map calibrations and residual point source levels, which result in a number of additional nuisance parameters shown in the last column. In combined fits, the SZ and CIB foreground templates are common with `Hillipop`.

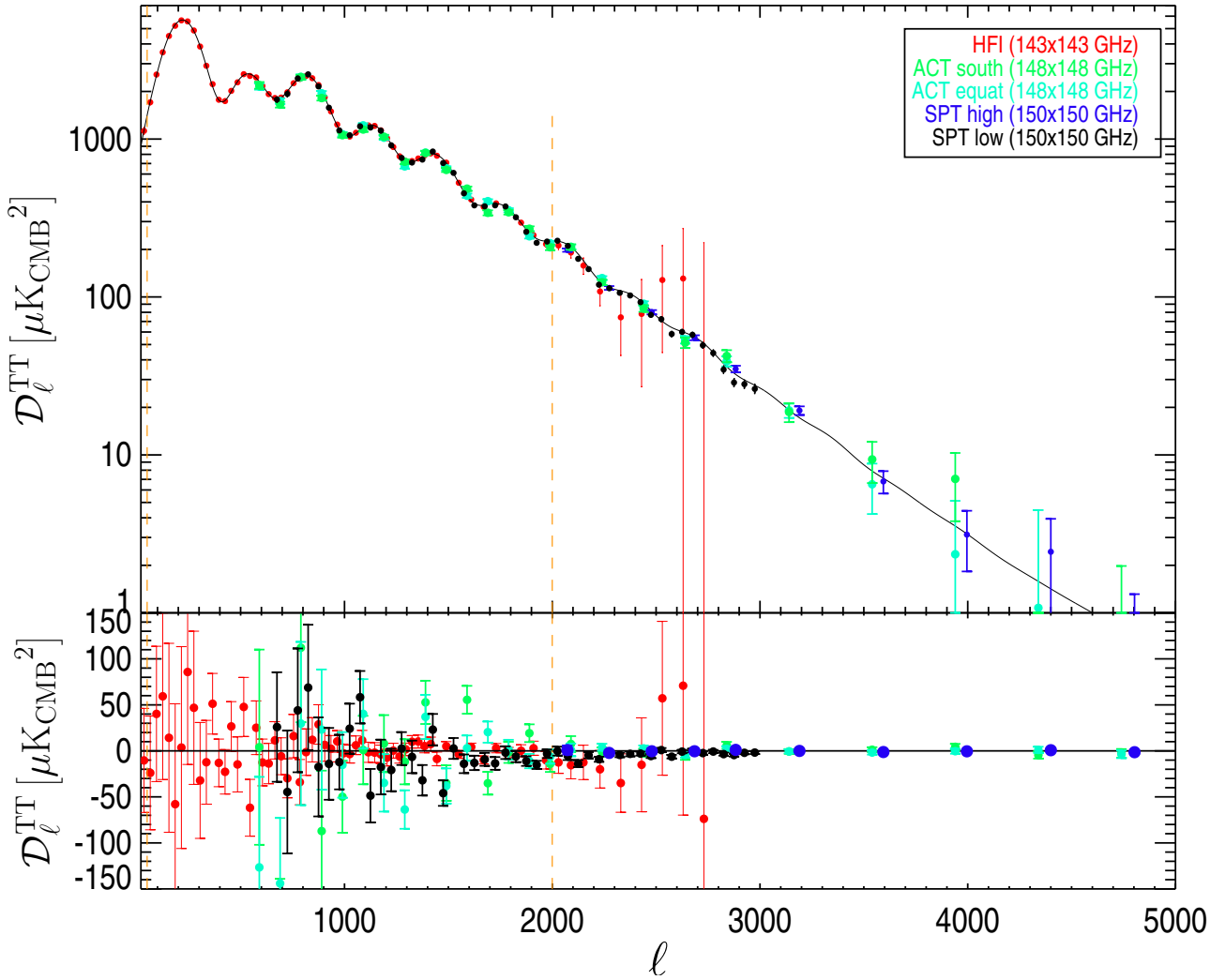

Figure 8.6: Foreground-subtracted CMB cross-spectra of all the experiments used at ≃150 GHz. The solid line is the best fit of the Hillipop+VHL combination and is subtracted to obtain the bottom residual plot. The Hillipop likelihood uses individual multipoles up to 2000 and window functions have been accounted for in the VHL data.

8.4.4 First results and global consistency check

We first check that the combination of the ACT+SPT likelihoods (hereafter VHL) gives results consistent with Hillipop. We therefore sample the Hillipop and VHL likelihoods independently and compare their ΛCDM estimates in Fig. 8.7. Both datasets lead to similar cosmological parameters. However, an accurate measurement of $\Omega_b h^2$ and $\Omega_c h^2$ requires a precise determination of the relative amplitudes of the CMB acoustic peaks for which the VHL datasets are less sensitive. This is reflected by the width of the posteriors shown in Fig. 8.7.
The χ^2 contributions to the Hillipop+VHL+lowTEB best fit of each of the VHL datasets are 58 /47(d.o.f.), 77 /90, and 651/710 for the SPT_low, SPT_high, and ACT datasets, respectively. None of these individual values indicate strong tension between the likelihood parts. We note that in all cases, the covariance matrices provided by the ACT and SPT groups, and used to compute the χ^2, include non negligible, non-diagonal elements.

8.4.5 A_L and τ results

As a second step, we perform the same analysis as in Sects. 8.2 and 8.3.2, adding the VHL likelihood to Hillipop and consider the A_L profile-likelihood (with lowTEB) in Fig. 8.8. The result becomes

$$A_L = 1.03 \pm 0.08 \quad \text{(Hillipop+lowTEB+VHL)}, \tag{8.12}$$

now fully compatible with one.
For τ, combining the VHL with the Hillipop likelihood removes any sign of tension with lowTEB as shown in Fig. 8.9, and we obtain

$$\tau = 0.052 \pm 0.035 \quad \text{(Hillipop+VHL)}, \tag{8.13}$$

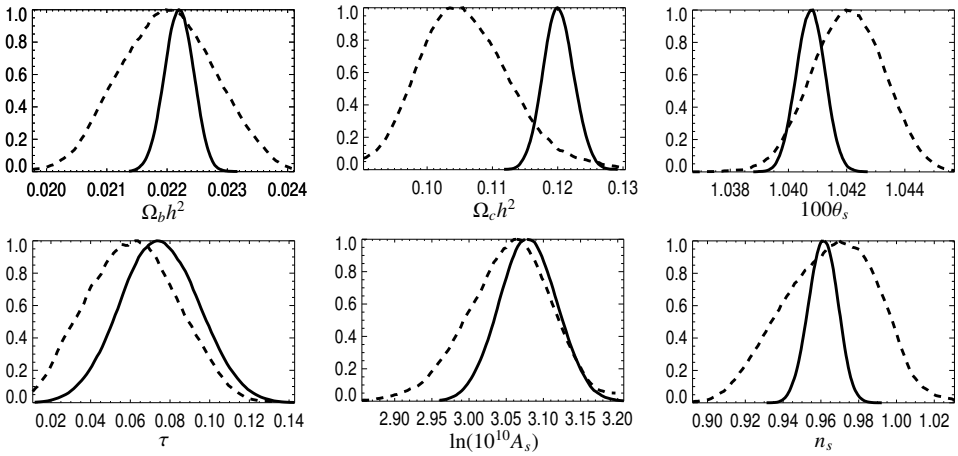

Figure 8.7: Posterior distributions of the cosmological parameters obtained by sampling the Hillipop (soled line) and ACT+SPT (dashed) likelihoods independently. A prior of τ=0.07±0.02 is used in both cases. For clarity, we only show the cosmological parameters, but all nuisances are sampled.

which is in excellent agreement with the lowTEB measurement (Eq. 8.6).

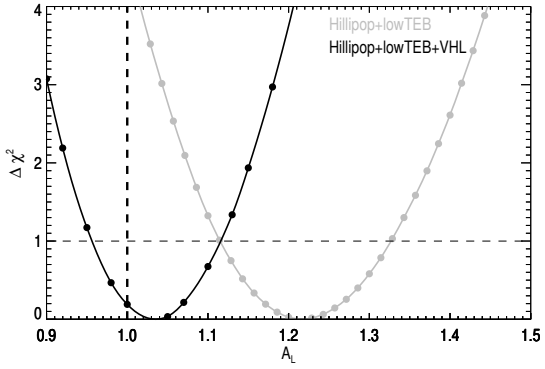

Figure 8.8: Profile-likelihood for A_L reconstructed from the Hillipop+lowTEB likelihood (in grey) and adding the VHL ACT and SPT data (VHL) discussed in the text (in black).

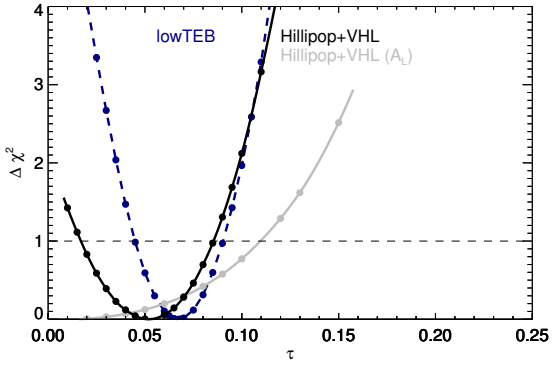

Figure 8.9: Hillipop+VHL and lowTEB likelihood constraints on τ. The grey profile shows the result for Hillipop+VHL when A_L is left free in the fits. The lowTEB one is in dashed blue.

As seen in Sect. 8.5, the inclusion of the VHL data does not greatly change the cosmological parameters but, as expected, strongly constrains all the foregrounds including, through correlations, the ones specific to Planck data (dust and point source amplitudes). This is shown in Fig. 8.10.
We note that all Hillipop nuisance amplitudes (but the point sources) represent coefficients scaling foreground templates: it is remarkable that, after adding the VHL likelihood, they all lie reasonably (at least those for which we have the sensitivity) around one, which is a strong support in favor of the coherence of the foregrounds description.

8.4.6 Robustness of the results

We tested a large number of configurations of the VHL dataset to establish whether the improvement comes from a particular one. Results are presented in Table 8.3.
It is difficult to draw firm conclusions from this exercise, since the number of extra nuisance parameters varyies in each case (see Table. 8.2). The improvement on A_L is most significant when combining several datasets, but also satisfactory as soon as one combines at least two of them. We note that all these results are highly correlated with each other, sinc they all make use of Hillipop. Even though central values very close to 1.0 may be preferable, it should be pointed out that there are several combinations that are compatible with 1.0 at the $\sim 1\sigma$ level. This may indicate that the better the constraint on the high end of the power spectrum, the better the constraint on the A_L control parameter (the lensing effect on C_ℓ^{TT} is not only a smearing of peaks and troughs but also a redistribution of power towards the high ℓ, above ~3000).
Since there is some overlap between SPT_low and SPT_high datasets, we expect some correlations between the SPT_low power-spectrum and, in particular, the 150 GHz spectrum of SPT_high. To check the impact on the results, we either removed the entire 150 GHz from SPT_high or the overlapping bins in multipole for each of the two datasets and re-ran the analysis. In all cases the results were similar with the combined one. For example, when removing the bins at ℓ<3000

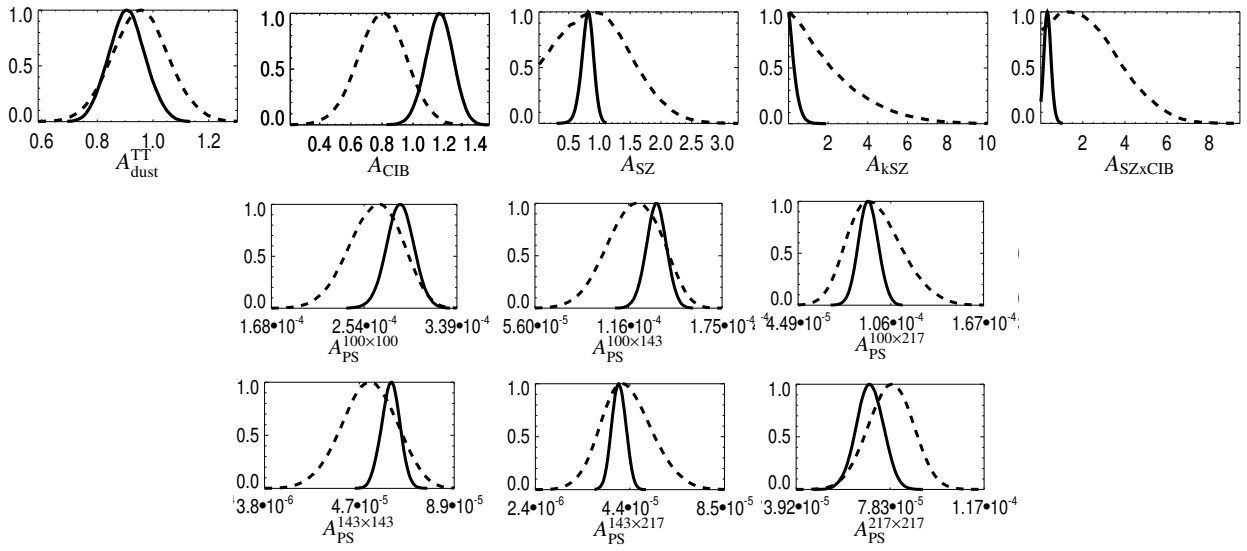

Figure 8.10: Posterior distributions of the foreground `Hillipop` parameters with (solid line) and without (dashed line) the VHL likelihood.

Dataset	A_L
`None`	1.22±0.11
`SPT_low`	1.16±0.10
`SPT_high`	1.12±0.10
`ACT`	1.19±0.10
`SPT_low+SPT_high`	1.02±0.08
`SPT_low+ACT`	1.09±0.09
`SPT_high+ACT`	1.12±0.09
`SPT_low+SPT_high+ACT`	1.03±0.08

Table 8.3: Results on A_L using `Hillipop+lowTEB` and various dataset combinations on the VHL side. For their exact definition see Sect. 8.4.

from the 150x150 GHz of `SPT_high`, we find A_L=0.99±0.08, which is in good agreement with unity and with the results reported in Table 8.3.
Finally, we noticed that the `SPT_high` 220×220 spectrum lies slightly high with respect to the best fit. Indeed, we get a better agreement in this case by increasing the contribution of the SPT dust amplitude. To check the impact on A_L, we re-run the analysis, multiplying the dust level for all SPT spectra, A^{SPT}_{dust}, by a factor of 3 and obtain

$$A_L=1.13\pm0.10 \text{ (Hillipop+lowTEB+SPT\_high, } A^{SPT}_{dust}\times3)$$
$$A_L=1.04\pm0.08 \text{ (Hillipop+lowTEB+VHL, } A^{SPT}_{dust}\times3).$$

Compared with Table 8.3, the details of the SPT dust amplitude do not affect the final results.

8.4.7 Where does the change on A_L come from?

Adding the ACT and SPT data lowered the A_L estimate. In this section, we try to pinpoint where the change came from. As discussed in Sect. 8.2.1, Planck included the VHL information in the `Plik` likelihood through a linear constraint between the thermal and kinetic components of the SZ foreground. When combining `Hillipop` with the VHL likelihood, a similar correlation is observed that in our units reads:

$$A^{kSZ}+3.5A^{tSZ}=3.16\pm0.25. \tag{8.14}$$

To check whether this correlation is sufficient to capture the essentials of the VHL information, we re-run the profile analysis adding to `Hillipop+lowTEB` only the prior in Eq. 8.14 and measure:

$$A_L=1.26^{+0.12}_{-0.10} \quad \text{(Hillipop+lowTEB+SZ-cor)}. \tag{8.15}$$

A comparison with Eq. 8.8 shows that, at least in our case, using this correlation does not capture the complexity of the full covariance matrix.

So, to check if the change came from a better constraint over all the foregrounds, we perform the following measurement: we use the `Hillipop+lowTEB` likelihood to determine A_L as in Sect. 8.3.2 but fixing all the nuisance parameters to the best-fit value of `Hillipop+lowTEB+VHL` likelihood. A profile-likelihood analysis gives

$$A_L = 1.09 \pm 0.08 \quad (\texttt{Hillipop+lowTEB}, \text{ fixed nuisances}),$$

compatible with unity at $\sim 1\sigma$ as when using the VHL data. We conclude that the shift for A_L seems to come from the better determination of the foregrounds parameters. To determine which particular foreground parameters impacts the A_L shift, we run an MCMC analysis sampling all the parameters (including A_L) with the `Hillipop+lowTEB` and `Hillipop+lowTEB+VHL` likelihoods. The posterior distributions for A_L and the foregrounds parameters in common between `Hillipop` and VHL are shown on Fig. 8.11. It is difficult to single out a particular correlation and we conclude

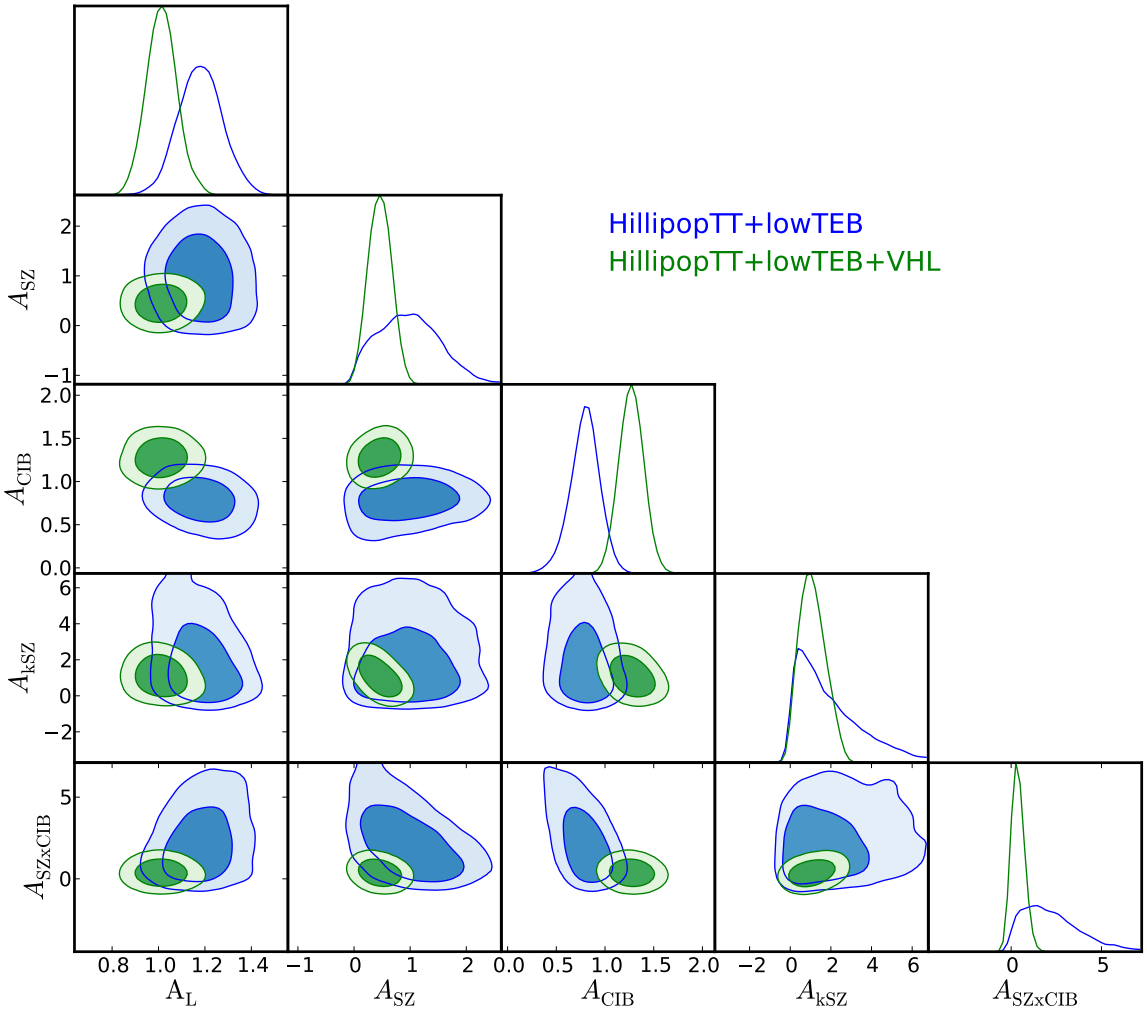

Figure 8.11: Posterior distritions (68 and 95% levels) obtained from sampling the `Hillipop+lowTEB` and `Hillipop+lowTEB+VHL` likelihoods. We display the parameters most constrained by VHL.

that the improvement comes from the overall better constraint of the foregrounds.

8.5 Results on ΛCDM parameters

We have shown how the `Hillipop` likelihood is regularized by including the VHL data. We have checked that it leads to results that are fully compatible with the `lowTEB` likelihood for τ and that their combination leads to an A_L value that is now compatible with one. We then combine the three likelihoods and fix A_L to one, to evaluate the impact on ΛCDM parameters. The comparison with the Planck published result is shown in Fig. 8.12. We note that:

- `Plik` and `Hillipop` likelihoods essentially share the same data;
- the problem pointed out by A_L is not a second-order effect: it directly affects Ω_b, τ, and A_s results;
- our regularized likelihood provides a lower σ_8 estimate.

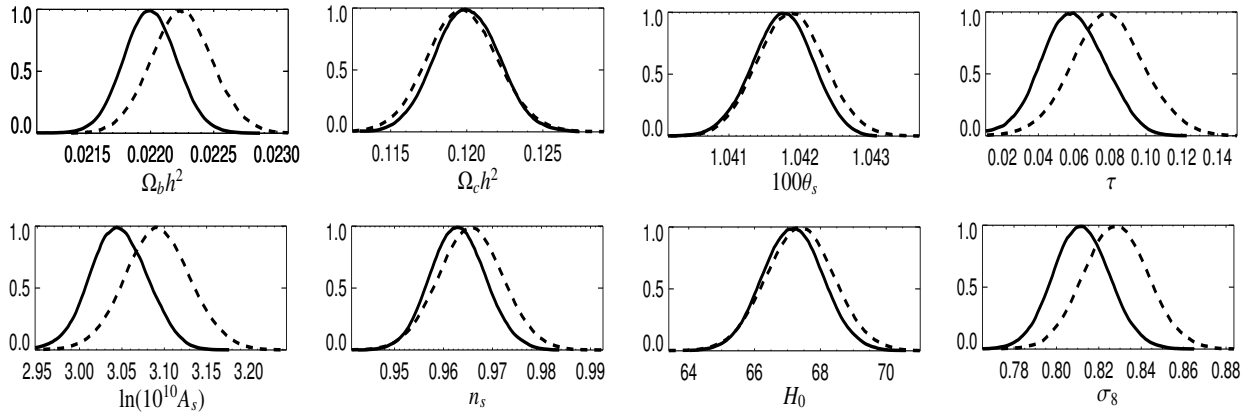

Figure 8.12: Posterior distributions of the ΛCDM cosmological parameters obtained with our regularized likelihood (`Hillipop+lowTEB+VHL`, full line), compared to the Planck baseline result (`Plik+lowTEB`, dashed line). We recall that this former also includes some VHL information through an SZ correlation discussed in PCP15. The last row shows derived parameters.

These results are obtained using only CMB data. To check the overall consistency and constrain the parameters, we also make use of some robust extra-information by including recent Baryon Acoustic Oscillations (BAO) and supernovae (SN) results.

The BAO are generated by acoustic waves in the primordial fluid, and can be measured today through the study of the correlation functions of galaxy surveys. Owing to the fact that their measurement is sensitive to different systematic errors than the CMB, they help break the degeneracies, and are therefore further used in this paper to constrain the cosmological parameters. Here, we have used: the acoustic-scale distance ratio $D_V(z)/r_{drag}$ measurements[6] from the 6dF Galaxy Survey at z=0.1 (Beutler et al. 2014), and from BOSS-LowZ at z=0.32. They have been combined with the BOSS-CMASS anisotropic measurements at z=0.57, considering both the line of sight and the transverse direction, as described in Anderson et al. (2014).

Type Ia supernovae had a major role in the discovery of late time acceleration of the Universe and constitutes a powerful cosmological probe complementary to CMB constraints. We have used the JLA compilation (Betoule et al. 2014), which covers a wide redshift range (from 0.01 to 1.2).

Parameter	`Hillipop+lowTEB`	`Hillipop+lowTEB` +VHL	`Hillipop+lowTEB` +VHL+BAO+SN
$\Omega_b h^2$	0.02220±0.00023	0.02203±0.00020	0.02211±0.00018
$\Omega_c h^2$	0.1193±0.0022	0.1196±0.0020	0.1183±0.0012
$100\theta_s$	1.04179±0.00043	1.04181±0.00042	1.04190±0.00038
τ	0.071±0.019	0.058±0.018	0.062±0.017
n_s	0.9644±0.0069	0.9626±0.0055	0.9654±0.0040
$\ln(10^{10}A_s)$	3.068±0.037	3.044±0.034	3.048±0.033
H_0	67.48±0.98	67.21±0.91	67.77±0.57
σ_8	0.816±0.015	0.809±0.013	0.807±0.013

Table 8.4: Estimates of cosmological parameters using MCMC techniques for the six ΛCDM parameters. First with our likelihood (`Hillipop`) and `lowTEB`. Then with our regularized likelihood (`Hillipop+lowTEB+VHL`, second column) and further adding some BAO and SN data (third column). Here θ_s, as computed by `class`, represents the exact angular size of the sound horizon and should not be identified with the `CosmoMC` θ_{MC} parameter.

Table 8.4 gives the results obtained with `Hillipop+lowTEB` (i.e., using only Planck data), then adding ACT+SPT likelihoods (i.e., only CMB) and finally also adding the BAO and SNIa likelihoods. Using only Planck data, the `Hillipop+lowTEB` results (first column in Table 8.4) are almost identical to the ones reported for 'Planck TT+`lowP`' in PCP15, but for τ and A_s that are smaller, as explained in Sects. 8.3.2 and 8.2.5.

As discussed throughout this paper, adding the VHL data (second column) releases the tension on the optical depth, leading to a value of τ around 0.06, as can be anticipated from Fig. 8.9. We also see a slight shift of $\Omega_b h^2$ that is difficult to analyze since, at this level of precision, this parameter enters several areas of the Boltzmann computations (e.g., Hu &

[6] $D_V(z)$ is a function of the redshift (z) and can be expressed in terms of the angular diameter distance and the Hubble parameter, r_{drag}, is the comoving sound horizon at the end of the baryon drag epoch.

White 1997). Then, adding the BAO and SN data (third column) increases the precision on the parameters but does not change substantially their value.
We note that in all cases, σ_8 is stable, e.g., `Hillipop+lowTEB` gives σ_8=0.816±0.015. This is only in mild tension with other astrophysical determinations such as weak lensing (Heymans et al. 2013) and Sunyaev-Zeldovich cluster number counts (Planck Collaboration XXIV 2016).

8.6 Conclusion

In this work, we have investigated the deviation of the $A_{\rm L}$ parameter from unity and have found it to be of 2.6σ, using the `Plik` high-ℓ and `lowTEB` low-ℓ Planck likelihoods. For these demanding tests, we chose to consistently use the profile-likelihood method, which is well-suited to such studies. We first showed how this $A_{\rm L}$ deviation is related to a difference in the τ estimations when performed using `Plik` or `lowTEB` alone.
The `Hillipop` likelihood has been built based on different foreground and nuisance parametrization. We have shown that `Hillipop` alone only very loosely constrains $A_{\rm L}$ towards high values, and that its τ estimate lies closer to the low-ℓ measurement, albeit on the high-end side.
We then added to `Hillipop`, high angular resolution CMB data from the ground-based ACT and SPT experiments to further constrain the high-ℓ part of the CMB power spectrum and the foreground parameters. Cosmological parameters derived from this setup are shown to be more self-consistent, in particular the reconstructed τ value is coherent with the low-ℓ determination that was extracted from the `lowTEB` likelihood. They also pass the $A_{\rm L}$=1.0 test.
We have shown that this regularization is quite robust against the details of the VHL datasets used, and specific foreground hypotheses. We have also shown that it is not only related to a better determination of the foreground amplitudes but also seems to lie in their correlations.
The cosmological parameters determined from this combined CMB likelihood are also stable when adding BAO and SNIa likelihoods. This is, in particular, the case for σ_8 that we always find close to 0.81. With respect to the cosmological parameters derived by the Planck collaboration, the main differences concern τ and $A_{\rm s}$, to which the former is directly correlated, and $\Omega_b h^2$, which shifts by a fraction of σ. Other parameters are almost identical.
Improving on $A_{\rm L}$ is a delicate task and it seems that the source of the regularization cannot be easily pinpointed. The choices of the `Hillipop` likelihood impact on the correlations between all the parameters, yielding a τ estimate in smaller tension with the low-ℓ likelihood. But this was not sufficient to relieve the $A_{\rm L}$ tension. It is only by further constraining foregrounds using VHL likelihoods that we were able to obtain a coherent picture over a broad range of multipoles.
One cannot exclude that the $A_{\rm L}$ deviation from unity still partly results from an incomplete accounting of some residual systematics in the ACT, SPT, or Planck data.
During the review of this article, the Planck Collaboration released an estimate of the optical depth based on HFI cleaned maps (Planck Collaboration Int. XLVII 2016) and using the `Lollipop` likelihood (Mangilli et al. 2015). This new low-ℓ-only result, τ=0.058±0.012, increases the tension with the high-ℓ likelihoods to 2.6σ with `Plik` and 1.5σ with `Hillipop` and is fully compatible with our `Hillipop`+VHL combination (Eq. 8.13).

We thank Guilaine Lagache for building and providing the point-source masks cleaned from Galactic compact structures, Marian Douspis for providing the SZ templates, and Marc Betoule for the development of the `C` *version of the* `JLA` *likelihood. This is part of a set of three scientific papers (Couchot et al. 2017c,b,a) produced by the Planck group at LAL.*

Bibliography

Anderson, L., Aubourg, É., Bailey, S., et al. 2014, MNRAS, 441, 24
Béthermin, M., Daddi, E., Magdis, G., et al. 2012, ApJ, 757, L23
Betoule, M., Kessler, R., Guy, J., et al. 2014, A&A, 568, A22
Beutler, F. et al. 2014, Mon.Not.Roy.Astron.Soc., 444, 3501
Blanchard, A. & Schneider, J. 1987, A&A, 184, 1
Blas, D., Lesgourgues, J., & Tram, T. 2011, J. Cosmology Astropart. Phys., 7, 034
Calabrese, E., Slosar, A., Melchiorri, A., Smoot, G. F., & Zahn, O. 2008, Phys. Rev. D, 77, 123531
Couchot, F., Henrot-Versillé, S., Perdereau, O., et al. 2017a, ArXiv e-prints [arXiv:1703.10829]
Couchot, F., Henrot-Versillé, S., Perdereau, O., et al. 2017b, A&A, 602, A41
Couchot, F., Henrot-Versillé, S., Perdereau, O., et al. 2017c, A&A, 597, A126
Das, S., Louis, T., Nolta, M. R., et al. 2014, J. Cosmology Astropart. Phys., 4, 14
Di Valentino, E., Melchiorri, A., & Silk, J. 2016, Phys. Rev. D, 93, 023513
Dunkley, J., Calabrese, E., Sievers, J., et al. 2013, J. Cosmology Astropart. Phys., 7, 25
George, E. M., Reichardt, C. L., Aird, K. A., et al. 2015, ApJ, 799, 177
Heymans, C. et al. 2013, Mon. Not. Roy. Astron. Soc., 432, 2433
Hu, B. & Raveri, M. 2015, Phys. Rev. D, 91, 123515
Hu, W. & White, M. 1997, ApJ, 479, 568
James, F. 2007, Statistical Methods in Experimental Physics (World Scientific)
Lagache, G. 2014, Planck internal note
Lesgourgues, J. 2011, ArXiv e-prints [arXiv:1104.2934]
Lewis, A. & Challinor, A. 2006, Phys. Rep., 429, 1
Lewis, A., Challinor, A., & Lasenby, A. 2000, ApJ, 538, 473
Mangilli, A., Plaszczynski, S., & Tristram, M. 2015, MNRAS, 453, 3174
Planck Collaboration XVI. 2014, A&A, 571, A16
Planck Collaboration XXX. 2014, A&A, 571, A30
Planck Collaboration I. 2016, A&A, 594, A1
Planck Collaboration XI. 2016, A&A, 594, A11
Planck Collaboration XIII. 2016, A&A, 594, A13
Planck Collaboration XXII. 2016, A&A, 594, A22
Planck Collaboration XXIV. 2016, A&A, 594, A24
Planck Collaboration Int. XVI. 2014, A&A, 566, A54
Planck Collaboration Int. XXX. 2016, A&A, 586, A133
Planck Collaboration Int. XLVII. 2016, A&A, 596, A108
Porter, F. 1996, Nuclear Instruments and Methods in Physics Research A, 368, 793
Reichardt, C. L., Shaw, L., Zahn, O., et al. 2012, ApJ, 755, 70
Story, K. T., Reichardt, C. L., Hou, Z., et al. 2013, ApJ, 779, 86
Tristram, M., Macías-Pérez, J. F., Renault, C., & Santos, D. 2005, MNRAS, 358, 833

Chapter 9

Reionisation

extracted from Planck Collaboration Int. XLVII (2016)

"*Planck* intermediate results. XLVII. Planck constraints on reionization history"

Between 2012 and 2016, I was in charged of the group for studying reionization history in Planck. The group was made of about 25 people. At early stages, we started working on the systematics that affect polarisation measurement for Planck-HFI. Then we built a likelihood function that can propagate as accurately as possible both systematic and foreground residuals: `lollipop`. *And finally, we use this likelihood, combined with Planck official high-ℓ likelihood to derive constraints on the reionisation models. I was in charge of the redaction of the Planck paper (Planck Collaboration Int. XLVII 2016) which is copied in the chapter.*

We investigate constraints on cosmic reionization extracted from the *Planck* cosmic microwave background (CMB) data. We combine the *Planck* CMB anisotropy data in temperature with the low-multipole polarization data to fit ΛCDM models with various parameterizations of the reionization history. We obtain a Thomson optical depth τ=0.058±0.012 for the commonly adopted instantaneous reionization model. This confirms, with data solely from CMB anisotropies, the low value suggested by combining *Planck* 2015 results with other data sets, and also reduces the uncertainties. We reconstruct the history of the ionization fraction using either a symmetric or an asymmetric model for the transition between the neutral and ionized phases. To determine better constraints on the duration of the reionization process, we also make use of measurements of the amplitude of the kinetic Sunyaev-Zeldovich (kSZ) effect using additional information from the high-resolution Atacama Cosmology Telescope and South Pole Telescope experiments. The average redshift at which reionization occurs is found to lie between z=7.8 and 8.8, depending on the model of reionization adopted. Using kSZ constraints and a redshift-symmetric reionization model, we find an upper limit to the width of the reionization period of Δz<2.8. In all cases, we find that the Universe is ionized at less than the 10 % level at redshifts above $z\simeq$10. This suggests that an early onset of reionization is strongly disfavoured by the *Planck* data. We show that this result also reduces the tension between CMB-based analyses and constraints from other astrophysical sources.

9.1 Introduction

The process of cosmological recombination happened around redshift $z\simeq$1100, after which the ionized fraction fell precipitously (Peebles 1968; Zel'dovich et al. 1969; Seager et al. 2000) and the Universe became mostly neutral. However, observations of the Gunn-Peterson effect (Gunn & Peterson 1965) in quasar spectra (Becker et al. 2001; Fan et al. 2006b; Venemans et al. 2013; Becker et al. 2015) indicate that intergalactic gas had become almost fully reionized by redshift $z\simeq$6. Reionization is thus the second major change in the ionization state of hydrogen in the Universe. Details of the transition from the neutral to ionized Universe are still the subject of intense investigations (for a recent review, see the book by Mesinger 2016). In the currently conventional picture, early galaxies reionize hydrogen progressively throughout the entire Universe between $z\simeq$12 and $z\simeq$6, while quasars take over to reionize helium from $z\simeq$6 to $\simeq$2. But many questions remain. When did the epoch of reionization (EoR) start, and how long did it last? Are early galaxies enough to reionize the entire Universe or is another source required? We try to shed light on these questions using the traces left by the EoR in the cosmic microwave background (CMB) anisotropies.

The CMB is affected by the total column density of free electrons along each line of sight, parameterized by its Thomson

scattering optical depth τ. This is one of the six parameters of the baseline ΛCDM cosmological model and is the key measurement for constraining reionization. Large-scale anisotropies in polarization are particularly sensitive to the value of τ. The *WMAP* mission was the first to extract a τ measurement through the correlation between the temperature field and the E-mode polarization (i.e., the TE power spectrum) over a large fraction of the sky. This measurement is very demanding, since the expected level of the E-mode polarization power spectrum at low multipoles (ℓ<10) is only a few times $10^{-2}\mu K^2$, lower by more than two orders of magnitude than the level of the temperature anisotropy power spectrum. For such weak signals the difficulty is not only to have enough detector sensitivity, but also to reduce and control both instrumental systematic effects and foreground residuals to a very low level. This difficulty is illustrated by the improvements over time in the *WMAP*-derived τ estimates. The 1-year results gave a value of τ=0.17±0.04, based on the temperature-polarization TE cross-power spectrum (Kogut et al. 2003). In the 3-year release, this was revised down to 0.10±0.03 using E-modes alone, whereas the combined TT, TE, and EE power spectra gave 0.09±0.03 (Page et al. 2007). Error bars improved in further *WMAP* analyses, ending up with 0.089±0.014 after the 9-year release (see Dunkley et al. 2009; Komatsu et al. 2011; Hinshaw et al. 2013). In 2013, the first *Planck* satellite[1] cosmological results were based on *Planck* temperature power spectra combined with the polarized *WMAP* data and gave the same value τ=0.089±0.014 (Planck Collaboration XVI 2014). However, using a preliminary version of the *Planck* 353 GHz polarization maps to clean the dust emission (in place of the *WMAP* dust model), the optical depth was reduced by approximately 1σ to τ=0.075±0.013 (Planck Collaboration XV 2014).

In the 2015 Planck analysis (Planck Collaboration XIII 2016), the Low Frequency Instrument (LFI) low-resolution maps polarization at 70 GHz were used. Foreground cleaning was performed using the LFI 30 GHz and High Frequency Instrument (HFI) 353 GHz maps, operating effectively as polarized synchrotron and dust templates, respectively. The optical depth was found to be τ=0.078±0.019, and this decreased to 0.066±0.016 when adding CMB lensing data. This value is also in agreement with the constraints from the combination "PlanckTT+lensing+BAO," yielding τ=0.067±0.016, which uses no information from low-ℓ polarization.

In this paper and its companion (Planck Collaboration Int. XLVI 2016), we derive the first estimate of τ from the *Planck*-HFI polarization data at large scales. For the astrophysical interpretation, the power spectra are estimated using a PCL estimate which is more conservative. Indeed, it gives a slightly larger distribution on τ than the QML estimator used in Planck Collaboration Int. XLVI (2016) but is less sensitive to the limited number of simulations available for the analysis. Using only E-mode polarization, the *Planck* `lollipop` likelihood gives $\tau=0.053^{+0.014}_{-0.016}$ for a standard instantaneous reionization model, when all other ΛCDM parameters are fixed to their *Planck*-2015 best-fit values. We show that in combination with the *Planck* temperature data the error bars are improved and we find τ=0.058±0.012.

In the ΛCDM model, improved accuracy on the reionization optical depth helps to reduce the degeneracies with other parameters. In particular, the measurement of τ reduces the correlation with the normalization of the initial power spectrum A_s and its spectral index n_s. In addition to this τ is a particularly important source of information for constraining the history of reionization, which is the main subject of this paper. When combined with direct probes at low redshift, a better knowledge of the value of the CMB optical depth parameter may help to characterize the duration of the EoR, and thus tell us when it started.

In addition to the effect of reionization on the polarized large-scale CMB anisotropies, reionization generates CMB temperature anisotropies through the kinetic Sunyaev-Zeldovich (kSZ) effect (Sunyaev & Zeldovich 1980), caused by the Doppler shift of photons scattering off electrons moving with bulk velocities. Simulations have shown that early homogeneous and patchy reionization scenarious differently affect the shape of the kSZ power spectrum, allowing us to place constraints on the reionization history (e.g., McQuinn et al. 2005; Aghanim et al. 2008). Zahn et al. (2012) derived the first constraints on the epoch of reionization from the combination of kSZ and low-ℓ CMB polarization, specifically using the low-ℓ polarization power spectrum from WMAP and the very high multipoles of the temperature angular power spectrum from the South Pole Telescope (SPT, Reichardt et al. 2012). However one should keep in mind that kSZ signal is complicated to predict and depends on detailed astrophysics which makes the constraints on reionization difficult to interpret (Mesinger et al. 2012).

In this paper, we investigate constraints on the epoch of reionization coming from *Planck*. Section 9.2 first briefly describes the pre-2016 data and likelihood used in this paper, which are presented in detail in Planck Collaboration Int. XLVI (2016). In Sect. 9.3 we then present the parameterizations we adopt for the ionization fraction, describing the reionization history as a function of redshift. In Sect. 9.4, we show the results obtained from the CMB observables (i.e., the optical depth τ and the amplitude of the kSZ effect) in the case of "instantaneous" reionization. Section 9.5 presents results based on the CMB measurements by considering different models for the ionization history. In particular, we derive limits on the reionization redshift and duration. Finally, in Sect. 9.6, we derive the ionization fraction as a function of redshift and discuss how our results relate to other astrophysical constraints.

[1] *Planck* (`http://www.esa.int/Planck`) is a project of the European Space Agency (ESA) with instruments provided by two scientific consortia funded by ESA member states and led by Principal Investigators from France and Italy, telescope reflectors provided through a collaboration between ESA and a scientific consortium led and funded by Denmark, and additional contributions from NASA (USA).

9.2 Data and likelihood

9.2.1 Data

The present analysis is based on the pre-2016 full mission intensity and polarization *Planck*-HFI maps at 100 and 143 GHz. The data processing and the beam description are the same as in the *Planck* 2015 release and have been detailed in Planck Collaboration VII (2016). *Planck*-HFI polarization maps are constructed from the combination of polarized detectors that have fixed polarization direction. The *Planck* scanning strategy produces a relatively low level of polarization angle measurement redundancy on the sky, resulting in a high level of I-Q-U mixing, as shown in Planck Collaboration VIII (2016). As a consequence, any instrumental mismatch between detectors from the same frequency channel produces leakage from intensity to polarization. This temperature-to-polarization leakage was at one point the main systematic effect present in the *Planck*-HFI data, and prevented robust low-ℓ polarization measurements from being included in the previous *Planck* data releases.

The maps that we use here differ in some respects from those data released in 2015. The updated mapmaking procedure, presented in Planck Collaboration Int. XLVI (2016), now allows for a significant reduction of the systematic effects in the maps. In particular, the relative calibration within a channel is now accurate to better than 0.001 %, which ensures a very low level of gain-mismatch between detectors. The major systematic effect that remains in the pre-2016 maps is due to imperfections of the correction for nonlinearity in the analogue-to-digital converters (ADCs) but produces very low level of residuals in the maps. In addition to the 100 GHz and 143 GHz maps, we also make use of 30 GHz LFI data (Planck Collaboration II 2016) and 353 GHz HFI data to remove polarized foregrounds.

Using the pre-2016 end-to-end simulations, we show that the power spectrum bias induced by the remaining nonlinearities is very small and properly accounted for in the likelihood. Figure 9.1 shows the bias (in the quantity $\mathcal{D}_\ell \equiv \ell(\ell+1)C_\ell/2\pi$, where C_ℓ is the conventional power spectrum) computed as the mean of the EE cross-power spectra from simulated maps, including realistic noise and systematic effects without and with Galactic foregrounds. In the latter case, the foregrounds are removed for each simulation using the 30 GHz and 353 GHz maps as templates for synchrotron and dust, respectively. The resulting bias in the EE 100×143 cross-power spectrum can be used to correct the measured cross-spectrum, but in fact has very little impact on the likelihood.

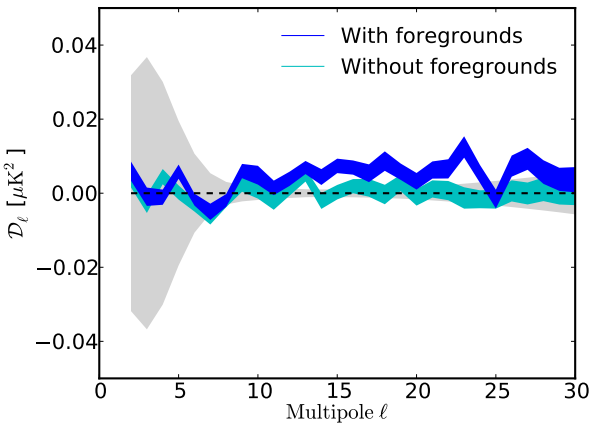

Figure 9.1: Bias in the 100×143 cross-power spectrum computed from simulations, including instrumental noise and systematic effects, with or without foregrounds (dark blue and light blue), compared to the cosmic variance level (in grey).

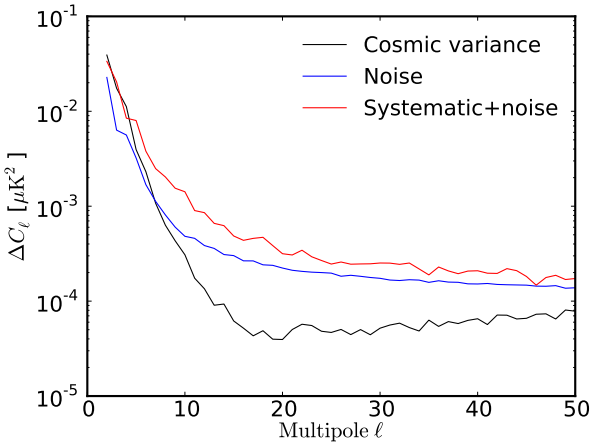

Figure 9.2: Variance of the 100×143 EE cross-power spectrum for simulations, including instrumental noise and noise plus systematic effects, compared to cosmic variance.

Furthermore, we use end-to-end simulations to propagate the systematic uncertainties to the cross-power spectra and all the way to the cosmological parameters. Figure 9.2 shows the impact on the variance due to the inclusion of the main ADC nonlinearity systematic effect, compared to realistic noise and cosmic variance. The resulting C_ℓ covariance matrix is estimated from these Monte Carlos. In the presence of such systematic effects, the variance of the C_ℓ is shown to be higher by roughly a factor of 2 compared to the pure noise case.

Polarized foregrounds at *Planck*-HFI frequencies are essentially dominated by Galactic dust emission, but also include a small contribution from synchrotron emission. We use the 353 GHz and 30 GHz *Planck* maps as templates to subtract dust and synchrotron, respectively, using a single coefficient for each component over 95 % of the sky (see Planck Collaboration IX 2016; Planck Collaboration X 2016). However, foreground residuals in the maps are still dominant over the CMB polarized signal near the Galactic plane. We therefore apply a very conservative mask, based on the amplitude of the polarized dust emission, which retains 50 % of the sky for the cosmological analysis. Outside this mask, the foreground residuals are found to be lower than 0.3 and 0.4 μK in Q and U Stokes polarization maps at 100 and 143 GHz, respectively. We have checked that our results are very stable when using a larger sky fraction of 60 %.

In this paper, we also make use of the constraints derived from the observation of the Gunn-Peterson effect on high-redshift quasars. As suggested by Fan et al. (2006a), these measurements show that the Universe was almost fully reionized at

redshift $z \simeq 6$. We later discuss the results obtained with and without imposing a prior on the redshift of the end of reionization.

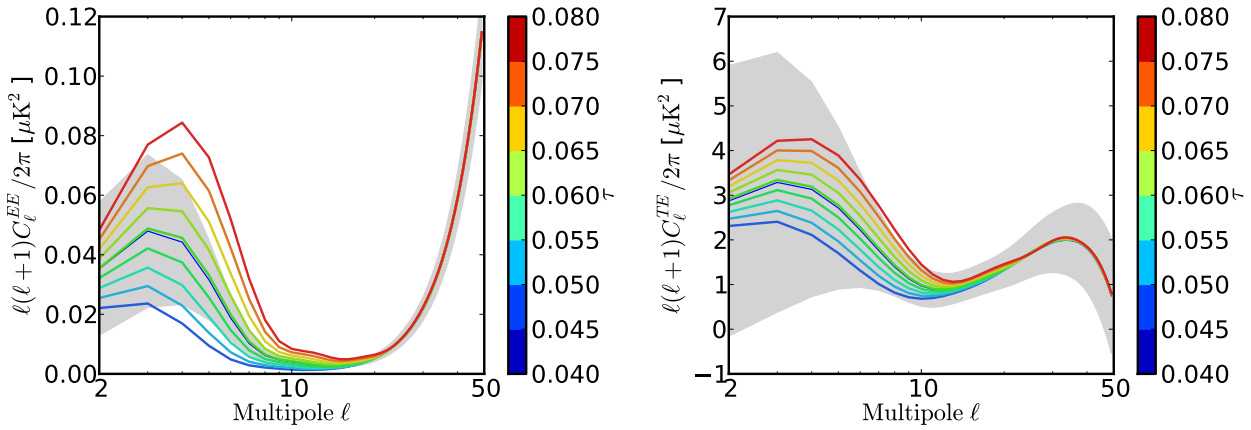

Figure 9.3: EE and TE power spectra for various τ values ranging from 0.04 to 0.08. The ionization fraction is modelled using a redshift-symmetric tanh function with δz=0.5. Grey bands represent the cosmic variance (full-sky) associated with the τ=0.06 model.

9.2.2 Likelihood

For temperature anisotropies, we use the combined *Planck* likelihood (hereafter "Planck TT+lowP"), which includes the TT power spectrum likelihood at multipoles ℓ>30 (using the `Plik` code) and the low-ℓ temperature-only likelihood based on the CMB map recovered from the component-separation procedure (specifically `Commander`) described in detail in Planck Collaboration XI (2016).

For polarization, we use the *Planck* low-ℓ EE polarization likelihood (hereafter `lollipop`), a cross-spectra-based likelihood approach described in detail in Mangilli et al. (2015) and applied to *Planck* data as discussed here in Chapter 5. The multipole range used is ℓ=4–20. Cross-spectra are estimated using the pseudo-C_ℓ estimator `Xpol` (a generalization to polarization of the algorithm presented in Tristram et al. 2005). For a full-sky analysis, the statistics of the reconstructed C_ℓ are given by a χ^2 distribution that is uncorrelated between multipoles. For a cut-sky analysis, the distribution is more complex and includes ℓ-to-ℓ correlations. Hamimeche & Lewis (2008) proposed an approximation of the likelihood for cut-sky auto-power spectra that was adapted by Mangilli et al. (2015) to be suitable for cross-spectra. Cross-spectra between independent data sets show common sky signal, but are not biased by the noise because this should be uncorrelated. This approximation assumes that any systematic residuals are *not* correlated between the different data sets; We have shown using realistic simulations (including *Planck*-HFI noise characteristics and systematic effect residuals), that the bias in the cross-spectra is very small and can be corrected for at the power-spectrum level. Nevertheless, we choose to remove the first two multipoles (ℓ=2 and ℓ=3), since they may still be partially contaminated by systematics. Using those simulations, we derive the C_ℓ covariance matrix used in the likelihood, which propagates both the noise and the systematic uncertainties. For the astrophysical interpretation, the power-spectra are estimated with a PCL estimate which is more conservative. Indeed, it gives a slightly larger distribution on τ than a QML estimator but is less sensitive to the limited number of simulations available for the analysis.

With *Planck* sensitivity in polarization, the results from the low-ℓ EE power spectrum dominate the constraints compared to the TE power spectrum, as can be seen in Fig. 9.3. This is because of the relatively larger cosmic variance for TE (arising from the temperature term) and the intrinsically weaker dependence on τ ($\propto\tau$ compared with τ^2 for EE), as well as the fact that there is only partial correlation between T and E. As a consequence, we do not consider the TE data in this analysis. Furthermore, we do not make use of the high-ℓ likelihoods in EE and TE from *Planck*, since they do not carry additional information on reionization parameters.

Planck temperature observations are complemented at smaller angular scales by measurements from the ground-based Atacama Cosmology Telescope (ACT) and South Pole Telescope (SPT). As explained in Planck Collaboration XI (2016), the high-ℓ likelihood (hereafter VHL) includes ACT power spectra at 148 and 218 GHz (Das et al. 2014), with a revised binning (described in Calabrese et al. 2013) and final beam estimates (Hasselfield et al. 2013), together with SPT measurements in the range 2000<ℓ<13000 from the 2540deg^2 SPT-SZ survey at 95, 150, and 220 GHz (George et al. 2015). To assess the consistency between these data sets, we extend the *Planck* foreground models up to ℓ=13000, with additional nuisance parameters for ACT and SPT (as described in Planck Collaboration XIII 2016). We use the same models for cosmic infrared background (CIB) fluctuations, the thermal SZ (tSZ) effect, kSZ effect, and CIB×tSZ components. The kSZ template used in the *Planck* 2015 results assumed homogeneous reionization. In order to investigate inhomogeneous reionization, we have modified the kSZ template when necessary, as discussed in Sect. 9.4.2.

We use the CMB lensing likelihood (Planck Collaboration XV 2016) in addition to the CMB anisotropy likelihood. The lensing information can be used to break the degeneracy between the normalization of the initial power spectrum A_s

and τ (as discussed in Planck Collaboration XIII 2016). Despite this potential for improvement, we show in Sect. 9.4.1 that *Planck*'s low-ℓ polarization signal-to-noise ratio is sufficiently high that the lensing does not bring much additional information for the reionization constraints.
The *Planck* reference cosmology used in this paper corresponds to the Planck TT+lowP+lowP+lensing best fit, as described in table 4, column 2 of Planck Collaboration XIII (2016), namely $\Omega_b h^2$=0.02226, $\Omega_c h^2$=0.1197, Ω_m=0.308, n_s=0.9677, H_0=67.81kms^{-1}Mpc^{-1}, for which Y_P=0.2453. This best-fit model comes from the combination of three *Planck* likelihoods: the temperature power spectrum likelihood at high ℓ; the "lowP" temperature+polarization likelihood, based on the foreground-cleaned LFI 70 GHz polarization maps, together with the temperature map from the `Commander` component-separation algorithm; and the power spectrum of the lensing potential as measured by *Planck*.

9.3 Parametrization of reionization history

The epoch of reionization (EoR) is the period during which the cosmic gas transformed from a neutral to ionized state at the onset of the first sources. Details of the transition are thus strongly connected to many fundamental questions in cosmology, such as what were the properties of the first galaxies and the first (mini-)quasars, how did the formation of very metal-poor stars proceed, etc. We certainly know that, at some point, luminous sources started emitting ultraviolet radiation that reionized the neutral regions around them. After a sufficient number of ionizing sources had formed, the average ionized fraction of the gas in the Universe rapidly increased until hydrogen became fully ionized. Empirical, analytic, and numerical models of the reionization process have highlighted many pieces of the essential physics that led to the birth to the ionized intergalactic medium (IGM) at late times (Couchman & Rees 1986; Miralda-Escude & Ostriker 1990; Meiksin & Madau 1993; Aghanim et al. 1996; Gruzinov & Hu 1998; Madau et al. 1999; Gnedin 2000; Barkana & Loeb 2001; Ciardi et al. 2003; Furlanetto et al. 2004; Pritchard et al. 2010; Pandolfi et al. 2011; Mitra et al. 2011; Iliev et al. 2014). Such studies provide predictions on the various reionization observables, including those associated with the CMB.
The most common physical quantity used to characterize reionization is the Thomson scattering optical depth defined as

$$\tau(z)=\int_{t(z)}^{t_0} n_e \sigma_T c \mathrm{d}t', \tag{9.1}$$

where n_e is the number density of free electrons at time t', σ_T is the Thomson scattering cross-section, t_0 is the time today, $t(z)$ is the time at redshift z, and we can use the Friedmann equation to convert dt to dz. The reionization history is conveniently expressed in terms of the ionized fraction $x_e(z)\equiv n_e(z)/n_H(z)$ where $n_H(z)$ is the hydrogen number density. In practice, the CMB is sensitive to the average over all sky directions of $x_e(1+\delta_b)$ (where δ_b denotes the baryon overdensity). The IGM is likely to be very inhomogeneous during reionization process, with ionized bubbles embedded in neutral surroundings, which would impact the relation between the optical depth and the reionisation parameters (see Liu et al. 2016) at a level which is neglected in this paper.
In this study, we define the redshift of reionization, $z_{re}\equiv z_{50\%}$, as the redshift at which x_e=0.5×f. Here the normalization, f=1+f_{He}=1+n_{He}/n_H, takes into account electrons injected into the IGM by the first ionization of helium (corresponding to 25 eV), which is assumed to happen roughly at the same time as hydrogen reionization. We define the beginning and the end of the EoR by the redshifts $z_{beg}\equiv z_{10\%}$ and $z_{end}\equiv z_{99\%}$ at which x_e=0.1×f and 0.99×f, respectively. The duration of the EoR is then defined as $\Delta z=z_{10\%}-z_{99\%}$.[2] Moreover, to ensure that the Universe is fully reionized at low redshift, we impose the condition that the EoR is completed before the second helium reionization phase (corresponding to 54 eV), noting that it is commonly assumed that quasars are necessary to produce the hard photons needed to ionize helium. To be explicit about how we treat the lowest redshifts we assume that the full reionization of helium happens fairly sharply at z_{He}=3.5 (Becker et al. 2011), following a transition of hyperbolic tangent shape with width δz=0.5. While there is still some debate on whether helium reionization could be inhomogeneous and extended (and thus have an early start, Worseck et al. 2014), we have checked that varying the helium reionization redshift between 2.5 and 4.5 changes the total optical depth by less than 1 %.
The simplest and most widely-used parameterizations describes the EoR as a step-like transition between an essentially vanishing ionized fraction[3] x_e at early times, to a value of unity at low redshifts. When calculating the effect on anisotropies it is necessary to give a non-zero width to the transition, and it can be modelled using a tanh function (Lewis 2008):

$$x_e(z)=\frac{f}{2}\left[1+\tanh\left(\frac{y_{re}-y}{\delta y}\right)\right], \tag{9.2}$$

where y=$(1+z)^{3/2}$ and $\delta y=\frac{3}{2}(1+z)^{1/2}\delta z$. The key parameters are thus z_{re}, which measures the redshift at which the ionized fraction reaches half its maximum and a width δz. The tanh parameterization of the EoR transition allows us to compute the optical depth of Eq. (9.1) for a one-stage almost redshift-symmetric[4] reionization transition, where the redshift interval between the onset of the reionization process and its half completion is (by construction) equal to the interval between

[2] The reason this is not defined symmetrically is that in practice we have tighter constraints on the end of reionization than on the beginning.
[3] The ionized fraction is actually matched to the relic free electron density from recombination, calculated using `recfast` Seager et al. (2000).
[4] For convenience, we refer to this parameterization as "redshift symmetric" in the rest of the paper, even although it is actually symmetric in y rather than z. The asymmetry is maximum in the instantaneous case, but the difference in x_e values around, for example, z_{re}=8±1, is less than 1 %.

half completion and full completion. In this parameterization, the optical depth is mainly determined by $z_{\rm re}$ and almost degenerate with the width δz. This is the model used in the *Planck* 2013 and 2015 cosmological papers, for which we have fixed δz=0.5 (corresponding to Δz=1.73). In this case, we usually talk about "instantaneous" reionization.

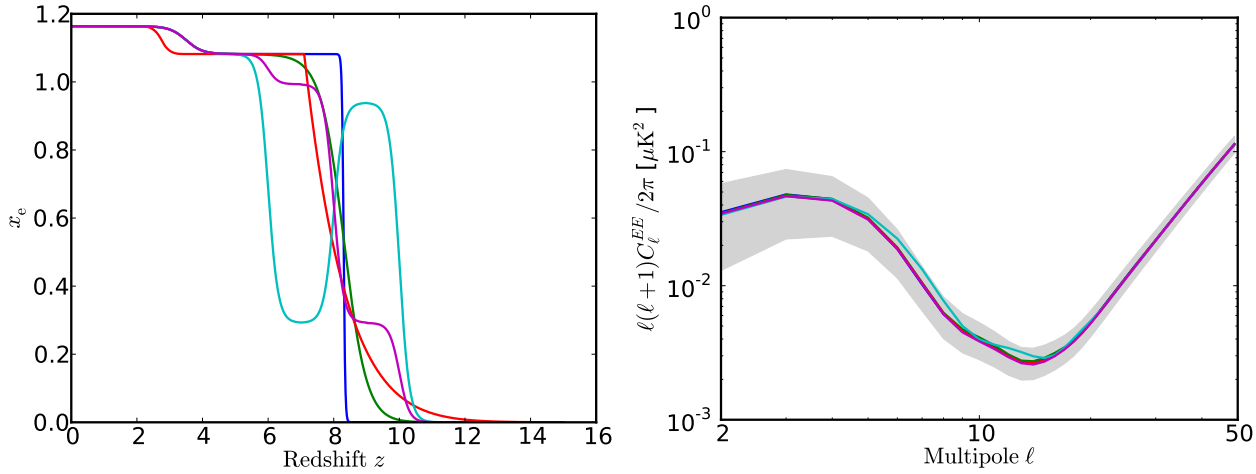

Figure 9.4: *Left*: Evolution of the ionization fraction for several functions, all having the same optical depth, τ=0.06: green and blue are for redshift-symmetric instantaneous (δz=0.05) and extended reionization (δz=0.7), respectively; red is an example of a redshift-asymmetric parameterization; and light blue and magenta are examples of an ionization fraction defined in redshift bins, with two bins inverted between these two examples. *Right*: corresponding EE power spectra with cosmic variance in grey. All models have the same optical depth τ=0.06 and are essentially indistinguishable at the reionization bump scale.

A redshift-asymmetric parameterization is a better, more flexible description of numerical simulations of the reionization process (e.g., Ahn et al. 2012; Park et al. 2013; Douspis et al. 2015). A function with this behaviour is also suggested by the constraints from ionizing background measurements of star-forming galaxies and from low-redshift line-of-sight probes such as quasars, Lyman-α emitters, or γ-ray bursts (Faisst et al. 2014; Chornock et al. 2014; Ishigaki et al. 2015; Robertson et al. 2015; Bouwens et al. 2015). The two simplest choices of redshift-asymmetric parameterizations are polynomial or exponential functions of redshift (Douspis et al. 2015). These two parameterizations are in fact very similar, and we adopt here a power law defined by two parameters: the redshift at which reionization ends ($z_{\rm end}$); and the exponent α. Specifically we have

$$x_{\rm e}(z)=\begin{cases} f & \text{for } z<z_{\rm end}, \\ f\left(\frac{z_{\rm early}-z}{z_{\rm early}-z_{\rm end}}\right)^{\alpha} & \text{for } z>z_{\rm end}. \end{cases} \tag{9.3}$$

In the following, we fix $z_{\rm early}$=20, the redshift around which the first emitting sources form, and at which we smoothly match $x_{\rm e}(z)$ to the ionized fraction left over from recombination. We checked that our results are not sensitive to the precise value of $z_{\rm early}$, as long as it is not dramatically different.

Non-parametric reconstructions of the ionization fraction have also been proposed to probe the reionization history. Such methods are based on exploring reionization parameters in bins of redshift (Lewis et al. 2006). They should be particularly useful for investigating exotic reionization histories, e.g., double reionization (Cen 2003). However, the CMB large-scale ($\ell \leq 10$) polarization anisotropies are mainly sensitive to the overall value of the optical depth, which determines the amplitude of the reionization bump in the EE power spectrum (see Fig. 9.3). We have estimated the impact on C_ℓ^{EE} for the two different models (tanh and power law) having the same τ=0.06 and found differences of less than 4 % for $\ell<10$. Even for a double reionization model, Fig. 9.4 shows that the impact on C_ℓ^{EE} is quite weak, given the actual measured value of τ, and cannot be distinguished relative to the cosmic variance spread (i.e., even for a full-sky experiment). We also checked that *Planck* data do not allow for model-independent reconstruction of $x_{\rm e}$ in redshift bins. Principal component analysis has been proposed as an explicit approach to try to capture the details of the reionization history in a small set of parameters (Hu & Holder 2003; Mortonson & Hu 2008). Although these methods are generally considered to be non-parametric, they are in fact based on a description of $x_{\rm e}(z)$ in bins of redshift, expanded around a given fiducial model for C_ℓ^{EE}. Moreover, the potential bias on the τ measurement when analysing a more complex reionization history using a simple sharp transition model (Holder et al. 2003; Colombo & Pierpaoli 2009) is considerably reduced for the (lower) τ values as suggested by the *Planck* results. Consequently, we do not consider the non-parametric approach further.

9.4 Measuring reionization observables

Reionization leaves imprints in the CMB power spectra, both in polarization at very large scales and in intensity via the suppression of TT power at higher ℓ. Reionization also affects the kSZ effect, due to the re-scattering of photons off newly

liberated electrons. We sample from the space of possible parameters with MCMC exploration using CAMEL[5]. This uses an adaptative-Metropolis algorithm to generate chains of samples for a set of parameters.

9.4.1 Large-scale CMB polarization

Thomson scattering between the CMB photons and free electrons generates linear polarization from the quadrupole moment of the CMB radiation field at the scattering epoch. This occurs at recombination and also during the epoch of reionization. Re-scattering of the CMB photons at reionization generates an additional polarization anisotropy at large angular scales, because the horizon size at this epoch subtends a much larger angular size. The multipole location of this additional anisotropy (essentially a bump) in the EE and TE angular power spectra relates to the horizon size at the new "last-rescattering surface" and thus depends on the redshift of reionization. The height of the bump is a function of the optical depth or, in other words, of the history of the reionization process. Such a signature (i.e., a polarization bump at large scales) was first observed by WMAP, initially in the TE angular power spectrum (Kogut et al. 2003), and later in combination with all power spectra (Hinshaw et al. 2013).

In Fig. 9.3 we show for the "instantaneous" reionization case (specifically the redshift-symmetric parameterization with δz=0.5) power spectra for the E-mode polarization power spectrum C_ℓ^{EE} and the temperature-polarization cross-power spectrum C_ℓ^{TE}. The curves are computed with the CLASS Boltzmann solver (Lesgourgues 2011) using τ values ranging from 0.04 to 0.08. For the range of optical depth considered here and given the amount of cosmic variance, the TE spectrum has only a marginal sensitivity to τ, while in EE the ability to distinguish different values of τ is considerably stronger.

In Fig. 9.4 (left panel), the evolution of the ionized fraction x_e during the EoR is shown for five different parameterizations of the reionization history, all yielding the same optical depth τ=0.06. Despite the differences in the evolution of the ionization fraction, the associated C_ℓ^{EE} curves (Fig. 9.4, right panel) are almost indistinguishable. This illustrates that while CMB large-scale anisotropies in polarization are only weakly sensitive to the details of the reionization history, they can nevertheless be used to measure the reionization optical depth, which is directly related to the amplitude of the low-ℓ bump in the E-mode power spectrum.

We use the *Planck* data to provide constraints on the Thomson scattering optical depth for "instantaneous" reionization. Figure 9.5 shows the posterior distributions for τ obtained with the different data sets described in Sect. 9.2 and compared to the 2015 Planck TT+lowP+lowP results (Planck Collaboration XIII 2016). We show the posterior distribution for the low-ℓ *Planck* polarized likelihood (lollipop) and in combination with the high-ℓ *Planck* likelihood in temperature (Planck TT+lowP). We also consider the effect of adding the SPT and ACT likelihoods (VHL) and the *Planck* lensing likelihood, as described in Planck Collaboration XV (2016).

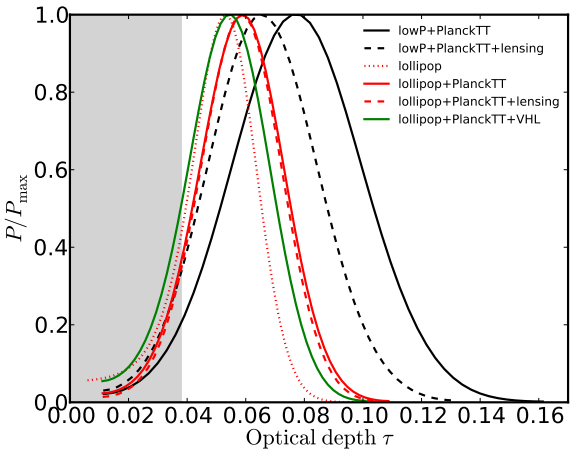

Figure 9.5: Posterior distribution for τ from the various combinations of *Planck* data. The grey band shows the lower limit on τ from the Gunn-Peterson effect.

The different data sets show compatible constraints on the optical depth τ. The comparison between posteriors indicates that the optical depth measurement is driven by the low-ℓ likelihood in polarization (i.e., lollipop). The *Planck* constraints on τ for a ΛCDM model when considering the standard "instantaneous" reionization assumption (symmetric

[5]available at camel.in2p3.fr

model with fixed δz=0.5), for the various data combinations are:

$$\tau = 0.053^{+0.014}_{-0.016}, \quad \texttt{lollipop}^{6}; \tag{9.4}$$

$$\tau = 0.058^{+0.012}_{-0.012}, \quad \texttt{lollipop}+\textsc{Planck}\ \text{TT}+\texttt{lowP}; \tag{9.5}$$

$$\tau = 0.058^{+0.011}_{-0.012}, \quad \texttt{lollipop}+\textsc{Planck}\ \text{TT}+\texttt{lowP}+\text{lensing}; \tag{9.6}$$

$$\tau = 0.054^{+0.012}_{-0.013}, \quad \texttt{lollipop}+\textsc{Planck}\ \text{TT}+\texttt{lowP}+\text{VHL}. \tag{9.7}$$

We can see an improvement of the posterior width when adding temperature anisotropy data to the `lollipop` likelihood. This comes from the fact that the temperature anisotropies help to fix other ΛCDM parameters, in particular the normalization of the initial power spectrum A_s, and its spectral index, n_s. CMB lensing also helps to reduce the degeneracy with A_s, while getting rid of the tension with the phenomenological lensing parameter A_L when using Planck TT+`lowP` only (see Planck Collaboration XIII 2016), even if the impact on the error bars is small. Comparing the posteriors in Fig. 9.6 with the constraints from Planck TT+`lowP` alone (see figure 45 in Planck Collaboration XI 2016) shows that indeed, the polarization likelihood is sufficiently powerful that it breaks the degeneracy between n_s and τ. The impact on other ΛCDM parameters is small, typically below 0.3σ (as shown more explicitly in Appendix 9.A). The largest changes are for τ and A_s, where the `lollipop` likelihood dominates the constraint. The parameter σ_8 shifts towards slightly smaller values by about 1σ. This is in the right direction to help resolve some of the tension with cluster abundances and weak galaxy lensing measurements, discussed in Planck Collaboration XX (2014) and Planck Collaboration XIII (2016); however, some tension still remains.

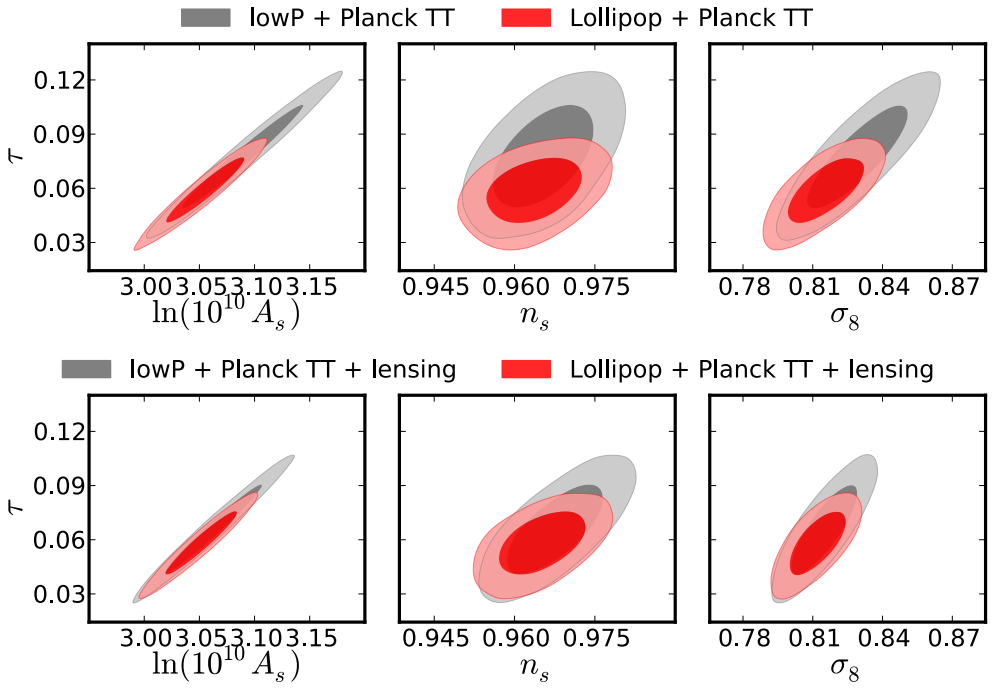

Figure 9.6: Constraints on τ, A_s, n_s, and σ_8 for the ΛCDM cosmology from Planck TT+`lowP`, showing the impact of replacing the lowP likelihood from *Planck* 2015 release with the new `lollipop` likelihood. The top panels show results without lensing, while the bottom panels are with lensing.

Combining with VHL data gives compatible results, with consistent error bars. The slight shift toward lower τ value (by 0.3σ) is related to the fact that the Planck TT+`lowP` likelihood alone pushes towards higher τ values (see Planck Collaboration XIII 2016), while the addition of VHL data helps to some extent in reducing the tension on τ between high-ℓ and low-ℓ polarization.

As mentioned earlier, astrophysics constraints from measurements of the Gunn-Peterson effect provide strong evidence that the IGM was highly ionized by a redshift of $z \simeq 6$. This places a lower limit on the optical depth (using Eq. 9.1), which in the case of instantaneous reionization in the standard ΛCDM cosmology corresponds to τ=0.038.

9.4.2 Kinetic Sunyaev-Zeldovich effect

The Thomson scattering of CMB photons off ionized electrons induces secondary anisotropies at different stages of the reionization process. In particular, we are interested here in the effect of photons scattering off electrons moving with bulk velocity, which is called the "kinetic Sunyaev Zeldovich" or kSZ effect. It is common to distinguish between the

[6] In this case only, other ΛCDM parameters are held fixed, including $A_s \exp(-2\tau)$.

"homogeneous" kSZ effect, arising when the reionization is complete (e.g., Ostriker & Vishniac 1986), and "patchy" (or inhomogeneous) reionization (e.g., Aghanim et al. 1996), which arises during the process of reionization, from the proper motion of ionized bubbles around emitting sources. These two components can be described by their power spectra, which can be computed analytically or derived from numerical simulations. In Planck Collaboration XI (2016), we used a kSZ template based on homogeneous simulations, as described in Trac et al. (2011).
In the following, we assume that the kSZ power spectrum is given by

$$\mathcal{D}_\ell^{\rm kSZ}=\mathcal{D}_\ell^{\rm h-kSZ}+\mathcal{D}_\ell^{\rm p-kSZ}, \tag{9.8}$$

where $\mathcal{D}_\ell=\ell(\ell+1)C_\ell/2\pi$ and the superscripts "h-kSZ" and "p-kSZ" stand for "homogeneous" and "patchy" reionization, respectively. For the homogeneous reionization, we use the kSZ template power spectrum given by Shaw et al. (2012) calibrated with a simulation that includes the effects of cooling and star-formation (which we label "CSF"). For the patchy reionization kSZ effect we use the fiducial model of Battaglia et al. (2013).
In the range ℓ=1000–7000, the shape of the kSZ power spectrum is relatively flat and does not vary much with the detailed reionization history. The relative contributions (specifically "CSF" and "patchy") to the kSZ power spectrum are shown in Fig 9.7 and compared to the "homogeneous" template used in Planck Collaboration XI (2016), rescaled to unity at ℓ=3000.

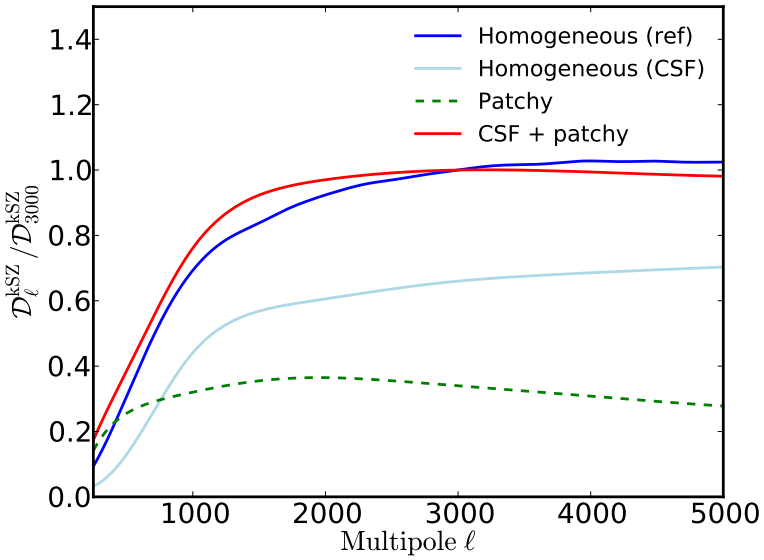

Figure 9.7: Power spectrum templates for the kSZ effect. The different lines correspond to: homogeneous reionization as used in Planck Collaboration XI (2016) (dark blue), based on Trac et al. (2011); "CSF" (light blue), which is a homogeneous reionization model from Shaw et al. (2012); Patchy (green dashed) based on patchy reionization model from Battaglia et al. (2013); and the sum of CSF and patchy (red).

The kSZ power spectrum amplitude does depend on the cosmological parameters (Shaw et al. 2012; Zahn et al. 2012). To deal with this, we adopt the scalings from Shaw et al. (2012), which gives the amplitude at ℓ=3000, $A_{\rm kSZ}\equiv\mathcal{D}^{\rm kSZ}_{\ell=3000}$:

$$A_{\rm kSZ}\propto\left(\frac{h}{0.7}\right)^{1.7}\left(\frac{\sigma_8}{0.8}\right)^{4.5}\left(\frac{\Omega_{\rm b}}{0.045}\right)^{2.1}\left(\frac{0.27}{\Omega_{\rm m}}\right)^{0.44}\left(\frac{0.96}{n_{\rm s}}\right)^{0.19}. \tag{9.9}$$

The amplitude of the kSZ power spectrum at ℓ=3000 for the fiducial cosmology, $A_{\rm kSZ}$ is another observable of the reionization history that can be probed by CMB data. Its scalings with the reionization redshift and the duration of the EoR can be extracted from simulations. We assume for the patchy and homogeneous kSZ effect, the scalings of Battaglia et al. (2013) and Shaw et al. (2012), respectively. For the *Planck* base ΛCDM cosmology given in Sect. 9.2.2, we find (in μK^2):

$$A^{\rm h}_{\rm kSZ}=2.02\times\left(\frac{\tau}{0.076}\right)^{0.44}; \tag{9.10}$$

$$A^{\rm p}_{\rm kSZ}=2.03\times\left[\left(\frac{1+z_{\rm re}}{11}\right)-0.12\right]\left(\frac{z_{25\%}-z_{75\%}}{1.05}\right)^{0.51}. \tag{9.11}$$

For the measured value τ=0.058±0.012, Eqs. (9.10) and (9.11) give amplitudes for the homogeneous and patchy reionization contributions of $A^{\rm h}_{\rm kSZ}$=1.79μK^2 and $A^{\rm p}_{\rm kSZ}$=1.01μK^2, respectively.
For the multipole range of *Planck*, the amplitude of the kSZ spectrum is dominated by other foregrounds, including Galactic dust, point sources, CIB fluctuations, and the tSZ effect. Moreover, the *Planck* signal-to-noise ratio decreases rapidly above ℓ=2000, where the kSZ signal is maximal. This is why we cannot constrain the kSZ amplitude using

Planck data alone. Combining with additional data at higher multipoles helps to disentangle the different foregrounds. We explicitly use the band powers from SPT (George et al. 2015) and ACT (Das et al. 2014), covering the multipole range up to ℓ=13000.
Despite our best efforts to account for the details, the kSZ amplitude is weak and there are large uncertainties in the models (both homogeneous and patchy). Moreover, there are correlations between the different foreground components, coming both from the astrophysics (we use the same halo model to derive the power spectra for the CIB and for CIB×tSZ as the one used for the kSZ effect) and from the adjustments in the data. We carried out several tests to check the robustness of the constraints on $A_{\rm kSZ}$ with respect to the template used for the CIB, CIB×tSZ, and kSZ contributions. In particular, the CIB×tSZ power spectrum amplitude is strongly anti-correlated with the kSZ amplitude and poorly constrained by the CMB data. As a consequence, if we neglect the CIB×tSZ contribution, the kSZ amplitude measured in CMB data is substantially reduced, leading to an upper limit much lower than the one derived when including the CIB×tSZ correlation. In the following discussion we consider only the more realistic case (and thus more conservative in terms of constraints on $A_{\rm kSZ}$) where the CIB×tSZ correlation contributes to the high-ℓ signal.
We combine the *Planck* likelihoods in TT (Planck TT+lowP) and from low-ℓ EE polarization (lollipop) with the very high-ℓ data from ACT and SPT (VHL), assuming a redshift-symmetric parameterization of the reionization. Figure 9.8 shows the 2D posterior distribution for τ and $A_{\rm kSZ}$ after marginalization over the other cosmological and nuisance parameters.

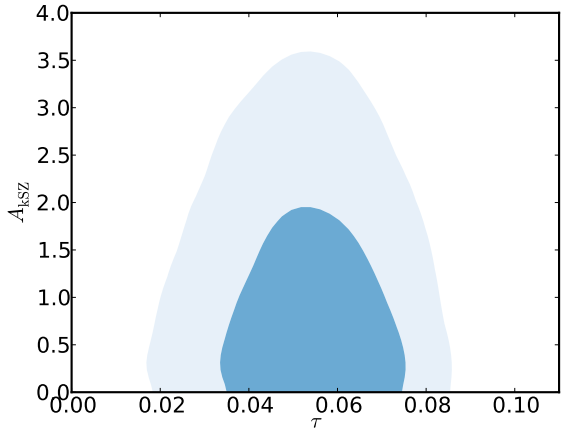

Figure 9.8: 68 % and 95 % confidence intervals on the reionization optical depth, τ, and the amplitude of the kinetic SZ effect, $A_{\rm kSZ}$, from the CMB (lollipop+Planck TT+lowP+VHL).

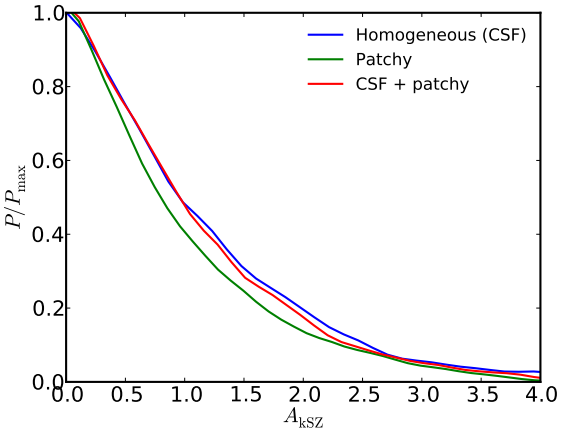

Figure 9.9: Constraints on the kSZ amplitude at ℓ=3000 using lollipop+Planck TT+lowP+VHL likelihoods. The three cases correspond to different kSZ templates.

Figure 9.9 compares the constraints on the kSZ power at ℓ=3000, $A_{\rm kSZ}$, obtained for three different kSZ templates: the "homogeneous" reionization template from Trac et al. (2011), which neglects contributions from inhomogeneous reionization; a more complex model "CSF & patchy," including both homogeneous and patchy contributions; and a pure "patchy" template from Battaglia et al. (2013). We find very similar upper limits on $A_{\rm kSZ}$, even in the case of pure patchy reionization.
Using the "CSF & patchy" model, the upper limit is

$$A_{\rm kSZ}<2.6\mu{\rm K}^2 \quad (95\ \%\ {\rm CL}). \tag{9.12}$$

Compared to *Planck* 2013 results, the maximum likelihood value $A_{\rm kSZ}=5.3^{+2.8}_{-1.9}\mu{\rm K}^2$ (Planck TT+lowP+WP+highL, Planck Collaboration XVI 2014) is reduced to an upper limit in this new analysis. The data presented here provide the best constraint to date on the kSZ power and is a factor of 2 lower than the limit reported in George et al. (2015). Our limit is certainly not in tension with the homogeneous kSZ template, which predicts $A_{\rm kSZ}=1.79\mu{\rm K}^2$. However, it does not leave much room for any additional kSZ power coming from patchy reionization.
Consistent with George et al. (2015), we find the total kSZ power to be stable against varying tSZ and CIB templates. We also find very little dependence on the choice of the kSZ template (Fig. 9.9). This confirms that there is only a modest amount of information in the angular shape of the kSZ signal with the current data.

9.5 Constraints on the reionization history

We now interpret our measurements of the reionization observables in terms of constraint on the reionization history. We mainly focus on the determination of the reionization redshift $z_{\rm re}$ and its duration $\Delta z=z_{\rm beg}-z_{\rm end}$. We show only the results for Δz greater than unity, which corresponds to approximatively 90 Myr at redshift z=8. We first begin by looking at constraints on the EoR for symmetric and asymmetric models using *Planck* data only (lollipop+Planck TT+lowP). Then we introduce the VHL data and discuss additional constraints from the kSZ amplitude. In each case, we also derive the constraints that follow from postulating that reionization should be completed at a redshift of 6 (see Sect. 9.2.1), i.e., when imposing the prior $z_{\rm end}>6$.

9.5.1 Redshift-symmetric parameterization

We use the *Planck* CMB likelihoods in temperature (Planck TT+lowP) and polarization (lollipop) to derive constraints on ΛCDM parameters, including the reionization redshift z_{re} and width Δz for a redshift-symmetric parameterization. Figure 9.10 shows (in blue) the posterior on z_{re} and Δz after marginalization over the other cosmological and nuisance parameters. As discussed in Sect. 9.3, the large-scale polarized CMB anisotropies are almost insensitive to the width δz of the tanh function. We thus recover the degeneracy in the direction of Δz. Imposing an additional Gunn-Peterson constraint on the ionization fraction at very low redshift can break this degeneracy. This is illustrated in Fig. 9.10, where we show (in green) the results of the same analysis with an additional prior $z_{end}>6$. In this case, we find $\delta z<1.3$ at 95 % CL, which corresponds to a reionization duration ($z_{beg}-z_{end}$) of

$$\Delta z<4.6 \quad (95\,\%\ \mathrm{CL}). \tag{9.13}$$

The posterior distribution of z_{re} is shown in Fig. 9.10 after marginalizing over Δz, with and without the additional constraint $z_{end}>6$. This suggests that the reionization process occurred at redshift

$$z_{re}=8.5^{+1.0}_{-1.1} \quad (\text{uniform prior}), \tag{9.14}$$

$$z_{re}=8.8^{+0.9}_{-0.9} \quad (\text{prior } z_{end}>6). \tag{9.15}$$

This redshift is lower than the values derived previously from WMAP-9 data, in combination with ACT and SPT (Hinshaw et al. 2013), namely $z_{re}=10.3\pm1.1$. It is also lower than the value $z_{re}=11.1\pm1.1$ derived in Planck Collaboration XVI (2014), based on *Planck* 2013 data and the WMAP-9 polarization likelihood.

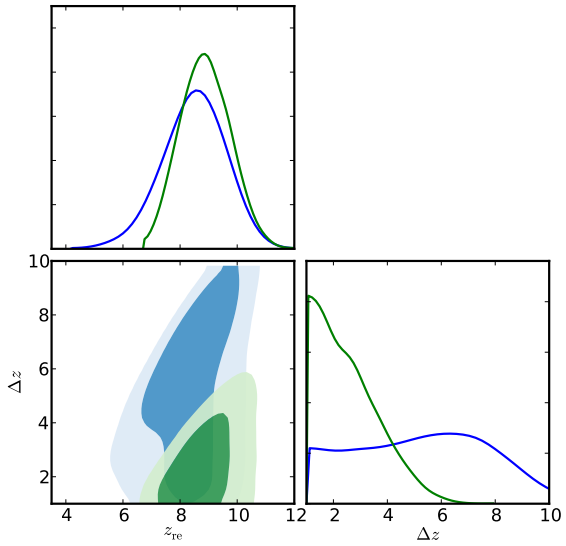

Figure 9.10: Posterior distributions (in blue) of z_{re} and Δz for a redshift-symmetric parameterization using the CMB likelihoods in polarization and temperature (lollipop+Planck TT+lowP). The green contours and lines show the distribution after imposing the additional prior $z_{end}>6$.

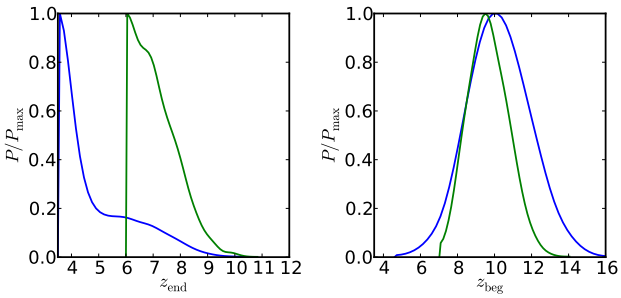

Figure 9.11: Posterior distributions on the end and beginning of reionization, i.e., z_{end} and z_{beg}, using the redshift-symmetric parameterization without (blue) and with (green) the prior $z_{end}>6$.

Although the uncertainty is now smaller, this new reionization redshift value is entirely consistent with the *Planck* 2015 results (Planck Collaboration XIII 2016) for Planck TT+lowP+lowP alone, $z_{re}=9.9^{+1.8}_{-1.6}$ or in combination with other data sets, $z_{re}=8.8^{+1.3}_{-1.2}$ (specifically for Planck TT+lowP+lowP+lensing+BAO) estimated with δz fixed to 0.5. The constraint from lollipop+Planck TT+lowP when fixing δz to 0.5 is $z_{re}=8.2^{+1.0}_{-1.2}$. This slightly lower value (compared to the one obtained when letting the reionization width be free) is explained by the shape of the degeneracy surface. Allowing for larger duration when keeping the same value of τ pushes towards higher reionization redshifts; marginalizing over Δz thus shifts the posterior distribution to slightly larger z_{re} values.
In addition to the posteriors for z_{re} and δz using the redshift-symmetric parameterization, the distributions of the end and beginning of reionization, z_{end} (i.e., $z_{99\%}$) and z_{beg} (i.e., $z_{10\%}$), are plotted in Fig. 9.11. In such a model, the end of reionization strongly depends on the constraint at low redshift. On the other hand, the constraints on z_{beg} depend only slightly on the low-redshift prior. These results show that the Universe is ionized at less than the 10 % level above $z=9.4\pm1.2$.

9.5.2 Redshift-asymmetric parameterization

We now explore more complex reionization histories using the redshift-asymmetric parameterization of $x_e(z)$ described in Sect. 9.3. In the same manner as in Sect. 9.5.1, also examine the effect of imposing the additional constraint from the Gunn-Peterson effect.

The distributions of the two parameters, $z_{\rm end}$ and $z_{\rm beg}$, are plotted in Fig. 9.13. With the redshift-asymmetric parameterization, we obtain $z_{\rm beg}=10.4^{+1.9}_{-1.6}$ (imposing the prior on $z_{\rm end}$), which disfavours any major contribution to the ionized fraction from sources that could form as early as $z\geq15$.

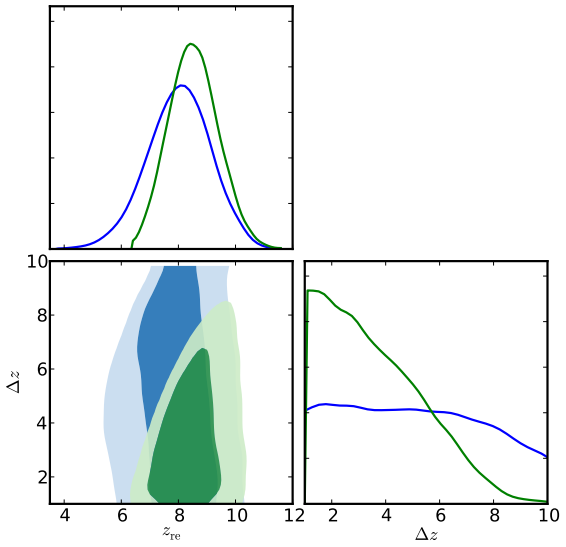

Figure 9.12: Posterior distributions for $z_{\rm re}$ and Δz using the redshift-asymmetric parameterization without (blue) and with (green) the prior $z_{\rm end}>6$.

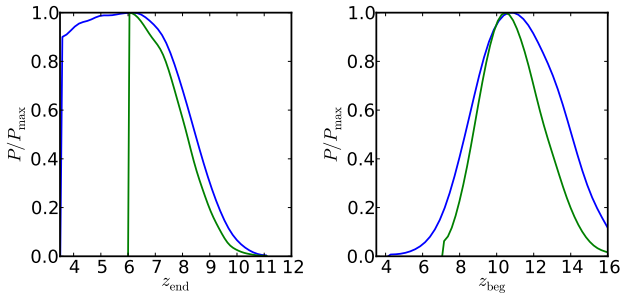

Figure 9.13: Posterior distributions of $z_{\rm end}$ and $z_{\rm beg}$ using the redshift-asymmetric parameterization without (blue) and with (green) the prior $z_{\rm end}>6$.

In Fig. 9.12, we interpret the results in terms of reionization redshift and duration of the EoR, finding

$$z_{\rm re}=8.0^{+0.9}_{-1.1} \quad \text{(uniform prior)}, \tag{9.16}$$

$$z_{\rm re}=8.5^{+0.9}_{-0.9} \quad \text{(prior } z_{\rm end}>6\text{)}. \tag{9.17}$$

These values are within 0.4σ of the results for the redshift-symmetric model. For the duration of the EoR, the upper limits on Δz are

$$\Delta z<10.2 \quad \text{(95 \% CL, unform prior)}, \tag{9.18}$$

$$\Delta z<\ 6.8 \quad \text{(95 \% CL, prior } z_{\rm end}>6\text{)}. \tag{9.19}$$

9.5.3 Combination with the kSZ effect

In order to try to obtain better constraints on the reionization width, we now make use of the additional information coming from the amplitude of the kinetic SZ effect. Since *Planck* alone is not able to provide accurate limits on the kSZ amplitude, we combine the *Planck* likelihoods in temperature and polarization with the measurements of the CMB TT power spectrum at high-resolution from the ACT and SPT experiments, "VHL."

Using the redshift-symmetric model, when adding the VHL data, we recover essentially the same results as in Sect. 9.5.1. The reionization redshift is slightly lower, as suggested by the results on τ (see Eq. 9.7 and the discussion in Sect. 9.4.1). We also see the same degeneracy along the Δz direction.

With the addition of kSZ information, we are able to break the degeneracy with Δz. This might allow us to determine how much kSZ power originated during reionization (i.e., patchy kSZ) and how much at later times, when the Universe became fully ionized (i.e., homogeneous kSZ). We use the templates from Shaw et al. (2012) and Battaglia et al. (2013) for the homogeneous and patchy kSZ contributions, respectively, with the dependency on ΛCDM cosmological parameters as described in Sect. 9.4.2. Those specific relations rely on a redshift-symmetric model for the description of the EoR. Note, however, that the results presented here are derived from specific simulations of the reionization process, and so explicit scalings need to be assumed, as discussed by Zahn et al. (2012) and George et al. (2015).

As described in Sect. 9.4.2, the amplitude of the kSZ power primarily depends on the duration of reionization, while the epoch is essentially constrained by the optical depth. Using the 2D distribution for τ and $A_{\rm kSZ}$, as measured by *Planck* in combination with very high-ℓ temperature data (Fig. 9.8), we derive a 2D likelihood function for $z_{\rm re}$ and Δz. We can then sample the reionization parameters (the epoch $z_{\rm re}$ and duration Δz of the EoR), compute the associated optical depth and kSZ power and derive constraints based on the 2D likelihood. The allowed models in terms of $z_{\rm re}$ and Δz are shown in Fig. 9.14 (in blue). We also plot (in green) the same constraints with the additional prior $z_{\rm end}>6$.

As discussed in Sect. 9.4.2, the measurement of the total kSZ power constrains the amplitude of patchy reionization, resulting in an upper limit of

$$\Delta z<4.8 \quad \text{(95 \% CL, uniform prior)}, \tag{9.20}$$

$$\Delta z<2.8 \quad \text{(95 \% CL, prior } z_{\rm end}>6\text{)}. \tag{9.21}$$

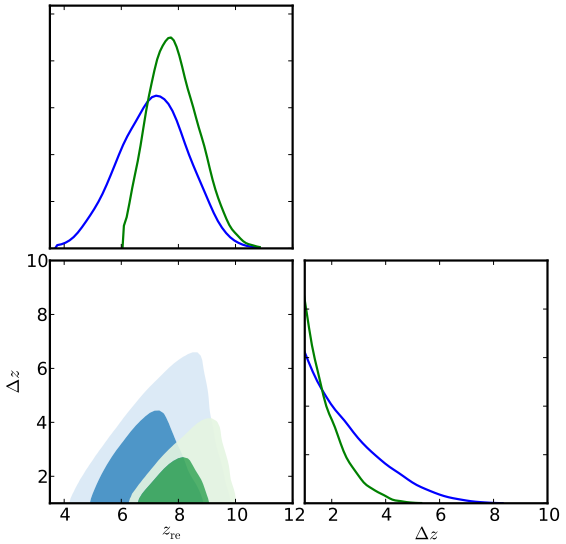

Figure 9.14: Posterior distributions on the duration Δz and the redshift z_{re} of reionization from the combination of CMB polarization and kSZ effect constraints using the redshift-symmetric parameterization without (blue) and with (green) the prior $z_{end}>6$.

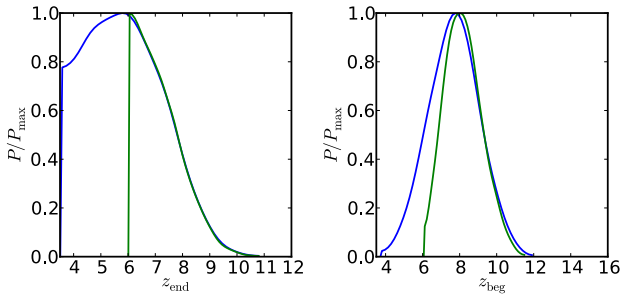

Figure 9.15: Posterior distributions of z_{end} and z_{beg} using the redshift-symmetric parameterization, combining *Planck* and VHL data, and using information from the kSZ amplitude, without (blue) and with (green) the prior $z_{end}>6$.

This is compatible with the constraints from George et al. (2015), where an upper limit was quoted of $z_{20\%}-z_{99\%}<5.4$ at 95 % CL. Our 95 % CL upper limits on this same quantity are 4.3 and 2.5 without and with the prior on z_{end}, respectively. For the reionization redshift, we find

$$z_{re}=7.2^{+1.2}_{-1.2} \quad \text{(uniform prior)}, \tag{9.22}$$

$$z_{re}=7.8^{+1.0}_{-0.8} \quad \text{(prior } z_{end}>6\text{)}, \tag{9.23}$$

which is compatible within 1σ with the results from CMB *Planck* data alone without the kSZ constraint (Sect. 9.5.1). The distributions of z_{end} and z_{beg} are plotted in Fig. 9.15. Within the redshift-symmetric parameterization, we obtain $z_{beg}=8.1^{+1.1}_{-0.9}$ (with the prior on z_{end}).
Adding information from the kSZ amplitude allows for somewhat tighter constraints to be placed on the reionization duration Δz and the beginning of reionization (corresponding to the 10 % ionization limit) z_{beg}. However, as discussed in Sect. 9.4.2, those results are very sensitive to details of the simulations used to predict both the shape and the parameter dependences of the kSZ template in the different reionization scenarios (patchy or homogeneous).

9.6 Discussion

The CMB has long held the promise of measuring the Thomson optical depth in order to derive constraints on the reionization history of the Universe. Despite its importance, this constraint is fundamentally limited by cosmic variance in polarization and is further challenged by foregrounds and systematic effects. The first results, from *WMAP*, gave $\tau=0.17\pm0.04$, suggesting a reionization redshift between 11 and 30 (Kogut et al. 2003). This was revised in the final 9-year *WMAP* results to a central value of $\tau=0.084$ (Hinshaw et al. 2013), which, in the instantaneous reionization model, implies $z_{re}=10.4$. However, with the context of the same model, the *Planck* 2015 results (Planck Collaboration XIII 2016), either alone ($z_{re}=9.9^{+1.8}_{-1.6}$) or in combination with other data sets ($z_{re}=8.8^{+1.3}_{-1.2}$), showed that the reionization redshift was smaller. The main result we present here, $z_{re}=8.2^{+1.0}_{-1.2}$, further confirms that reionization occurred rather late, leaving little room for any significant ionization at $z\geq15$. This is consistent with what is suggested by other reionization probes, which we now discuss (for reviews, see e.g., Becker et al. 2015; McQuinn 2015).
The transition from neutral to ionized gas is constrained by absorption spectra of very distant quasars and gamma ray bursts (GRBs), revealing neutral hydrogen in intergalactic clouds. They show, through the Gunn-Peterson effect, that the diffuse gas in the Universe is mostly ionized up to a redshift of about 6 (Fan et al. 2006a). Given the decline in their abundance beyond redshift $z\simeq6$, quasars and other active galactic nuclei (AGN) cannot be major contributors to the early stages of reionization (e.g., Willott et al. 2010; Fontanot et al. 2012, but see Madau & Haardt 2015; Khaire et al. 2016, for alternative AGN-only models). A faint AGN population can produce significant photoionization rates at redshifts of 4–6.5, consistent with the observed highly ionized IGM in the Ly-α forest of high-z quasar spectra (Giallongo et al. 2015). Star-forming galaxies at redshifts $z\geq6$ have therefore been postulated to be the most likely sources of early reionization, and their time-dependent abundance and spectral properties are crucial ingredients for understanding how intergalactic hydrogen ceased to be neutral (for reviews, see Barkana & Loeb 2001; Fan et al. 2006a; Robertson et al. 2010; McQuinn 2015). The luminosity function of early star-forming galaxies, in particular in the UV domain, is thus an additional and

powerful probe of the reionization history (e.g., Kuhlen & Faucher-Giguère 2012; Robertson et al. 2013, 2015; Bouwens et al. 2015). Based on comparison of the 9-year WMAP results to optical depth values inferred from the UV luminosity function of high-z galaxies, it has been suggested that either the UV luminosity density flattens, or physical parameters such as the escape fraction and the clumping factor evolved significantly, or alternatively, additional, undetected sources (such as X-ray binaries and faint AGN) must have existed at $z \geq 11$ (e.g., Kuhlen & Faucher-Giguère 2012; Ellis et al. 2013; Cai et al. 2014; Ishigaki et al. 2015).

The *Planck* results, both from the 2015 data release and those presented here, strongly reduce the need for a significant contribution of Lyman continuum emission at early times. Indeed, as shown in Fig. 9.16, the present CMB results on the Thomson optical depth, $\tau = 0.058 \pm 0.012$, are perfectly consistent with the best models of star-formation rate densities derived from the UV and IR luminosity functions, as directly estimated from observations of high-redshift galaxies (Ishigaki et al. 2015; Robertson et al. 2015; Bouwens et al. 2015). With the present value of τ, if we maintain a UV-luminosity density at the maximum level allowed by the luminosity density constraints at redshifts $z < 9$, then the currently observed galaxy population at $M_{\rm UV} < -17$ seems to be sufficient to comply with all the observational constraints without the need for high-redshift ($z = 10$–15) galaxies.

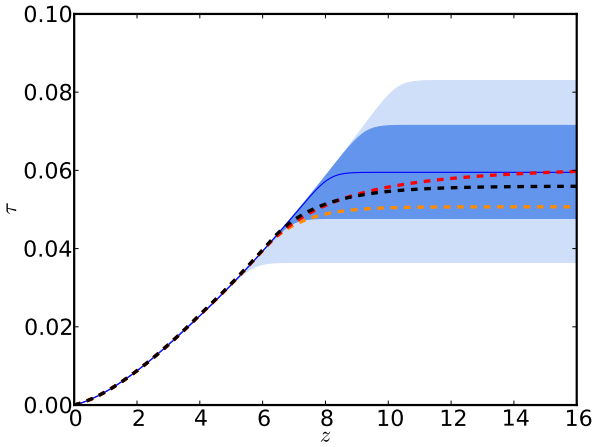

Figure 9.16: Evolution of the integrated optical depth for the tanh functional form (with $\delta z = 0.5$, blue shaded area). The two envelopes mark the 68 % and 95 % confidence intervals. The red, black, and orange dashed lines are the models from Bouwens et al. (2015), Robertson et al. (2015), and Ishigaki et al. (2015), respectively, using high-redshift galaxy UV and IR fluxes and/or direct measurements.

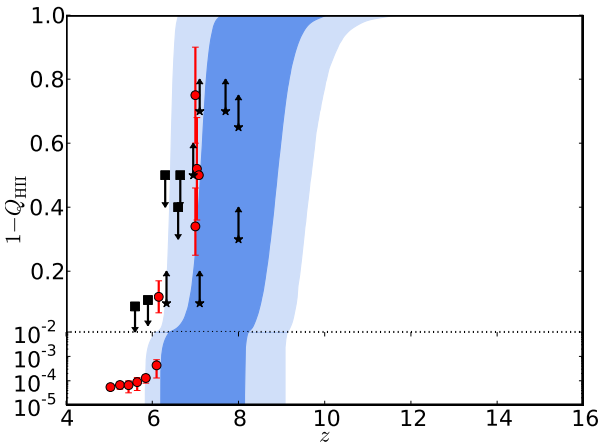

Figure 9.17: Reionization history for the redshift-symmetric parameterization compared with other observational constraints coming from quasars, Ly-α emitters, and the Ly-α forest (compiled by Bouwens et al. 2015). The red points are measurements of ionized fraction, while black arrows mark upper and lower limits. The dark and light blue shaded areas show the 68 % and 95 % allowed intervals, respectively.

The *Planck* data are certainly consistent with a fully reionized Universe at $z \simeq 6$. Moreover, they seem to be in good agreement with recent observational constraints on reionization in the direction of particular objects. The H I absorption along the line of sight to a distant γ-ray burst, GRB-140515A (Chornock et al. 2014), suggests a Universe containing about a 10 % fraction of neutral hydrogen at $z = 6$–6.3. At even higher redshifts $z \simeq 7$, observation of Ly-α emitters suggests that at least 70 % of the IGM is neutral (Tilvi et al. 2014; Schenker et al. 2014; Faisst et al. 2014). Similarly, quasar near-zone detection and analysis (including sizes, and Ly-α and β transmission properties) have been used to place constraints on $z_{\rm end}$ from signatures of the ionization state of the IGM around individual sources (Wyithe & Loeb 2004; Mesinger & Haiman 2004; Wyithe et al. 2005; Mesinger & Haiman 2007; Carilli et al. 2010; Mortlock et al. 2011; Schroeder et al. 2013). However, interpretation of the observed evolution of the near-zone sizes may be complicated by the opacity caused by absorption systems within the ionized IGM (e.g., Bolton et al. 2011; Bolton & Haehnelt 2013; Becker et al. 2015). Similarly, it is difficult to completely exclude the possibility that damped Ly-α systems contribute to the damping wings of quasar spectra blueward of the Ly-α line (e.g., Mesinger & Furlanetto 2008; Schroeder et al. 2013). Nevertheless, most such studies, indicate that the IGM is significantly neutral at redshifts between 6 and 7 (see also Keating et al. 2015), in agreement with the current *Planck* results, as shown in Fig. 9.17.

Although there are already all the constraints described above, understanding the formation of the first luminous sources in the Universe is still very much a work in progress. Our new (and lower) value of the optical depth leads to better agreement between the CMB and other astrophysical probes of reionization; however, the fundamental questions remain regarding how reionization actually proceeded.

9.7 Conclusions

We have derived constraints on cosmic reionization using *Planck* data. The CMB *Planck* power spectra, combining the EE polarization at low-ℓ with the temperature data, give, for a so-called "instantaneous" reionization history (a redshift-

symmetric tanh function $x_e(z)$ with δz=0.5), a measurement of the Thomson optical depth

$$\tau=0.058\pm0.012 \quad (\texttt{lollipop}+\textsc{Planck}\ \text{TT}+\texttt{lowP}), \tag{9.24}$$

which is significantly more accurate than previous measurements. Thanks to the relatively high signal-to-noise ratio of the low-ℓ polarization signal, the combination with lensing or data from high-resolution CMB anisotropy experiments (ACT and SPT) does not bring much additional constraining power. The impact on other ΛCDM parameters is only significant for the amplitude of the initial scalar power spectrum A_s and (to a lesser extent) on its tilt n_s. Other parameters are very stable compared to the *Planck* 2015 results.

Using *Planck* data, we have derived constraints on two models for the reionization history $x_e(z)$ that are commonly used in the literature: a redshift-symmetric form using a hyperbolic tangent transition function; and a redshift-asymmetric form parameterized by a power law. We have also investigated the effect of imposing the condition that the reionization is completed by z=6.

Allowing the ionization fraction shape and duration to vary, we have found very compatible best-fit estimates for the optical depth (0.059 and 0.060 for the symmetric and asymmetric model, respectively), showing that the CMB is indeed more sensitive to the value of the optical depth than to the exact shape of the reionization history. However, the value of the reionization redshift does slightly depend on the model considered. In the case of a symmetric parameterization, we have found slightly larger estimates of z_{re} than in the case of instantaneous reionization. This can be understood through the shape of the degeneracy surface between the reionization parameters. For an asymmetric parameterization, z_{re} is smaller, due to the fact that $x_e(z)$ changes more rapidly at the end of reionization than the beginning. We specifically find:

$$z_{re}=8.8\pm0.9 \quad \text{(redshift-symmetric)}, \tag{9.25}$$

$$z_{re}=8.5\pm0.9 \quad \text{(redshift-asymmetric)}\ . \tag{9.26}$$

Assuming two different parameterizations of the reionization history shows how much results on effective parameters (like the redshift of reionization or its duration) are sensitive to the assumption of the reionization history shape. The best models of symmetric and asymmetric parameterization give similar values for τ, and provide reionization redshifts which differ by less than 0.4σ. Constraints on the limits of possible early reionization are similar, leading to 10 % reionization levels at around z=10.

To derive constraints on the duration of the reionization epoch, we combined CMB data with measurements of the amplitude of the kSZ effect. In the case of a redshift-symmetric model, we found

$$\Delta z<2.8 \quad (95\ \%\ \text{CL}), \tag{9.27}$$

using the additional constraint that the Universe is entirely reionized at redshift 6 (i.e., z_{end}>6).

Our final constraints on the reionization history are summarized on Table 9.1 and plotted in Fig. 9.18 for each of the aforementioned cases, i.e., the redshift-symmetric and redshift-asymmetric models, using only the CMB, and the redshift-symmetric case using CMB+kSZ (all with prior z_{end}>6). Plotted this way, the constraints are not very tight and are still fairly model dependent. Given the low value of τ as measured now by *Planck*, the CMB is not able to give tight constraints on details of the reionization history. However, the *Planck* data suggest that an early onset of reionization is disfavoured. In particular, in all cases, we found that the Universe was less than 10 % ionized for redshift z>10. Furthermore, comparisons with other tracers of the ionization history show that our new result on the optical depth eliminates most of the tension between CMB-based analyses and constraints from other astrophysical data. Additional sources of reionization, non-standard early galaxies, or significantly evolving escape fractions or clumping factors, are thus not needed.

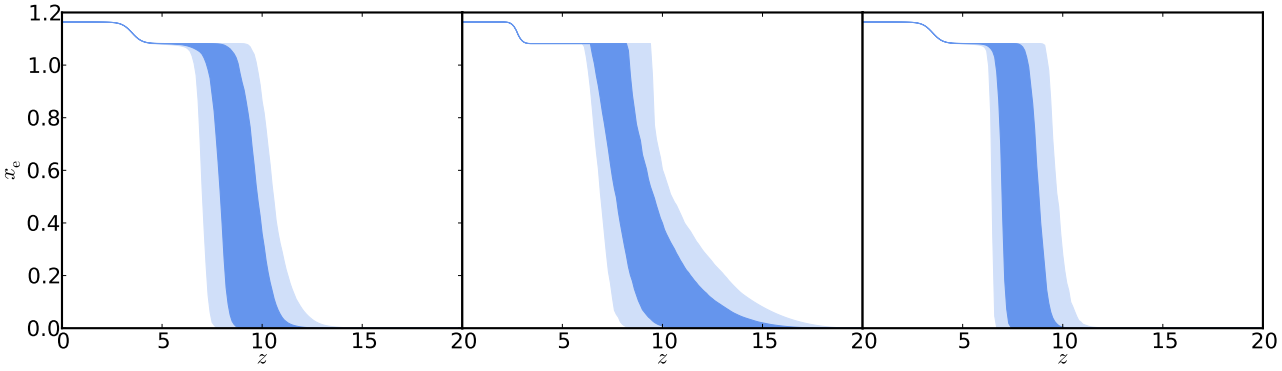

Figure 9.18: Constraints on ionization fraction during reionization. The allowed models, in terms of z_{re} and Δz, translate into an allowed region in $x_e(z)$ (68 % and 95 % in dark blue and light blue, respectively), including the z_{end}>6 prior here. *Left*: Constraints from CMB data using a redshift-symmetric function ($x_e(z)$ as a hyperbolic tangent with δz=0.5). *Centre*: Constraints from CMB data using a redshift-asymmetric parameterization ($x_e(z)$ as a power law). *Right*: Constraints from CMB data using a redshift-symmetric parameterization with additional constraints from the kSZ effect.

Ongoing and future experiments like LOFAR, MWA, and SKA, aimed at measuring the redshifted 21-cm signal from neutral hydrogen during the EoR, should be able to probe reionization directly and measure its redshift and duration to high accuracy. Moreover, since reionization appears to happen at redshifts below 10, experiments measuring the global emission of the 21-m line over the sky (e.g., EDGES, Bowman & Rogers 2010, LEDA, Greenhill & Bernardi 2012, DARE, Burns et al. 2012), NenuFAR, Zarka et al. 2012, SARAS, Patra et al. 2013, SCI-HI, Voytek et al. 2014, ZEBRA, Mahesh et al. 2014, and BIGHORNS, Sokolowski et al. 2015) will also be able to derive very competitive constraints on the models (e.g., Liu et al. 2016; Fialkov & Loeb 2016).

model	z_{re}	Δz	z_{end}	z_{beg}
redshift-symmetric	8.8±0.9	<4.6	<8.6	9.4±1.2
redshift-asymmetric . . .	8.5±0.9	<6.8	<8.9	10.4±1.8
redshift-symetrical with kSZ	7.8±0.9	<2.8	<8.8	8.1±1.0

Table 9.1: Constraints on reionization parameters for the different models presented in this paper when including the z_{end}>6 prior. We show 68% limit for z_{re} and z_{beg}, while we quote 95% upper limit for Δz and z_{end}.

The Planck Collaboration acknowledges the support of: ESA; CNES, and CNRS/INSU-IN2P3-INP (France); ASI, CNR, and INAF (Italy); NASA and DoE (USA); STFC and UKSA (UK); CSIC, MINECO, JA, and RES (Spain); Tekes, AoF, and CSC (Finland); DLR and MPG (Germany); CSA (Canada); DTU Space (Denmark); SER/SSO (Switzerland); RCN (Norway); SFI (Ireland); FCT/MCTES (Portugal); ERC and PRACE (EU). A description of the Planck Collaboration and a list of its members, indicating which technical or scientific activities they have been involved in, can be found at http://www.cosmos.esa.int/web/planck/planck-collaboration.

Appendix

9.A Impact on ΛCDM parameters

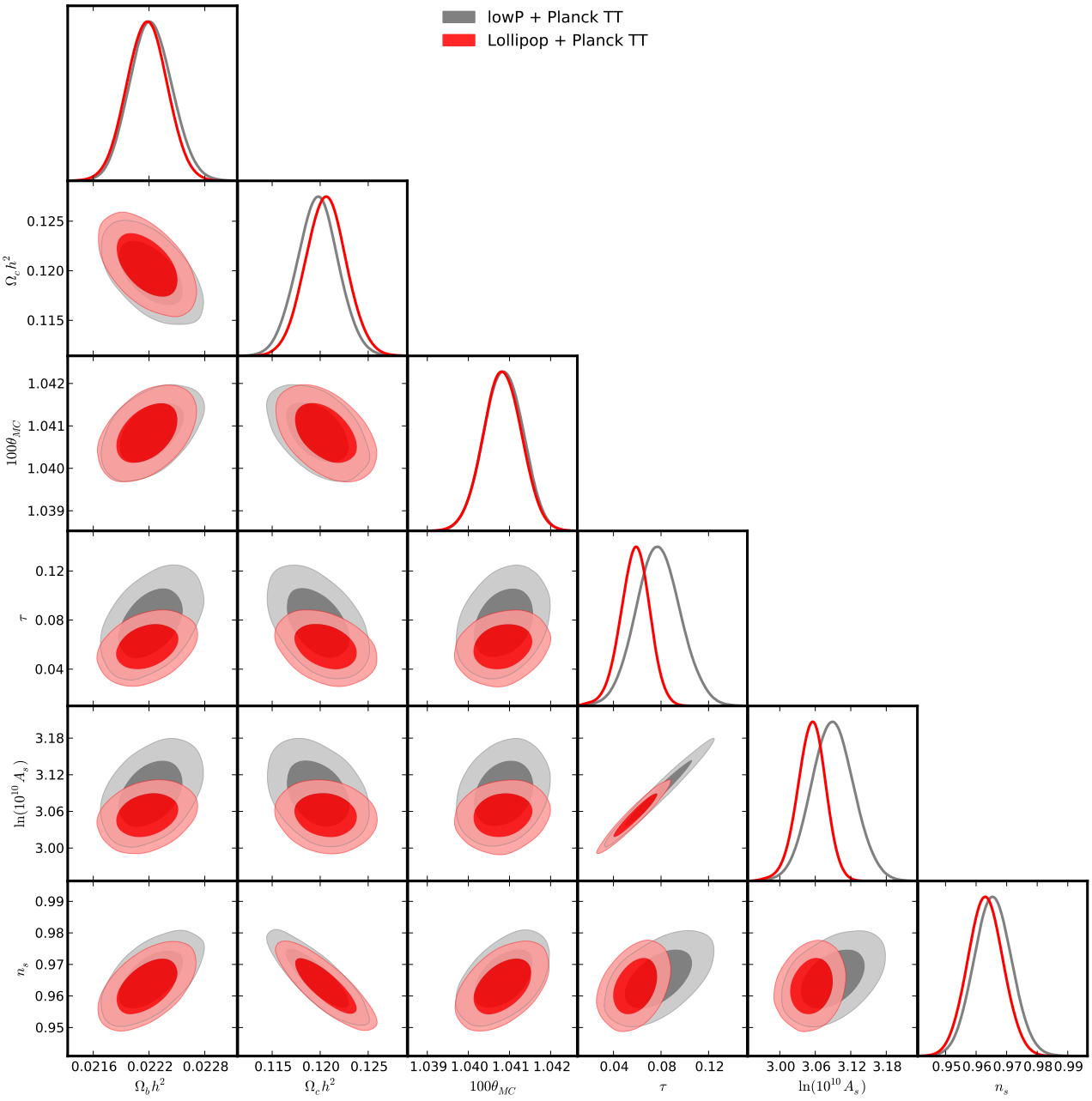

Figure 9.19: ΛCDM parameters for Planck TT+lowP combined with the low-ℓ polarization likelihood from the *Planck* 2015 release (lowP, in grey) and from this work (lollipop, in red).

In addition to the restricted parameter set shown in Fig. 9.6, we describe here the impact of the lollipop likelihood on ΛCDM parameters in general. Figure 9.19 compares results from lollipop+Planck TT+lowP with the lowP+Planck TT+lowP 2015. The new low-ℓ polarization results are sufficiently powerful that they break the degeneracy between n_s and τ. The contours for τ and A_s, where the lollipop likelihood dominates the constraint, are significantly reduced. The impact on other ΛCDM parameters are small, typically below 0.3σ.

Bibliography

Aghanim, N., Desert, F. X., Puget, J. L., & Gispert, R. 1996, A&A, 311, 1
Aghanim, N., Majumdar, S., & Silk, J. 2008, Reports on Progress in Physics, 71, 066902
Ahn, K., Iliev, I. T., Shapiro, P. R., et al. 2012, ApJ, 756, L16
Barkana, R. & Loeb, A. 2001, Phys. Rep., 349, 125
Battaglia, N., Natarajan, A., Trac, H., Cen, R., & Loeb, A. 2013, ApJ, 776, 83
Becker, G. D., Bolton, J. S., Haehnelt, M. G., & Sargent, W. L. W. 2011, MNRAS, 410, 1096
Becker, G. D., Bolton, J. S., & Lidz, A. 2015, PASA, 32, e045
Becker, R. H., Fan, X., White, R. L., et al. 2001, AJ, 122, 2850
Bolton, J. S. & Haehnelt, M. G. 2013, MNRAS, 429, 1695
Bolton, J. S., Haehnelt, M. G., Warren, S. J., et al. 2011, MNRAS, 416, L70
Bouwens, R. J., Illingworth, G. D., Oesch, P. A., et al. 2015, ApJ, 811, 140
Bowman, J. D. & Rogers, A. E. E. 2010, Nature, 468, 796
Burns, J. O., Lazio, J., Bale, S., et al. 2012, Advances in Space Research, 49, 433
Cai, Z.-Y., Lapi, A., Bressan, A., et al. 2014, ApJ, 785, 65
Calabrese, E., Hlozek, R. A., Battaglia, N., et al. 2013, Phys. Rev. D, 87, 103012
Carilli, C. L., Wang, R., Fan, X., et al. 2010, ApJ, 714, 834
Cen, R. 2003, ApJ, 591, 12
Chornock, R., Berger, E., Fox, D. B., et al. 2014, ArXiv e-prints [arXiv:1405.7400]
Ciardi, B., Ferrara, A., & White, S. D. M. 2003, MNRAS, 344, L7
Colombo, L. P. L. & Pierpaoli, E. 2009, New A, 14, 269
Couchman, H. M. P. & Rees, M. J. 1986, MNRAS, 221, 53
Das, S., Louis, T., Nolta, M. R., et al. 2014, J. Cosmology Astropart. Phys., 4, 14
Douspis, M., Aghanim, N., Ilić, S., & Langer, M. 2015, A&A, 580, L4
Dunkley, J., Komatsu, E., Nolta, M. R., et al. 2009, ApJS, 180, 306
Ellis, R. S., McLure, R. J., Dunlop, J. S., et al. 2013, ApJ, 763, L7
Faisst, A. L., Capak, P., Carollo, C. M., Scarlata, C., & Scoville, N. 2014, ApJ, 788, 87
Fan, X., Strauss, M. A., Becker, R. H., et al. 2006a, AJ, 132, 117
Fan, X., Strauss, M. A., Richards, G. T., et al. 2006b, AJ, 131, 1203
Fialkov, A. & Loeb, A. 2016, ApJ, 821, 59
Fontanot, F., Cristiani, S., & Vanzella, E. 2012, MNRAS, 425, 1413
Furlanetto, S. R., Zaldarriaga, M., & Hernquist, L. 2004, ApJ, 613, 1
George, E. M., Reichardt, C. L., Aird, K. A., et al. 2015, ApJ, 799, 177
Giallongo, E., Grazian, A., Fiore, F., et al. 2015, A&A, 578, A83
Gnedin, N. Y. 2000, ApJ, 535, 530
Greenhill, L. J. & Bernardi, G. 2012, ArXiv e-prints [arXiv:1201.1700]
Gruzinov, A. & Hu, W. 1998, ApJ, 508, 435
Gunn, J. E. & Peterson, B. A. 1965, ApJ, 142, 1633
Hamimeche, S. & Lewis, A. 2008, Phys. Rev. D, 77, 103013
Hasselfield, M., Moodley, K., Bond, J. R., et al. 2013, ApJS, 209, 17
Hinshaw, G., Larson, D., Komatsu, E., et al. 2013, ApJS, 208, 19
Holder, G. P., Haiman, Z., Kaplinghat, M., & Knox, L. 2003, ApJ, 595, 13
Hu, W. & Holder, G. P. 2003, Phys. Rev. D, 68, 023001
Iliev, I. T., Mellema, G., Ahn, K., et al. 2014, MNRAS, 439, 725
Ishigaki, M., Kawamata, R., Ouchi, M., et al. 2015, ApJ, 799, 12
Keating, L. C., Haehnelt, M. G., Cantalupo, S., & Puchwein, E. 2015, MNRAS, 454, 681
Khaire, V., Srianand, R., Choudhury, T. R., & Gaikwad, P. 2016, MNRAS, 457, 4051
Kogut, A., Spergel, D. N., Barnes, C., et al. 2003, ApJS, 148, 161
Komatsu, E., Smith, K. M., Dunkley, J., et al. 2011, ApJS, 192, 18
Kuhlen, M. & Faucher-Giguère, C.-A. 2012, MNRAS, 423, 862
Lesgourgues, J. 2011, ArXiv e-prints [arXiv:1104.2932]
Lewis, A. 2008, Phys. Rev. D, 78, 023002
Lewis, A., Weller, J., & Battye, R. 2006, MNRAS, 373, 561
Liu, A., Pritchard, J. R., Allison, R., et al. 2016, Phys. Rev. D, 93, 043013
Madau, P. & Haardt, F. 2015, ApJ, 813, L8
Madau, P., Haardt, F., & Rees, M. J. 1999, ApJ, 514, 648
Mahesh, N., Subrahmanyan, R., Udaya Shankar, N., & Raghunathan, A. 2014, ArXiv e-prints [arXiv:1406.2585]
Mangilli, A., Plaszczynski, S., & Tristram, M. 2015, MNRAS, 453, 3174
McQuinn, M. 2015, ArXiv e-prints [arXiv:1512.00086]
McQuinn, M., Furlanetto, S. R., Hernquist, L., Zahn, O., & Zaldarriaga, M. 2005, ApJ, 630, 643
Meiksin, A. & Madau, P. 1993, ApJ, 412, 34

Mesinger, A., ed. 2016, Astrophysics and Space Science Library, Vol. 423, Understanding the Epoch of Cosmic Reionization (Springer International Publishing)
Mesinger, A. & Furlanetto, S. R. 2008, MNRAS, 385, 1348
Mesinger, A. & Haiman, Z. 2004, ApJ, 611, L69
Mesinger, A. & Haiman, Z. 2007, ApJ, 660, 923
Mesinger, A., McQuinn, M., & Spergel, D. N. 2012, MNRAS, 422, 1403
Miralda-Escude, J. & Ostriker, J. P. 1990, ApJ, 350, 1
Mitra, S., Choudhury, T. R., & Ferrara, A. 2011, MNRAS, 413, 1569
Mortlock, D. J., Warren, S. J., Venemans, B. P., et al. 2011, Nature, 474, 616
Mortonson, M. J. & Hu, W. 2008, ApJ, 672, 737
Ostriker, J. P. & Vishniac, E. T. 1986, ApJ, 306, L51
Page, L., Hinshaw, G., Komatsu, E., et al. 2007, ApJS, 170, 335
Pandolfi, S., Ferrara, A., Choudhury, T. R., Melchiorri, A., & Mitra, S. 2011, Phys. Rev. D, 84, 123522
Park, H., Shapiro, P. R., Komatsu, E., et al. 2013, ApJ, 769, 93
Patra, N., Subrahmanyan, R., Raghunathan, A., & Udaya Shankar, N. 2013, Experimental Astronomy, 36, 319
Peebles, P. J. E. 1968, ApJ, 153, 1
Planck Collaboration XV. 2014, A&A, 571, A15
Planck Collaboration XVI. 2014, A&A, 571, A16
Planck Collaboration XX. 2014, A&A, 571, A20
Planck Collaboration II. 2016, A&A, in press [arXiv:1502.01583]
Planck Collaboration VII. 2016, A&A, in press [arXiv:1502.01586]
Planck Collaboration VIII. 2016, A&A, in press [arXiv:1502.01587]
Planck Collaboration IX. 2016, A&A, in press [arXiv:1502.05956]
Planck Collaboration X. 2016, A&A, in press [arXiv:1502.01588]
Planck Collaboration XI. 2016, A&A, in press [arXiv:1507.02704]
Planck Collaboration XIII. 2016, A&A, in press [arXiv:1502.01589]
Planck Collaboration XV. 2016, A&A, in press [arXiv:1502.01591]
Planck Collaboration Int. XLVI. 2016, A&A, submitted [arXiv:1605.02985]
Planck Collaboration Int. XLVII. 2016, A&A, submitted [arXiv:1605.03507]
Pritchard, J. R., Loeb, A., & Wyithe, J. S. B. 2010, MNRAS, 408, 57
Reichardt, C. L., Shaw, L., Zahn, O., et al. 2012, ApJ, 755, 70
Robertson, B. E., Ellis, R. S., Dunlop, J. S., McLure, R. J., & Stark, D. P. 2010, Nature, 468, 49
Robertson, B. E., Ellis, R. S., Furlanetto, S. R., & Dunlop, J. S. 2015, ApJ, 802, L19
Robertson, B. E., Furlanetto, S. R., Schneider, E., et al. 2013, ApJ, 768, 71
Schenker, M. A., Ellis, R. S., Konidaris, N. P., & Stark, D. P. 2014, ApJ, 795, 20
Schroeder, J., Mesinger, A., & Haiman, Z. 2013, MNRAS, 428, 3058
Seager, S., Sasselov, D. D., & Scott, D. 2000, ApJS, 128, 407
Shaw, L. D., Rudd, D. H., & Nagai, D. 2012, ApJ, 756, 15
Sokolowski, M., Tremblay, S. E., Wayth, R. B., et al. 2015, PASA, 32, e004
Sunyaev, R. A. & Zeldovich, I. B. 1980, MNRAS, 190, 413
Tilvi, V., Papovich, C., Finkelstein, S. L., et al. 2014, ApJ, 794, 5
Trac, H., Bode, P., & Ostriker, J. P. 2011, ApJ, 727, 94
Tristram, M., Macías-Pérez, J. F., Renault, C., & Santos, D. 2005, MNRAS, 358, 833
Venemans, B. P., Findlay, J. R., Sutherland, W. J., et al. 2013, ApJ, 779, 24
Voytek, T. C., Natarajan, A., GarcÃŋa, J. M. J., Peterson, J. B., & LÃşpez-Cruz, O. 2014, The Astrophysical Journal Letters, 782, L9
Willott, C. J., Delorme, P., Reylé, C., et al. 2010, AJ, 139, 906
Worseck, G., Prochaska, J. X., Hennawi, J. F., & McQuinn, M. 2014, ArXiv e-prints [arXiv:1405.7405]
Wyithe, J. S. B. & Loeb, A. 2004, Nature, 432, 194
Wyithe, J. S. B., Loeb, A., & Carilli, C. 2005, ApJ, 628, 575
Zahn, O., Reichardt, C. L., Shaw, L., et al. 2012, ApJ, 756, 65
Zarka, P., Girard, J. N., Tagger, M., & Denis, L. 2012, in SF2A-2012: Proceedings of the Annual meeting of the French Society of Astronomy and Astrophysics, ed. S. Boissier, P. de Laverny, N. Nardetto, R. Samadi, D. Valls-Gabaud, & H. Wozniak, 687–694
Zel'dovich, Y. B., Kurt, V. G., & Syunyaev, R. A. 1969, Soviet Journal of Experimental and Theoretical Physics, 28, 146